INFORMATION TO USERS

This manuscript has been reproduced from the microfilm master. UMI films the text directly from the original or copy submitted. Thus, some thesis and dissertation copies are in typewriter face, while others may be from any type of computer printer.

The quality of this reproduction is dependent upon the quality of the copy submitted. Broken or indistinct print, colored or poor quality illustrations and photographs, print bleedthrough, substandard margins, and improper alignment can adversely affect reproduction.

In the unlikely event that the author did not send UMI a complete manuscript and there are missing pages, these will be noted. Also, if unauthorized copyright material had to be removed, a note will indicate the deletion.

Oversize materials (e.g., maps, drawings, charts) are reproduced by sectioning the original, beginning at the upper left-hand corner and continuing from left to right in equal sections with small overlaps.

Photographs included in the original manuscript have been reproduced xerographically in this copy. Higher quality 6" x 9" black and white photographic prints are available for any photographs or illustrations appearing in this copy for an additional charge. Contact UMI directly to order.

Bell & Howell Information and Learning
300 North Zeeb Road, Ann Arbor, MI 48106-1346 USA

UMI®
800-521-0600

Enhancement of Crashworthiness in Car-Truck Collisions using Damped Under-ride Guard and Composite Crush Elements

Mahesh Balike

A Thesis

in

The Department

of

Mechanical Engineering

Presented In Partial Fulfillment of the Requirements
for the Degree of Doctor of Philosophy at
Concordia University
Montreal, Quebec- H3G 1M8

June 1998

ABSTRACT

Enhancement of Crashworthiness in Car-Truck Collisions using Damped Under-ride Guard and Composite Crush Elements

Mahesh Balike

Concordia University, June 1998

A systematic study is performed to understand the dynamics of collisions involving a modern light weight passenger car and a heavy freight vehicle and to design an improved crash energy management system to reduce the severity of collisions. A concept of an energy dissipating under-ride guard is analytically modeled and the performance potentials are investigated under direct and oblique impacts to enhance the crashworthiness of automobiles involved in collisions with heavy freight vehicles. The under-ride guard is analytically modeled incorporating non-linearities due to asymmetric damping, stiffness, clearance spring and kinematics of linkages, using the principle of conservation of momentum and Lagrangian dynamics. Hardware-in-the-loop tests are performed to evaluate the impact energy dissipated by the damper and to verify the proposed model. The performance benefits of the proposed guard are investigated using a performance criterion based upon the magnitude of intrusion of the car mass, peak car mass acceleration, and dissipated energy. A multi-variable design optimization is performed to minimize the magnitude of intrusion and peak acceleration, and maximize the energy dissipated by the damper.

A lumped parameter model of a lightweight vehicle is further formulated to study the car-to-truck collision and is analyzed under impacts with conventional and damped under ride guards. The dynamic response characteristics of different lumped masses subject to direct impacts at different velocities are analyzed and the guard parameters are

optimized to achieve minimum peak acceleration level. A detailed finite element model of the car structure is further developed using DYNA3D and an elastic-plastic analysis of the car-to-under-ride guard is performed. The results obtained using the rigid body, lumped parameter model and the finite element analysis are discussed to illustrate the relative merits of the methods. The crashworthiness of the automobile impacting heavy freight vehicles is further enhanced by incorporating crush elements to absorb the impact energy. Experimental studies are conducted to enhance an understanding of the crash behavior, energy absorption capacity and the strain rate effect on the energy absorption capacity of crush elements made of different composite materials. The advantages of using crush elements made of composite materials to reduce passenger casualty are investigated through analysis of lumped parameter and finite element models. The results of the study show that the severity of a crash involving an automobile and a heavy vehicle can be significantly reduced by the proposed

To

Meghana

ACKNOWLEDGEMENTS

If there is somebody I have to mention first, it has to be Dr. R.B. Bhat, who inspired me to enter the world of research. It would have been impossible to complete this thesis, without continued support and encouragement by him and his family.

I am grateful to my supervisors, Drs. S. Rakheja and S.V. Hoa for their help, guidance throughout the research work, thesis writing, and financial support. Dr. Rakheja was very tolerant on the liberties I had taken in the English Language while compiling the thesis and he corrected me repeatedly.

I am thankful to all the technical staff of the Mechanical Engineering Department, Concordia University who provided me with invaluable support in both conducting Experiments and analyzing them. Special mention has to be made about Danius Juras, John Elliot, Dale Rathwell, Quy Wang and Joe Hulet. I would like to acknowledge the technical advice by Dr. Rajaligham, help by Mr. Ajai in Hardware-in the-Loop simulation and Mr. Sudheer in the fabrication of composite tubes. Further, I would like to recognize the Concordia University for giving me the opportunity to expand my knowledge and NSERC, FCAR for the financial support during the thesis work.

Most importantly, I would like to divulge the encouragement and support provided by my best friend Meghana in many ways ever since the beginning of thesis work. I am obliged to Meghana for everything she has done including the help in typing the thesis. I can't find a better way of appreciating her and hence I dedicate this work to Meghana.

There are a number of other friends and well wishers who encouraged and backed me on several occasions. I thank Meghana, Pooja, Rashmi, Miki, Rachit, Jasjit, Shradha, Sitaram, Venkatesh, Sriram, Girish, Vijay, Muttu and many others - with whom I shared wonderful times and I shall always treasure those moments.

The most important people in my life – my parents, brothers Prasad and Ravi, sisters Mamatha and Aparna – have been a great source of assurance and strength to me. Special thanks are due to them.

TABLE OF CONTENTS

LIST OF FIGURES

LIST OF TABLES

NOMENCLATURE

a, b, c	Distances to define the contact point with respect to the center of gravity the car mass.
C	Damping coefficient during the compression stroke.
F_d	Force due to damper.
F_k	Force due to primary spring.
F_{st}	Force due to stop spring.
F_x	Contact force along X-axis.
F_y	Contact force along Y-axis.
g	Acceleration due to gravity
k_{11},k_{12}	Primary spring stiffness.
k_{21}	Stop spring stiffness.
l	Distance of the impact point from the guard hinge point.
l_1	Vertical distance of the guard spring attachment from the hinge point.
l_2	Horizontal distance of the guard spring attachment from the hinge point.
l_3	Stop spring gap.
m_c	Mass of the car
m_{c1}	Car body mass
m_{c2}	Car engine mass.
m_{c3}	Suspension and transmission mass.
m_{c4}	Car bumper mass.
m_{c5}	Crush element attachment mass.
m_b	Under-ride guard bumper mass.

m_d	Under-ride guard drop arm mass.
n_c, n_e	Damping reduction factors related to blow off damping in the compression and rebound strokes.
p	Ratio of rebound to compression damping coefficient.
S_1	Deflection of primary spring.
S_2	Deflection of stop spring.
v_0	Initial speed of the car.
v_c, v_e	Blow off velocities of the damper in the compression and rebound strokes.
$x_b, \dot{x}_b$	Displacement and velocity of the contact point on the under-ride guard.
$x_c, \dot{x}_c, \ddot{x}_c$	Displacement, velocity and acceleration of the car mass.
$\phi, \dot{\phi}, \ddot{\phi}$	Yaw displacement, velocity and accelerations of the car.
η	Non-dimensionalized mass of the car.
μ	Coefficient of friction for the contact surface.
$\theta, \dot{\theta}, \ddot{\theta}$	Angular deflection, velocity and accelerations of the guard.
ψ	Under-ride guard spring-damper attachment angle with horizontal.

CHAPTER 1

LITERATURE REVIEW AND SCOPE OF THE DISSERTATION

1.1 INTRODUCTION

Study of crash safety of road vehicles encompasses systematic investigations of excitations and various component characteristics, such as excitations attributed to different types of collisions, occupant behavior during crash, vehicle damageability and energy absorption properties, and vehicle aggressiveness towards other vehicles and pedestrians. The degree of damage incurred by the vehicle and hence the occupant casualty depends upon many factors, such as the severity and type of accident, the relative weights and dimensions of the two vehicles involved in the collisions, the relative speed, and the energy absorption capacity of the structure. Highway accidents involving a car-to-heavy vehicle collision, specifically, pose a unique challenge due to high ground clearance and inertia of the heavy vehicle. Such collisions present an unreasonably high risk of fatalities and injuries among the occupants of the automobile, which is primarily attributed to: (i) the high kinetic energy, the disproportionate mass, size and power-to-weight ratio of the heavy vehicle; and (ii) under-running of the automobile structure under the heavy vehicle structure due to high ground clearance of the heavy vehicle. While the current trends are directed towards design of lighter passenger vehicles, to address concerns related to environment and energy conservation, the freight transportation sector has indicated continued interests for further relaxation in

weights and dimension regulations for enhancing the transportation economy. Furthermore, the population of heavy vehicles on our highways has been increasing steadily. The crashworthiness of automobiles thus necessitates enhanced efforts to improve the safety of the highway and the occupants. In collisions involving an automobile and a heavy vehicle, the energy absorbing capabilities of the car structure are severely reduced, since the heavy vehicle structure is located well above the energy absorbing car structure [1]. The car tends to wedge under the heavy vehicle structure in such cases. The need to develop effective crash energy absorbing systems has thus been emphasized to enhance the highway safety associated with car-to-heavy vehicle collision [2].

The development of an effective crash-energy management system involves a systematic study to establish an understanding of the dynamics of such collisions. This dissertation research is thus directed towards analysis of dynamics of collisions, the associated energy flow, stress distribution due to dynamic loads and forces transmitted to the passenger compartment during an impact with the conventional truck guards using an elastic-plastic analysis. An energy management system based upon partial dissipation of energy is proposed. The crash safety maybe further enhanced by reducing the degree of under-ride, or the intrusion of the car under the heavy vehicle, which is known to be the primary cause of fatalities encountered in such accidents. An under-ride guard comprising pendulum type drop arms, bumper beams, nonlinear springs and asymmetric dampers, is thus proposed, to reduce the magnitude of intrusion and to dissipate part of the crash energy. The flow of crash energy during direct and oblique impacts with conventional and proposed guards is investigated through development and analysis of

lumped-parameter and finite element models. A performance criterion based upon intrusion, passenger safety and energy dissipation is formulated and analyzed to derive optimal design parameters of the proposed guard. A hardware-in-the- loop test method is further developed to achieve limited validation of the proposed energy management system. The energy absorption properties of different crash elements are further analyzed to enhance the crash safety of the automobile.

1.2 REVIEW OF RELEVANT LITERATURE

Highway collisions involving automobiles are known to pose high risks to the fatalities and injuries among the occupants. In view of increasing volume of highway traffic and efforts in development of lightweight automobiles, the FMVSS (Federal Motor Vehicle Safety Standards) [3] has formulated a series of design and test codes to enhance the crash safety. The FMVSS code for different types of barrier impact tests was established in early 70s, which has been further revised many times with minor modifications [3,4,5]. Some of the safety standards developed to assess normal, and oblique front end barrier impacts, and front, side and rear end collisions are summarized in Table 1.1 [3,4]. Sections 571.203 and 571.204 limit the maximum deflection of the steering column during a collision test [4]. The occupant injury criteria outlined in section 571.208, propose limits on the maximum accelerations and forces transmitted to different parts of a test dummy evaluated using the test procedure described in SAE J944 [4]. The standard proposed upper limits of accelerations of 36g and 60g transmitted to the driver's head and chest levels, respectively, under direct and oblique front and side impacts. The standard further proposed a maximum intrusion of 45 *cm* under a 30 *cm* diameter static

pole penetration test, and 12.7 *cm* under a specified load applied at the front corner of the roof. A number of similar test codes have also been proposed and adapted in many other countries.

Table 1.1: Federal Motor Vehicle Safety Standards (FMVSS) Affecting Structures (Energy absorption bumpers not included).

FMVSS Section	Structures	Test Specification	Performance Limits
571.204	Front	Front Barrier impact at 48 *km/h* (30 mph)	Maximum rearward dynamic displacement of steering column of 12.7 *cm* (5 *in*).
571.208	Front, Side, Roof	Front and 30° oblique impact at 48 *km/h*; Side barrier impact at 32 *km/h*; Rollover at 48 *km/h*	Occupant injury criteria Maximum acceleration at the - driver head level : 36g - driver chest level : 60g
571.214	Doors	Static 30 *cm* (12 *in*) diameter pole penetration	Maximum intrusion of 45 *cm* (18 *in*) under a specified load history.
571.216	Roof	Static front roof corner load	Maximum intrusion of 12.7 *cm* at specified load history.

The design of vehicles satisfying the federal requirements was traditionally achieved by repetitive barrier impacts performed under controlled conditions [6,7]. The poor efficiency and high cost associated with development of various prototypes and repetitive tests prompted the development of different crash analysis models of the vehicles. The crashworthiness of automobiles has been extensively investigated using different analytical models of varying complexities [8,9]. Many studies have reported enhancement of crashworthiness of vehicles through design of structures [10-12] and development of crash elements [13]. The enhancement of crashworthiness of automobiles

involved in collision with the heavy vehicles necessitates additional consideration of the heavy vehicle design factors. Such studies involve systematic investigations into collision dynamics, crashworthiness of the automobile and barrier structures, energy flow analysis, and design of the under-ride guard. The reported literature is reviewed and grouped under appropriate topics in subsequent section in order to formulate the scope of the dissertation research.

1.2.1 Crash Simulation Models

A large number of crash simulation models of varying complexities have been reported in the literature. Melosh and Kelly [14] described different analytical techniques for the evaluation of crashworthiness of vehicle structures. Various crash simulation models can be grouped in three broad classes based upon their modeling approach: lumped parameters, finite element and hybrid models.

LUMPED PARAMETER MODELS

The lumped parameter models are perhaps the most widely used analytical tools for the design of crash-energy management system for automobiles. Such models are formulated upon integrating the distributed inertial and stiffness characteristics of the components into various lumped masses and springs. These models are relatively simple one-dimensional models, where the crush energy absorption characteristics of the structural members are represented by non-linear force-deflection formulations derived from static crush tests [15-20]. Although the reported lumped parameter models are very similar in their basic principles, these models may be further classified into two different groups based upon the objectives of the analysis to provide analysis for evaluation of

crashworthiness. The first group of models is developed to provide an evaluation of crashworthiness, and it incorporated the structural behavior suited to derive reasonably accurate results for a specific accident condition [15-17]. The second group of models is developed with an objective to perform design analyses, and thus need to incorporate more accurate characteristics of the major structural components. Such models are frequently used to study the influence of variations in the component characteristics to seek near optimal designs [18-20].

A number of simple models have been reported for evaluating the crashworthiness of vehicles through simulation of primary structure behavior [15-17]. These models incorporate non-linear restoring properties of structural elements, in the form of either a one-sided spring element or hysteretic load-deformation histories. The body and engine are generally treated as either one lumped mass or two individual lumped masses, while only a limited number of models include the rate dependent effects [16], and linear damping elements [15]. Figure 1.1 illustrates a typical model of a 1000 kg vehicle subject to a barrier impact, which falls into the first group of lumped parameter models [16]. The equations of motion of such models are easily formulated using D'Alembert's principle and solved as an initial value problem. These models have been invariably used to infer the crashworthiness of vehicles as a function of lumped stiffness and mass parameters, and type of collision.

An early model for simulation for crashworthiness design was first proposed by Kamal [21] in 1970. The model was developed for a front engine and a rear wheel drive vehicle with a separate frame construction. The vehicle fore-structure was represented by

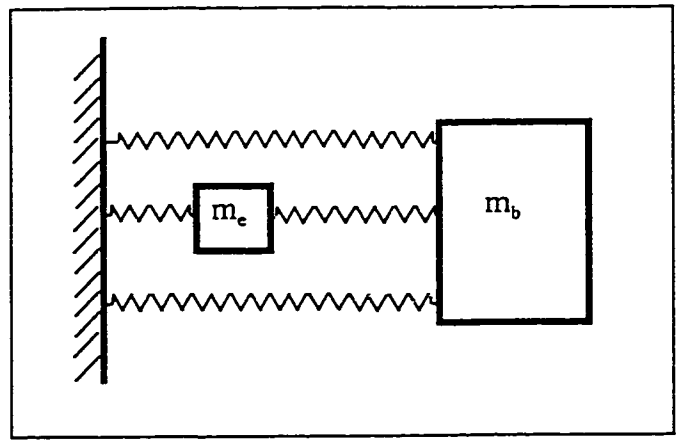

Figure 1.1: Tani and Emori [16] barrier impact model.

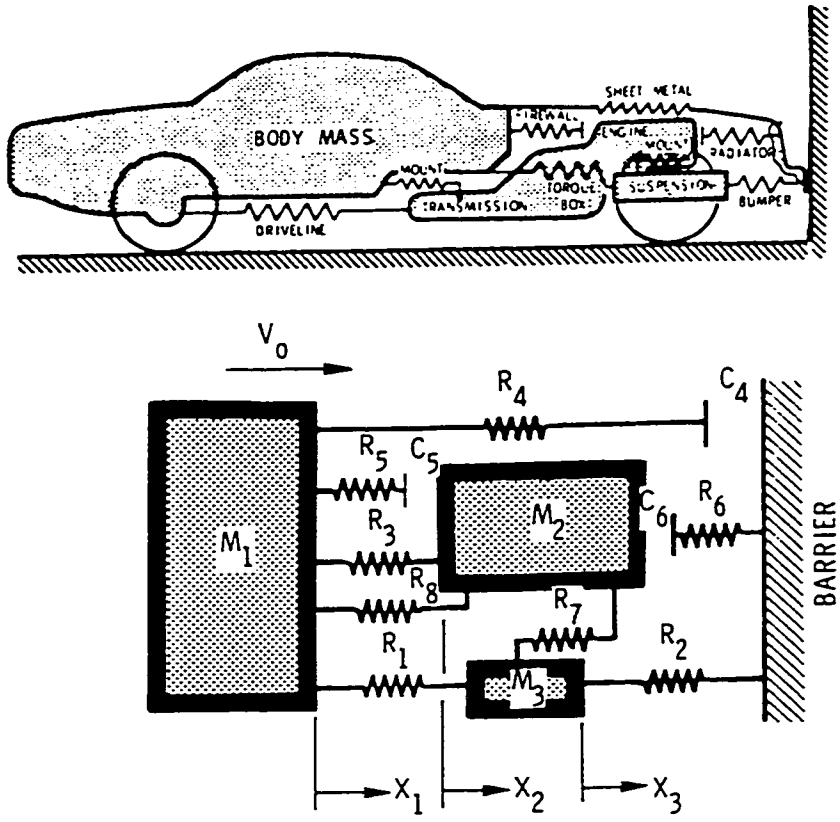

Figure 1.2: Vehicle Barrier Impact Model by Kamal [21].

eight different significant members and three lumped masses, which may undergo deformation during impact, as shown in Figure 1.2. The study further assumed that the different members subject to inertia and reaction do not necessarily collapse in a progressive manner, from front to the rear of the vehicle. The members subject to inertia and reaction forces exceeding their ultimate load limit will experience failure first, irrespective of their geometric location. The dynamic force functions in the study were attained from the static force functions super imposed by a linear dependence of the rate of displacement.

The early study by Kamal [21] has been followed by continuous efforts to develop model applicable for different types of collisions, such as bumper to barrier, frontal-frontal, rear and side impacts. Kuang-Huei Lin [22] extended the work done by Kamal [21] to derive a rear-end barrier impact simulation model for a uni-body passenger car. The proposed model consisted of an idealization of the rear end barrier impact situation by five lumped masses and seven deformable non-linear spring elements. An interesting approach to study the side impact was reported by Wingenbach and Schwarz [23] by incorporating the side door intrusion of an experimental safety vehicle. The model consisted of a superposition of elastic and plastic door beam action, elastic and plastic sheet membrane stretching, and crush of the honeycomb core. The load-deflection characteristics of the honeycomb structure were determined empirically. The model was proven to be quite effective in predicting the intrusion within 0.625 *cm* for a 17.8 *cm* penetration during a side impact against a 33 *cm* diameter rigid pole at a speed of approximately 24 *km/h*.

The above studies considered the design and crashworthiness analysis under direct impacts only. Only few studies have attempted to investigate the crash behavior under oblique impacts using lumped parameter models, due to complexities associated with modeling of crush behavior under such impacts. A simple crash analysis model to simulate a two-car oblique side impact has been proposed by Tomassoni [24]. Although a large number of comprehensive finite element models have been developed to study the crash behavior of automobiles [25-30], the lumped parameter models are frequently being utilized to predict the vehicle response. The effectiveness of such models, however, is limited for the study of new concepts for which neither the crush characteristics nor the collapse mechanisms are known.

FINITE ELEMENT MODELS

The Finite Element (FE) solution to the crash analysis offer considerable advantage over the lumped parameter models, since the changing crush resistance of different structural elements can be analyzed more accurately. The FE models further permit the analyses based upon the geometry and properties of the individual structural components. The variable dynamically inter-dependent stiffness characteristics of the components can be conveniently formulated to derive the strain, stress, and force response characteristics, which are then used to study the crash performance of individual components and the entire system. A FE model of an automobile, when validated can serve as an effective design tool to determine near optimal material and geometric design parameters for enhancement of the crash performance.

Non-linear finite element codes such as DYNA3D [31] and DYCAST [32] have been developed with an intent to simulate the crash behavior of structures on a component and/or subsystem level. Finite difference codes [33,34] were developed, nearly two decades before the finite element codes, to analyze two-dimensional plastic deformation problems involving large deflections. The finite element codes, however, have replaced the finite difference codes in recent years due to their many advantages over the finite difference methods. Although, a larger number of FE models of different vehicles have been reported in the literature [25-32,35-37], the majority of these models were used to perform the durability and fatigue analyses [32-35]. The application of FE methods for the crash analysis was proposed by Melosh and Kelly [14]. One of the earliest applications of the finite element analysis technique for the crash analysis, for the analysis of vehicle crash behavior was reported by the Grumman Aerospace Corporation in 1981 [25]. Winter *et al.* [25] performed a 48 km/h frontal barrier impact analysis of a rear-engine automobile with fiber reinforced resin body using one of the earlier versions of the non-linear structural dynamic finite element code, DYCAST. The FE model was developed for the fully loaded conditions including curb weight, and weights due to occupant, cargo and the luggage. Triangular membrane elements were used to form the body panels and beam elements were used for body stiffeners, door-posts, body cross members and the roof. Some of the structural parts (bumper, front-end energy absorbing struts, radiator-fan assembly, tire and wheel assembly etc., were represented by energy dissipating non-linear spring elements, while their force-deflection characteristics were obtained through tests or analyses.

The study concluded that the glass fiber reinforced front-end structure does not dissipate enough energy by itself or provide enough crush resistance under a 48-km/h impact. The vehicle was successfully brought to rest with the addition of energy absorbing struts, while failures in the central tunnel, the primary load path through the under-body, were encountered. The study thus proposed many design alternatives to achieve a strong and ductile load path as a backbone through the body, such as changing the tunnel structure to steel, reinforcing the existing cross-members, and attachment of the front end of the struts to the steel cross members. The crash analyses of different types of vehicles subject to different accident situations, performed using finite element codes have been extensively reported in the literature [25-32,38]. Some of these studies have been directed towards enhancing the computing speed for crash analyses of large-scale structures. One such effort was the development and application of DYNA3D software for the crashworthiness analysis of large scale structures, realized by Hellcats *et al.* of the Lawrence Livermore National Laboratory and Igarshi *et al.* of the Suzuki Motor Company Ltd. in 1986 [28]. While most of the finite element models consisted of 10000 to 50000 elements, the resulting crush distance and the magnitude of force transmitted compared well with the experimental results obtained at the Suzuki Research Laboratory [28].

The finite element programs, such as DYNA3D were integrated by General Motors Corporation in 1985 to study the crashworthiness of the structures [29], while the initial studies were limited to the component level, a half vehicle model was developed in 1987 to study the response of the forward load bearing structure of a car with engine and transmission to a frontal barrier impact [28]. The finite element model of a full vehicle

incorporating the power plant components was further developed and analyzed under a frontal barrier crash to evaluate the resource requirement and the applicability of the results to the design release process [29]. A number of other models have also been reported to study the crashworthiness of vehicles under different crash situations using DYNA3D [39-42].

HYBRID MODELS

The hybrid models [43-45] attempt to combine the simplicity of the lumped parameter modeling approach with the flexibility and the advantages of the finite element method. The hybrid models were first proposed by Mclvor [43] in 1974 to study the crash behavior of automobiles. In this method, the lumped-parameter model is generalized to either two or three dimensions depending upon the crash situation. Similar to the FE models, hybrid models are load-path dependant, since they employ a priori derived spring representation for the structural members.

The hybrid methods have provided many promising developments in the area of predictive techniques for crash energy absorbing sheet metal components. The studies reported by Weierzbicki [46], Abramowicz [47] and others [48-50] are specifically notable, since they address the important design related issues. These studies have developed simple design oriented formulations to predict the crash behavior of thin walled structural members, which permit the determination of their size and stability during crush. Wierzbicki [46] and Abramowicz [47] derived these formulations directly from the assumed collapse and folding mechanisms, while the other studies have also employed buckling considerations enhanced with experimentally determined coefficients

[48,50]. The hybrid analysis technique has been further extended to the systems level by Mahmood *et al.* [51], using beam type members.

1.2.2 Energy Absorbing Members

Vehicle structures are designed to absorb crash energy through plastic deformation of structural components, while maintaining structural integrity of the passenger compartment. The structures of a passenger car, designed for normal service loads, do not exhibit sufficient energy absorbing capacity to dissipate the kinetic energy, developed in a 48km/h frontal barrier crash test as recommended in FMVSS [3] in a controlled manner. The passenger compartment may thus deform considerably posing high risks of fatality and injuries among the occupants. Furthermore, the Federal Agencies have been considering increasing the barrier test speed limit from the present 48km/h to 60km/h or more [52].

Additional crash elements are thus frequently employed to enhance the energy absorption properties of the front end during a crash [53-57]. These crash elements are considered non-structural components, since they are extended to undergo significant crush during an impact such that maximum possible crash energy is absorbed. Figure 1.3 illustrates two crash elements located behind the bumper [58]. This approach allows the vehicle's functional components to absorb certain energy through deformation within a specified crash distance, while the remaining energy is absorbed by various add-on energy absorbing devices placed in series with the existing load paths. The crush behavior of an automobile is strongly related to its inertia and energy absorption properties of the structure. The additional crush elements are thus designed as a function of the specific

vehicle mass or energy level, such that the total vehicle crush and the passenger compartment deformation would not exceed their respective allowable levels. The factors, such as the loading direction, packaging functional clearances, and service accessibility, may require further considerations in the design process. Light weight crash elements and high specific energy absorption capacity are considered desirable, such that the vehicle inertia does not increase significantly. For example, composite materials or honeycomb structures may thus be desirable for the energy absorption devices.

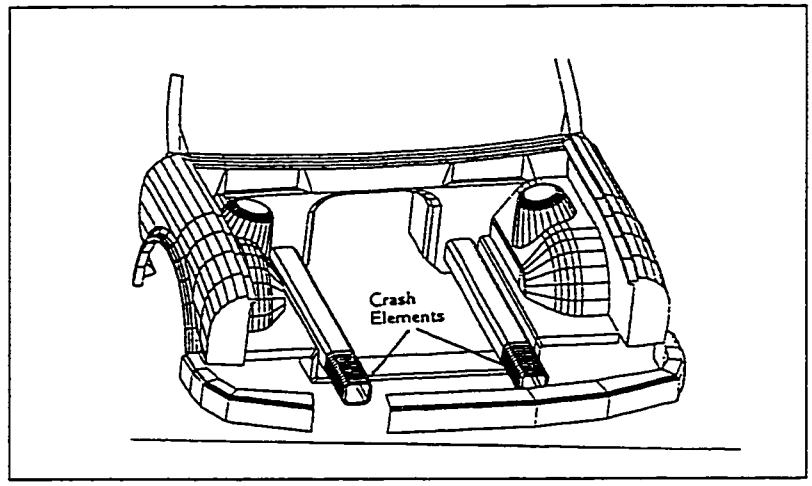

Figure 1.3: Use of crash elements in automobile [58].

Many of the early experimental safety vehicles employed additional crash elements in the form of hydraulic cylinders, foam and honeycomb structures to enhance the impact energy absorption capabilities [53-56]. Similar mechanical devices have also been investigated for application in aircraft's to improve their energy absorption capability [57]. The effectiveness of the add-on energy absorption devices for automotive

vehicles was analytically investigated in 1989 by Lin and Mase [59]. The design was primarily based on the performance requirements related to energy absorption, and crush distance evaluated from the vehicle-barrier impact analysis. An analytical model based upon the lumped parameter model proposed by Kamal [21] was developed to analyze the energy absorption capacity of a car with and without the crash members. From the analysis of the model, comprising five lumped masses and thirteen nonlinear spring elements, it was concluded that the energy absorption capacity of simple tubes and honeycombs in the axial crushing modes is far more effective than that of complex devices, such as an inversion tube.

Many references [60-70] can be cited in the literature where authors have examined the energy absorption capability of different composite materials. With the aid of several experiments, the majority of these studies have concluded that the energy absorption capability of composite materials is considerably greater than that of conventional automotive materials, which is primarily attributed to the difference in their crush behavior [60,67]. Although, a precise theory of crack initiation and propagation in composite materials has not been established, it has been shown that the composite materials failure comprises several micro-fracture phenomena, such as fiber breakage, matrix cracking, de-bonding, de-lamination [66,71], etc. Each one of these micro-fracture phenomena absorb certain amount of energy, which yields enhanced total absorbed energy when compared to that absorbed by the deformation of metals. The energy absorption capacity of different conventional and composite materials have been compared in many studies using different measures, such as specific energy to weight ratio, specific energy to cost ratio, and specific energy to volume ratio [71-73]. The

results of these studies revealed that a glass fiber/epoxy composite material is the most economical one, which provides reasonably good energy absorption.

The effectiveness of various crush elements made of composite and conventional (steel and aluminum) materials [71-75] in increasing the crashworthiness of lightweight vehicles have also been reported in few studies. Kerth and Maier [58] presented a brief survey of basic material models for composites crash analysis, which have been implemented into the finite element code DYNA3D. An optimal design of a composite material, tubular structure was proposed for implementation in the front structure of vehicles.

Although many studies have clearly demonstrated the advantages of the composite crash elements, the majority of the test results have been reported under static conditions. Only few studies have attempted to study the high strain rate-crushing behavior of fiber reinforced crash elements [76-79]. These studies have reported inconsistent and conflicting results. Experiment studies of tubular structures made from 0/90 Fabric prepegs, conducted by Thorton [61], showed negligible influence of strain rate on the crushing characteristics. While the tests performed by Kirsh and Jahnie [76] on glass/polyester revealed similar results, the studies performed by Schmueser and Wickliff [77] concluded lower specific energy at higher strain rates. Based on experimental results, Farely [68] concluded that the specific energy of the $(0_2/\pm\theta)$ graphite/epoxy composites is independent of the crash speed, while that of the $(\pm\theta)_3$ graphite/epoxy composites increased up to 30% at a crash speed of 12 m/s. It should be notified that majority of the tests were conducted at strain rates, which are considered lower than those encountered during a crash.

1.2.3 Recent Developments in the Crashworthiness Design

Recent trends in the design of lightweight automobiles have been prompted by many efforts directed towards design and analysis of vehicle structures and crash elements in an attempt to enhance the crashworthiness of road vehicles. Majorities of these efforts have extensively utilized explicit finite element codes coupled with analytical and experimental investigations for design and development. Various modeling and vehicle crash simulation studies performed by the automotive industries have resulted in development of many new elements and analysis algorithms, which have been integrated into the DYNA3D library functions [31,78]. Kecman *et al.* [78] developed a compound beam element with moment-deflection curves for side impact and roof crush analyses using DYNA3D program. The proposed beam element combines the existing Belytschko-Schwer beam element with rotational springs, which exhibit highly non-linear moment-deflection, characteristics in the elastic plastic and deep collapse range.

Tammy [79] revised the well-known planar collision model of the vehicles to study the elastic-plastic collision behavior by introducing elastic rebound after the object approaches the common contact velocity. Kaiser [80] presented some examples of numerical simulation in vehicle safety development using many commercial finite element codes, including DYNA3D. The study proposed some further developments to enhance the benefits of the software, such as post processing of the data in view of the Head Injury Criteria [81], simplified formulation of contact problems, and integration of a data system to exchange and supplement the structural components.

Sheh *et al.* [82] conducted several experiments and developed analytical models using lumped parameter and finite element techniques for an experimental vehicle in

order to evaluate the compatibility and interrelationship of the two numerical methods for crashworthiness simulations. The objective of the numerical simulation was to simulate the vehicle crashworthiness under a 48 *km/h* frontal impact at 0°. The study utilized LS-DYNA3D in view of its capability to handle both nonlinear FE as well as rigid body dynamics analyses. The study concluded that finite element and lumped parameter analyses, and physical testing can be effectively used in conjunction with each other to provide meaningful and flexible crashworthiness analysis.

The effectiveness of simple lumped parameter and framework models has been further illustrated by Walker *et al.* [83] for vehicle crashworthiness and occupant protection analysis under both frontal and side impacts. The vehicle crashworthiness analysis was carried out for all stages through out the design process, using OASYS-DYNA3D. A simplified design approach for the development of crashworthy structure was proposed by Kecman *et al.* [84] based upon integration of system analysis of the impact energy and force transmission chain in a situation of interest, and priorities in the crash management. The priority issues at both the component and the overall assembly levels were discussed for structural and occupant simulations.

Dandekar and Van [85] investigated the barrier impact of automotive bumper systems, using different finite element methods, which compared and evaluated based on experimental data. The study proposed certain important considerations for effective finite element analysis of an automotive bumper system, including: i) transient dynamic analysis to evaluate the impact response of the bumper system; ii) analysis of permanent deformations and plastic damping effects using elastic-plastic material properties; iii)

large deformation analysis of the thin-walled open section of the bumper structure, using shell theory.

Despite a large number of analytical and experimental studies, the effective designs of structure crashworthiness has been limited due to the lack of understanding of the mechanism of load transmission through vehicle structures during a crash. It has been established that a thorough knowledge of load transmission path and the failure mechanism can facilitate the design of load carrying and energy absorbing components [86]. Reid and Sheh [86] presented a load path analysis to gain more understanding of the load transmission mechanism during a crash event. The load-path analysis, carried out using FE analysis, involve the study of variations in the forces and moments transmitted through the structure between the barrier and the passenger compartment [87-90]

1.2.4 Under-Ride Protection System for Heavy Vehicles

A collision between an automobile and a heavy freight vehicle poses severe risks to the safety of the highway, and more specifically to the occupants of the automobile. In nearly all the highway accidents involving heavy freight vehicles and cars, the fatalities and magnitude of injuries can be related to mass, size and rigidity of the heavy vehicles [2]. The effectiveness of energy absorbing capabilities of the car structure is severely reduced in a car-to-truck collision, since the heavy vehicle structure is located well above the energy absorbing structure of the car [1]. The car tends to wedge under the heavy vehicle structure in such cases as shown in Figure 1.4 [91]. Despite many passive and active safety measures, such as air bags improved driver training to avoid accidents in automobiles, nearly 23% of the total car occupant fatalities arise from impacts with heavy

Figure 1.4: Intrusion (under-running) of automobiles during impacts with heavy vehicles.

vehicles [92]. A characteristic of fatal under-run accidents is the high magnitude of intrusion of the passenger compartment of the car. A study of such accidents in U.K. has concluded that approximately 85% of cars involved in collision with heavy vehicles experienced significant intrusion of the front compartment [93]. In such accidents, the effectiveness of the air bags is severely reduced due to associated shear loads.

A survey of highway accidents conducted in Germany concluded that car-to-truck collision account for nearly 52% of highway accidents involving heavy vehicles, as illustrated in Figure 1.5 [92]. Another study performed in Germany further confirmed that nearly 53% of the highway accidents involving heavy vehicles are attributed to passenger cars striking the heavy vehicle [94]. Accident studies in United States and Canada [95] have also reported similar trends in car-to-heavy vehicle collisions. Such accidents are known to cause serious fatalities and injuries among the occupants of the vehicles, as illustrated in Table 1.2. The severity of such accidents is mostly attributed to the degree of intrusion or under-run of the automobile under the heavy vehicle structure.

Table 1.2: Summary of fatalities and injuries resulting from highway accidents involving heavy vehicles - 1991 [77].

Nature of Vehicle and Accident	Number of Deaths	Number of Injuries
Medium/heavy Truck Occupants	659	48000
Occupants of other vehicles involved in collisions with medium/heavy trucks	3764	63000
Pedestrian/cyclists involved in accidents with medium/heavy trucks	426	2000
All accidents involving heavy vehicles	4849	113000
All accidents	40798	3116000

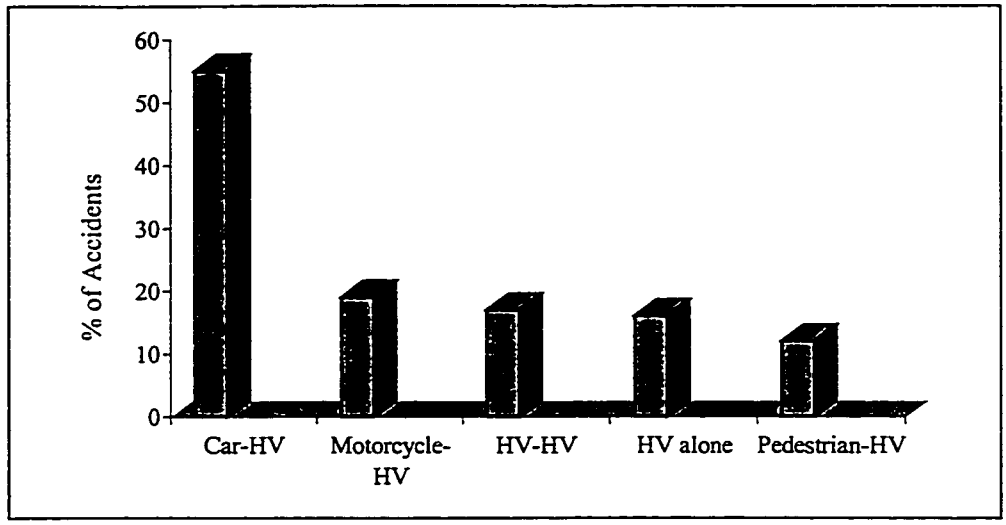

Figure 1.5: Summary of highway accidents involving Heavy Vehicles (HV) [75].

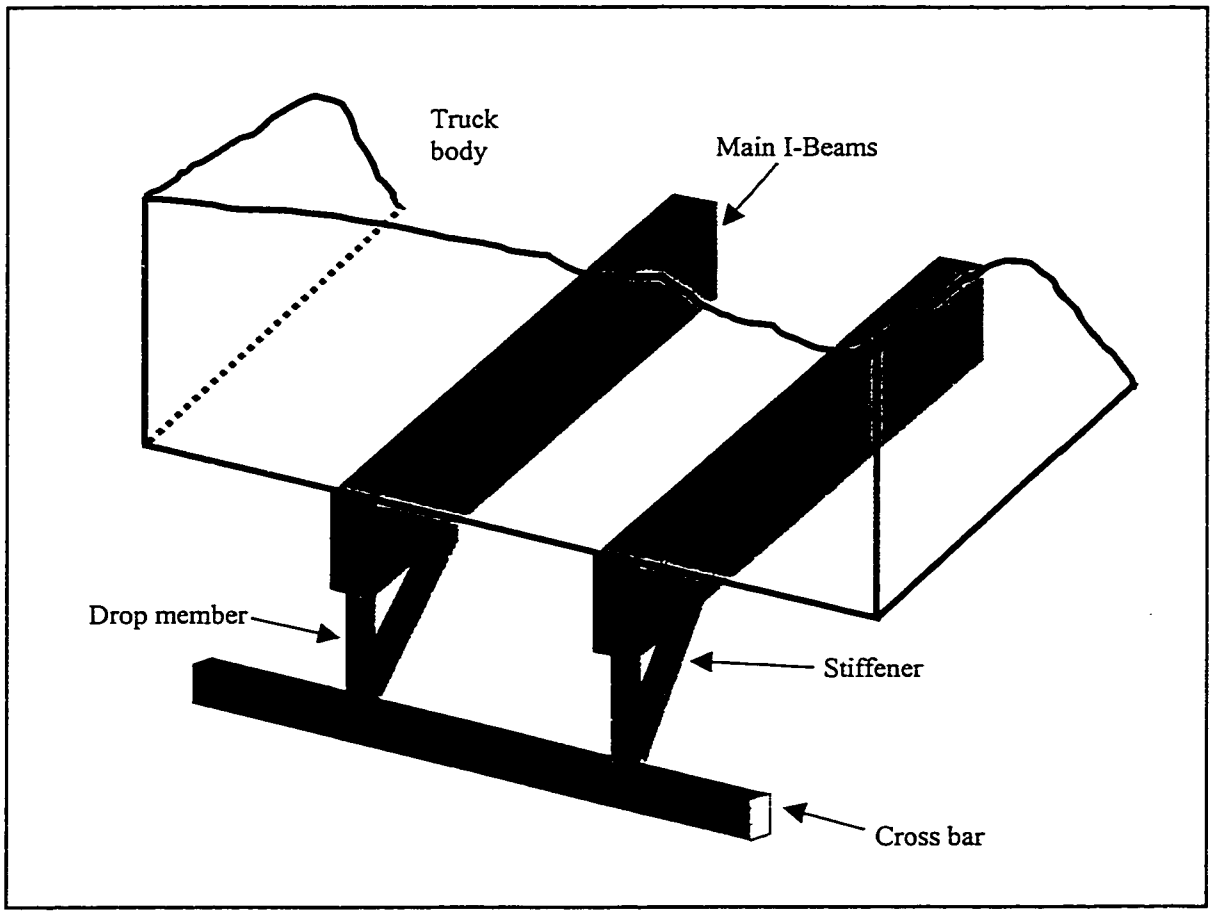

Figure 1.6: Rigid Under-ride Guard at the Rear End of the Trucks and Trailers.

Riley [2] suggested that implementation of a measure to avoid under-running of the car can save nearly 385 lives every year in UK alone. The conventional rigid under-ride guard shown in Figure 1.6, is attached to the chassis with a ground clearance of approximately 80 *cm*, while the ground clearance of most automobile bumpers range from 30 *cm* to 50 *cm* [1]. The impact forces thus occur at a location other than the main energy-absorbing member (bumper) of the car. Although the maximum ground clearance of 55 *cm* has been recently proposed for implementation in 1998, which is still inadequate to avoid the under-riding of the cars [96].

The International Organization for motor vehicles has emphasized that rear, side and front under-ride protection systems for the heavy vehicles can considerably contribute to the attainment of improved highway safety [97]. While majority of the studies conducted in U.S.A., Canada, U.K. and Australia have provided exhaustive data related to highway safety risks associated with car to heavy vehicle collisions, a European study has proposed active safety measures to avoid under-running of cars [98].

Persicke and Child [99] proposed a concept of an energy dissipating under-ride guard comprising drop arms, bumper beam and hydraulic struts to avoid rear under-run, while the ground clearance was maintained identical to that of a conventional guard. From a number of tests conducted on the prototype it was concluded that the proposed guard subject to a direct impact at 48 km/h yields reduced levels of acceleration and force transmitted to the head and the neck of the dummy. The prototype guard did not comprise an energy-storing device in order to minimize the storage of energy during the crash and possibility of repetitive impacts.

Murray [1] investigated various crash situations involving cars and trucks and proposed the necessity of energy absorbing under-ride guards. The study based on analysis of a simple rigid body dynamics model, proposed the concept of a damped under-ride guard and its energy absorption requirements. Although the energy absorption through deformation of a guard is highly desirable, study of crash behavior of passenger cars against beam like structures representing the under-ride guard, by Beerman, proposed the use of a sufficiently rigid guard to prevent the under-run [100]. The study further illustrated the adverse effects of impacts occurring at locations other than the car bumper, and emphasized the design of under-ride guard to allow the impact to occur on the primary energy absorbing member of the automobile. While the need to introduce front, side and rear under-ride guards has been emphasized to enhance the highway safety, the additional weight of the extremely long guards has been a limiting factor in the implementation of such guards. Alternatively, light weight rear and side under-ride guards in conjunction with hydraulic dampers with enhanced energy dissipation capabilities, may yield improved highway safety and thus reduce the risk of fatalities and body injuries.

1.3 SCOPE AND OBJECTIVES OF THE DISSERTATION RESEARCH

The review of literature presented in the previous section, clearly revealed that majority of the analytical and experimental research efforts on enhancing the highway safety associated with collision accidents have been directed in two areas: (i) car-to-barrier impacts; and (ii) car-to-car impact. Although, unreasonably high risks to the occupant of the automobile involved in a car-to-truck collision have been well documented, only few

efforts have been made to enhance the safety of the driver in such accidents. It has been further established that energy absorption characteristics of an automobile are considerably reduced when involved in a collision with a heavy vehicle with relatively high ground clearance. Upon recognizing the need to minimize the intrusion (under-run) of the automobile under the heavy vehicle structures, the desire to design and implement front, side and rear under-ride guards has been emphasized.

While a concept of an energy dissipating under-ride guard has been proposed, systematic studies on energy absorption and dissipation characteristics of the coupled guard-automobile system have not been reported in the literature. The design of an effective lightweight energy absorbing under-ride guard necessitates systematic investigations involving impact analysis of coupled automobile-guard system incorporating kinematics and dynamics of the linkages, optimization studies to determine asymmetric nonlinear damping, and force-deflection characteristics of the guard, and visco-elastic properties of the bumper beam. The scope of the thesis dissertation is thus formulated to develop effective analytical models of the coupled system, and to carry out design optimization to enhance the energy absorption and dissipation capabilities of the guard, under varying angles of impacts and speeds. The absorption or dissipation of high crash energy involves careful energy management. While a part of the crash energy be absorbed through plastic deformations of the proposed guard and the automotive structure, a portion of the energy can be dissipated through an asymmetric hydraulic damper. The enhancement of energy absorption characteristics further necessitates development of effective crash elements.

In a flexible under-ride guard, the dissipation of crash energy may be realized through hydraulic dampers with either large stroke or very high damping properties. A large damper stroke can yield high intrusion of the car structure, while a short stroke may result in a guard with relatively high rigidity. While a highly damped guard may result in extremely high acceleration of the car and its occupants under an impact, a lightly damped guard will lead to reduce energy dissipation and increased intrusion. The selection of energy dissipation properties of the guard thus requires multi-variable optimization studies to minimize the intrusion and to maximize the dissipated energy. The crashworthiness of automobiles involved in collision with heavy vehicles can be enhanced using additional crash elements, which may further reduce the force transmitted to the passenger compartment. The crash energy management and investigation of crash energy absorption performance of composite material crash elements form another scope of the dissertation research.

1.3.1 Objectives of the Dissertation Research

The overall objective of the dissertation research is to enhance crashworthiness of an automobile subject to an impact with a heavy vehicle through systematic analysis of a flexible under-ride guard and composite material crash elements. The specific objectives of the study are:

a) Study the energy absorption characteristics of a conventional rear under-ride guard of a heavy vehicle using elastic-plastic analysis under different impact conditions.

b) Configure a rear under-ride-guard protection system comprising a horizontal bumper beam, drop arms, and the energy restoring dissipating devices.

c) Formulate a set of performance criteria comprising the magnitude of intrusion, rebound velocity, force transmitted and the energy absorbed, to perform relative evaluations of the guards.

d) Develop an analytical model of the protection guard incorporating kinematics and dynamics of the linkages, asymmetric nonlinear damping properties, nonlinear force-deflection characteristics of the restoring element. Analyze the performance characteristics of the proposed design analyzed for direct and oblique impacts through development and analysis of lumped-parameter and finite-element models.

e) Formulate and solve optimization problem comprising weighted functions of intrusion, rebound velocity, force transmitted to the passenger compartment of the lightweight vehicle and the energy dissipated by the under-ride guard damper, to derive optimal parameters of the guard.

f) Develop a Hardware-in-the-Loop test algorithm to measure the dissipated energy under different impacts, and validate the analytical model of the guard.

g) Fabricate different composite material tubular crash elements, and perform crash tests to study their crushing mechanisms and energy absorption characteristics and select suitable fiber/matrix combinations for the crash elements.

h) Develop mathematical model of the crash elements made of composite materials to predict their energy absorption capacity and validate using experimentally obtained results.

i) Investigate the crash energy absorption performance of the car structure with the addition of crash members under different impacts against the proposed under-ride guard through development and analysis of a lumped-parameter model.

j) Investigate the crashworthiness performance of crash elements and the flexible under-ride guard through elastic-plastic analysis using DYNA3D software.

1.4 THESIS ORGANIZATION

One-dimensional analytical models for the analysis of impact of car with the proposed energy dissipating under-ride guard are developed and presented in Chapter 2 incorporating non-linearities due to asymmetric damping, stiffness and kinematics of linkages, using the principle of conservation of momentum and Lagrangian dynamics. The analytical model is developed to incorporate different angles of impact and

coefficients of friction between the automobile bumper and the under-ride guard. A performance criteria based upon the magnitude of intrusion of the car mass, car mass acceleration, and dissipated energy is developed to investigate the performance benefits of the proposed guard at different impact angles. A multi-variable design optimization is performed to minimize a weighted function of performance variables and to determine the optimal asymmetric damping and stiffness properties of the guard. A brief description of the non-linear finite element code DYNA3D is given along with the strain-rate sensitive material models.

Chapter 3 presents the implementation of Hardware-in the-Loop (HIL) simulation technique to validate the analytical models developed in Chapter 2 for the impact between light weight and heavy freight vehicles. The experimental setup, software and hardware interface and the test methodology used to perform the HIL simulation are described in detail. The performance of conventional under-ride guard impacted by a rigid body is analyzed using different models in DYNA3D and the results are presented. The performance of proposed guard impacted by a car mass at different angles is discussed in detail using the results obtained from the analytical models developed in Chapter 2. The optimal parameters of the guard are obtained for different constraint sets and the benefits of optimized guard are discussed.

The performance of the proposed energy dissipating under-ride guard is further studied using lumped parameter and FE models of the car in Chapter 4. In the lumped parameter model, the car body is represented by discrete masses connected by non-linear springs and the responses of different masses at different impact velocities are obtained in terms of the performance criteria. A detailed finite element model of the car structure

is developed using non-linear explicit FE code DYNA3D. An elastic-plastic analysis of the car-to-under-ride guard impact is performed at different velocities and the performance characteristics of the guard are discussed comparing the results with lumped parameter model.

In Chapter 5, fabrication and experimental studies for the development of crash energy absorbing members is discussed in detail. Circular tubes of three different material types, namely, Kevlar/epoxy, graphite/epoxy, and glass/epoxy, tailored to the required size, are fabricated in laboratory. The tubes are tested under static and dynamic loading conditions to assess their energy absorption capabilities at different loading conditions. The results are compared and suggestion for the selection of material type for the energy absorbers is given at the end of the chapter.

The potential benefits of the addition of crush elements incorporated within the front end of an automobile are studied in Chapter 6, using both lumped parameter and the finite element models. The crush elements are represented by non-linear spring elements having measured force-displacement characteristics discussed in Chapter 5. Simulations are performed for vehicle impacts with both conventional rigid and the energy dissipating proposed under-ride guards. The advantages of crush elements along with the proposed under-ride guard are studied in terms of the performance criteria defined in Chapters 2 and 4.

Finally, the conclusions derived from the study together with the highlights of the dissertation and recommendation for further development of the proposed guard are presented in Chapter 7.

CHAPTER 2

ANALYTICAL MODELS OF UNDER-RIDE GUARDS

2.1 INTRODUCTION

In a car-to-truck collision, the energy absorption properties of the automobile are severely reduced due to its intrusion under the heavy vehicle and high rigidity of the conventional guard. The severity of such collisions can be considerably reduced by transferring the impact forces to primary energy absorbing element (bumper) of the car, and by dissipating portion of the energy. A flexible and damped under-ride guard implemented to the heavy vehicle can easily meet the above requirements. The added weight due to the side, and rear guards raises many concerns related to the freight transportation economy due to reduced payload capacity of the heavy vehicle. The designs of light weight flexible under-ride guards are thus considered highly desirable for enhancement of highway safety associated with such collisions.

In this chapter, a concept of an energy dissipating under-ride rear guard is proposed. The proposed under-ride guard is analytically modeled and its performance characteristics are investigated under different speeds and angles of rear impact. The analytical model comprises the nonlinear force-deflection and force-velocity properties of the energy restoring and dissipative elements of the guard, respectively. While the inertia due to heavy vehicle is neglected, the car is represented by a rigid mass to evaluate the energy dissipation properties of the proposed guard. Although the lumped-parameter

model is developed for a rear under-ride guard subject to both direct and oblique impacts, the model can be easily utilized to study the response to side impacts. A performance criteria comprising the magnitude of intrusion, car mass acceleration and dissipated energy is formulated to study the effectiveness of the proposed guard. A multi-variable constrained optimization problem is formulated and solved using nonlinear programming technique to derive optimal parameters for the guard.

2.2 ANALYSIS OF A CONVENTIONAL REAR UNDER-RIDE GUARD

The design requirements of a conventional rear under-ride guard are outlined in SAE J260 [101], which emphasizes the ground clearance, and lacks in specifying its size, shape and energy absorbing requirements. The practice recommends the use of a rigid under-ride guard to prevent the intrusion of an impacting vehicle to the fullest extent. In recent years, the International Organization for Motor Vehicles has emphasized the need to implement rear, side and front under-ride protection systems for the heavy vehicles in order to attain improved highway safety [97].

The conventional rigid under-ride guard may not be considered suitable to protect the occupants of the light weight vehicle during an impact due to its high rigidity and ground clearance. Since the under-ride guard is attached to the chassis of the heavy vehicle with a ground clearance of approximately 80 *cm*, forces and moments occur at a location other than the primary energy-absorbing member (bumper) of the car. The high rigidity nature of the under-ride guard and the main beams cause very high levels of acceleration transmitted to the occupant of the impacting vehicle. The energy absorption characteristics of a conventional under-ride guard can be quantified under direct and

oblique impacts of the car using elastic-plastic analysis of the guard. The explicit finite element code DYNA3D [31,102] can be conveniently used to determine the impact response of the conventional guard. The impacting car may be considered as a rigid body to perform relative evaluations in an efficient manner.

2.2.1 An Overview of DYNA3D

DYNA3D is a general-purpose, explicit time integration nonlinear finite element structural dynamics code, which is extensively used to determine the response behavior under elastic-plastic impact conditions. The validity of the code has been demonstrated in many studies involving experimental investigations [28,39,40]. The code constitutes an extensive array of material models, which allows simulation of elastic (isotropic and orthotropic), visco-elastic, elasto-plastic and rigid materials. The software also permits the integration of both strain hardening and strain rate effects with the elastic-plastic material models under dynamic loading. The software further incorporates sliding surface contact models, with particular emphasis on single surface contacts, to study the response to angular impacts.

The software utilizes updated Lagrangian mechanics, where spatial discretization is accomplished by casting the global balance of linear momentum in terms of a weak integral virtual work form. Linear iso-parametric displacement distributions within the element are assumed and one point Gauss Quadrature algorithm is used to solve for the element forces. The differential equations of motion are solved using an explicit central difference technique, where, the time step is computed to satisfy the Courant stability

criterion [31,103], which requires that the solution shall not propagate through an element faster than the speed of sound wave in the material.

The one point Gauss quadrature solution method used in DYNA3D gives rise to spurious zero energy modes or "hourglass modes" within an element of the mesh. The element must then be stabilized to eliminate the zero energy modes. The stabilization is effectively accomplished in DYNA3D using hourglass stiffness and damping values. The default algorithms assume pre-defined values for these constants and handle almost any situation. The stability of the solution can be assessed by monitoring the hourglass energy balance during the simulation.

2.2.2 Strain Rate Dependent Material Model

The deformations and thus the energy absorption properties of materials subject to dynamic loads are strongly dependent upon strain rate of the material. The study of energy absorption capabilities of an under-ride guard thus necessitates a material model incorporating the effects of strain rate on the stresses developed. The DYNA3D material library comprises many such material models, some of which are considered applicable for a certain range of strain rate values. The strain rate dependent isotropic elastic-plastic model provided in the software (material type 19) has been frequently used in automotive applications [28]. The yield condition for the above material model is defined as [31]

$$\phi = \bar{\sigma} - \sigma_y(\bar{\varepsilon}^p, \dot{\bar{\varepsilon}}) \tag{2.1}$$

where $\bar{\sigma}$ is the effective stress and σ_y is the current yield stress, which may depend upon on the effective plastic strain $\bar{\varepsilon}^p$ and the current effective strain rate $\dot{\bar{\varepsilon}}$. The effective

stress and strain rate are computed from the deviatoric stress tensor s_{ij} and strain rate tensor $\dot{e}_{ij}$:

$$\sigma = \left(\frac{3}{2} s_{ij} s_{ij}\right)^{1/2}; \qquad \dot{\bar{\varepsilon}} = \left(\frac{2}{3} \dot{e}_{ij} \dot{e}_{ij}\right)^{1/2} \tag{2.2}$$

The isotropic strain hardening is expressed in the following form as a function of the strain rate $\dot{\bar{\varepsilon}}$, effective plastic strain, $\bar{\varepsilon}^p$ and the plastic hardening modulus E_p:

$$\sigma_y = \sigma_0(\dot{\bar{\varepsilon}}) + E_p \bar{\varepsilon}^p \tag{2.3}$$

where σ_0 is the initial yield stress, determined from the load curve specification of σ_0 - $\dot{\bar{\varepsilon}}$.

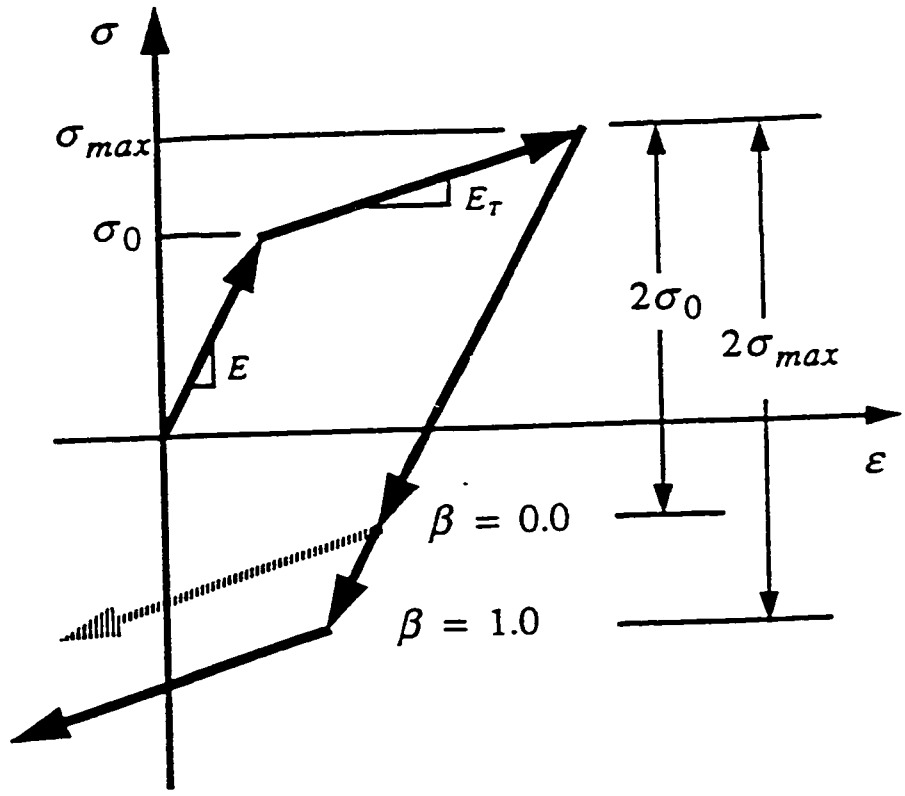

Figure 2.1: Strain Rate Dependent Material Model.

The plastic modulus E_p represents the slope of the effective stress- effective strain curve, and the tangent modulus E_T represents the inelastic portion of the uniaxial stress - uniaxial strain curve. The plastic modulus can be written in terms of the Young's modulus E and the tangent modulus E_T as:

$$E_p = \frac{EE_T}{E - E_T} \tag{2.4}$$

Both the Young's and the tangent modulus can also be expressed as functions of strain rate.

2.2.3 Post-processing of DYNA3D Results

The results of an analysis in DYNA3D are available in three forms: a state database, time history database and a force database. The state database contains primitive data for all node points and elements at a relatively few time intervals during an analysis. The primitive data consists of displacements, element stresses and resultants. The time history database contains nodal and elemental information for a lesser number of nodes or elements, but at a higher frequency of output. Time history database is useful for evaluating the results, which provide the data on a time scale much smaller than the interval selected for state dumps. The force database is used to determine the resultant forces transmitted along or across of an interface of interest. The post-processor code TAURUS, which reads the three forms (state, time history and force history database) of binary output files from DYNA3D, can be used to display, plot or list the analysis results. TAURUS processes the DYNA3D analysis results and the information can be extracted in four different ways: (i) a nodal time history plot or list of nodal kinematics, stress and

strain information; (ii) elemental time history plot or list, which provides kinematic, stress and strain, averaged over specified element; (iii) material time history plot, or list which provides kinematic and energy information averaged over specified material number; and (iv) A global kinematic and energy information averaged over the entire model. The displacement, velocity, acceleration responses of individual components of a model cab be conveniently obtained by identifying each component of a model with a separate material number and using the third output option of TAURUS.

2.2.4 Interface Slide Surface Options

DYNA3D contains a robust and efficient capability for modeling the mechanical interactions between two bodies or two parts of a single body. Fourteen different options of 'slide surfaces' are offered by DYNA3D in a wide variety of situations. These options include facilities for treating interactions between two surfaces, between discrete nodes and surfaces, or between a body and a rigid wall. All slide surfaces accommodate arbitrarily large relative motions and slide surfaces may be defined between surfaces of different element types. Surface sliding interface is defined by specifying one master surface and either one slave surface or set of slave nodes, as required by the type of slide surface chosen.

Sliding surface and contact in DYNA3D are formulated using a 'node on surface' concept. Slave nodes are restricted from penetrating the master surfaces. Conceptually, the surface algorithms could thus be thought of as looping over all slave nodes, and for each slave node checking that there is no penetration through the master segment defined

for the sliding interface. All the slide surface types may use either a penalty formulation or a Lagrangian projection formulation. When a penalty formulation is chosen to enforce a contact constraint, a restoring force is placed on a penetrating node to return it to the surface. The force is proportional to the depth of penetration, the bulk modulus of the penetrated material, the dimensions of the penetrated element and a scale factor specified by the user. When a Lagrangian formulation is chosen to enforce the contact constraint, a restoring force is again placed on a penetrating node to return it to the surface. This option, however, predicts, the force by determining the location of a node on the interface at the end of each time step, and computing the contact force required to place the node on the surface at the end of the time step. The interface pressure distribution on a slide surface may be written to an output file for post-processing purpose.

2.2.5 Rigid Body Impact Analysis on the Conventional Guard

Two designs of conventional guards, comprising two drop-arms, a cross-member and two square tube section stiffeners are analyzed under a direct central impact in a plane parallel to the ground plane. The two designs of the guards, considered in the study and referred to as A and B, are quite similar with the exception of the location of the stiffeners, as shown in the Figure 2.2. The stiffeners in design A are mounted between the bumper beam and the main I-beam of the trailer, while those in design-B are located between the middle of the drop arms and the main-beams of the trailer frame. The 600 mm long drop arms, made of 60-*mm* X 60-*mm* square section with 5-mm thickness, are considered to be rigidly attached to the main I-beams of trailer frame. Since the car is assumed to be a rigid body, the impact is assumed to occur at the cross member of the guard. The performance

characteristics of the conventional guards subject to direct and oblique impacts are analyzed using DYNA3D.

The drop arms and the cross members are modeled using shell elements, while the stiffeners are modeled using beam elements. The rigid truck and the car masses are modeled as elastic solid elements. The elastic-plastic properties of the structural steel members are considered in the analysis to incorporate the influence of strain rate on the yield strength, as described in Equation (2.1) to (2.4). The yield strength properties of structural steel as a function of strain rate are obtained from reference [104]. The car mass was given the required initial velocity and the rectangular block representing the truck I-beam and the truck are assumed stationary due to the heavy inertia. The simulation was performed for 0.1 *s* in for all the initial velocity since this time duration was sufficient for the impact process. DYNA3D selects the optimum time step for the solution of the differential equations of motion based on the Courant's stability criteria. The static and kinematic friction coefficients at the contact surface was assumed to be 0.33 and 0.3, respectively, as suggested by reference [28], while the density of steel is assumed as 7800 kg/m^3. The impact analyses are performed at four initial speeds of the car mass and the results are presented in the next chapter. The performance behavior of the conventional guard is evaluated for impacts at four different speeds: 10, 30, 50 and 70 *km/h*, and the data is analyzed to yield peak car mass acceleration. The results are compared with those derived for the proposed guard to demonstrate the potential benefits of the proposed concept.

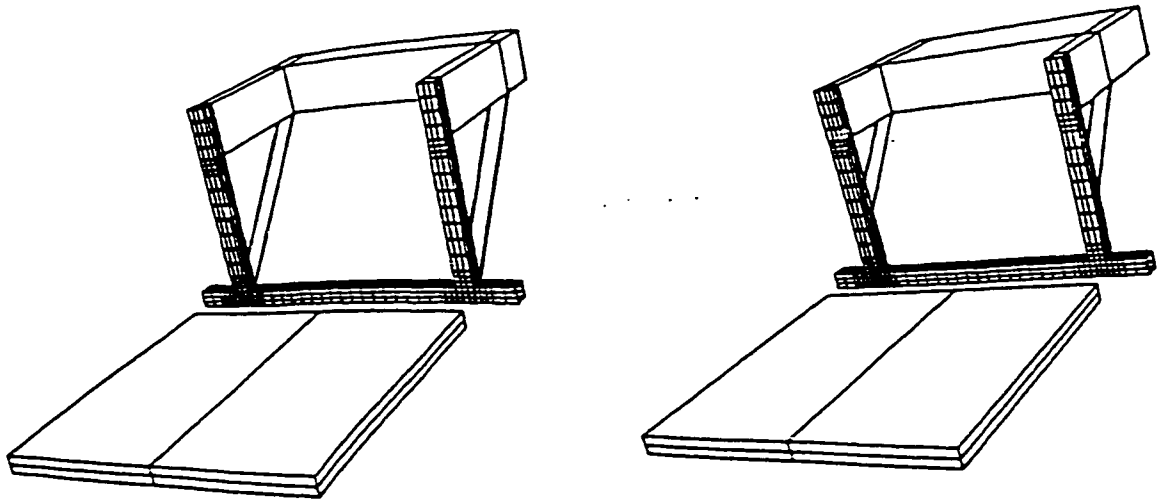

Figure 2.2: Two designs of the conventional under-ride guards.

2.3 DESIGN DETAILS OF THE PROPOSED GUARD

The proposed under-ride guard, schematically shown in Figure 2.3, comprises two drop arms hinged at the primary load carrying main-beams of the trailer structure, a bumper beam, and energy restoring and dissipating components attached between the drop arms and the trailer structure. The non-linear springs of the guard store the energy temporarily, while the asymmetric damper is used to dissipate the stored energy. A design with undamped springs may yield re-impacts between the car body and the guard, while the design with damper alone may pose increased requirements on the damper, specifically under impact loads at higher speeds. In a conventional under-ride guard, the impact energy is mostly absorbed by the plastic deformation of the drop arms and bumper beam of the guard, and that of the car structure. The proposed guard design is thus realized upon the utilizing the drop arms, which are hinged to permit certain motion of the impacting body by the energy dissipating and storing devices.

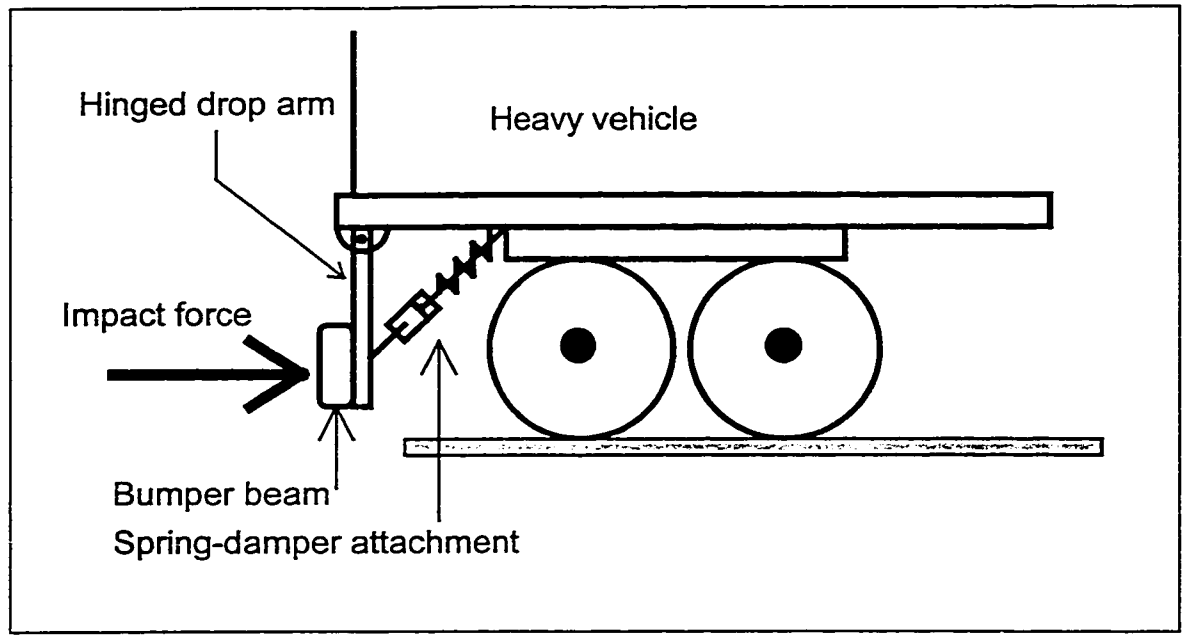

Figure 2.3: Schematic representation of the proposed under-ride guard.

While the damper and spring can be attached to the drop arm- bumper beam assembly in many different manners, the proposed geometry, shown in Figure 2.3, is selected for many reasons. Firstly, as suggested in Reference [70], the triangular shape arrangement yields a mean mechanical advantage of 3:1, which may vary with angular motion of the guard during the impact process. Secondly, the inclined damper installation limits the space requirements that may be posed by the considerable damper travel. The third design factor originates from the fact that an impacting car under deceleration tends to dive towards the front. The bumper beam in the proposed design undergoes an upward vertical motion associated with the angular motion of the guard, which may help to lift the impacting mass and thus restore its horizontal position. The springs and dampers in the proposed design are attached directly to the primary load carrying members of the trailer structure, thus eliminating the need for additional linkages or complex joints.

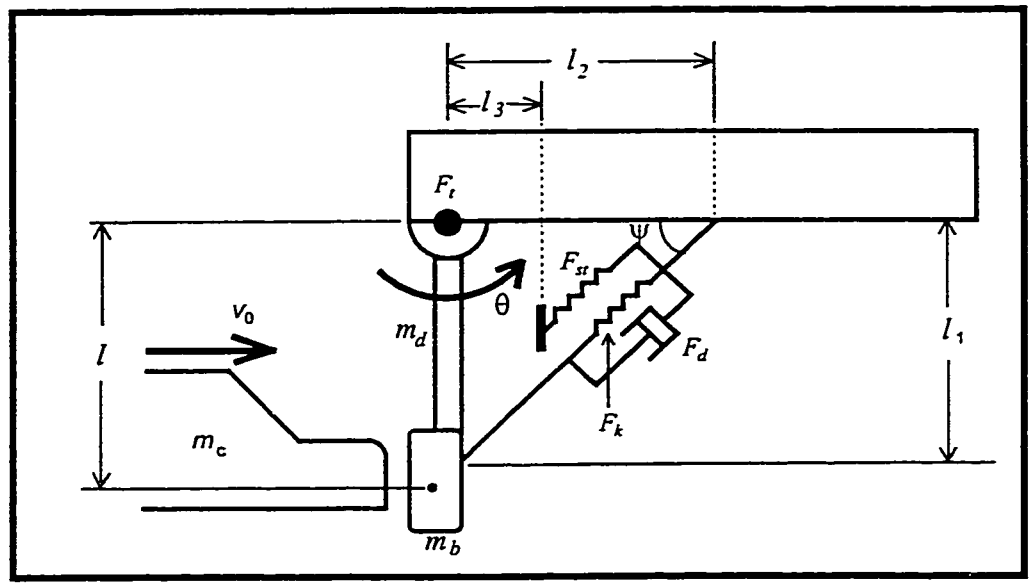

Figure 2.4: Analytical model of the proposed guard under direct impact.

The intrusion of the impacting car under the trailer structure is limited by an elastic bump stop placed in parallel with the spring-damper combination. Bushings with high torsional stiffness are introduced at the two hinge points of the drop arms to minimize its oscillations under normal driving conditions. The ground clearance of the bumper beam is selected to coincide with the height of the primary energy absorbing structure of most cars (300 mm). The intrusion of the impacting mass is further limited by selecting the springs with progressively hardening force-deflection characteristics, which is modeled as a cubic function of the displacement. Figure 2.4 illustrates the dimension details of the proposed guard.

While the magnitude of intrusion of the car mass under the heavy vehicle depends on the compression stroke damping, the rebound velocity of the car is related to the rebound stroke damping. The force-velocity properties of the damper are thus considered

to be asymmetric in compression and rebound with two stages of compression damping associated with bleed and blow-off flows. A detailed discussion on the damper design is given in the next chapter.

2.4 DEVELOPMENT OF ANALYTICAL MODEL - DIRECT IMPACT

A simplified in-plane analytical model of the under-ride guard and the car body is developed to evaluate the relative performance potentials of the proposed energy dissipating guard. The proposed under-ride guard is analytically modeled to study its performance potentials under direct and oblique impacts. Figure 2.4 illustrates the analytical model developed under direct impacts. Since the inertia of the heavy vehicle is considerably larger than that of the car, the dynamic interactions of the trailer mass are considered negligible. The drop arms are considered to be hinged to the trailer structure, which is modeled as a rigid barrier to carry out relative performance evaluations in a simplified manner.

Although the study of crashworthiness of automobiles necessitates considerations of the flexibility and energy absorbing properties of its various components, the relative performance benefits of the proposed guard can be conveniently derived through a simple rigid mass representation of the car. The car mass is assumed to move in a horizontal direction at a constant speed prior to the impact. The point of impact on the bumper beam, however, varies as a function of the intrusion of the car mass and dynamics of the drop arm and the beam mass, attributed to the angular deflection of the drop arms. The bumper beam thus tends to slip with respect to the impacting mass along the axial direction of the drop arms, in a plane normal to the line of contact. The friction between

the two sliding surfaces is assumed to be negligible. The model assumes a direct central impact in a plane parallel to the ground, and a central oblique impact in a plane perpendicular to ground and passing through the line of contact. The analytical model is formulated assuming a perfectly plastic impact during the contact duration, while the dynamics of the under-ride guard and the car masses are modeled independently when the contact is lost.

In the model shown in Figure 2.4, l represents the vertical distance between the center of mass (c.g.) of the bumper beam and the hinge point which is a function of angular deflection θ of the drop arm. The point of contact is initially assumed to coincide with the c.g. of the bumper beam. l_1 is the vertical distance between the spring and damper mounting on the bumper beam and the hinge. l_2 is the constant horizontal distance from the hinge to the spring and damper mountings on the main beam. Motion limiting bump stops are also introduced to the magnitude of intrusion of the car mass. The elastic bump is modeled as a clearance spring with a clearance of l_3

2.4.1 Equations of Motion

The development of the analytical model of the proposed guard and the car mass impact involves consideration of three sequential phases: (i) the application of the principle of impulse and momentum to determine the velocity of the combined car and bumper beam masses, immediately after the impact; (ii) dynamic analysis of the coupled system for the contact duration; and (iii) dynamic analysis of uncoupled masses, when the contact force becomes zero during the impact process. The loss of contact between the two bodies can occur either during compression or rebound stroke of the guard.

The principle of impulse and momentum is applied in the first phase of the analysis to determine the velocity of the bumper beam immediately after the impact, while the car mass (m_c) is assumed to be in contact with the beam. Figure 2.5 illustrates the forces acting on the two masses, and their respective momenta, before and immediately after the impact. Equating the moment of momenta about the hinge point O before and immediately after the impact, while assuming negligible deflection of the bumper at the point of impact, yields:

$$m_c \dot{x}_{c0} l = m_c \dot{x}_{c1} l + m_b \dot{x}_b l + m_d \frac{\dot{x}_b}{2} \frac{l}{2} + \frac{1}{12} m_d l^2 \frac{\dot{x}_b}{l} \tag{2.5}$$

where m_c, m_b and m_d are the masses of the car body, under-ride guard bumper beam and drop arms, respectively. l is the distance of the impact point (assumed to be at the center of bumper beam) from the hinge point O, $\dot{x}_{c0}$ is the impact velocity of the car mass, $\dot{x}_{c1}$ and $\dot{x}_b$ are the velocities of the car mass and bumper beam masses respectively, after the impact. Owing to the flexibility of the under-ride guard along its rotational degree-of-freedom (DOF), the impact is considered to be perfectly plastic (coefficient of restitution, $e = 0$). The car mass and the point of impact on bumper beam thus experience identical velocity, $\dot{x}_{c1} = \dot{x}_b$, which maybe derived from Equation (2.5), as follows:

$$\dot{x}_{c1} = \frac{m_c \dot{x}_{c0}}{\left[m_c + m_b + \frac{m_d}{3} \right]} \tag{2.6}$$

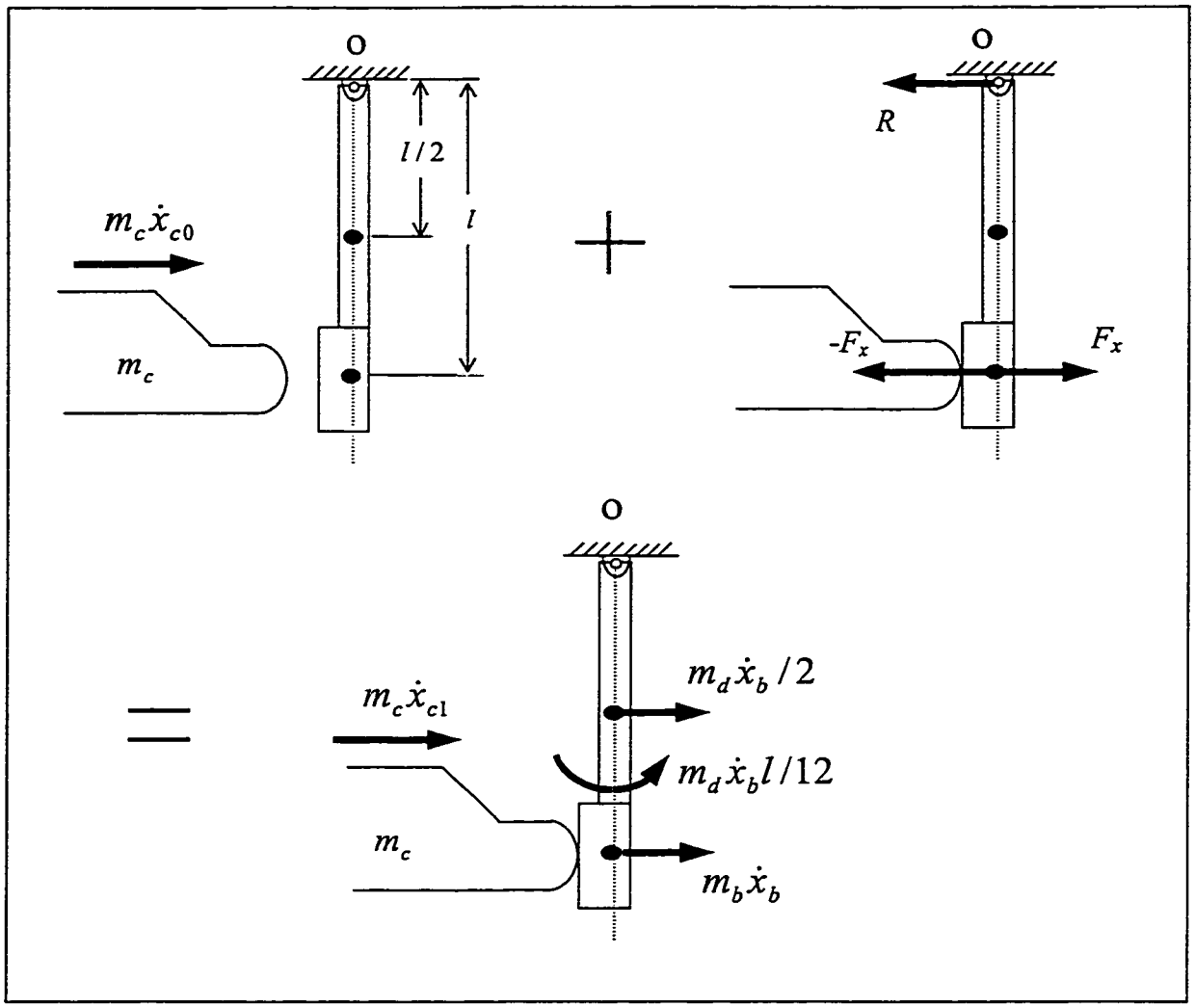

Figure 2.5: Forces and momentum before and after impact.

The motion of the coupled masses can then be analyzed using Lagrangian dynamics in the second phase of the impact process. Let θ be the rotation of the drop arm during the impact process. The motion of the coupled under-ride guard and car masses can be described by a single DOF, assuming that the components of velocities of both impacting masses along the line of contact are equal. The vertical coordinate of the point of contact on the bumper beam, however, varies due to angular deflection of the drop

arm. Figure 2.6(a) illustrates the kinematic motion of the drop arm and the bumper beam during the impact process. The point P refers to the point of contact at the bumper beam surface corresponding to the time of impact ($t = 0$), while P' describes the instantaneous position of the contact point. The distance from the hinge point to the instantaneous contact point (l') can be related to the initial contact point distance from the geometry:

$$l' = \frac{l}{\cos\theta} \tag{2.7}$$

For velocity continuity between the two impacting bodies, the velocities of the two bodies along the line of contact should be equal. In the car-to-under-ride guard impact the car body is assumed to move in the horizontal direction, while the under-ride guard

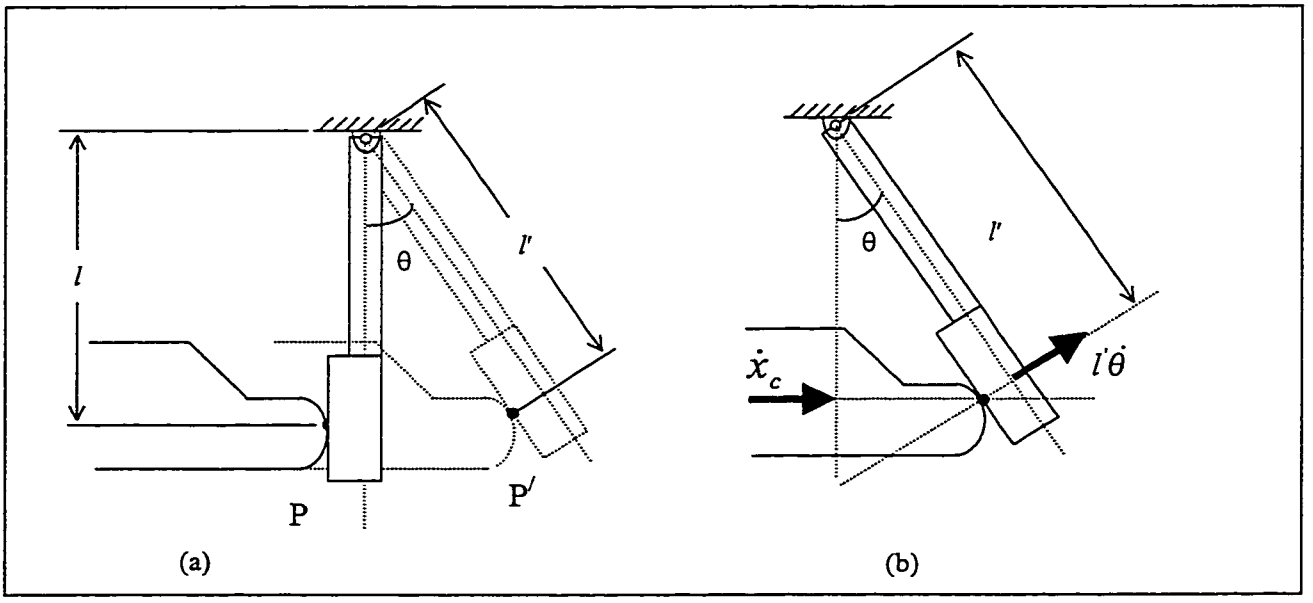

Figure 2.6: Geometry to evaluate the lengths.

deflects by angle θ. With reference to Figure 2.6(b), and using Equation (2.7), the instantaneous velocity of the car mass during the contact, can thus be written as:

$$\dot{x}_c = \frac{l\,\dot{\theta}}{\cos^2\theta} \tag{2.8}$$

The total kinetic energy and potential energy of the coupled system can be derived as:

$$KE = \frac{1}{2}m_c l^2\left[\frac{\dot{\theta}}{\cos^2\theta}\right]^2 + \frac{1}{2}\left[m_b + \frac{m_d}{3}\right]l^2\dot{\theta}^2 \tag{2.9}$$

$$PE = \left[m_b + \frac{m_d}{2}\right]gl(1-\cos\theta) + \int F_k dS_1 + \int F_{st} dS_2 + \int F_t d\theta \tag{2.10}$$

where KE and PE are the total kinetic and potential energy due to the coupled system respectively, g is the acceleration due to gravity and F_k is the nonlinear force developed due to deflection S_1 of the primary spring, given by:

$$F_k = k_{11}S_1 + k_{12}S_1^3 \tag{2.11}$$

where k_{11} and k_{12} the linear and cubic stiffness coefficients. F_t represents the moment due to the linear torsional spring rate k_t of the bushings at the hinge, given by $F_t = k_t\theta$. F_{st} is the force due to the elastic bump stop modeled as a linear spring with stiffness constant of k_{st}, given by:

$$F_{st} = \begin{cases} k_{st}S_2 & \text{if } l_4\sin\theta > l_3 \\ 0 & \text{if } l_4\sin\theta < l_3 \end{cases} \tag{2.12}$$

where l_4 is the distance between the hinge and the point of the contact of the drop arm with the bump stop, as illustrated in Figure 2.7(b) and given by:

$$l_4 = \left\{ \left[(l_2 - l_3) \tan\psi \right]^2 + l_3^2 \right\}^{1/2}$$

S_1 and S_2 are the deflections of primary and stop springs, respectively, derived from the geometry shown in Figure 2.7(a) and (b), respectively:

$$S_1 = \frac{l_1}{\sin\psi_0} - \frac{l_2 - l_1 \sin\theta}{\cos\psi} \quad ; \quad S_2 = \frac{l_2 - l_3}{\cos\psi_0} - \frac{l_2 - l_4 \sin\theta}{\cos\psi} \tag{2.13}$$

where ψ_0 is the initial angle of installation of the primary springs and damper with respect to the horizontal axis, and ψ is the instantaneous angle, which is related to the deflection of the drop arms in the following manner:

$$\psi = \tan^{-1}\left(\frac{l_1 \cos\theta}{l_2 - l_1 \cos\theta} \right)$$

The dissipation function (DF) of the under-ride guard is derived from the nonlinear and asymmetric damping force, F_d:

$$DF = \int F_d dS_1 \tag{2.14}$$

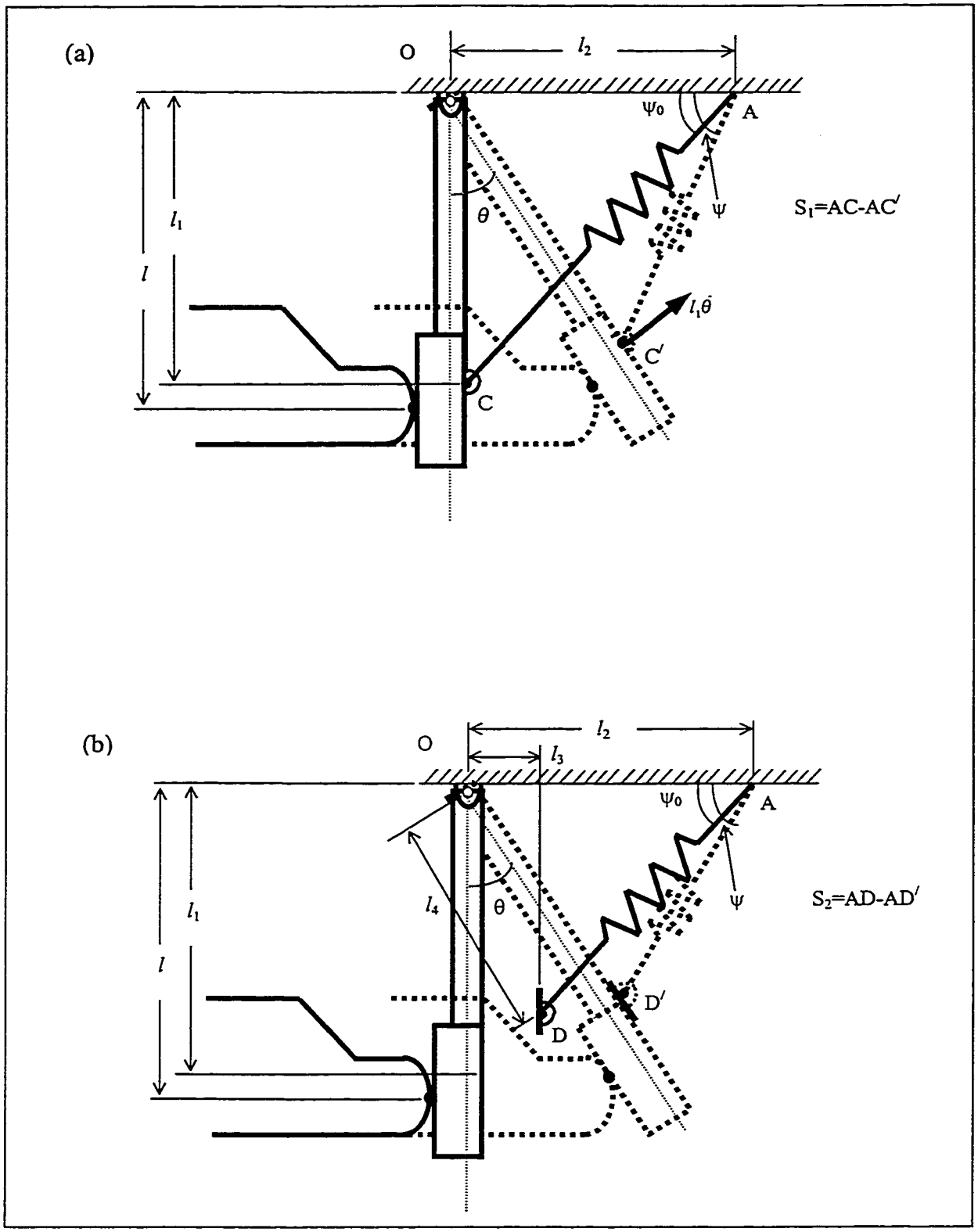

Figure 2.7: Deflections of the drop arms, and primary and bump stop springs during the impact process.

Assuming typical force-velocity characteristics of a hydraulic damper, shown in Figure 2.8, the damping force is expressed as:

$$F_d = \begin{cases} C\dot{S}_1 & \text{for } 0 < \dot{S}_1 < v_c \\ C[v_c + n_c(\dot{S}_1 - v_c)] & \text{for } \dot{S}_1 > v_c \\ pC\dot{S}_1 & \text{for } v_e < \dot{S}_1 < 0 \\ pC[v_e + n_e(\dot{S}_1 - v_e)] & \text{for } \dot{S}_1 < v_e \end{cases} \tag{2.15}$$

where C is the viscous damping coefficient associated with the bleed flows in the compression mode, n_c and n_e are the damping reduction constants related to blow-off damping during compression and rebound respectively, v_c and v_e are the respective blow-off velocities and asymmetry constant p is the ratio of rebound to compression damping

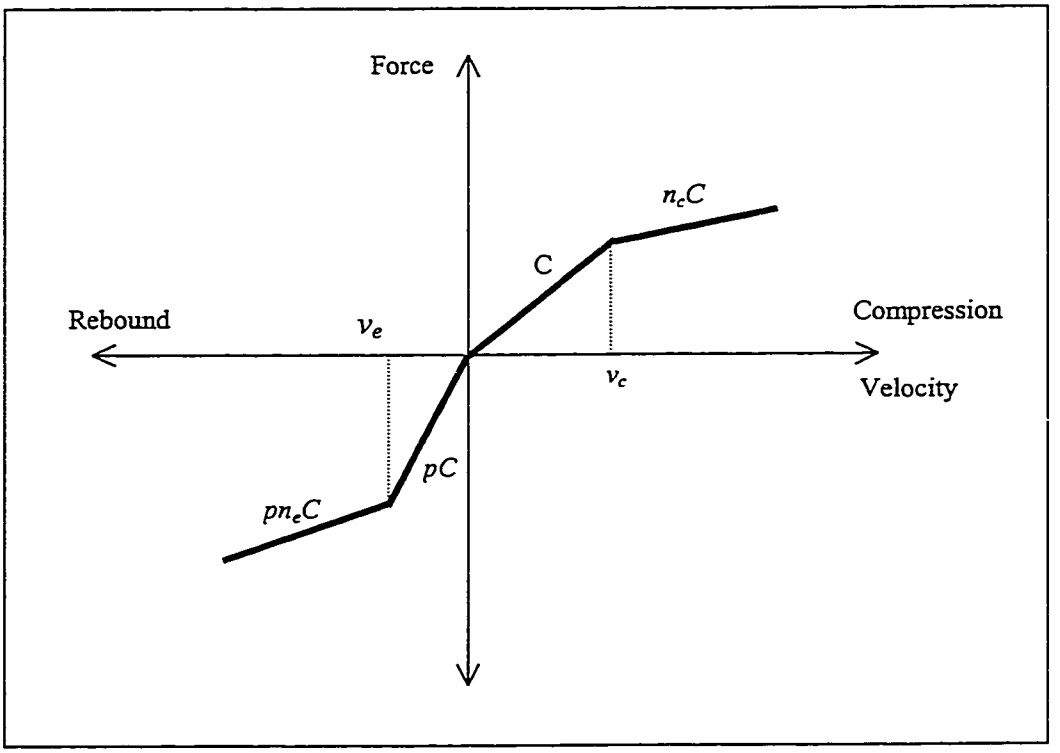

Figure 2.8: Typical force-velocity characteristics of a hydraulic damper.

coefficients corresponding to bleed flows. While the magnitude of intrusion of the car mass under the heavy vehicle and the magnitude of acceleration transmitted to the car mass depend on the compression stroke damping, the rebound velocity of the car is related to the rebound stroke damping. The force-velocity properties of the damper are thus considered to be asymmetric in compression and rebound with two stages of compression damping associated with bleed and blow-off flows.

Substitution of the energy terms from Equations (2.9), (2.10) and (2.15) in the Lagrangian Equation [69] yields the equation of motion for the single DOF coupled system, as follows:

$$\left\{\frac{m_c}{\cos^4\theta}+m_b+\frac{m_d}{3}\right\}l^2\ddot{\theta}+2m_c l^2\left(\frac{\sin\theta}{\cos^5\theta}\right)\dot{\theta}^2+l_1F_d + \left(m_b+\frac{m_d}{2}\right)gl\sin\theta+F_k\frac{\partial S_1}{\partial\theta}+F_{st}\frac{\partial S_2}{\partial\theta}+k_t\theta=0 \tag{2.16}$$

where the partial derivatives can be obtained from the equations:

$$\frac{\partial S_1}{\partial\theta}=\frac{-l_1\cos\psi}{\sin^2\psi}\frac{\partial\psi}{\partial\theta}-\frac{l_2\sin\psi}{\cos^2\psi}\frac{\partial\psi}{\partial\theta}+\frac{l_1\left(\cos\psi\cos\theta+\sin\psi\sin\theta\dfrac{\partial\psi}{\partial\theta}\right)}{\cos^2\psi}$$

$$\frac{\partial S_2}{\partial\theta}=\frac{(l_3-l_2)\cos\psi}{\sin^2\psi}\frac{\partial\psi}{\partial\theta}-\frac{l_2\sin\psi}{\cos^2\psi}\frac{\partial\psi}{\partial\theta}+\frac{l_4\left(\cos\psi\cos\theta+\sin\psi\sin\theta\dfrac{\partial\psi}{\partial\theta}\right)}{\cos^2\psi}$$

$$\frac{\partial\psi}{\partial\theta}=\frac{(l_1^2-l_1l_2\sin\theta)}{\left(l_1^2+l_2^2-2l_1l_2\sin\theta\right)}$$

Equation (2.16) describes the angular deflection of the drop arm θ, and is considered valid for the duration of contact between the two masses. The differential Equation of motion is solved, subject to initial conditions, $\theta(0)=0;\ \dot{\theta}(0)=\frac{\dot{x}_{c1}}{l}$, to derive the angular deflection response of the guard. While the velocity ($\dot{x}_c$) of car mass is evaluated from Equation (2.7), the magnitude of intrusion (x_c) and acceleration $\ddot{x}_c$ of the car mass are derived from integration and differentiation of Equation (2.7), respectively, expressed as:

$$x_c = l\tan\theta$$

$$\ddot{x}_c = l\sec^2\theta(\ddot{\theta}+2\dot{\theta}^2\tan\theta) \tag{2.17}$$

The solution is terminated when the contact force between the two bodies ($F_x = m_c\ddot{x}_c$) approaches zero due to the loss of contact. The dynamics response characteristics of the car and the guard masses are then analyzed separately in the final phase of the impact process. The displacement of the car mass is evaluated from the dynamics of a particle under a constant velocity, given by:

$$x_c = l\tan\theta\big|_{t=t_l} + \dot{x}_c\big|_{t=t_l}(t-t_l) \tag{2.18}$$

where t_l is the time at which loss of contact occurs. The angular motion of the bumper beam, after the loss of contact, can be evaluated using the differential Equation (2.12), by letting $m_c = 0$. The displacement response characteristics of the two masses derived from the above Equations must be further examined to detect the possible occurrence of

repeated impact. A repeated impact between the bumper beam and the car mass is assumed to occur when the difference between the car body displacement is less than 0.1 mm, which is considerably smaller when compared to the dimensions of the car body and under-ride guard:

$$\left|\dot{x}_c - l\cos\theta\right| < 0.0001 \tag{2.19}$$

Equation (2.12) is solved to determine the motions of the two bodies in the event of a repeated impact between the two bodies.

2.5 DEVELOPMENT OF ANALYTICAL MODEL - OBLIQUE IMPACT

The highway accidents involving automobiles impacting the rear of a heavy vehicle can be frequently characterized by an oblique impact. In such impacts, the car mass approaches the under-ride guard with two predominant velocity components: forward velocity v_0 and the yaw velocity, $\dot{\phi}_0$. The analysis involving oblique impacts thus requires considerations of linear as well as angular momentum with respect to the center of rotation. The friction properties of the impacting surfaces further influence the severity of the impact. Lack of friction may cause relative sliding of the impacting mass along the lateral axis of the guard leading to a rapid loss of contact. An analytical model of the proposed guard is thus formulated based upon the linear and angular momenta to study its performance behavior under oblique impacts.

The governing equations of motion of the combined car mass and under-ride guard system are developed using two coordinate systems, (X_1,Y_1,Z_1) and (X,Y,Z), fixed at the c.g.'s of the car and the beam masses, respectively, as shown in Figure 2.9. The impact process is considered in three sequential phases to derive the differential equation

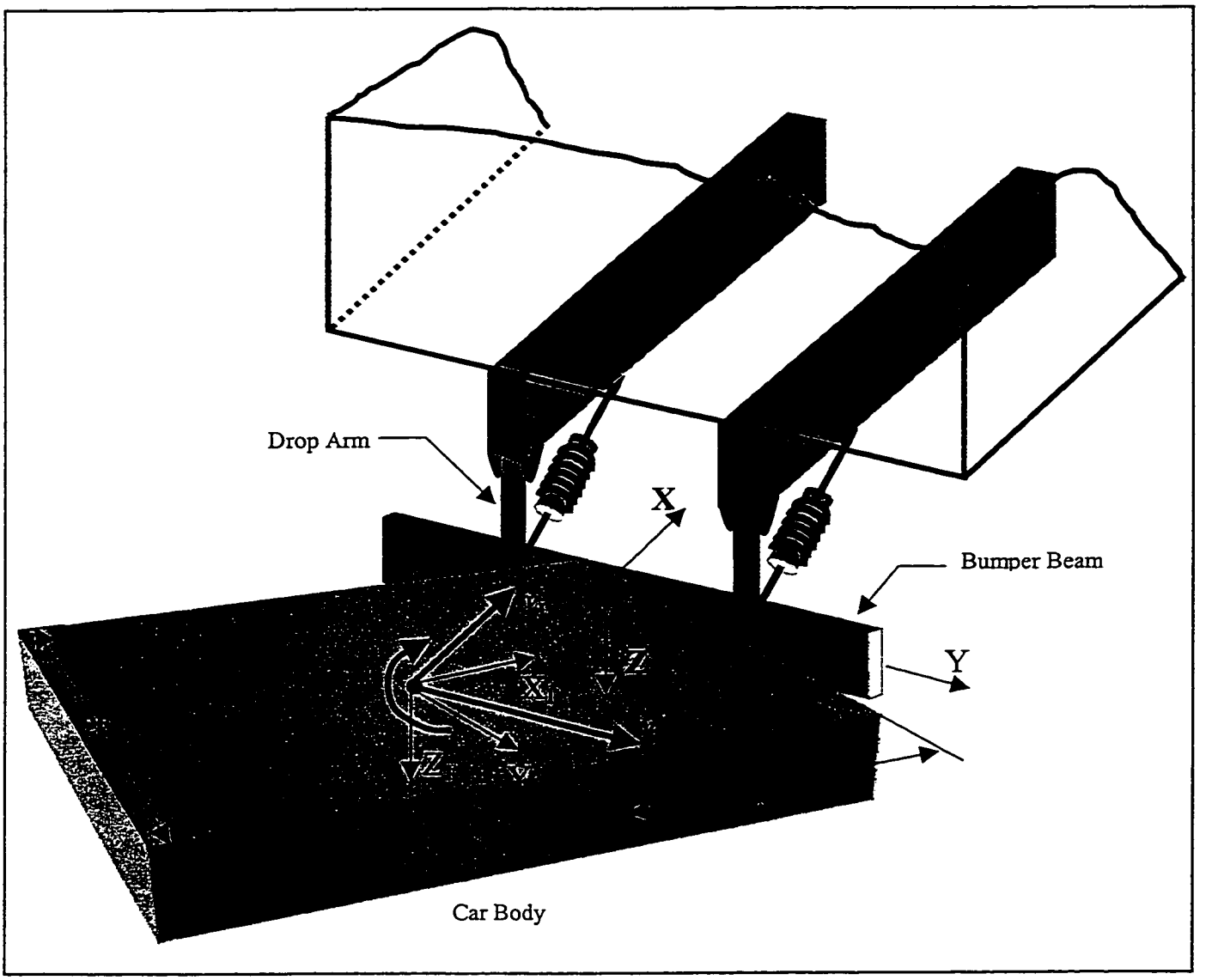

Figure 2.9: Schematic of the energy-dissipative under-ride guard depicting the coordinate system.

of motion as described earlier in section 2.4.1. The principle of impulse and momentum is initially applied to determine the velocity of the coupled masses immediately after the impact, which is followed by the dynamic analysis of the coupled system for the contact duration. The dynamics of the car and bumper beam masses are derived independently in the final phase, when the contact force approaches zero during the impact process.

The mathematical model may be further simplified by applying the three phases of analysis independently, thus eliminating the need for deriving the moment of momentum of the car body with respect to line passing through the two hinges (PP′). The motion of the car body is represented in terms of three velocity components: namely, linear velocities along the fixed X and Y axes, and the angular velocity about the fixed Z axis (yaw velocity). The application of principle of impulse and momentum to the car mass yields:

$$m_c \dot{x}_{c0} - \int_0^t F_x dt = m_c \dot{x}_{c1}$$

$$m_c \dot{y}_{c0} - \int_0^t F_y dt = m_c \dot{y}_{c1}$$

$$I_{cz}\dot{\phi}_0 + h_1 \int_0^t F_x dt - h_2 \int_0^t F_y dt = I_{cz}\dot{\phi}_1 \tag{2.20}$$

where F_x and F_y are the contact forces along the fixed X and Y directions, respectively, as shown in Figure 2.10. $\dot{x}_c$ and $\dot{y}_c$ are the velocities of the car mass along the X and Y axis and $\dot{\phi}$ is its angular velocity about the fixed Z-axis. The subscripts '0' and '1' denote the velocities at the beginning and end of the first phase of impact, respectively. I_{cz} represents the mass moment of inertia of the car mass with respect to Z_1 axis. a and b are the

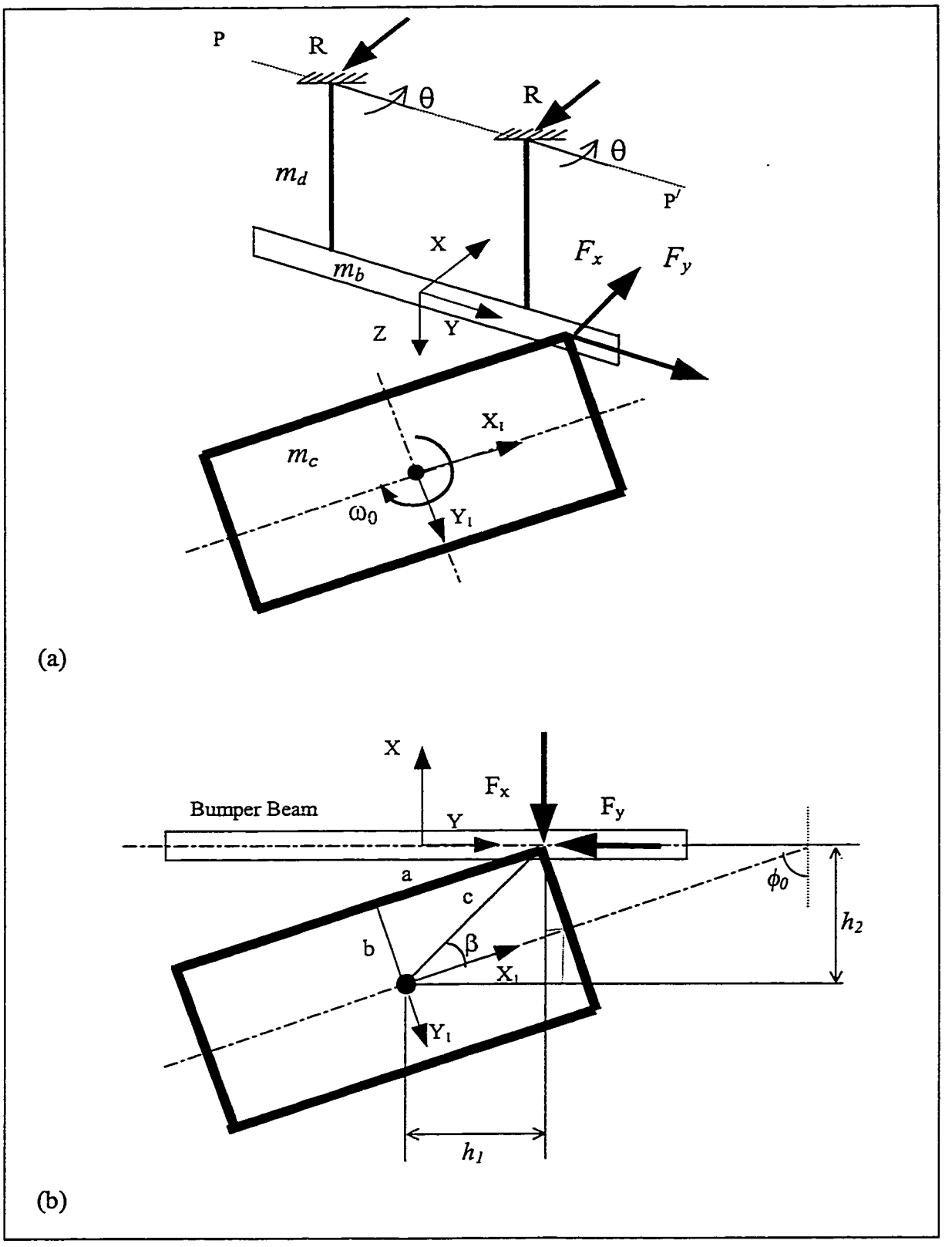

Figure 2.10: (a) Forces, moments and momentum during impact of a car mass with under-ride guard, (b) Geometry to evaluate h_1 and h_2.

coordinates of the contact point with respect to the car mass c.g. in the body fixed (X_1,Y_1) axis system. The quantities h_1 and h_2 are the moment arms along the X and Y axes, respectively given by:

$$h_1 = a\sin\phi_0 - b\cos\phi_0; \qquad h_2 = a\cos\phi_0 + b\sin\phi_0$$

The lateral force F_y, attributed to the contact friction, is assumed to be proportional to the normal force F_x, such that $F_y = \mu F_x$, where μ is the coefficient of friction. Assuming perfectly plastic impact, moment of momentum and impulse for the under-ride guard yields:

$$\int_0^t F_x dt = \left[\frac{I_{dy} + I_{by}}{l^2} + \frac{m_d}{4} + m_b\right]\dot{x}_{b1} \tag{2.21}$$

While the momentum of the under-ride guard at the beginning of the first phase of impact process is zero, $\dot{x}_{b1}$ refers to the longitudinal velocity of the guard at the end of first phase of the impact. I_{dy} is the mass moment of inertia of the drop arms with respect to an axis passing through the c.g. and parallel to Y-axis. Similarly I_{by} represents the mass moment of inertia of the bumper beam about the Y-axis. m_b and m_d are the masses due to drop arms and bumper beam respectively. Velocity $\dot{x}_b$ is related to the horizontal and angular velocities of the car mass, in the following manner:

$$\dot{x}_{c1} = \dot{x}_{b1} - c\dot{\phi}_1\sin(\phi_0 - \beta) = \dot{x}_{b1} - h_1\dot{\phi}_1 \tag{2.22}$$

where c and β are derived from the geometry shown in Figure 2.10. From Equations (2.20) to (2.22), the velocity of the contact point $\dot{x}_{b1}$ can be expressed as:

$$\dot{x}_{b1} = \frac{\dot{x}_{c0} + h_1\dot{\phi}_1}{1+\eta} \tag{2.23}$$

where η is a non-dimensional quantity expressed as a ratio of effective mass of the under-ride guard to the car mass:

$$\eta = \frac{1}{m_c}\left[\frac{m_d}{4} + \frac{I_{dy}}{l^2} + m_b + \frac{I_{by}}{l^2}\right] \tag{2.24}$$

The angular velocity of the car body at the end of first phase of impact is derived from Equation (2.20), upon substituting for $\dot{x}_{c1}$ from Equations (2.22) and (2.23):

$$\dot{\phi}_1 = \frac{I_{cc}\dot{\phi}_0 + \frac{\eta}{1+\eta} m_c \dot{x}_{c0}(h_1 - \mu\, h_2)}{I_{cc} - \frac{\eta}{1+\eta} h_1 m_c (h_1 - \mu\, h_2)} \tag{2.25}$$

The components of the car mass velocity along the fixed X and Y axes at the end of the first phase of analysis can be derived from Equations (2.20), (2.22) and (2.23):

$$\dot{x}_{c1} = \frac{\dot{x}_{c0} - \eta h_1 \dot{\phi}_1}{1+\eta}; \qquad \dot{y}_{c1} = \dot{y}_{c0} + \frac{\eta\mu}{1+\eta}\left(\dot{x}_{c0} + h_1\dot{\phi}_1\right) \tag{2.26}$$

Owing to the momentum transfer from the car mass, the coupled masses continue to move with a common velocity at the contact point during the second phase of the impact process. The dynamic motion of the car mass (x_c, y_c, ϕ) along the fixed (X,Y,Z) axis system, and angular motion of the guard (θ) can be derived from the four governing differential equations of motion. The equations of motion, however, can be considerably simplified using various constraints arising from the geometry and the kinematic motion of the two masses. The lateral displacement of the car mass at the contact point along the Y-axis, y_b can be expressed as:

$$y_c = y_b - h_3 \tag{2.27}$$

where $h_3 = a\sin\phi - b\cos\phi$, and ϕ is the instantaneous angular displacement of the car mass about the fixed Z-axis. The instantaneous position and velocity of the contact point, x_b and $\dot{x}_b$ along the X direction can be related to the angular velocity ($\dot{\theta}$) and deflection (θ) of the under-ride guard:

$$x_b = l\tan\theta \;; \qquad \dot{x}_b = \frac{l\dot{\theta}}{\cos^2\theta} \tag{2.28}$$

The instantaneous position, velocity and acceleration of the car mass c.g. along the X-axis can be expressed as:

$$x_c = x_b - h_4$$

$$\dot{x}_c = \dot{x}_b + h_4\dot{\phi}$$

$$\ddot{x}_c = l\left[\frac{\ddot{\theta} + 2\tan\theta\dot{\theta}^2}{\cos^2\theta}\right] + h_4\dot{\phi}^2 + h_3\ddot{\phi} \tag{2.29}$$

where $h_4 = a\cos\phi + b\sin\phi$. Referring to Figure 2.11, the equations of motion for the car mass can be written as:

$$m_c\ddot{x}_c + F_x = 0$$

$$m_c\ddot{y}_c + F_y = 0$$

$$I_{cz}\ddot{\phi} + m_c\ddot{x}_c h_3 - m_c\ddot{y}_c h_4 = 0 \tag{2.30}$$

The equation of motion for the under-ride guard, incorporating the restoring and dissipative forces, is derived using Lagrage's equation approach. The equation of motion for the guard is thus identical to that derived earlier under a direct impact, given by:

$$\left\{m_b + \frac{m_d}{3}\right\}l^2\ddot{\theta} + l_1F_d + \left(m_b + \frac{m_d}{2}\right)gl\sin\theta + F_k\frac{\partial S_1}{\partial\theta} + F_{st}\frac{\partial S_2}{\partial\theta} + k_t\theta = \frac{F_x l'}{\cos\theta} \tag{2.31}$$

where g is the acceleration due to gravity, F_k and F_{st} are the nonlinear restoring forces developed due to deflections S_1 and S_2 of the primary and the clearance springs of the under-ride guard. Equation (2.30) together with Equation (2.29), yields the contact point force along the X-direction during an oblique impact:

$$F_x = -m_c\left\{l\left[\frac{\ddot{\theta} + 2\tan\theta\dot{\theta}^2}{\cos^2\theta}\right] + h_3\dot{\phi}^2 + h_4\ddot{\phi}\right\} \tag{2.32}$$

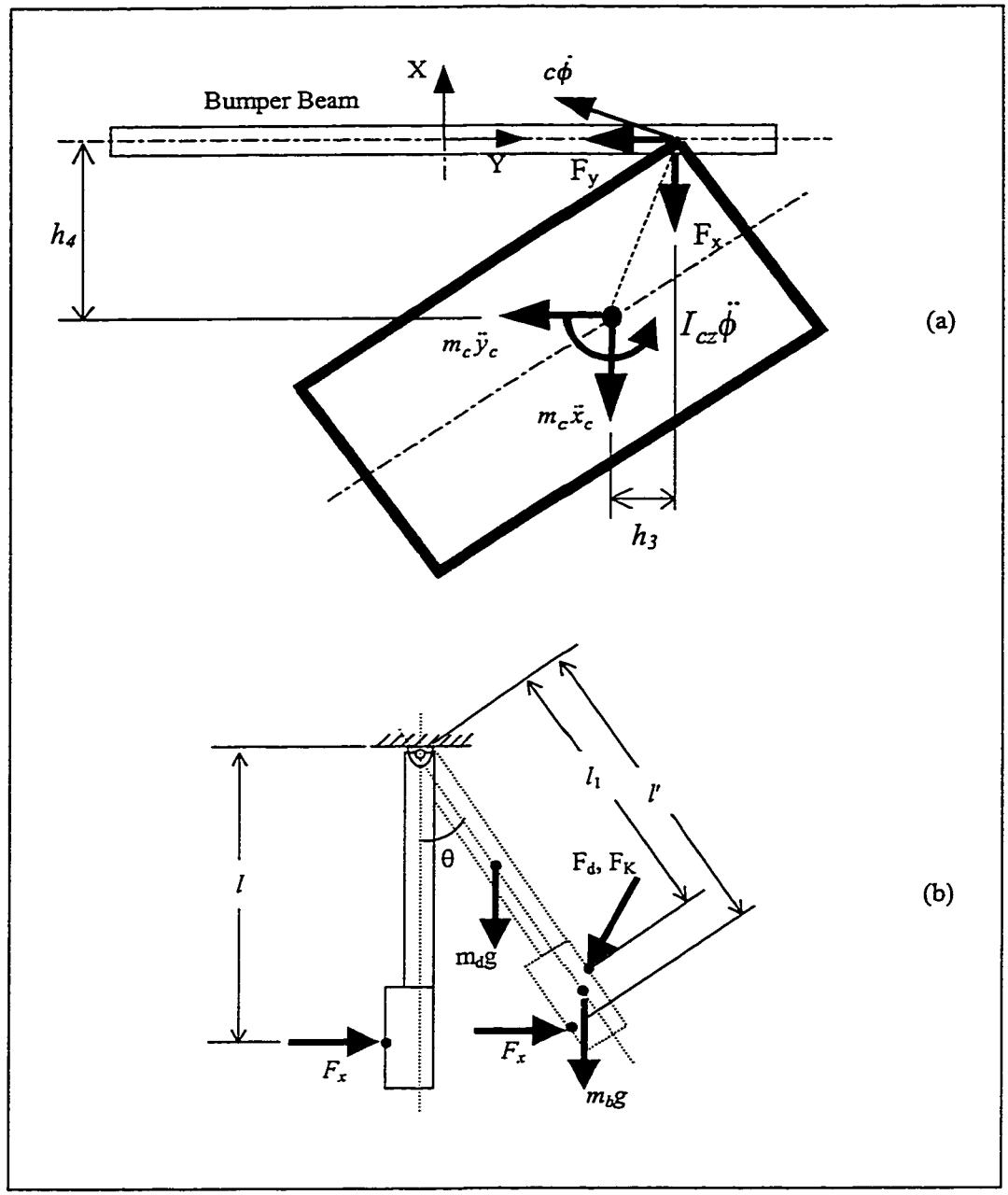

Figure 2.11: Free body diagram of the car mass and the under-ride guard showing the displacement, velocity, forces and moments.

Upon substituting for F_x from above Equation into Equations (2.30) and (2.31), the following Equations of motion describing the pitch coordinates of the under-ride guard and the yaw coordinates of the car mass subject to an oblique impact can be expressed as:

$$\left\{\frac{m_c}{\cos^4\theta}+m_b+\frac{m_d}{3}\right\}l^2\ddot{\theta}+2m_c l^2\left(\frac{\sin\theta}{\cos^5\theta}\right)\dot{\theta}^2+l_1F_d+\left(m_b+\frac{m_d}{2}\right)gl\sin\theta$$
$$+F_k\frac{\partial S_1}{\partial\theta}+F_{st}\frac{\partial S_2}{\partial\theta}+k_t\theta+\frac{m_c l}{\cos^2\theta}\left[h_3\ddot{\phi}+h_4\dot{\phi}^2\right]=0 \qquad (2.33)$$

$$\left[I_{cz}+m_c h_3(h_3-\mu h_4)\right]\ddot{\phi}+m_c h_4(h_3-\mu h_4)\dot{\phi}^2-\frac{m_c l}{\cos^2\theta}(h_3-\mu h_4)(\ddot{\theta}+2\tan\theta\dot{\theta}^2)=0$$

.....(2.34)

Equations (2.33) and (2.34) represent the governing equations of motion of the car mass and the under-ride guard in the second phase of the impact process. The coupled equation of motion are solved to derive the angular motions of the bodies subject to initial conditions obtained from the analysis of first phase of the impact:

$$\theta(0)=0; \quad \phi(0)=\phi_0; \quad \dot{\theta}(0)=\frac{\dot{x}_{b1}}{l}; \quad \dot{\phi}(0)=\dot{\phi}_1 \qquad (2.35)$$

The magnitude of intrusion, velocity and acceleration response of the car mass, and the contact force can then be evaluated from the kinematic relations expressed in Equation (2.29). The solution is terminated when the contact force approaches zero, owing to the loss of contact between the two bodies. The response characteristics of the car mass and the guard masses are then evaluated through analysis of the uncoupled equations of motion in the final phase of the impact process. The angular deflection of the guard mass

is derived by letting $m_c = 0$ in Equation (2.33), while the motion of the car mass is evaluated using particle dynamics at a constant velocity. The displacement response of the two bodies is then examined to detect the occurrence of repeated contact between them due to oscillatory motion of the guard. The Equations of motion, (2.33) and (2.34), representing the second phase of impact are then analyzed under different initial conditions.

2.6. PERFORMANCE ASSESSMENT OF THE UNDER-RIDE GUARD

The effectiveness of the under-ride guard in the event of a car-to-truck rear and side collisions is evaluated in terms of degree of under-ride. The severity of a highway accident involving car-to-truck collision, in general, is related to the magnitude of intrusion of the car under the heavy vehicle structure, and magnitudes of forces or acceleration transmitted to the occupants. The magnitude of intrusion and accelerations transmitted to the vehicle is also related to the crash speed, the relative inertia of the two vehicles and the energy absorption/dissipation characteristics of the structure. The performance of the proposed guard can be evaluated in terms of the magnitude of intrusion, accelerations transmitted to the automobile and the magnitude of energy dissipated by the damper. The performance of the proposed guard is studied in this thesis using these parameters for the rear under-ride guard. The performance measures can, however, be used to evaluate the performance of side under-ride guards.

2.6.1 Performance Criteria

A performance criterion based upon the above factors is formulated to access the relative potential benefits of the proposed guard. The proposed performance criteria comprises the following three components:

a. Magnitude of Intrusion: The intrusion of the car mass under the heavy vehicle structure relates to the degree of under-ride, which is derived from the displacement of the car mass beyond the projection of the hinge point on the ground plane. For convenience of analysis, the peak magnitude of intrusion, $(x_c)_{max}$ is normalized with respect to the wheel-base of the car (L), such that:

$$\mu_d = \frac{(x_c)_{max}}{L} \tag{2.36}$$

where μ_d is the normalized value of intrusion of the car mass.

b. Peak Acceleration: An acceleration response measure is proposed as the peak acceleration of the car mass, normalized with respect to 32g. The normalizing value of 32g is selected based upon the acceleration limit described in the head injury criteria [81], The car mass acceleration response measure, μ_a is thus derived as:

$$\mu_a = \frac{(\ddot{x}_c)_{max}}{32g} \tag{2.37}$$

c Dissipated Energy: The energy dissipated by the damper forms an important criterion for evaluating the performance of the proposed guard. The energy dissipated by the damper, ΔE is evaluated from [105]:

$$\Delta E = \int F_d dS_1 \tag{2.38}$$

The energy dissipated by the damper over the impact cycle is normalized with respect to the initial kinetic energy of the car mass. The energy dissipated by the damper can be evaluated as:

$$\Delta E = pcl_1 \int \dot{\theta} \cos^2(\psi - \theta) d\theta \tag{2.39}$$

Hence, the normalized dissipated energy (μ_e) due to a nonlinear asymmetric damper is given by:

$$\mu_e = \frac{pcl_1 \int \dot{\theta} \cos^2(\psi - \theta) d\theta}{0.5(m_c v_0^2 + I_{cz} \dot{\phi}_0^2)} \tag{2.40}$$

where p is taken as unity to determine the normalized dissipated energy during compression stoke.

2.6.2 Design Optimization

The peak intrusion, acceleration of the car mass, and the magnitude of energy dissipated by the guard are strongly related to the stiffness and damping properties, and the geometry of the guard. The results of the parametric study, presented in the following chapter, revealed that a heavily damped guard with stiff spring yields low intrusion, and high car mass acceleration and dissipated energy. The lightly damped and soft guard, on the other hand, yields excessive under-ride with lower car body acceleration. The need to determine optimal design parameters of the guard is thus identified to achieve the best compromise between the peak intrusion and the car mass acceleration. A constrained

optimization function comprising the three criteria described in section 2.6.1 is thus formulated as:

$$U(\bar{x}) = \text{minimize}\left[\alpha_1(\mu_d) + \alpha_2(\mu_a) + \alpha_3 \frac{1}{\mu_e}\right] \tag{2.41}$$

subject to:

$$g_1(\bar{x}) = q_1 - \mu_d \geq 0$$

$$g_2(\bar{x}) = q_2 - \mu_a \geq 0$$

where $\bar{x}$ is a vector of design variables, given by:

$$\bar{x} = \{\xi_c \;\; n_c \;\; v_c \;\; p \;\; n_e \;\; v_e \;\; k_{11} \;\; k_{12} \;\; k_{st}\}^T$$

q_1 and q_2 are the limiting values of normalized maximum intrusion and acceleration transmitted to the car mass, respectively, and α_i (i = 1,2,3) are the weighting factors. . ξ_c is the damping ratio of the guard, defined as the ratio of compression damping to the critical damping coefficient of the guard, assuming small deflections in the linear range:

$$\xi_c = \frac{c}{2\sqrt{k_{11}(m_c + m_b + m_d/3)}} \tag{2.42}$$

The selection of weighting factors, however, is quite complex due to excessive variations in the magnitudes of different performance variables. For instance, while the performance variable μ_d will have values smaller than 0.1, the values of μ_a may vary in the range 0-1.0. The performance variable corresponding to the intrusion thus needs to be weighted heavily in order to reflect its influence on the overall objective function. Thus the values

of weighting factors are selected to ensure nearly equal contribution of each performance variable to the optimization function. For example, when the constraint set $\{q_1, q_2\}$ is selected as {0.1, 1.0}, the values of $\{\alpha_1, \alpha_2, \alpha_3\}$ are assumed as {10, 1.0, 1.2} such that the values of the three terms in Equation (2.41) are approximately unity. Three sets of constraint values are selected in the optimization study, which are discussed in the following chapters. For the remaining selected constraint sets $\{q_1, q_2\}$= {0.15, 0.75} and {0.2, 0.5}, the values of $\{\alpha_1, \alpha_2, \alpha_3\}$ are respectively assumed as {6.67, 1.33, 1.2} and {5.0, 2.0, 1.2}. The weighting factors may also be selected to minimize either one or two of the performance variables

Since a soft guard yields lower car mass acceleration and high intrusion, the constrained optimization problem, Equation (2.41), is solved using nonlinear programming technique for different limiting values for $\{q_1, q_2\}$.

2.7 SUMMARY

An analytical model of the damped proposed under-ride guard under-ride guard is attempted and performance characteristics are investigated under different speeds and angles of rear impact. The analytical model comprises the nonlinear force-deflection and force-velocity properties of the energy restoring and dissipative elements of the guard, respectively. A performance criteria comprising the magnitude of intrusion, car mass acceleration and dissipated energy is formulated to study the effectiveness of the proposed guard. A multi-variable constrained optimization problem is formulated and solved using nonlinear programming technique to derive optimal parameters for the guard.

CHAPTER 3

PERFORMANCE CHARACTERISTICS OF THE DAMPED UNDER-RIDE GUARD

3.1 INTRODUCTION

Upon recognizing the severity and potential safety risks associated with car-to-truck collisions, concepts of impact energy dissipation have been briefly outlined in few studies [1,99]. Persicke and Child [99] performed experimental evaluations of a concept, in rear under-ride guard with enhanced energy dissipation capabilities. The studies concluded that a damped under-ride guard can yield significant potential performance benefits in terms of reduced levels of acceleration and force transmitted to a test dummy. A concept of the energy dissipating guard was proposed and its analytical model was developed in the previous chapter. A performance criteria comprising the magnitude of intrusion, car-mass acceleration and dissipated energy was formulated to study the effectiveness of the proposed guard.

The energy absorption capabilities of such an under-ride guard are enhanced by combining the energy absorption properties of the structure through its plastic deformations and energy dissipation properties of the asymmetric and nonlinear hydraulic dampers. While the study of energy absorption capabilities of the structure have been carried out using crash analysis software, such as DYNA3D [31], the energy dissipation characteristics of the guard can be conveniently analyzed through simple lumped parameter models. The energy dissipation properties can be further evaluated,

analytically and experimentally, using the Hardware-in-the-Loop (HIL) technique in a highly efficient manner. Since the hydraulic damper, the primary nonlinear component of the guard, determines the degree of energy dissipation, a limited validity of the analytical model may be realized through HIL tests performed on the damper. The damping forces developed by the damper however, comprise strongly nonlinear and significant contributions due to hysteresis caused by fluid compressibility, backlash, Coulomb friction, gas spring and asymmetric valving. Although a large number of damper models, incorporating contributions due to dry friction, air spring and asymmetric damping, have been developed based upon functions and constants derived from laboratory experiments, the influence of variations in the temperature, fluid viscosity and cavitation can not be characterized accurately [108, 109]. The HIL method allows the use of actual damper in the simulation process, such that the contributions of various complex non-linearities can be easily incorporated in deriving the dissipation of crash energy.

In this chapter, the potential benefits of the fast emerging HIL simulation method are exploited to study the energy dissipation characteristics of the under-ride guard. The results derived from the HIL simulation is analyzed to determine the amount of energy dissipated, acceleration level, rebound velocity and the magnitude of intrusion. The results of the study are used to validate the analytical model formulated in the previous chapter. The model validation, however, is limited to extremely low velocity direct impacts (2 *m/s*) due to the limitations of the available servo-hydraulic hardware. Since the primary functions of the proposed guard are to minimize the intrusion and the forces transmitted to the car mass by dissipating part of the crash energy, the HIL test is undertaken to study the energy dissipated by the damper.

The effectiveness of the proposed guard to reduce the severity of accidents under various crash situations is illustrated using the results of a comprehensive parametric study. The effects of under-ride guard parameters, linear and yaw velocities of the impacting mass, angle of impact and friction properties of the contacting surfaces on the accident severity are studied based on the performance criteria developed in the previous chapter. The results of the parametric study are compared to those of a conventional guard obtained through DYNA3D modeling. A set of optimal parameters of the proposed guard is derived using the optimization formulation discussed in Chapter 2.

3.2 HARDWARE-IN-THE-LOOP (HIL) SIMULATION OF THE GUARD

Hardware-in-the-Loop (HIL) simulation technique is an emerging real time simulation tool for the efficient evaluation of electronic and mechanical components, and control systems. HIL has found innumerable applications in aerospace and missile development programs [110-112]. Although some applications of the HIL were reported nearly two decades ago [113], the technology was limited only for certain special applications due to high cost and limited computer hardware performance. With advances in the computer hardware and software, however, the HIL is rapidly becoming an extremely efficient tool for the development and assessment of control systems, electronic control units and new mechanical components. In the recent years, the HIL simulation technique has been implemented for wide range of applications in the automotive sector [109, 114-117].

Besinger *et al.* [109] described the laboratory testing of hydraulic dampers using the HIL method and the accuracy of the test method was investigated. A simplified mathematical model of a hydraulic shock absorber was then developed based on the test

results. Krohm [114] has attempted the use of HIL simulation method for the development of Electronic Clutch Management System (ECM), which is used for automatic engagement of the clutch during start and gear change in a vehicle with a gear box, obviating the need for a clutch pedal. The paper describes the development process, the HIL structure, problems in implementing real-time models, evaluation of models and comparison of numerical integration methods. Hansselmann [115, 116] further discussed the hardware requirement and the various capabilities of HIL simulation using the real-time option of the SIMULINK software.

3.2.1 Methodology

The HIL method is used to simulate the impact of the car mass with the energy dissipative under-ride guard. The dynamics of the guard and the impacting car mass, derived from the principle of impulse and momentum and expressed in Equation (2.16), is rewritten with unknown damping force F_d. A commercially available heavy vehicle damper is installed between a load cell and a vibration exciter, as shown in Figure 3.1. A MATLAB SIMULINK model of the Equation (2.16), as shown in Figure 3.2, is developed to solve the equations of motion in conjunction with the instantaneous damping force derived from the damper test stand. The solution is initiated assuming negligible damping force prior to the impact, and the relative deflection response across the damper is computed at each integration step. A displacement command signal is generated from the relative displacement response using the digital to analog converter (DAC), which is used to drive the servo-hydraulic damper test system, as shown in Figure 3.1. As the impact process progresses, the measured damping force is acquired

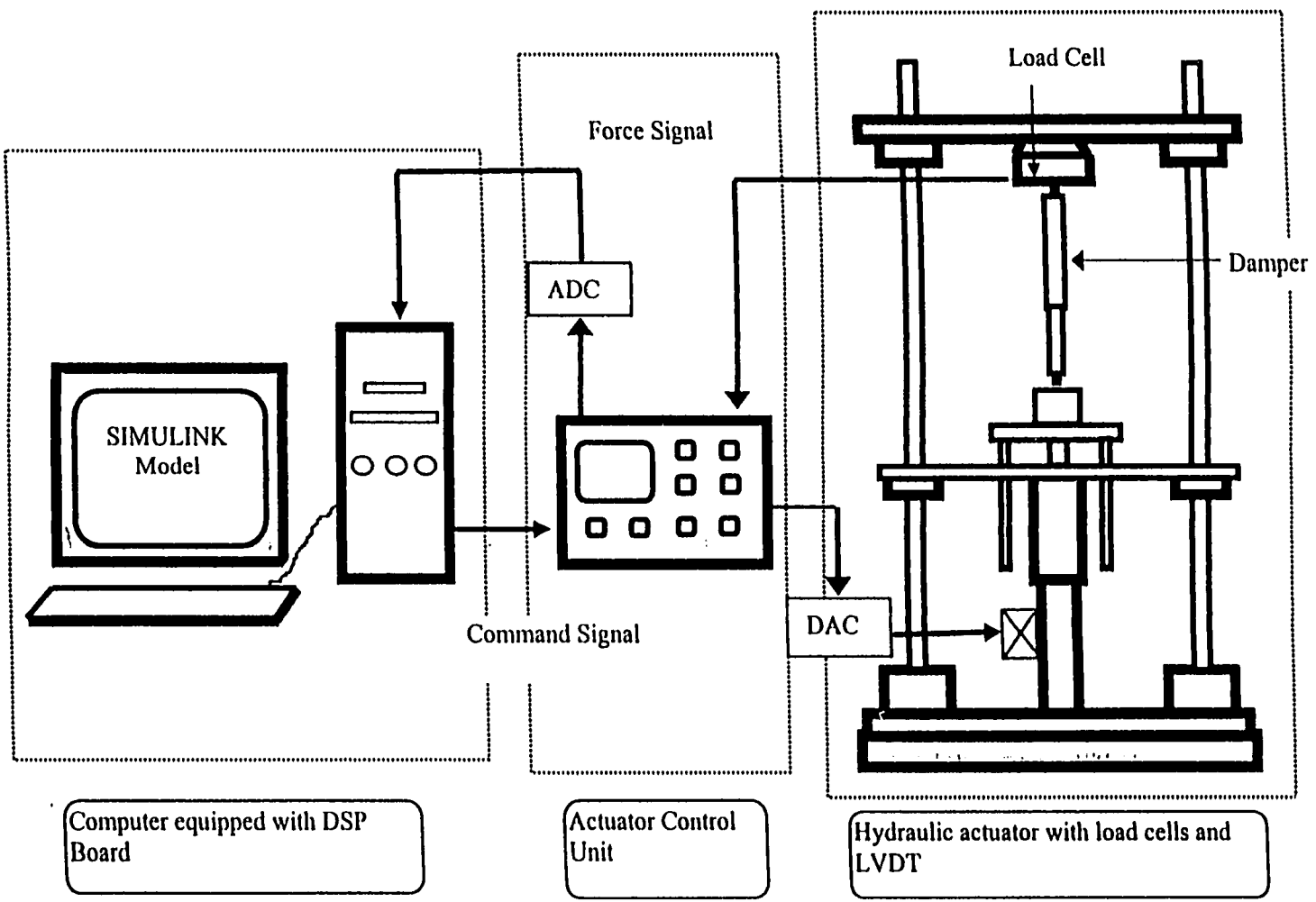

Figure 3.1: Hardware-in the Loop Simulation Setup.

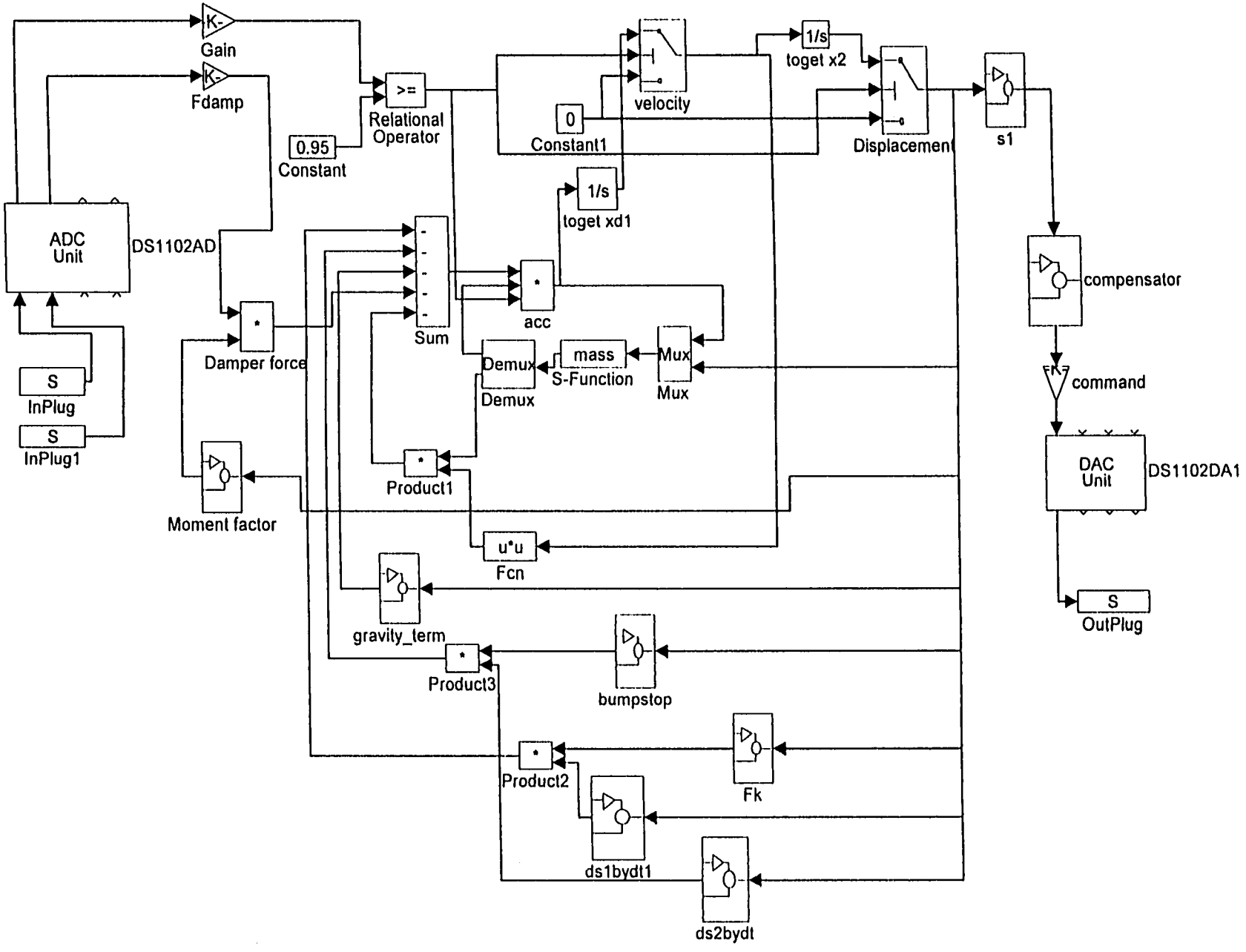

Figure 3.2: MATLAB SIMULINK model of the car-to-under-ride guard impact.

and interfaced with the SIMULINK model using an Analog-to-Digital-Converter (ADC), at each integration step. The third-order Runge-Kutta integration algorithm was used to perform the HIL simulation, to achieve a trade-off between the accuracy and the computation time [115]. The dynamics of the guard and the car mass are then evaluated through solutions of equation of motion of the two uncoupled bodies.

HYDRAULIC ACTUATOR SYSTEM

The hydraulic actuator system consists of two parts, namely, a two-stage, four-way servo valve (MTS MODEL 252.25) and an actuator (MTS MODEL 242.02). The nozzle-flapper design with mechanical feedback from the spool provides positive internal closed-loop flow control. The flow rate is also limited to a maximum of 56 *liter/minute* (15 *gpm*) over servo-system frequency range (up to 25 *Hz*), for full flow conditions where a full valve opening command signal of 40 *mA* is applied. The actuator contains a double-ended piston, which has equal areas of 594 mm^2 on both sides for balanced performance and a closed-housing linear variable differential transformer (LVDT) to provide accurate indication of piston rod displacement. The LVDT is connected to the servo controller. The actuator has a static stroke of 216 *mm*, and a dynamic stroke of 203 *mm* after the total cushion length of 13 *mm* is deducted. The optimum operating pressure is 21 *MPa* for system performance and reliability with a maximum force of 10 *kN*.

SERVO CONTROLLER

The servo controller (MTS MODEL 407) is a single channel, digitally-supervised Proportional, Integral, Derivative and Feed Forward (PIDF) controller that provides complete control of one servo hydraulic channel/station in the test system. This includes

AC and DC transducer conditioning, basic function generation (with the capability to accept externally generated command signals), servo-valve drive signal generation, and hydraulic pressure control. The menu driven controller is convenient for the user to select PID control parameters for closed-loop control. The feature of limit settings enables the user to define various force and displacement limit settings as a safety measure.

HOST COMPUTER AND I/O INTERFACE

A microcomputer was used as a host to generate the command displacement signal to the servo controller using the system model response and the measured force signal through an I/O interface. A DS1102 I/O device was used to interface the actuator hardware and the computer. The DS1102 is designed for development of high-speed multi-variable real-time simulations, and is based on the Texas Instruments TMS320C31 third generation floating point Digital Signal Processor providing fast instruction cycle time for numeric intensive algorithms. The TMS320C31 supports a total memory space of 16-M 32-bit words, including program, data and I/O space.

SIMULATION ALGORITHM

The equations of motion of the system to be tested in HIL can be solved using many different algorithms available in the SIMULINK routine. However, for faster computation in real-time the efficiency of each algorithm has to be considered. Hanselmann [115] conducted a detailed study on the relative merits of Euler, third and forth-order Runge-Kutta methods to simulate the ABS system of an automobile. The study concluded the following:

- The execution time should be predictable, and preferably same in each time step, hence avoiding the variable time step size methods.

- Trial and error methods are not suitable due to the real-time nature of the simulation, where the equations have to be solved in one 'shot'.

- The use of higher order methods, which increase the minimum step size due to higher computational load, is normally recommended. Higher order solution routines also give more fidelity if the model has switching or logic built in.

By comparing the solutions obtained using different methods, Hanselmann concluded that third order Runge-Kutta method yields a good compromise between the accuracy and efficiency of the solution. The vehicle impact problem considered in this study, has a very short time duration (0.1 *s*) and hence requires a fast computation. The third-order Runge-Kutta method was thus selected for solving the governing equations of motion in this study.

3.2.2 Hydraulic System Time Lag

The HIL test method can serve as a highly efficient tool to evaluate the performance characteristics or the contributions of a subsystem, while incorporating the dynamics behavior of the overall system. The effectiveness of the HIL test, however, impinges on its ability to interface the hardware signals with the simulation software in real time. The servo-hydraulic system, in general, yields certain time delays arising from the limited band-width of the servo-valve and actuator dynamics. The processing of measured and command signal may yield some additional delays.

In the HIL test performed in this study, the third phase of solution after the loss of contact resulted in highly unstable motion of the servo-hydraulic exciter. This instability was partly attributed to the sharp discontinuity in the effective mass after the loss of contact between the car mass and under-ride guard mass (Section 3.2.4), and partly due to

the time lag associated with the servo-hydraulic system. The frequency response characteristics of the servo-hydraulic system equipped with a 5 *ms* servo-valve, were thus measured and analyzed to quantify and compensate for the time lag. The measured frequency response of the servo-hydraulic system under no-load revealed a nearly constant time delay of 6.5 *ms* between the command and actuator displacement signals in the 0-500 *Hz* frequency range. The unstable actuator response was thus mostly attributed to this time delay, and efforts were made to design a lag-lead compensator.

SERVO-HYDRAULIC SYSTEM MODEL

A system function for the servo-hydraulic system is derived using proportional feedback control. The servo-valve is modeled as a first-order dynamic system with gain K_Q and valve time constant of τ_v. The actuator is represented by a linear flow-rate-displacement transformer, neglecting the seal friction and inertia effects. A block diagram model of the proportional feedback servo-hydraulic system is illustrated in Figure 3.3. In Figure 3.3, e_c and e_f represent the position command and feed back signals, respectively. The servo-valve input current is designated as i, and s is the Laplace operator. Q is the flow-rate, and x is the piston position of the servo-valve. The piston cross sectional area and servo-amplifier gains are respectively represented by A and K_A.

The frequency response function of the closed-loop serve-hydraulic, system is derived as:

$$H(s) = \frac{K_A K_Q}{s^2 + \frac{1}{A\tau_v}s + \frac{K_A K_Q K_F}{A\tau_v}} \tag{3.1}$$

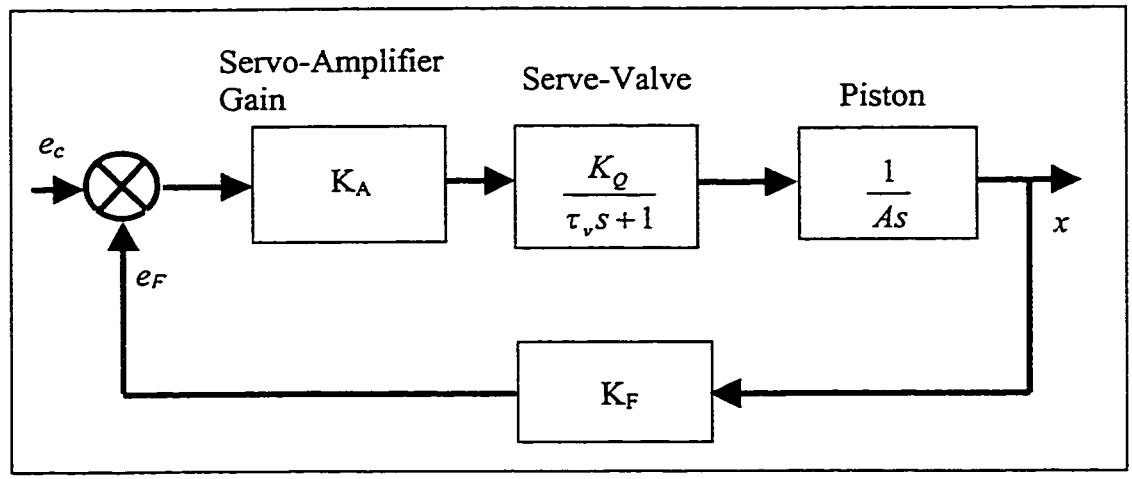

Figure 3.3: The block diagram representation of the hydraulic actuator.

PARAMETERS OF THE SIMPLIFIED SYSTEM MODEL

The above simplified system model was validated by comparing the model response with the experimental results of the actual hydraulic system. The frequency response characteristics of the simplified system model were obtained using the following parameters:

Piston area (A) = 594 mm^2; Servo-amplifier gain (K_A): 225 *mA/V*; Position transducer gain (K_F): 0.0396 *V/mm*.

Since the resistance of the servo-valve is 40 Ohms, the servo-amplifier gain 225 *mA/V* is equivalent to 9 *V/V*, as set in the controller. In the test, the command displacement signal to the system is generated and the piston displacement is recorded by a signal analyzer (B&K 2032) through the I/O interface. A sinusoidal sweep command signal in the range 0-25 *Hz* with an amplitude of 2.54 *mm* was generated in the analyzer and used to process the system transfer function characteristics. The system was then tested under operating

supply pressure P_s = 21 MPa and the servo-amplifier gain K_A = 225 *mA/V*. Although the time constant of the valve is known to be 5 ms under ideal flow conditions, it may vary depending upon the coupled dynamics of the system. The no-load flow gain K_Q also need to be determined. The measured frequency of the system is analyzed I conjunction with the model response obtained by varying K_Q, τ and A. The servo-valve time constant was varied within the range of 4.6 ms to 6.4 ms, while the servo-valve no-load flow gain and the piston area were varied in the range of 7529 - 10176 $mm^3/s.mA$ and 548 - 613 mm^2, respectively. The model parameters were selected to achieve reasonable correlation with the measured response.

VALIDATION OF THE SYSTEM MODEL

Figures 3.4 to 3.6 illustrate the measured frequency response of the system and the simulation results with varying servo-valve time constant τ (K_Q=8849 $mm^3/s.mA$ and A=587 mm^2), varying servo-valve no-load flow gain K_Q (τ= 5 ms, A=587 mm^2) and varying A (τ = 5 ms, K_Q=8849 $mm^3/s.mA$), respectively. Comparison of simulation and test results reveal that the simplified model represents the hydraulic system quite well up to 20 *Hz*. The experimental phase plot shows a small phase lag between the measured and simulation results. This may be caused by the time delay in the actual system, which was not considered in the model, for example, the time delay in A/D and D/A conversion, data acquisition and signal processing.

The servo-valve time constant τ, influences the system performance in a significant manner. An increase in the servo-valve time constant induces the magnitude to increase in the entire frequency range of interest, and the phase to decrease at higher frequencies. A servo-valve time constant of 5.0 *ms* provides the best matching of the

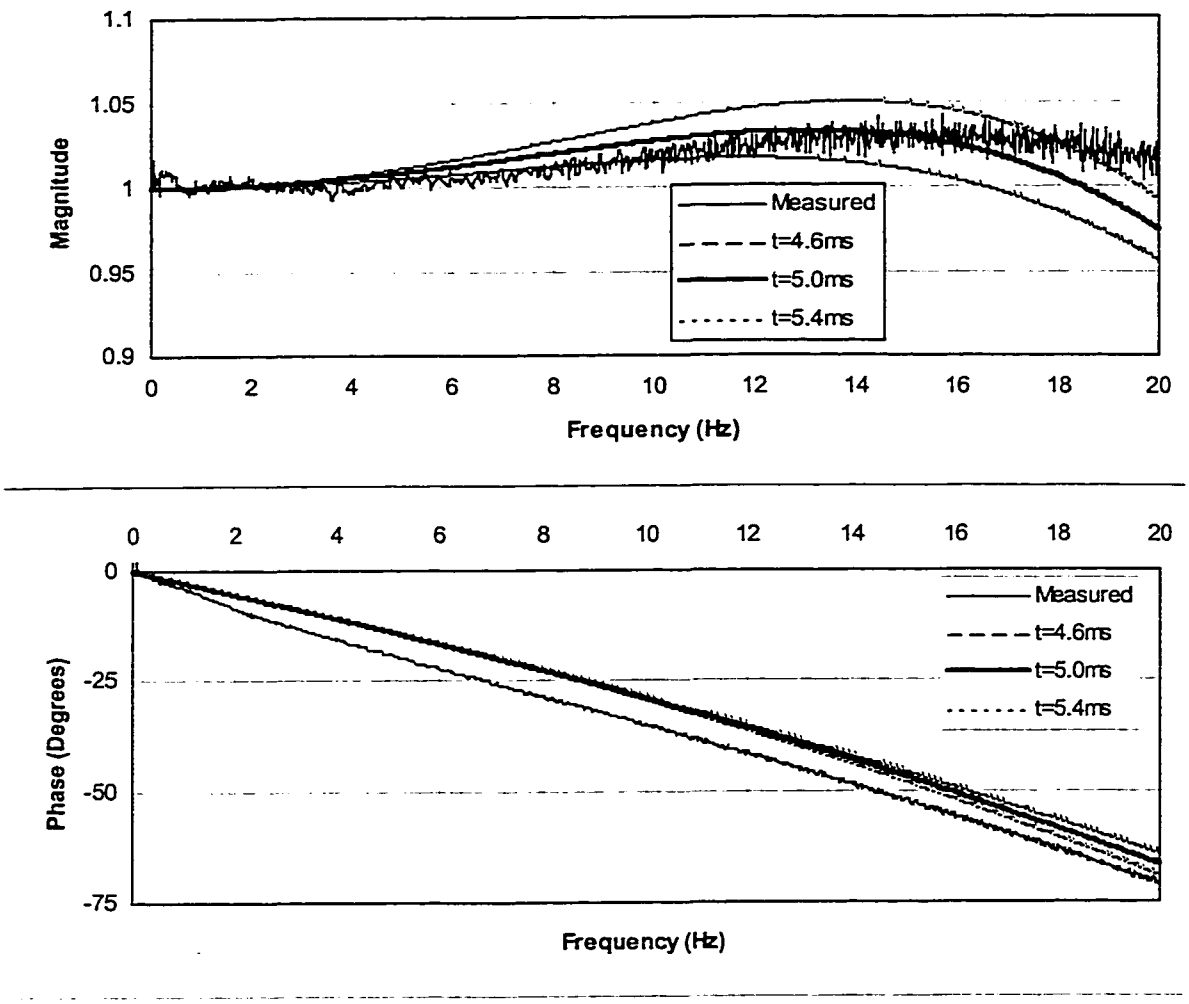

Figure 3.4: Experimental response and simulation results with varying τ.

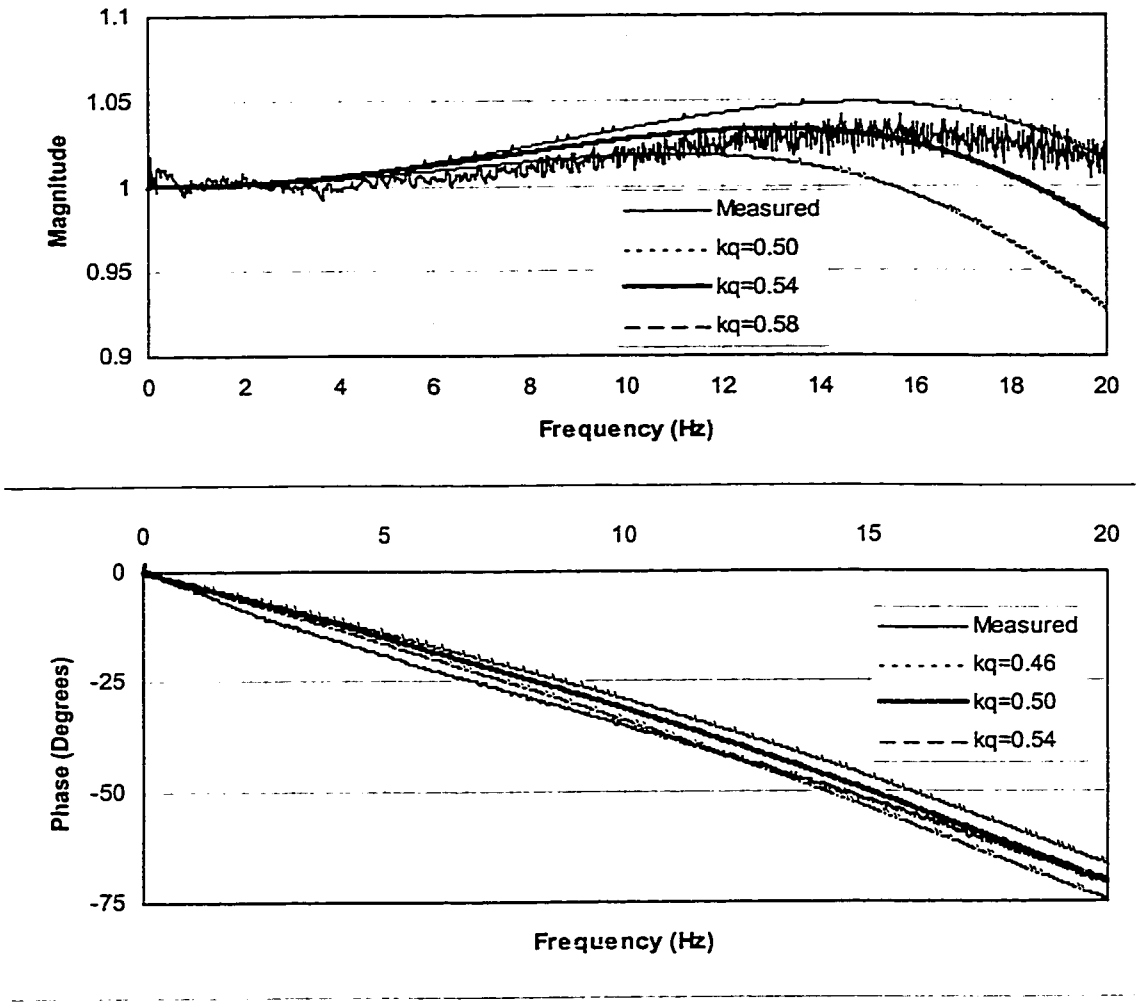

Figure 3.5: Experimental response and simulation results with varying K_Q.

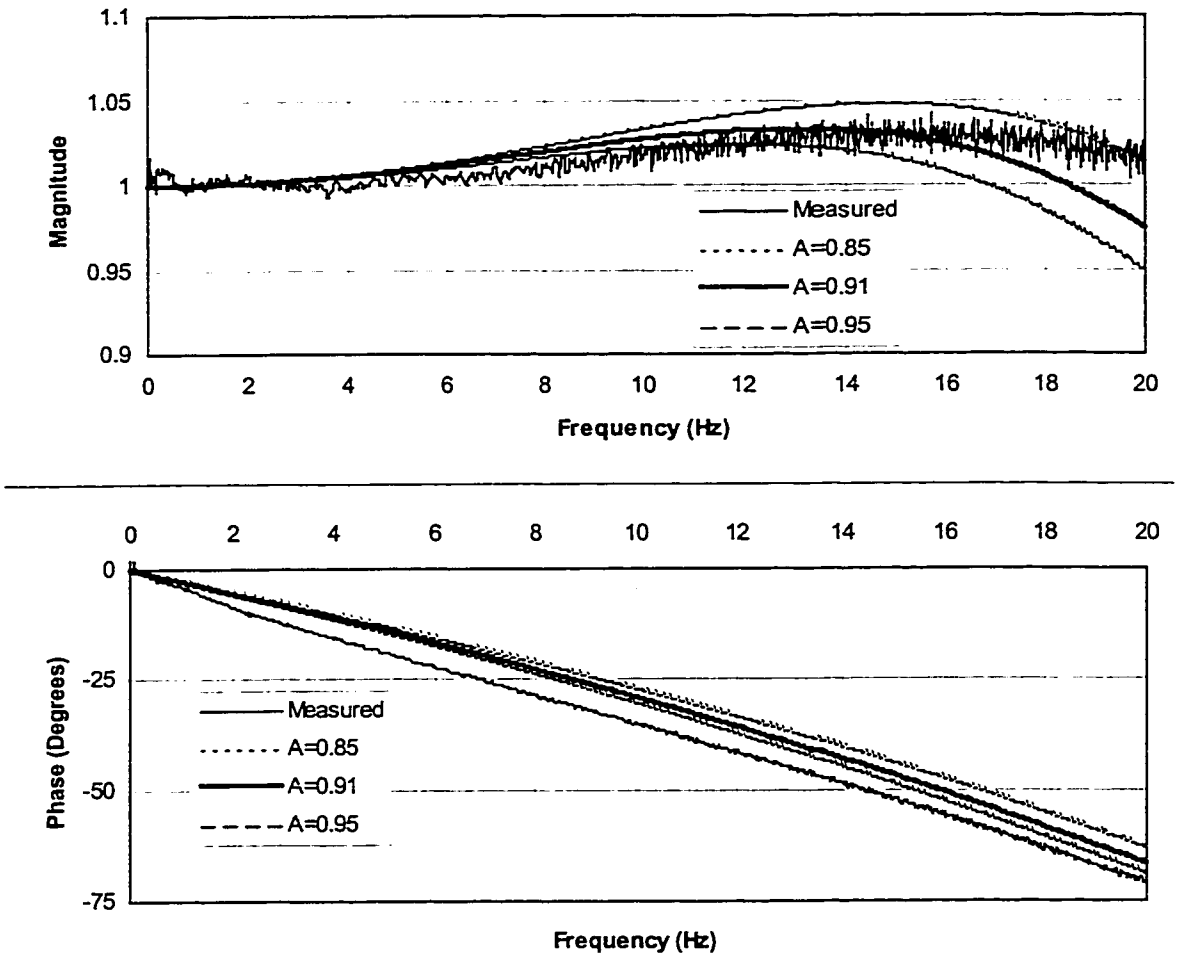

Figure 3.6: Experimental response and simulation results with varying A.

magnitude and the phase within 20 *Hz*, which also confirms with the manufacturer's specifications. A servo-valve time constant of 5.0 *ms* can thus be determined to be the proper parameter in the model. The servo-valve no-load flow gain also influences the system performance in a significant manner. An increase in the servo-valve no-load flow gain induces both the magnitude and the phase to increase within the entire frequency range of interest. It can be observed that the influence is quite similar to that of the proportional gain. A servo-valve no-load flow gain of 8849 $mm^3/s.mA$ provides the best agreement between the measured and model response in both the magnitude and the phase up to approximately 20 *Hz*. A no-load flow gain of 8849 $mm^3/s.mA$ can thus be determined to be the proper parameter in the model. The analysis revealed that value of 587 mm^2, given by the manufacture, yields close agreement between the measured and model response up to 20 *Hz*.

COMPENSATION FOR TIME-DELAY

In this study, the lag-compensation was initially achieved by introducing a lead of 6.5 *ms* in the command signal. Although this approach provided a constant lead in a relatively simpler manner, the influence of frequency and actuator speed, as limited by the flow characteristics of the servo-valve, on the overall response could not be incorporated. Alternatively, a lead compensation function G(s) can be derived from the inverse of H(s) as:

$$G(s) = \frac{s^2 + \frac{1}{A\tau_v}s + \frac{K_A K_Q K_F}{A\tau_v}}{K_A K_Q} \tag{3.2}$$

The above compensator was implemented in the servo-control loop and measurements were performed to determine the frequency response function, $H_1(s) = G(s) \bullet H(s)$, of the servo-hydraulic system. The magnitude and phase response characteristics, illustrated in Figure 3.7, clearly show significant reduction in the phase delay, with unity magnitude upto approximately 500 *Hz*. The corresponding time delay was observed to be in the order of 0.3 *ms* in the 0-500 *Hz* frequency range. The lead-compensation, however, resulted in deterioration in the magnitude response at higher frequencies.

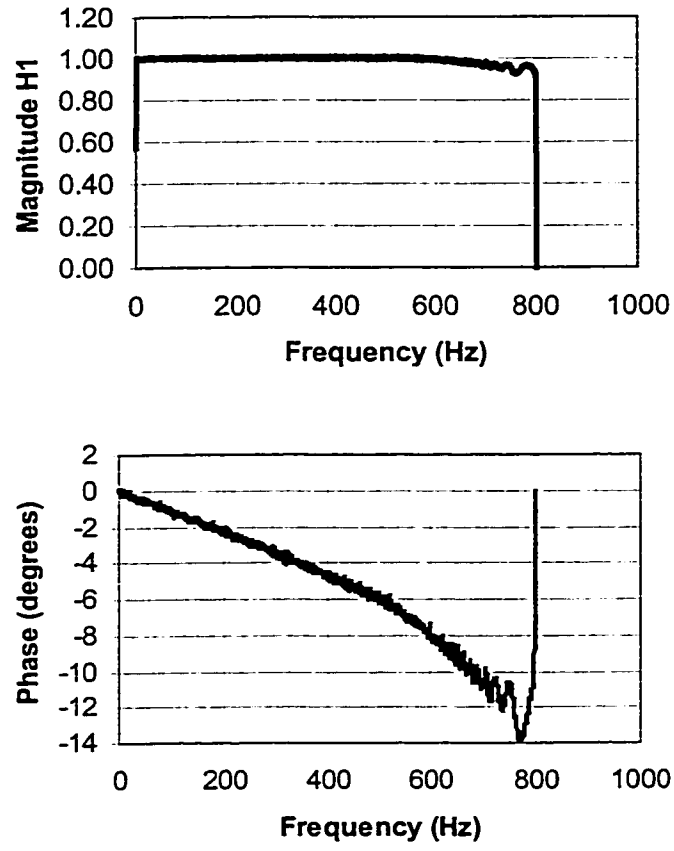

Figure 3.7: Magnitude and phase response of compensated hydraulic system.

3.2.3 Test Damper

A hydraulic damper employed in heavy freight vehicles was chosen as a test damper for the study, and its force-velocity characteristics were identified through laboratory tests. The damper was mounted between a fixed inertial frame and a servo-hydraulic vibration exciter. A load cell was installed between the damper and the inertial frame to measure the damping force, while the damper velocity and deflection were measured using LVT and LVDT transducers, respectively. The damper was excited under constant peak velocity sinusoidal excitations in the 1-15 *Hz* frequency range. The damping force revealed considerable hysteresis at higher frequency excitations, and relatively low level force due to the air spring. The acquired data was analyzed to derive the average peak force-peak velocity characteristics, as shown in Figure 3.8.

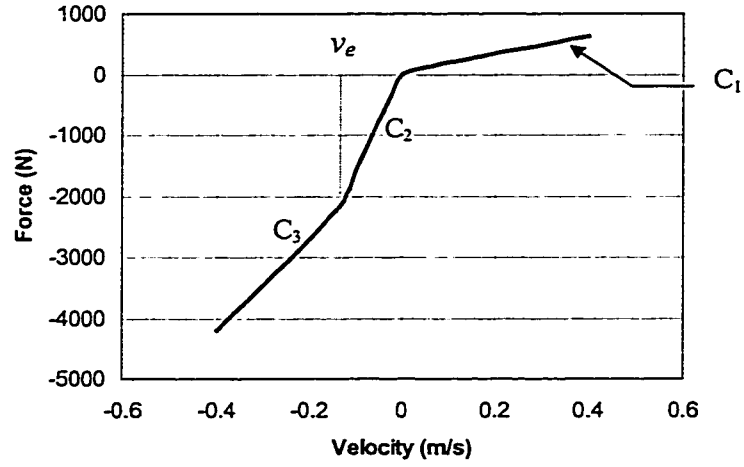

Figure 3.8: Measured force-velocity characteristics of the test damper.

The results show that the average compression force varies nearly linearly with the velocity, and is considerably smaller than the rebound force. The rebound damping coefficient is considerably higher at low velocities due to bleed flows, and reduces to a lower value at higher velocities due to flows through blow-off valves. Although the test results showed significant dependence of the hysteresis on the excitation frequency, specifically in the rebound stroke, the mean damping force was observed to be relatively less sensitive to variations in the frequency and peak displacement amplitude. Upon neglecting the hysteretic effects, the average force-velocity characteristics of the damper was expressed as:

$$F_d = \begin{cases} C\dot{S}_1 & \text{for} \quad 0 < \dot{S}_1 < v_c \\ C[v_c + n_c(\dot{S}_1 - v_c)] & \text{for} \quad \dot{S}_1 > v_c \\ pC\dot{S}_1 & \text{for} \quad v_e < \dot{S}_1 < 0 \\ pC[v_e + n_e(\dot{S}_1 - v_e)] & \text{for} \quad \dot{S}_1 < v_e \end{cases} \tag{3.3}$$

where C is the viscous damping coefficient associated with the bleed flows in the compression mode, $\dot{S}_1$ is the relative velocity, n_c and n_e are the damping reduction constants related to blow-off damping during compression and rebound respectively, v_c and v_e are the respective blow-off velocities and asymmetry constant p is the ratio of rebound to compression damping coefficients corresponding to bleed flows. The peak force-peak velocity characteristics of the damper revealed single stage compression damping coefficient, C = 1625 *Ns/m*. The parameters for the damper model, described in Equation (3.3), were established from the test data as: C = 1625 *Ns/m*; n_c = 1.0; v_c = 0 *m/s*; p = 9.39; n_e = 0.526; and v_e = -0.144 *m/s*.

3.2.4 Test Results and Model Validation

The equation of motion of the damped under-ride guard subject to a direct impact, given in Equation (2.16), is solved to determine the energy dissipation properties of the under-ride guard using the damper model described in Equation (3.3). The analytical model of the proposed guard is solved under direct impact at different impact velocities using numerical integration techniques to determine the performance characteristics of the guard in terms of magnitude of intrusion, rebound velocity, acceleration response of the car mass and the under-ride guard, and the energy dissipated by the nonlinear damper. The simulation parameters used for the study are: $l = 0.6\ m$, $l_1 = 0.6\ m$, $l_2 = 0.6\ m$, $m_c = 1000\ kg$, $m_b = 12\ kg$, $m_d = 20\ kg$, The analyses are performed at only low impact velocities due to the flow limitations of the test hardware. Four different initial velocities are selected: 0.5, 1.0, 1.5, and 2.0 *m/s*. The SIMULINK model of the under-ride guard incorporating the damper model, described in Equation (3.3), is further developed and analyzed under the same range of impact velocities. The acceleration response of the car mass and bumper beam, magnitude of intrusion, rebound velocity, and the energy dissipated by the damper were derived from the SIMULINK model. The results were observed to be identical to those derived from numerical integration of Equation (2.16).

The SIMULINK model of the under-ride guard was modified by replacing the damping force model with the measured damping force signal in the HIL configuration. The HIL tests were performed under different magnitude of direct impact velocities and the corresponding force-velocity and force-displacement characteristics of the damper were acquired. The force-displacement characteristics of the damper are analyzed to derive the energy dissipated, using Equation (2.40). The response characteristics in terms

of instantaneous intrusion, rebound velocity and accelerations were extracted from the HIL SIMULINK model.

The displacement, velocity and acceleration response of the coupled car mass and under-ride guard during the initial impact process, derived from the analytical model are compared with those obtained from the HIL simulation under impact speeds of 1.0 and 2.0 *m/s*, as shown in Figures 3.9 and 3.10, respectively. The results show excellent correlation between the analytical and HIL test results in view of the velocity and acceleration response for both impact speeds. The analytical displacement response also correlates very well with the HIL simulation results in the interval, $0 < t < 0.25$, for 1.0 *m/s* impact velocity and $0 < t < 0.22$ for 2.0 *m/s* impact velocity. These intervals represent the duration of the second phase of the impact process, prior to the loss of contact between the two bodies. A comparison of the response characteristics of the guard under impact velocities 1.0 *m/s* and 2.0 *m/s* show similar behavior. The response characteristics of the guard subject to an initial velocity of 2.0 *m/s* is discussed further to demonstrate the validity of the analytical model, in the following subsections.

The contact between the car mass and the guard occurs at $t = 0$ at the specified initial velocity. The magnitude intrusion of the car mass approach nearly 0.1 *m* and 0.16 *m*, under impact at 1 *m/s* and 2 *m/s* respectively, due to the relatively low damping in the compression mode. The magnitude of acceleration of the coupled car mass and the guard also approach approximately 13 m/s^2 and peak values of 30 m/s^2 at the same time. The flexible guard together with the car mass then undergoes rebound motion, while the magnitude of acceleration and displacement decrease gradually, as shown in Figure 3.9 and 3.10. A loss of contact between the two bodies occurs at $t = 0.255$ *s* and $t = 0.22$ *s*,

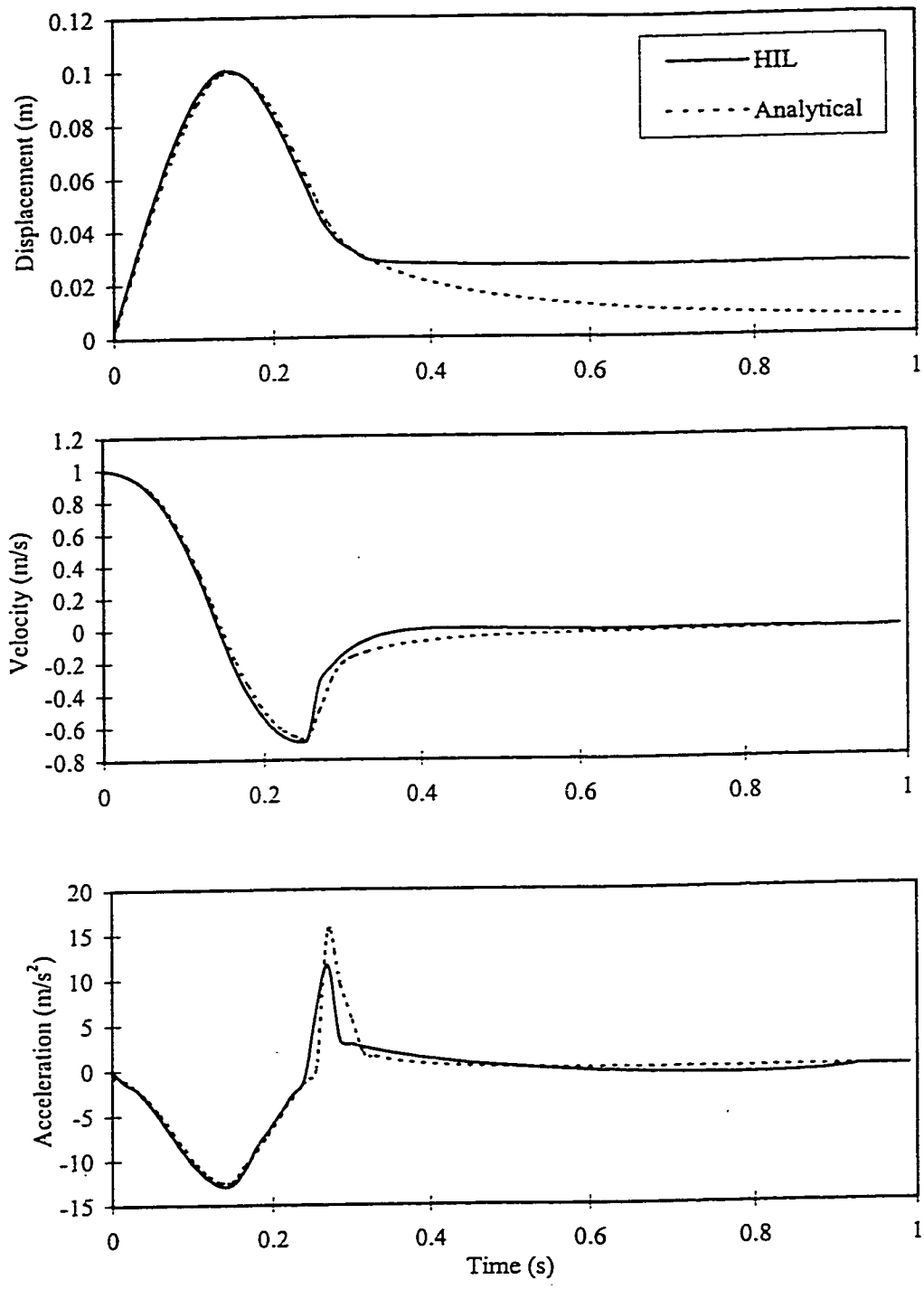

Figure 3.9: Comparison of displacement, velocity and acceleration response of the under-ride guard derived from HIL test and the analytical model (Direct impact at 1.0 *m/s*).

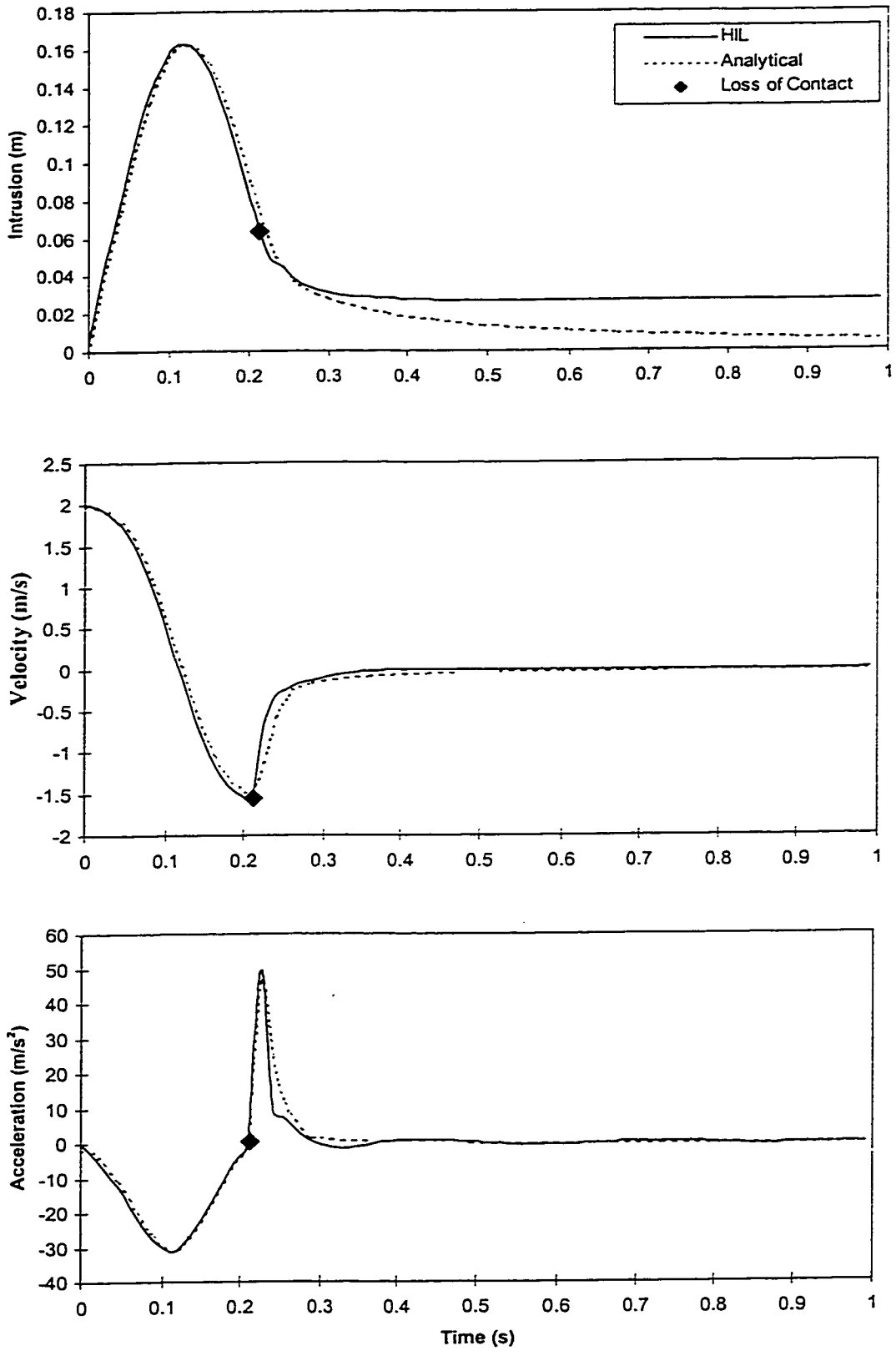

Figure 3.10: Comparison of displacement, velocity and acceleration response of the under-ride guard derived from HIL test and the analytical model (Direct impact at 2.0 *m/s*).

under the two different impact velocities, when the contact force diminishes. The velocities of the car mass gradually decrease after the impact, and approach peak rebound velocities of 0.73 *m/s* and 1.5 *m/s* prior to the loss of contact, under initial impact velocities of 1 *m/s* and 2 *m/s*, respectively. The results presented in the Figure 3.10 further show that the displacement, velocity and acceleration response of the guard mass, derived from the HIL test, correlate reasonably well with those obtained from the analytical model, prior to the loss of contract.

The loss of contact represents a sudden discontinuity in the total mass of the coupled system, which reduces to a very low value due to the mass of the bumper beam and the drop arms alone. The solution of Equation (2.16) with $m_c = 0$ thus yields a rapid increase in the acceleration response of the guard, which can be attributed to the transmission of high damping forces to a relatively light mass. The response of the decoupled damped guard is similar to that of an over-damped system. The displacement response of the guard asymptotically approaches the equilibrium in a gradual manner. The displacement response of the guard after the loss of contact derived from the HIL simulation, however, is considerably lower than that of the analytical model response. This discrepancy is most likely attributed to the time delays associated with the electro-hydraulic system, high natural frequency and relatively high dumping ratio of the uncoupled guard. This discrepancy is further observed in the time history of the measured damping force and force-displacement characteristics of the damper, as shown in Figures 3.11 and 3.12, for initial velocities of 1.0 *m/s* and 2.0 *m/s*, respectively.

The measured damping force during compression stroke correlates very well with that obtained from the analytical model, as observed from the force-time and

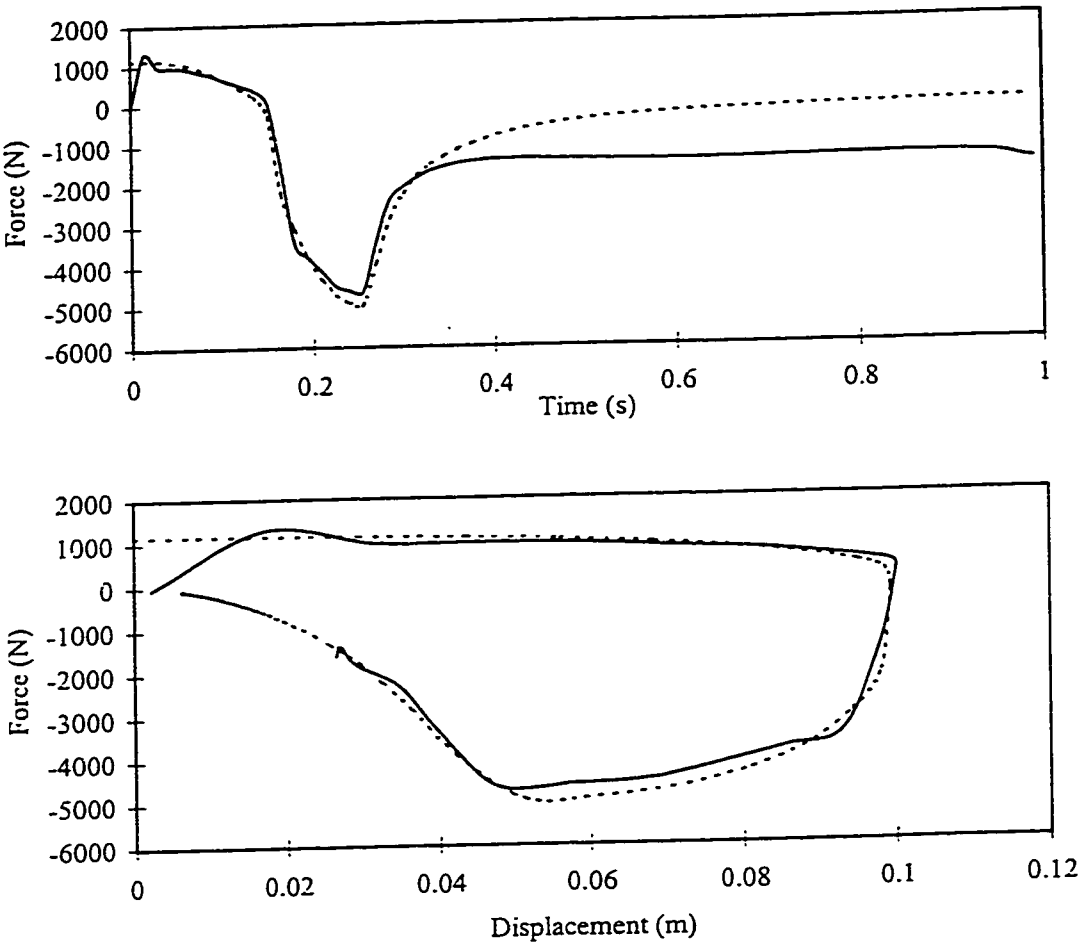

Figure 3.11: Comparison of force-time and force-displacement response of the under-ride guard derived from HIL test and Analytical Model (Direct impact, $v_0 = 1.0\ m/s$).

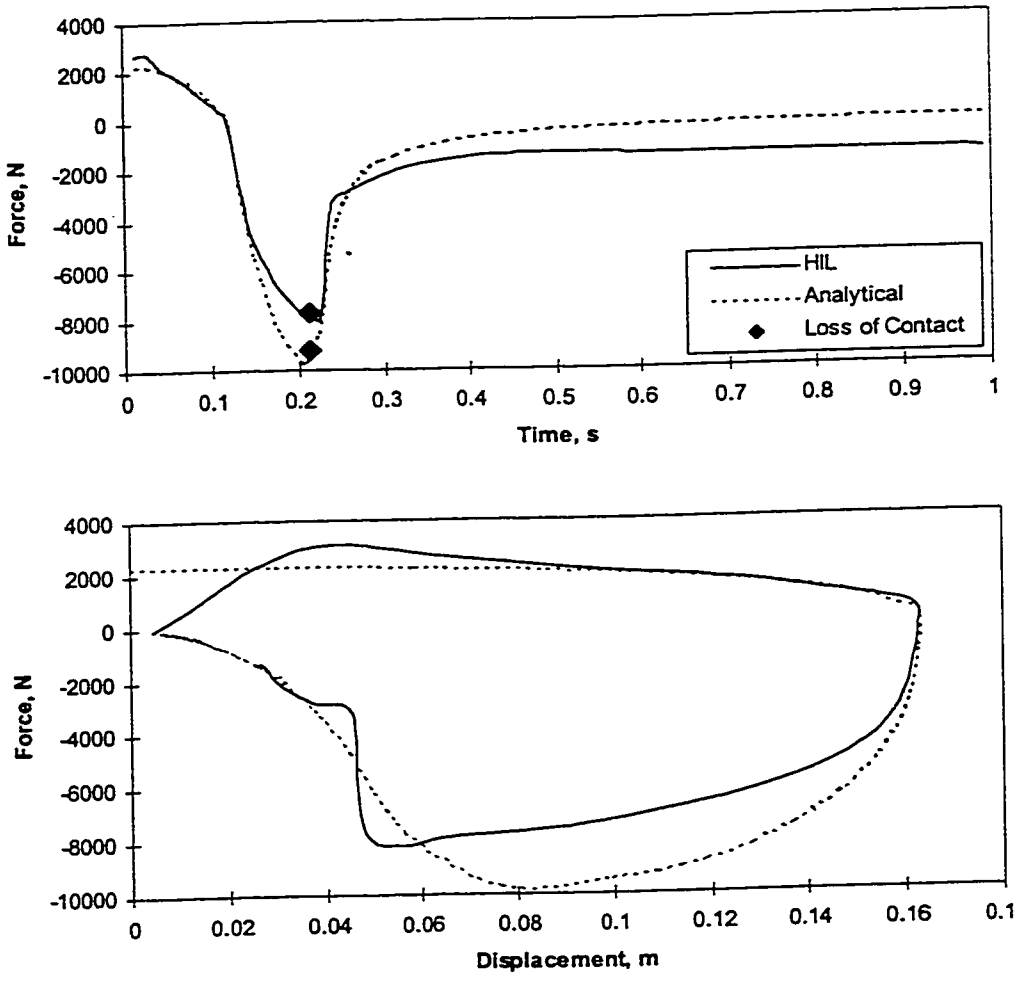

Figure 3.12: Comparison of force-time and force-displacement response of the under-ride guard derived from HIL test and Analytical Model (Direct impact, $v_0 = 2.0\ m/s$).

force-displacement characteristics. While the analytical model yields a damping force of approximately 1100 N and 2200 N at $t = 0$, corresponding to the initial velocities 1.0 *m/s* and 2.0 *m/s*, respectively, the HIL test reveals gradual increase in the damping force due to the time delays. The measured damping force near the peak rebound velocity, however, is lower than that obtained from the analytical model in both cases. This discrepancy in the rebound damping force is mostly attributed to the high hysteresis or compressibility effects of the damping fluid during the rebound stroke. The error between the peak damping forces derived from the analytical model and HIL test tends to be considerably larger under impact at higher velocity. The results derived from the HIL test further exhibit residual displacement response after the loss of contact, which is likely, caused by residual damping force, high damping ratio and sudden change in the effective mass.

The measured force-time and force-displacement characteristics of the damper are further analyzed to determine the energy dissipated during the impact, and compared with those obtained from the analytical model. The HIL tests and analytical simulations are performed for four different impact velocities, ranging from 0.5 *m/s* to 2.0 *m/s*, and the results are analyzed to determine the dissipated energy. The dissipated energy derived from both simulations, are expressed in percent of total kinetic energy of the car mass are compared in Table 3.1. The HIL test, in general, yields slightly lower values of dissipated energy due to hysteresis effects and relatively lower rebound force. The results show that the HIL test yields dissipated energy, which is generally 10% to 11.5% lower than that estimated from the analytical model. The results further show that the hydraulic damper can effectively dissipate a considerable portion of the kinetic energy of the car mass. The

damper tends to dissipate nearly 85% of the kinetic energy of the car mass at low speed impact of 0.5 *m/s*, which reduces to 57% at an impact speed of 2 *m/s*.

While the speed of impact between a car and truck may vary in the range of 0 – 120 *km/h*, the FMVSS recommendation requires limited damage to the automobile and its passenger at a maximum speed of 50 *km/h*. Hence, an impact simulation model has to be validated at least in the range of 0 – 50 *km/h*. The HIL simulation method, presented in this section, however, yields a limited validation for a relatively low impact speed range of 0 – 7 *km/h* owing to the limitations in the available hardware.

Table 3.1: Comparison of energy dissipated by the damper at different impacting velocities.

Impact Speed (*m/s*)	KE of the car mass (*Nm*)	Energy Dissipated (*Nm*)				% error
		HIL		Analytical		
		Total	% of KE	Total	% of KE	
0.5	125.0	106.69	85.3	120.06	96.73	10.0
1.0	500.0	357.54	71.5	393.66	78.73	10.0
1.5	1125.0	698.08	62.05	797.97	70.93	11.0
2.0	2000.0	1142.47	57.12	1328.36	66.42	11.5

3.3 RESPONSE CHARACTERISTICS OF CONVENSIONAL UNDER-RIDE GUARDS

The impact response characteristics of two different designs of conventional guards, presented in Section 2.2 are evaluated under a direct impact at different speeds, ranging from 10 *km/h* to 70 *km/h*, using DYNA3D. The simulation results are analyzed to

determine the response characteristics of the two guards in terms of maximum intrusion and car mass acceleration. The post-processor code TAURUS is used to extract the analysis results from DYNA3D binary output files.

The rigid impacting body, under-ride guard bumper beam and the drop arms, stiffeners are identified with different material numbers and the kinematic and energy information of each component is obtained using the third output option available in TAURUS, as described in Section 2.2.3. The intrusion of car mass can be defined as the peak displacement of the rigid impacting mass in a direction perpendicular to the plane of under-ride guard. The displacement of the impacting mass prior to the impact is subtracted to obtain the correct value of intrusion. The peak acceleration of the car mass can be obtained in the similar manner using the time history plot of the acceleration response of the rigid impacting body. The sum of internal energies of the bumper beam, drop arms and the stiffeners at each time interval as obtained from TAURUS is evaluated to determine the total amount of energy absorbed by the under-ride guard. It should be noted that, the car mass and other structural members of the truck are modeled as rigid brick elements and hence are not capable of absorbing any form of energy. The energy absorbed by the conventional guards is presented in terms of the difference in kinetic energy of the car mass before and after the impact, normalized with respect to the initial kinetic energy.

Figure 3.13 illustrates the deformations of the two conventional guards before, during and after the impact. The design-A with stiffeners located at the cross member, results in rebound of car mass after the impact, with minimal intrusion. The design-B with stiffeners located at the mid-section of the two-drop arms, however, resulted in

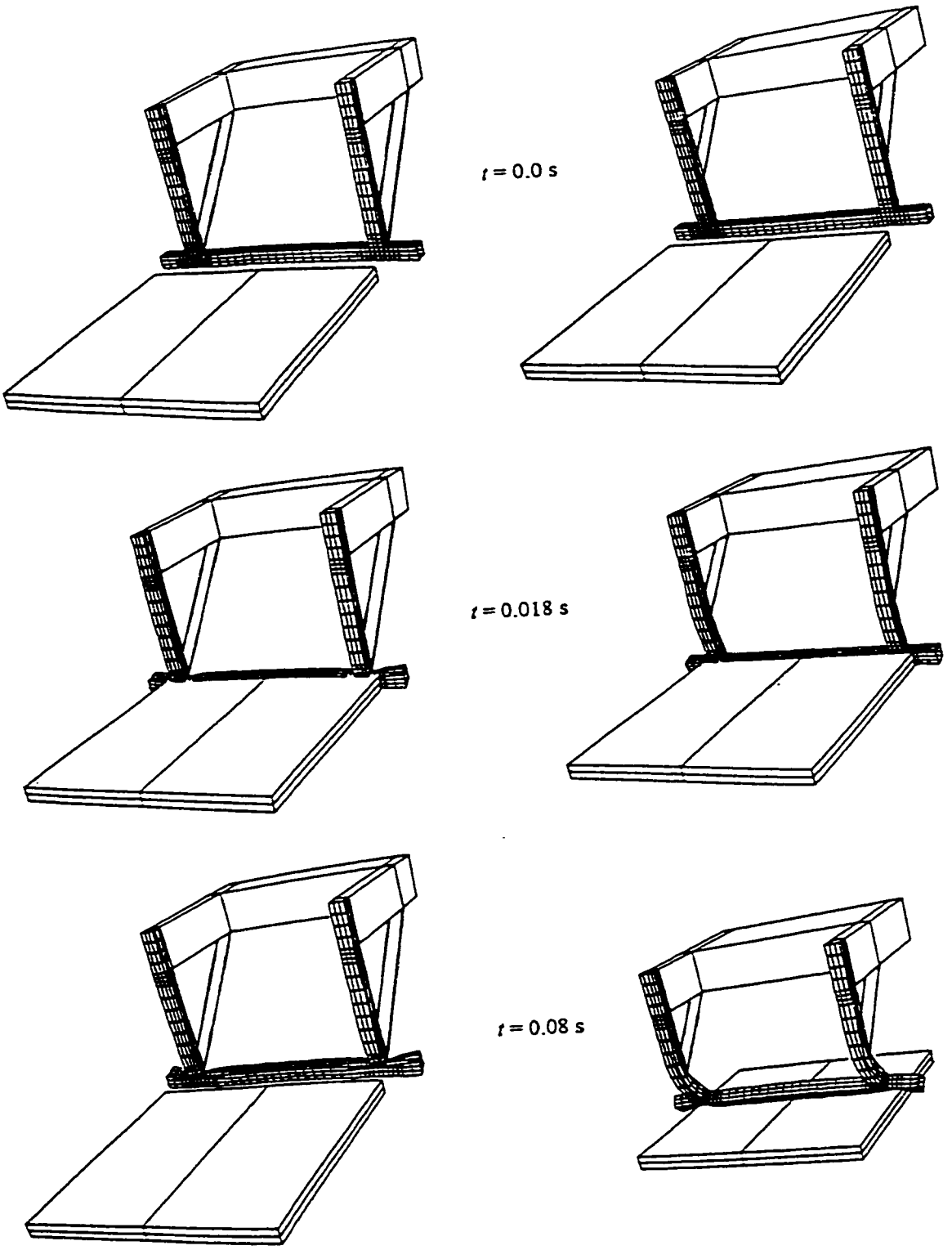

Figure 3.13: Deform shapes of the conventional under-ride guards (model-A and model-B) at different time instants during impact ($v_0 = 50$ *km/h*).

considerable deformation of the drop arms, as seen in the figure. The impacting car mass thus continues to intrude under the deformed guard. The design A, with it's large stiffness, yields smaller intrusion but higher acceleration, as shown in Figure 3.13. The design B yields considerably lower value of car mass acceleration due to high intrusion and lower stiffness. The peak acceleration values, however, increase with the initial impact speed. Such a design, however, may lead to more severe crash, since the impact may continue to occur at structural elements of car, other than the bumper. Figure 3.14 illustrates the peak intrusion, acceleration and energy absorption responses of the two designs. The results presented in Figure 3.13 and 3.14 clearly show that the peak car mass acceleration can be reduced only at the expense of high intrusion, relatively stiff guards can transmit excessive acceleration to the occupants, ranging from 90g to 250g in the speed range considered in the study.

The maximum intrusion, acceleration response of the car mass and normal energy absorbed under impact with the two designs of conventional guards are further summarized in Table 3.2. The results illustrated in Figure 3.14 and Table 3.2 show that the stiff guard (design-A) results in extremely high acceleration (220g) of the car mass with minimal intrusion (5 *cm*), under direct impact at 50 *km/h*. The peak acceleration response of the car mass impacting the soft guard (design-B), at the same speed however, approaches only 23g. The car mass, however, continues to intrude due to increased clearance between the deformed drop arms and the ground plane. The design-A results in absorption of most of the kinetic energy (91.1%) of the car mass due to limited intrusion, while the design-B tends to absorb only 48.2% of the initial kinetic energy due to unlimited under-ride of the car mass. The results further reveal that, the peak acceleration

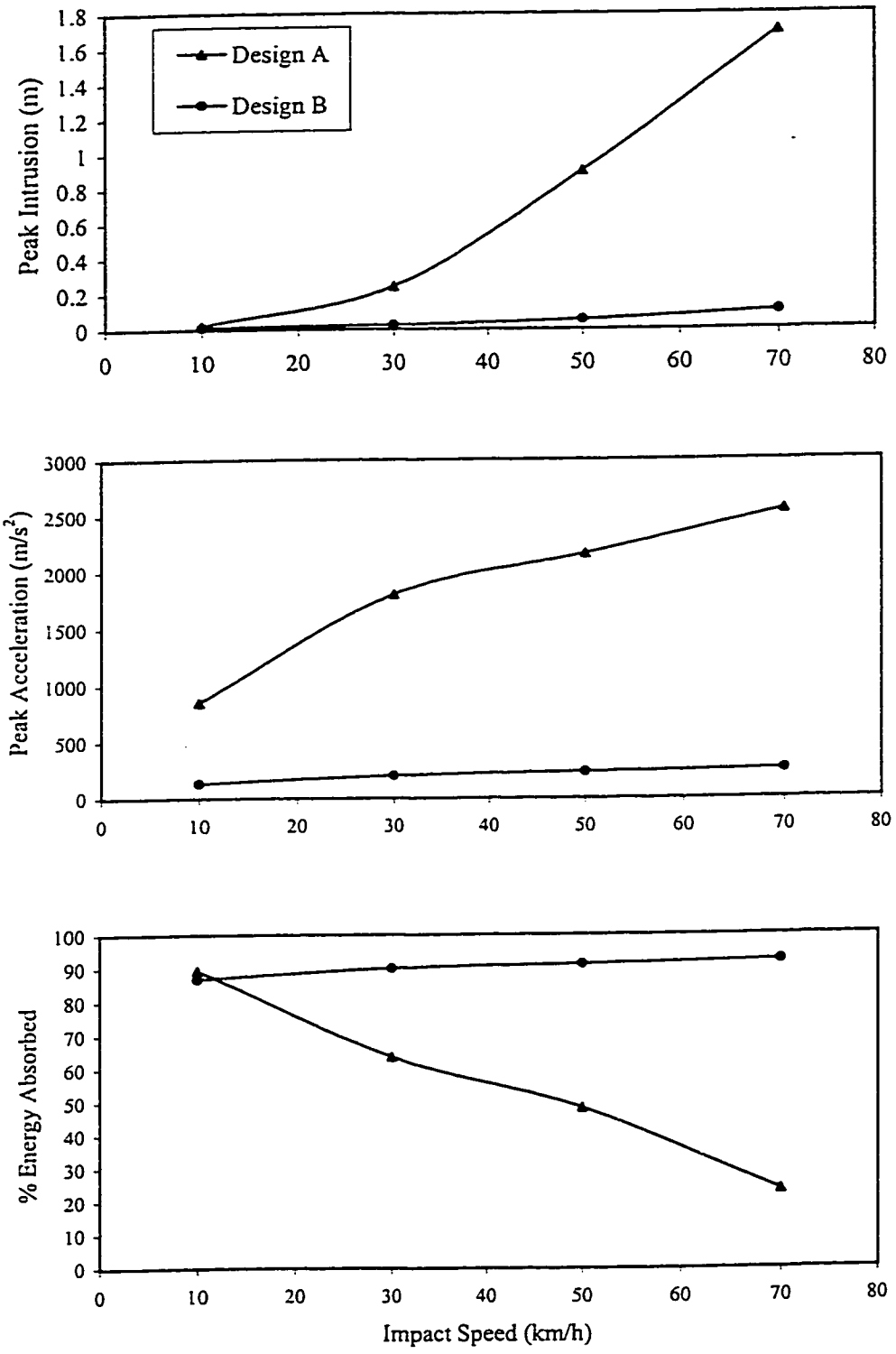

Figure 3.14: Comparison of peak intrusion, peak acceleration and energy absorption levels of the conventional guard designs at different impact speeds obtained by FE analysis.

Table 3.2: Comparison of peak acceleration, peak intrusion, and normalized energy absorbed by the conventional guard designs.

Impact Speed (km/h)	Design A			Design B		
	Peak Acceleration (m/s^2)	Peak Intrusion (m)	Normalized Energy Absorbed (%)	Peak Acceleration (m/s^2)	Peak Intrusion (m)	Normalized Energy Absorbed (%)
10	850	0.01	86.8	130	0.02	89.4
30	1800	0.022	90.0	200	0.24	63.6
50	2160	0.05	91.1	230	0.9	48.2
70	2550	0.1	92.2	250	1.7	23.4

and intrusion responses increase with the speed of impact in both designs. The percentage of energy absorption increases with the speed of impact in design A, which may be attributed to the higher strain rate of deformation. The percentage of energy absorption in Design B, however, decreases with the impact speed. The results show that both the designs result in either excessive acceleration or under-ride and pose serious risks to the occupants.

3.4 RESPONSE CHARACTERISTICS OF THE PROPOSED DAMPED GUARD

The governing equations of motion are solved to determine the magnitude of intrusion and acceleration response of the car mass, and the dissipated energy under direct (Equation 2.16) and angular impacts (Equations 2.33, 2.34) at different speeds. The simulation parameters used for the study are: $l = 0.6\ m$, $l_1 = 0.6\ m$, $l_2 = 0.6\ m$, $m_c = 1000$ kg, $m_b = 12\ kg$, $m_d = 20\ kg$, $L = 3.0\ m$. The bumper beam and drop arms are assumed to

be made of 6 *mm* thick rectangular sections. The simulations are performed for four different initial velocities: 10, 30, 50 and 70 *km/h*, and the response characteristics are expressed in terms of the performance measures. The impact analysis is terminated when a loss of contact occurs between two bodies or when the bumper beam approaches its static equilibrium. In the event of loss of contact, equation of motion for the uncoupled car mass, Equation (2.18), is further solved to determine the relative motion between the car mass and the guard. The simulations are terminated only if the relative motion response tends to diverse, such that the possibility of a re-impact does not exist. A maximum allowed deflection of the guard is considered to be another criteria for terminating the simulation. In the present analysis, if the guard deflects beyond 45°, the simulations are stopped.

3.4.1 Dynamic Response of the Proposed Damped Guard under Direct Impact

The dynamic response characteristics of the proposed guard are evaluated in terms of magnitudes of intrusion, velocity and acceleration of the car mass, and the normalized dissipated energy. The dynamic response of the guard is strongly dependent on many design variables, such as compression damping ratio (ξ_c), damping asymmetry factor (p), stiffness coefficients (k_{11} and k_{12}), bump stop stiffness (k_{st}), and permissible travel limit (l_3). A comprehensive parametric study is thus performed to establish the influence of various design variables on the performance characteristics.

INFLUENCE OF COMPRESSION AND REBOUND DAMPING

Figure 3.15 illustrates the influence of variations in the compression and rebound damping on different performance variables under impact at a speed of 50 km/h. The response characteristics of the coupled car mass-guard system are presented for the duration of the contact. The results clearly show that the lightly damped guard results in loss of contact in relatively shorter duration. An increase in compression damping yields considerable reduction in maximum intrusion through increase in dissipated energy. It should be noted that the results are desired assuming linear viscous damping ($p = 1$). An increase in the compression damping coefficient beyond 0.6, however, does not result in significant reduction in the peak intrusion. The peak car mass acceleration encountered at the time of impact, however, increases considerably. A lightly damped guard yields considerably lower car body acceleration, with significantly large intrusion of the car mass and rebound velocity of the flexible guard, as shown in the figure. An increase in the guard damping yields increased values of peak acceleration of the car mass. The energy dissipated by the damped guard is a function of both the damping coefficient and the intrusion. The maximum dissipated energy tends to increase with increase in damping coefficient. The relative increase, however, tends to decrease when ξ_c is increased beyond 0.6. This is mostly attributed to reduced relative motion across the damper.

Figure 3.16 illustrates the influence of rebound damping on the performance measures of the damped guard. The variations in rebound damping are expressed in terms of the asymmetry factor, p, ranging from 0.2 to 3.0, while the compression mode damping coefficient (ξ_c) is taken as 0.4. An increase in the rebound to compression damping ratio ($p > 1$) yields considerably lower rebound velocity, while the maximum

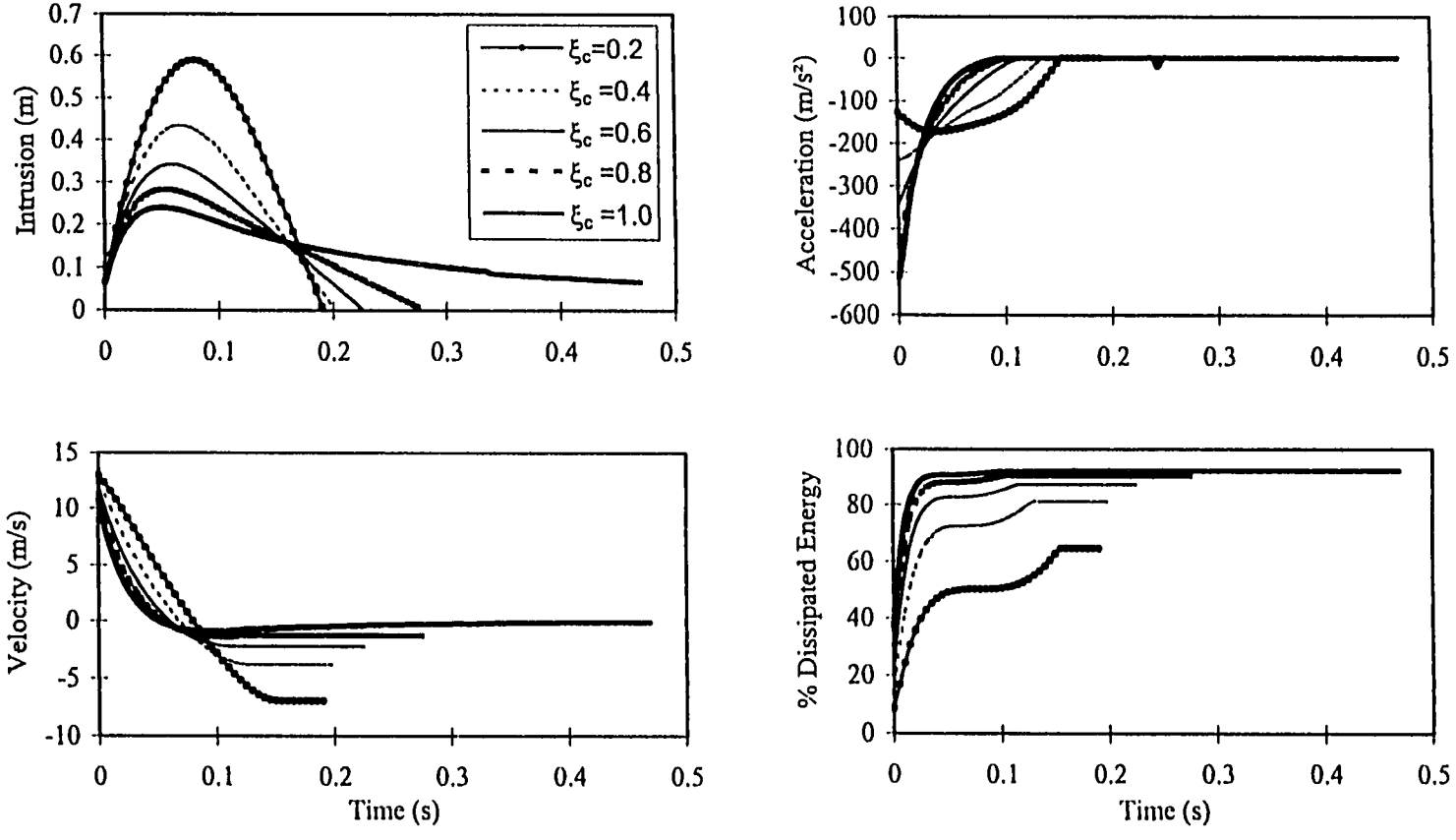

Figure 3.15: Influence of compression damping ratio on the performance of proposed under-ride guard.

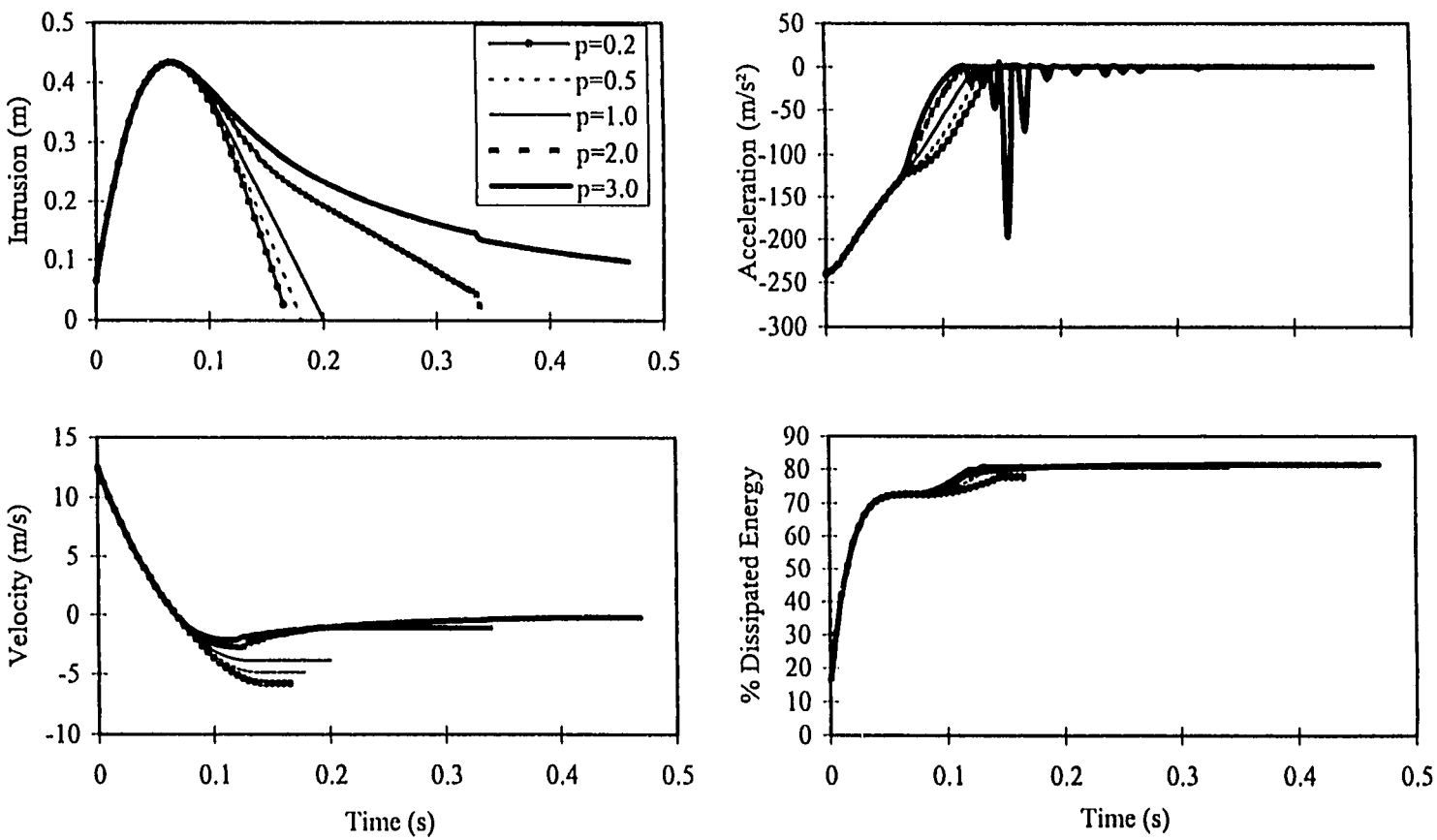

Figure 3.16: Influence of rebound damping ratio on the performance of proposed under-ride guard.

intrusion is not affected by the asymmetry factor, p. The variations in the rebound damping thus affect the maximum dissipated energy in an insignificant manner. The high rebound damping (p = 3), however, causes repeated impacts of the car mass with the bumper beam during the rebound stroke due to low car mass velocity. These repeated impacts result in extremely high acceleration of the car mass, as shown in the Figure 3.16. Although it is desirable to reduce the rebound velocity of the bumper beam, the beam mass may tend to accelerate during the downward stroke when the contact is lost. The repetitive impacts of the bumper beam and the car mass may thus be encountered. While lower values of the asymmetry constant yield high rebound velocity and rapid loss of contact, a high value of p yields high repeated acceleration peaks.

INFLUENCE OF SPRING STIFFNESS

The influence of the restoring properties of the proposed guard on the performance variables is presented in Figures 3.17 and 3.18. The influence of the linear (k_{11}) and cubic (k_{12}) stiffness constants is illustrated for v_0 = 50 km/h. The damping parameters are selected as $\xi_c = 0.4$ and $p = 1$. An increase in the linear spring rate k_{11} yields considerable reduction in the magnitude of intrusion with increase in the peak acceleration. While the soft spring ($k_{11} = 0.1 \times 10^6$) results in peak acceleration below 8g, the intrusion of car mass under the rigid trailer frame exceeds 0.7 m, well beyond the permissible limit of 45° considered for the angular deflection of the drop arm. Furthermore, a very soft guard will lead to rapid loss of contact during the compression stroke.

The total dissipated energy tends to increase with increase in the spring rate (k_{11}), which is attributed to increase in the contact duration and the velocity of the guard.. Although the cubic stiffness coefficient affects the peak acceleration and the total

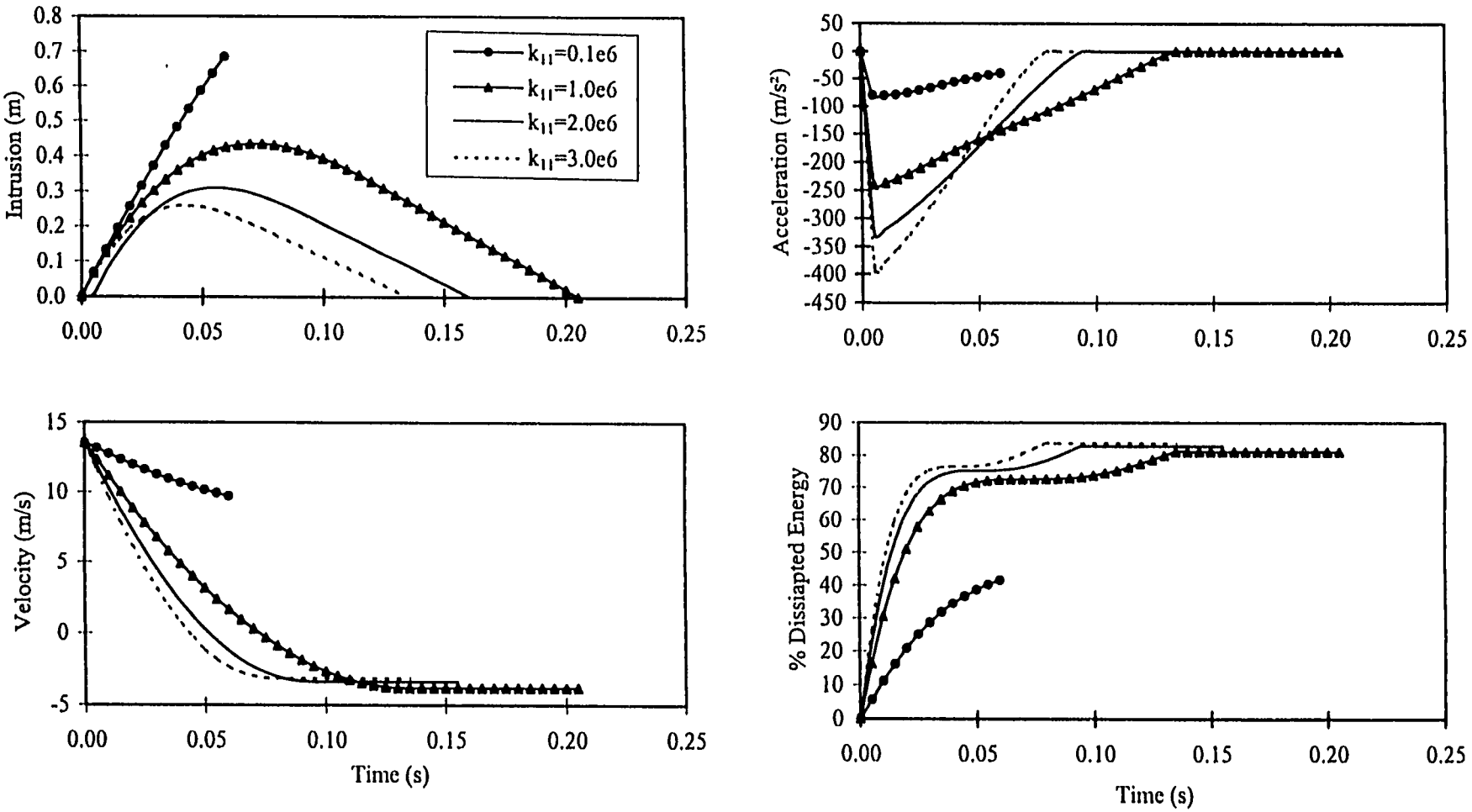

Figure 3.17: Influence of primary spring stiffness on the performance of proposed guard.

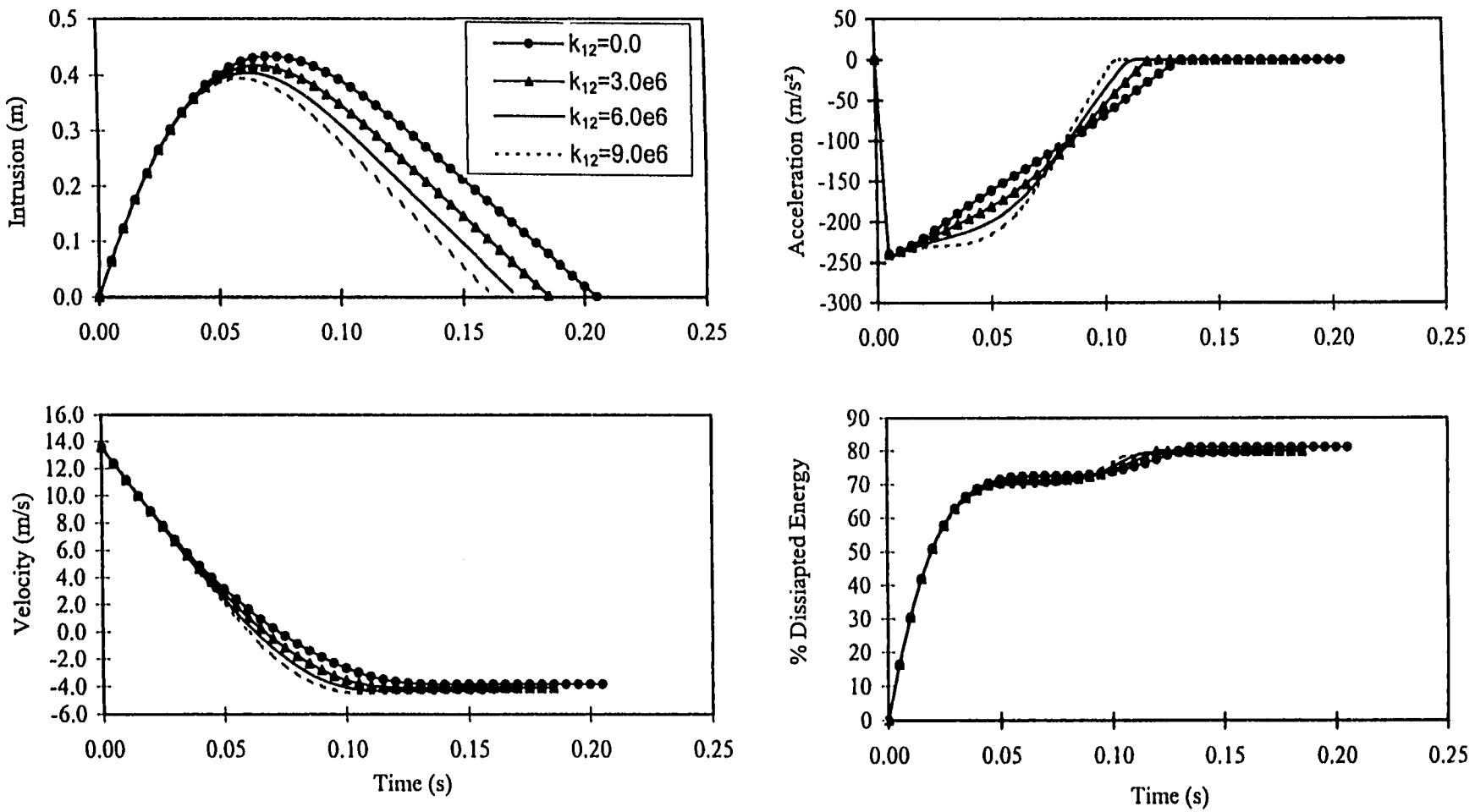

Figure 3.18: Influence of cubical spring stiffness on the performance of proposed guard.

dissipated energy in an insignificant manner, the maximum intrusion can be limited by selecting high values for k_{12}, as illustrated in Figure 3.18. The intrusion of the car mass and the peak acceleration response immediately after the impact remains unaffected by variations in k_{12}. An increase in k_{12}, however, reduces the maximum intrusion with increase in the corresponding acceleration response, as shown in Figure 3.18. The variations in the linear as well as cubic stiffness coefficient ($k_{11} \geq 1\text{x}10^6$), however, yield minimal influence on the final velocity response of the car mass and the bumper beam. The influence of variations in the bump stop stiffness on the performance variables shown in Figure 3.19, is quite similar to that presented in Figure 3.18 for variation in k_{12}. A reduction in permissible travel (l_3), however, reduces the maximum intrusion with increase in corresponding acceleration and rebound velocity, as shown in Figure 3.20.

INFLUENCE OF IMPACT SPEED

Figure 3.21 illustrates the influence of initial speed of impact v_0, on the performance characteristics of the proposed guard, while the guard parameters are chosen as, $\xi_c = 0.4$, $p = 1$, $k_{11} = 1\text{x}10^6$ and $k_{11} = 0$. The results clearly sow that all the performance variables are strongly influenced by the impact speed. An impact at low speed of 10 *km/h* yields minimum intrusion (less than 0.1 *m*), low car mass acceleration (less than 5*g*), low rebound velocity, and maximum normalized dissipated energy. The maximum intrusion and acceleration of the car mass approach very high values of 0.65 *m* and 35*g*, respectively, when the impact speed increases to 70 *km/h*. Although the energy dissipated by the damper increases with increase in the impact speed, the normalized dissipated energy decreases due to increase in the kinetic energy of the impacting car mass.

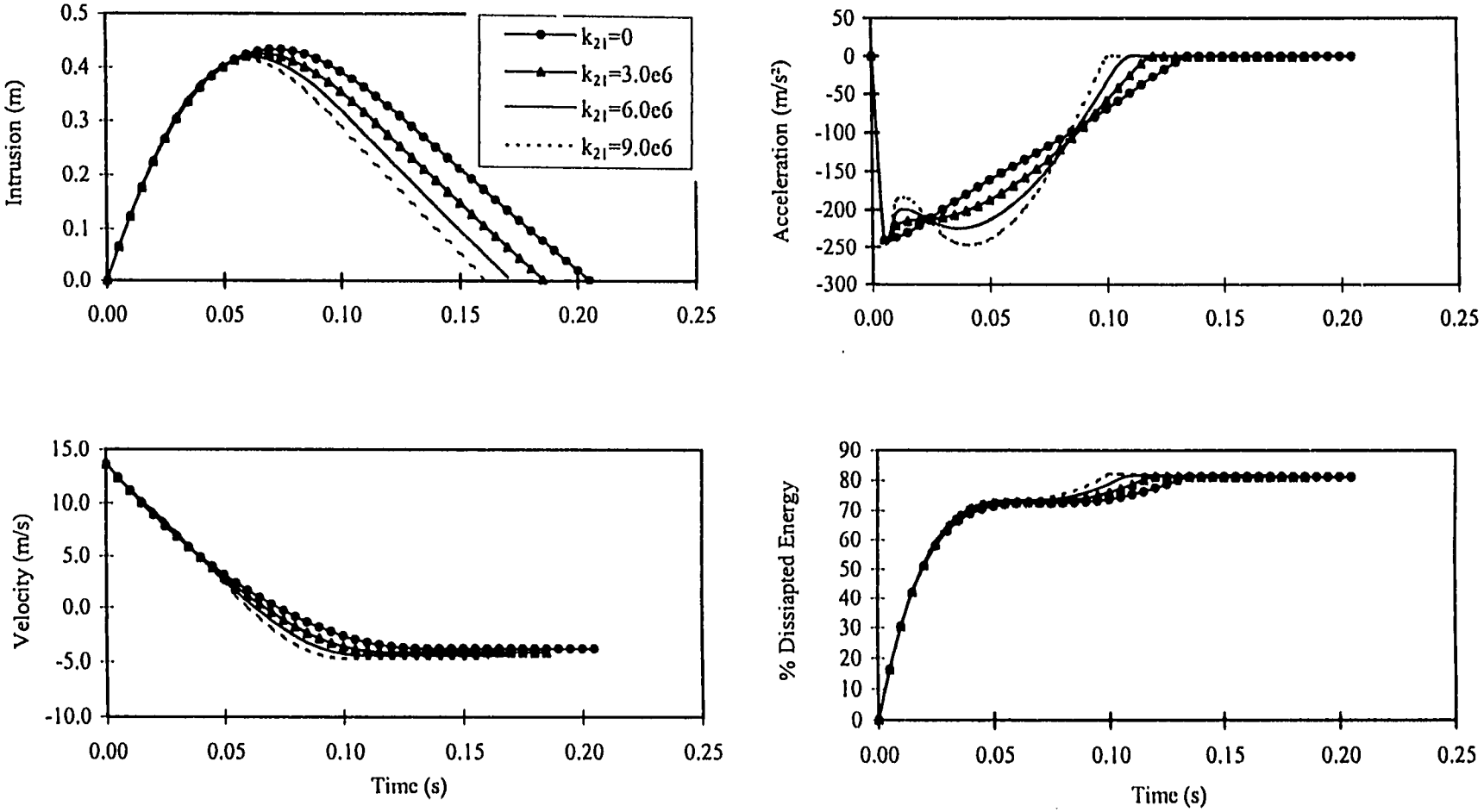

Figure 3.19: Influence of stop spring stiffness on the performance of proposed guard.

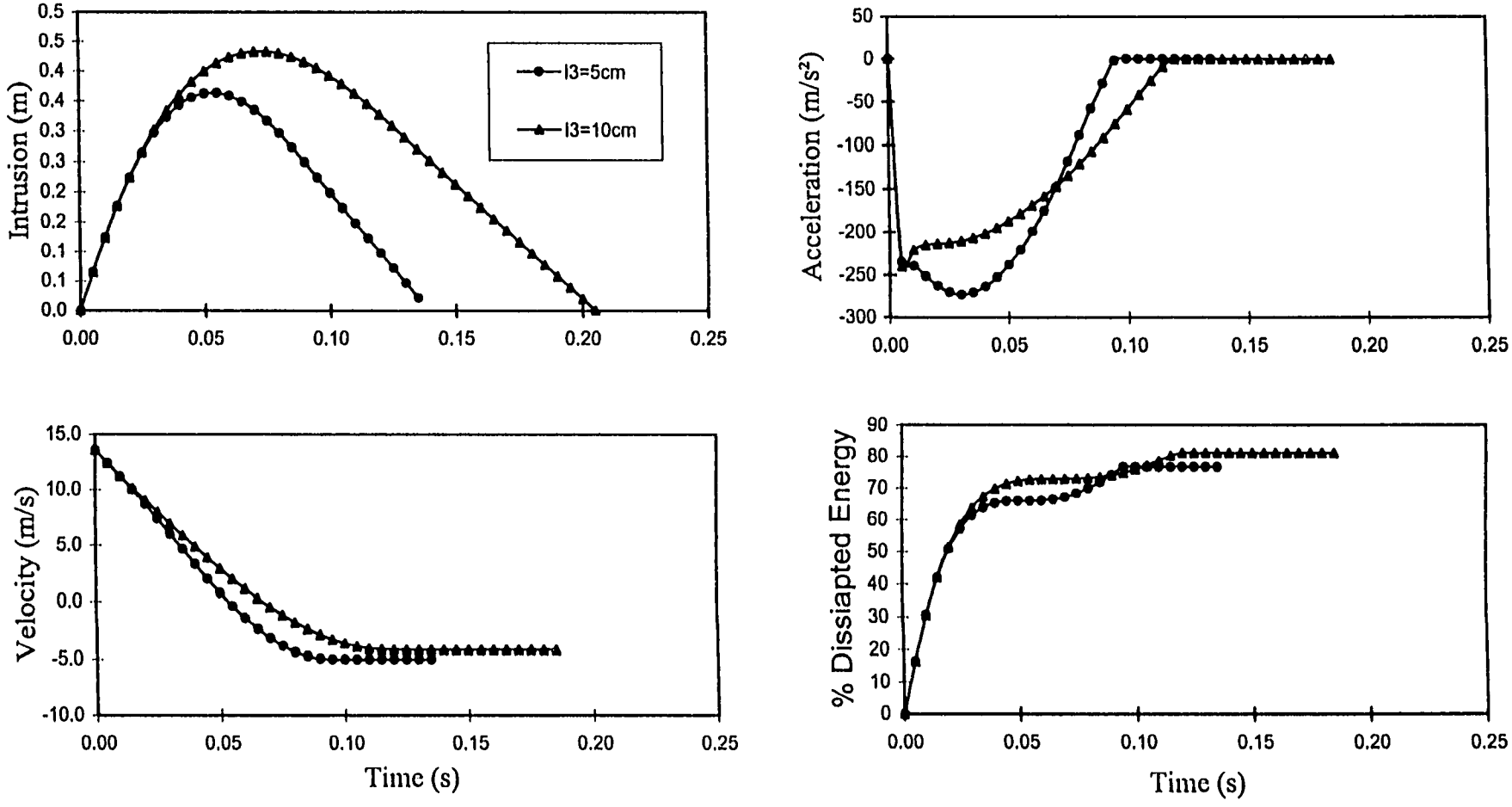

Figure 3.20: Influence of stop spring gap on the performance of the proposed guard.

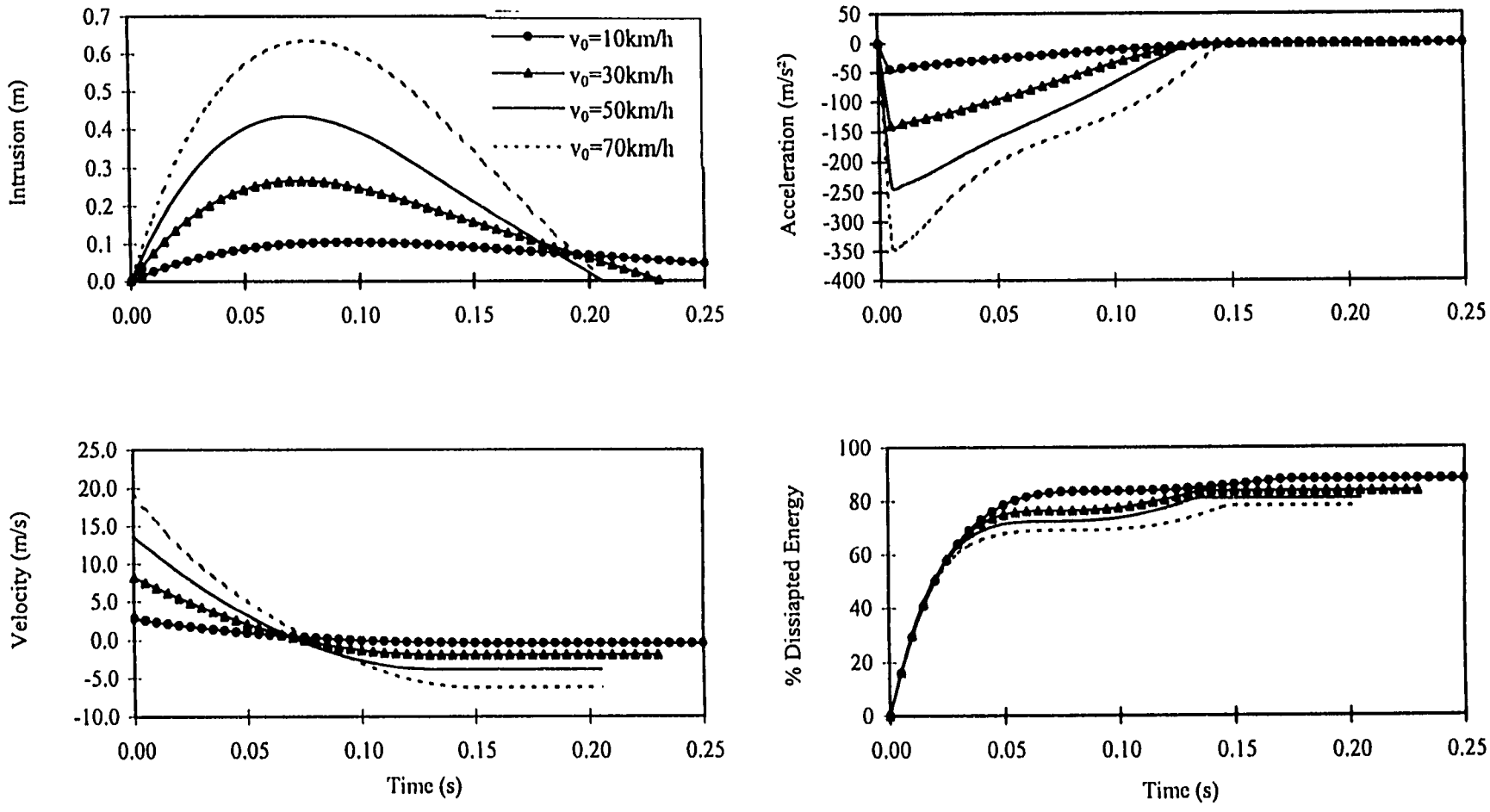

Figure 3.21: Influence of impact speed on the performance of the proposed guard.

3.4.2 Dynamic Response of the Damped Guard under Oblique Impact

The results discussed in the previous section revealed that the performance characteristics of the proposed guard subject to a direct impact are strongly related to its stiffness and damping properties, initial impact velocity, and the permissible intrusion. The performance characteristics of the guard subject to an oblique impact are further related to the angle of impact, yaw velocity of the impacting car mass and the friction properties of the contacting surfaces. The analytical model, described in Section 2.5, is thus analyzed under the oblique impacts to study the influence of variations in the above parameters on the performance of the damped guard.

INFLUENCE OF IMPACT ANGLE

The equations of motion for the car-under-ride guard system are solved for different initial angles and velocities of impact. The response characteristics of the guard are evaluated in terms of the performance measures described in Chapter 2. The computation is terminated, when the two bodies separate, and repeated impacts between them are not expected to occur. The relative coordinates and velocities of the guard and the car mass contact locations are examined at each step to determine the possible occurrence of a re-impact. The influence of impact angle on the performance of the guard is investigated by selecting the stiffness and damping coefficients as, $k_{11} = 1\text{x}10^6$ *N/m*, $k_{12} = k_{st} = 0$, $\xi_c = 0.4$, $n_c = n_e = 1$, $\mu = 0.1$, and $v_0 = 50$ *km/h*.

Figure 3.22 illustrates the displacement response of the contact point of the car mass with the under-ride guard along the X and Y directions, and the acceleration of the car mass as a function of initial angle of impact. The results clearly show that a direct

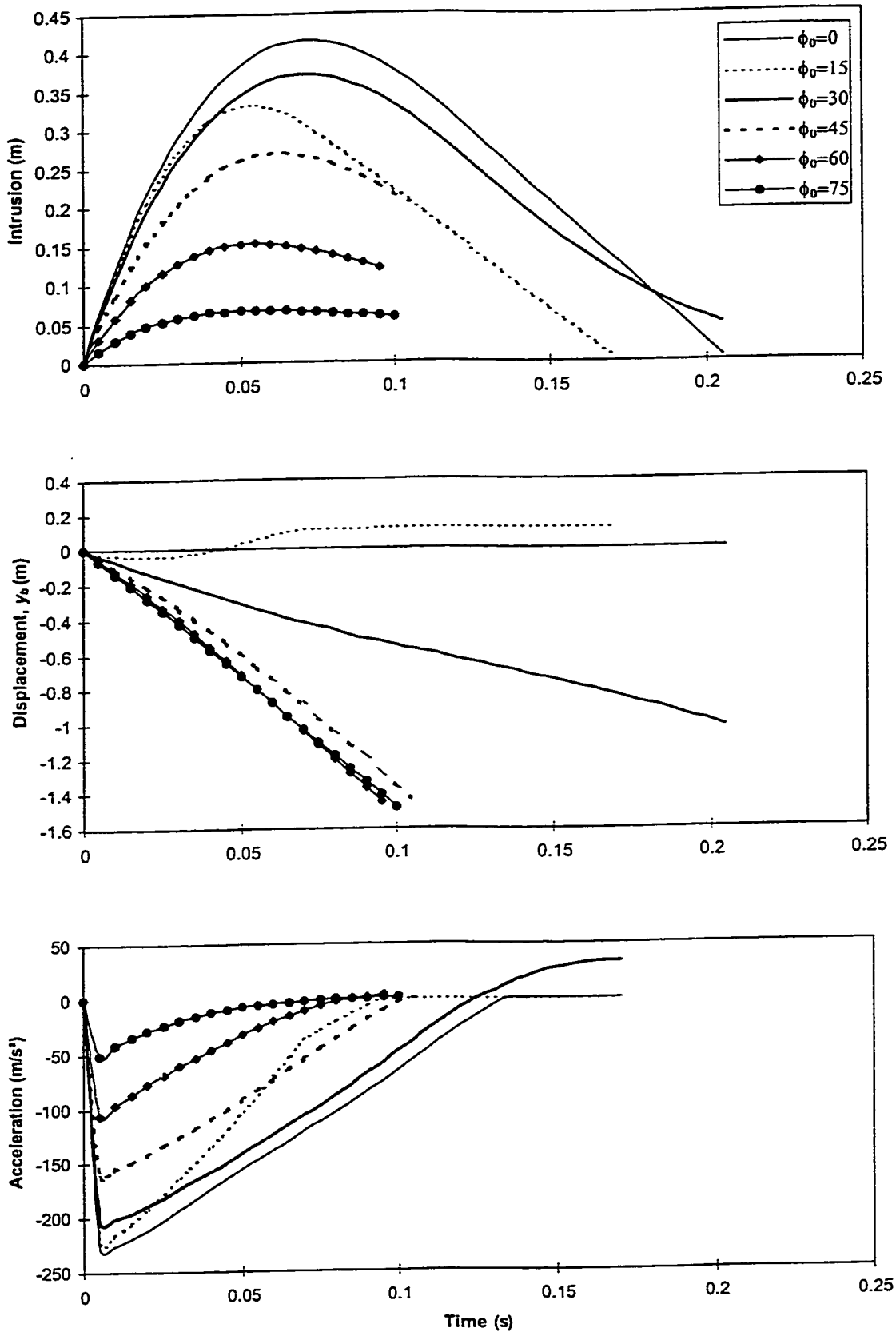

Figure 3.22: Influence of variations in the impact angle on the displacement and acceleration response of the car mass ($v_0 = 50$ *km/h*, $\dot{\phi}_0 = 0$ *rad/s*).

impact ($\phi_0 = 0$) yields maximum intrusion and acceleration of the car mass. A higher value of impact angle results in lesser amount of intrusion due to reduction in the amount of momentum transfer to the under-ride guard along the x-axis. The results shown in Figure 3.22, however, show that the decrease in the amount of intrusion due to increased impact angle is not linear. While $\phi_0 = 15°$ impact resulted in a maximum intrusion of 0.33 m at $t = 0.052$ s, $\phi_0 = 30°$ produced a maximum intrusion of 0.37 m at t = 0.54 s. The discrepancy in the amount of peak intrusion of the car mass at lower impact angles may be attributed to the non-linear nature of the governing equations of motion. An examination of the angular motion response of the car mass during the impact event revealed that car mass impacting at 15° tends to straighten itself during the impact, as shown in Figure 3.23. The angular motion of the car mass is observed to approach zero rapidly, at $t = 0.064$ s. The oblique impact analysis then reduces to a direct impact problem, thereby eliminating the contribution due to nonlinear terms associated with the angular motion. An impact angle of 30°, however, results in only slight variations in the angular position of the car mass. Higher values of impact angles result in reduced intrusion due to increase in the momentum along the Y direction. The displacement response of the car mass along the Y-direction, y_c, shown in Figure 3.22, reveals that the car mass tends to slip away from the under-ride guard in the Y-direction, thereby, avoiding the possible repeated impacts.

The acceleration response of the car mass during the impact event, illustrated in Figure 3.22, shows that the maximum acceleration is experienced when the initial impact is direct. The figure shows that the peak acceleration of the car mass is approximately 235 m/s^2. The peak acceleration level of the car mass, however, decreases considerably

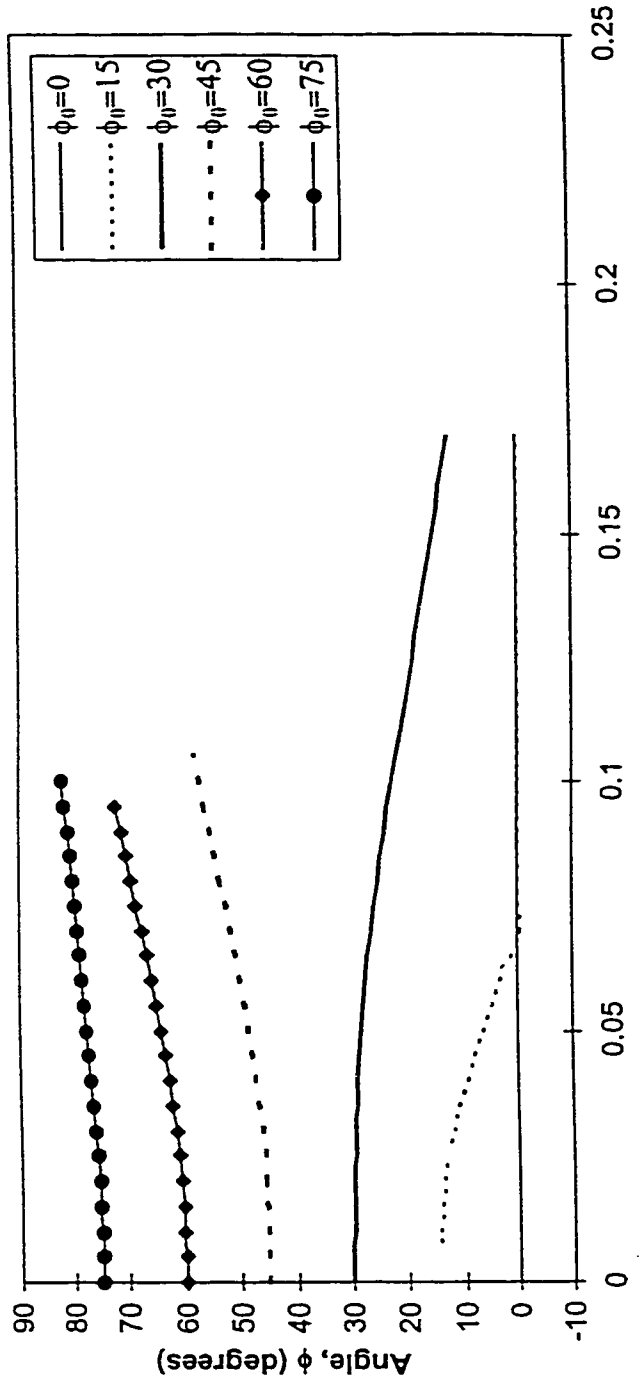

Figure 3.23: Influence of variations in the impact angle on the angular motion of the car mass ($v_0 = 50$ *km/h*, $\dot{\phi}_0 = 0$ *rad/s*).

with increase in the impact angle. The peak acceleration level reduces to as low as 56.4 m/s^2, when the initial impact angle is 75°. It should be noted that the acceleration level of the impacting car mass is related to the contact force along the X-axis. Since the contact force in the Y-direction is only a fraction of that encountered along the X-direction, the maximum acceleration is experienced in the X-direction. The discrepancy in the acceleration response under oblique impacts at low angles is observed in Figure 3.20. The acceleration and displacement encountered under a 15° impact are observed to be considerably lower than those obtained for 0° and 30° impacts.

Figure 3.24 illustrates the influence of impact angle on the energy dissipated by the guard. Since the energy dissipated by the under-ride guard damper is strongly related to the velocity of the under-ride guard, a direct impact yields maximum energy dissipation. An increase in the impact angle in general yields lower energy dissipated by the damper, while the impacts at 15° and 30° reveal some conflicting trends discussed earlier. The influence of impact angles on the performance variables is further summarized in Figure 3.25. All the performance variables exhibit highest values under direct impact. The peak intrusion and the energy dissipated by the under-ride guard damper decrease gradually for impact angles up to 17°, while the peak car mass acceleration reduces only slightly. The peak intrusion and the energy dissipation by the damper then tend to increase for impact angles ranging from 17° to 30°, with relatively small reduction in the peak acceleration. Larger impact angles result in gradual reduction in all the performance variable, as shown in the Figure.

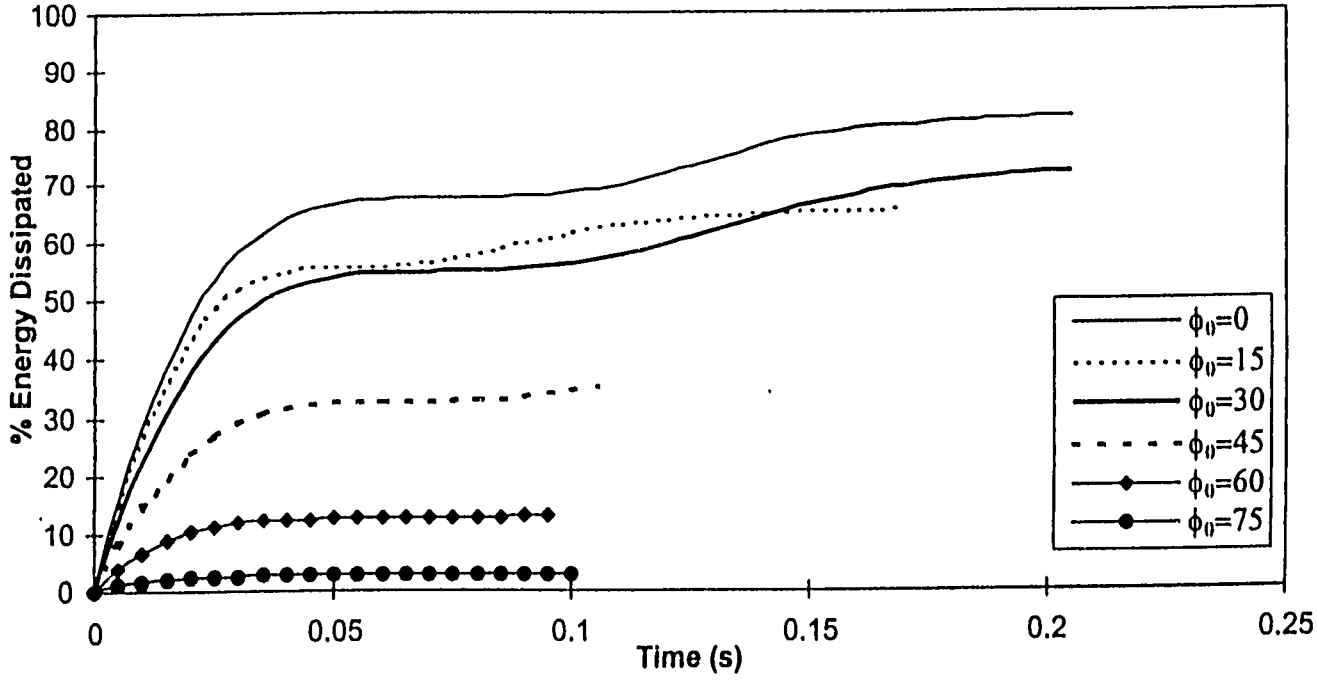

Figure 3.24: Influence of variations in the impact angle on the amount of energy dissipated by the under-ride guard damper ($v_0 = 50$ *km/h*, $\dot{\phi}_0 = 0$ *rad/s*).

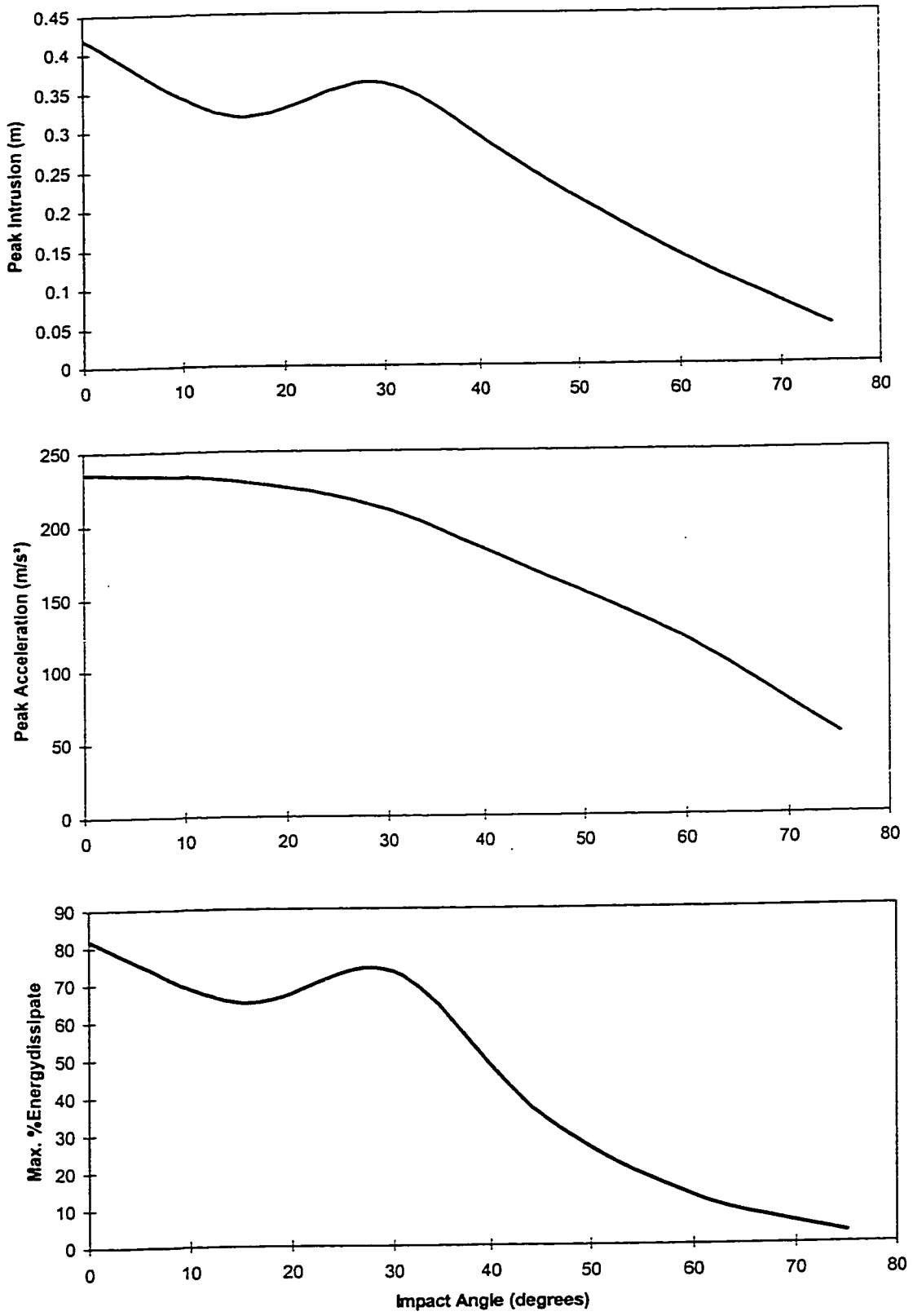

Figure 3.25: Influence of variations in the impact angle on the performance of the under-ride guard ($v_0 = 50$ *km/h*, $\dot{\phi}_0 = 0$ *rad/s*).

INFLUENCE OF IMPACT YAW VELOCITY

The performance characteristics of the under-ride guard are further evaluated for impacts occurring at varying values of initial yaw velocities for v_0 = 50 *km/h*. The governing equations of motion for the combined car mass and the under-ride guard are solved at four different initial yaw velocities: 0 rad/s, 0.07 rad/s, 0.14 rad/s and 0.28 rad/s. The displacement and acceleration response of the car mass and the energy dissipated by the under-ride guard damper for impacts occurring at different initial yaw velocities are illustrated in Figure 3.26.

The results show that the influence of initial yaw velocity of the impacting mass on its peak intrusion and energy dissipated by the guard is almost insignificant, except when $\phi_0 = 0$. The car mass tends to slip away from the under-ride guard, in the Y-direction, before approaching the zero-displacement along the X-direction. A higher initial angular velocity of the impacting car, however, results in higher amount of residual intrusion before the loss of contact, as illustrated in Figure 3.26. The influence of variation in the initial angular velocity of the car mass on its peak acceleration response is also observed to be negligible. The peak acceleration value was obtained as 164 m/s^2 for the range of yaw velocities considered in the study, with $\phi_0 = 45°$. It can be observed that the acceleration response of the car mass subject to zero initial yaw velocity approaches zero relatively faster, when compared to that of the car mass subject to non-zero initial yaw velocity. The impacts occurring at a higher yaw velocity yields more gradual reduction of the acceleration response of the car mass, which approaches positive values prior to the loss of contact along the Y-axis.

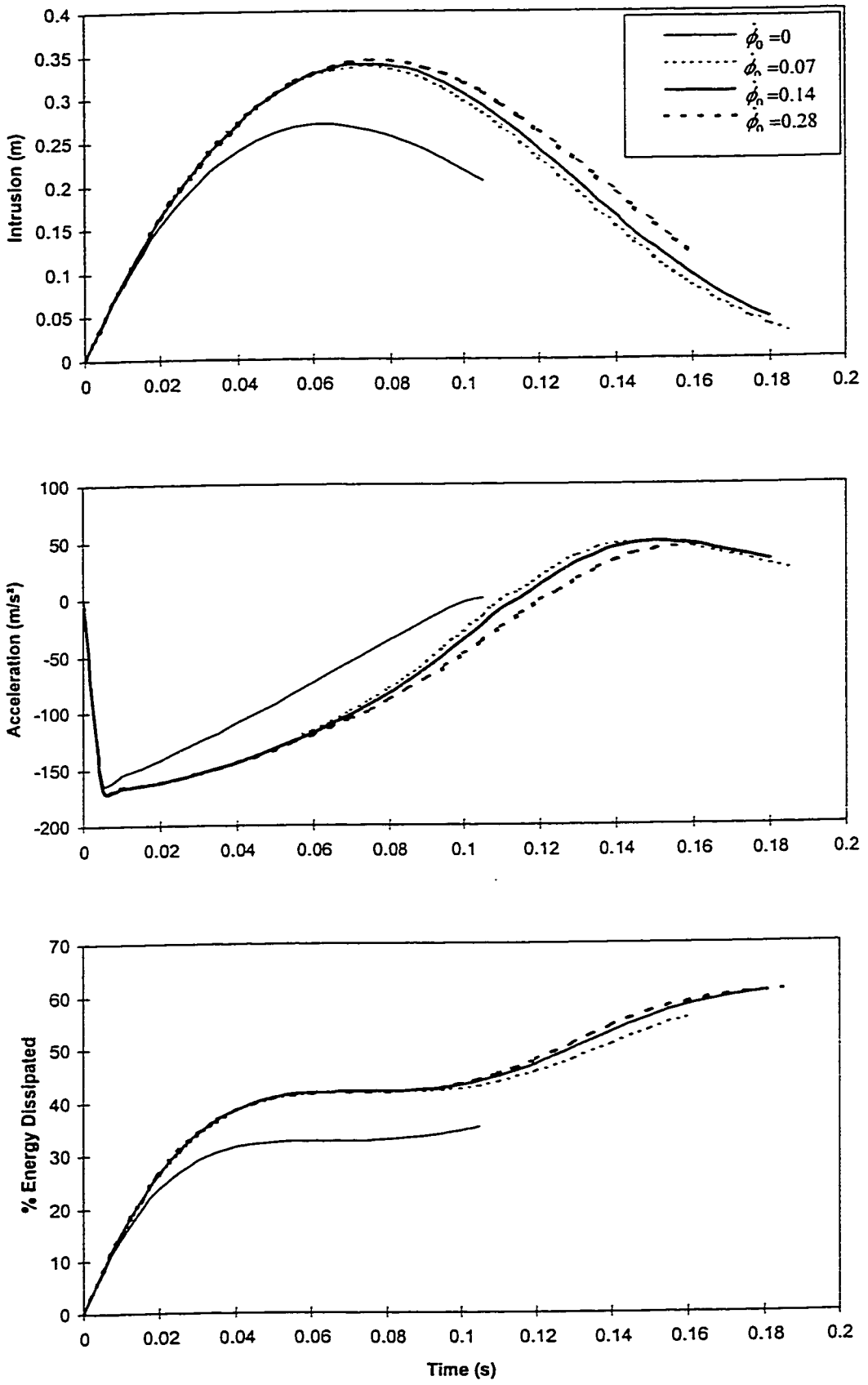

Figure 3.26: Influence of variations in the initial yaw velocity of the impacting car on the performance of the under-ride guard ($v_0 = 50$ *km/h*, $\phi_0 = 45°$).

INFLUENCE OF COEFFICIENT OF FRICTION

Figure 3.27 illustrates the influence of coefficient of friction between the contacting surfaces, ranging from 0.1 to 0.8, on the performance measures while the simulation parameters are selected as $k_{11} = 1x10^6$ *N/m*, $k_{12} = k_{st} = 0$, $\xi_c = 0.4$, $n_c = n_e = 1$, $v_0 = 50$ *km/h*. The range of friction coefficients in the study are selected based upon the reported data for commonly used materials, such as steel and rubber [118].

The peak intrusion of the car mass under low angles of impact is not effected by the coefficient of friction. The peak intrusion occurring at higher impact angles, $0 < \phi_0 \leq 30°$, however, tends to be lower when coefficient of friction is increased. The peak intrusion of the car mass is approximately 0.42 *m* under direct impacts, which reduces to approximately 0.21 *m* under 15° impact and $\mu = 0.8$. An increase in the impact angle above 40°, yields a considerable increase in the magnitude of intrusion, with tighter coefficient of friction. The variations in the coefficient of friction do not effect the resulting peak acceleration of the car mass along the X-axis, as shown in Figure 3.27. The results clearly illustrate the potential performance benefits of employing car bumpers and bumper beams with higher friction properties. The total amount of energy dissipated by the damper, being a function of the guard velocity during the impact event, varies with initial impact angles in a manner similar to that observed for the peak intrusion.

3.5 PERFORMANCE CHARACTERISTICS OF THE OPTIMAL GUARD

The optimization problem, described in Equation (2.41), is solved to determine optimal parameters of the proposed guard. A Fortran subroutine known as NCONF available in the IMSL math library functions [106] is used to solve the constrained optimization

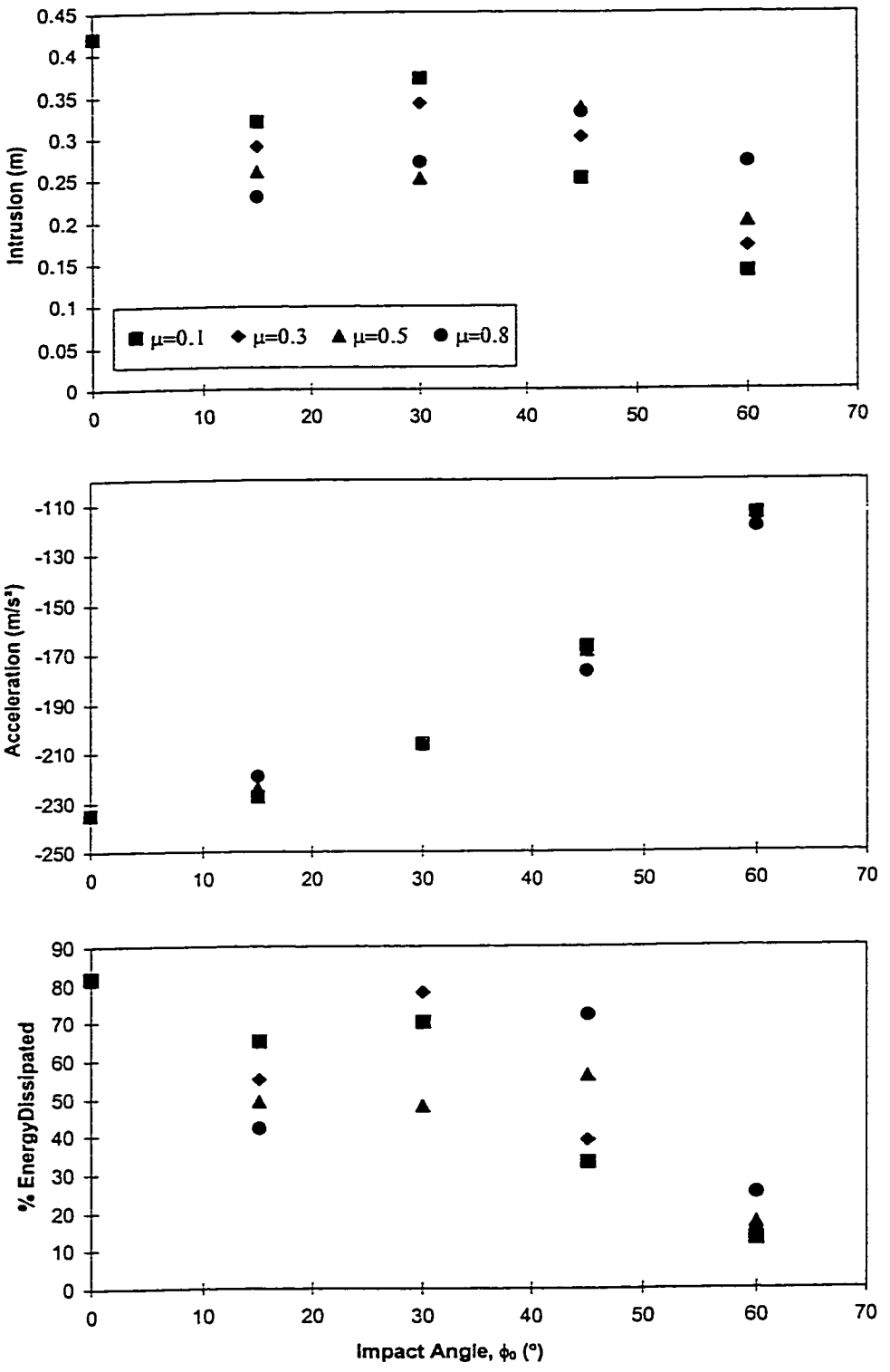

Figure 3.27: Influence of variations in the friction coefficient on the performance of under-ride guard ($v_0 = 50$ *km/h*, $\dot{\phi}_0 = 0$ *rad/s*).

problem. The subroutine uses a successive quadratic programming method with finite-difference gradients. From the results derived in the parametric study, it is apparent that the maximum intrusion can be limited only at the expense of higher car acceleration. The peak intrusion and car acceleration are therefore constrained in the optimization study. The optimization problem is solved for three different values of constraints imposed on the peak normalized intrusion and acceleration (q_1, q_2,): (0.1, 1.0), (0.15, 0.75), (0.2, 0.5). The weighting factors (α_1, α_2, α_3) are selected as (10.0, 1.0, 1.0) for q_1=0.1 and q_2=1.0 and the optimization is performed for an impact speed of 50 *km/h*. Different weighting factors are selected for different values of q_1 and q_2. The limiting constants for the design parameters were identified from the results of the parametric study, and the optimization was performed for different sets of starting values. Majority of the solutions resulted in convergence to similar values of the objective function and the design parameters. The design parameters derived for different constraints and the resulting performance variables are summarized in Table 3.3.

Examination of the results summarized in Table 3.3 shows that the acceleration level on the car mass can be limited to 32g, if the car mass is permitted with a maximum intrusion of 0.3 *m*. The peak car mass acceleration level, however, can be limited to 16g by relaxing the permissible intrusion to 0.6 *m*. The results show a nearly linear relationship between the maximum of intrusion and the maximum acceleration response of the car mass, which is further evident from Figure 3.28. The results further reveal a good compromise between the peak acceleration and intrusion can be achieved by selecting compression stroke damping ratio in the 0.35 to 0.5 range, depending on the constraint imposed on the peak intrusion and acceleration.

Table 3.3: Summary of Optimal Design and Performance Variables of the Proposed and Conventional Guard ($v_0 = 50$ *km/h*).

Design Parameter	Constraint (q_1, q_2)		
	(0.1, 1.0)	(0.15, 0.75)	(0.2, 0.5)
ξ_c	Parameter Value		
	0.500	0.353	0.370
N_e, n_c	0.679, 1.0	0.911, 1.0	0.884, 1.0
v_c (*m/s*)	2.000	2.293	2.000
P	1.111	1.500	1.043
k_{11} (*MN/m*)	2.424	1.407	0.572
k_{12} (*MN/m*^{3})	3.083	1.650	0.926
k_{st} (*MN/m*)	4.032	1.423	0.934
Performance Variable			
Maximum intrusion, x_b (*m*)	0.300	0.398	0.600
Peak acceleration, $\ddot{x}_c$ (*m/s*^{2})	-312.8	-235.4	-156.2
Normalized dissipated energy (%)	81.6	76.4	71.3

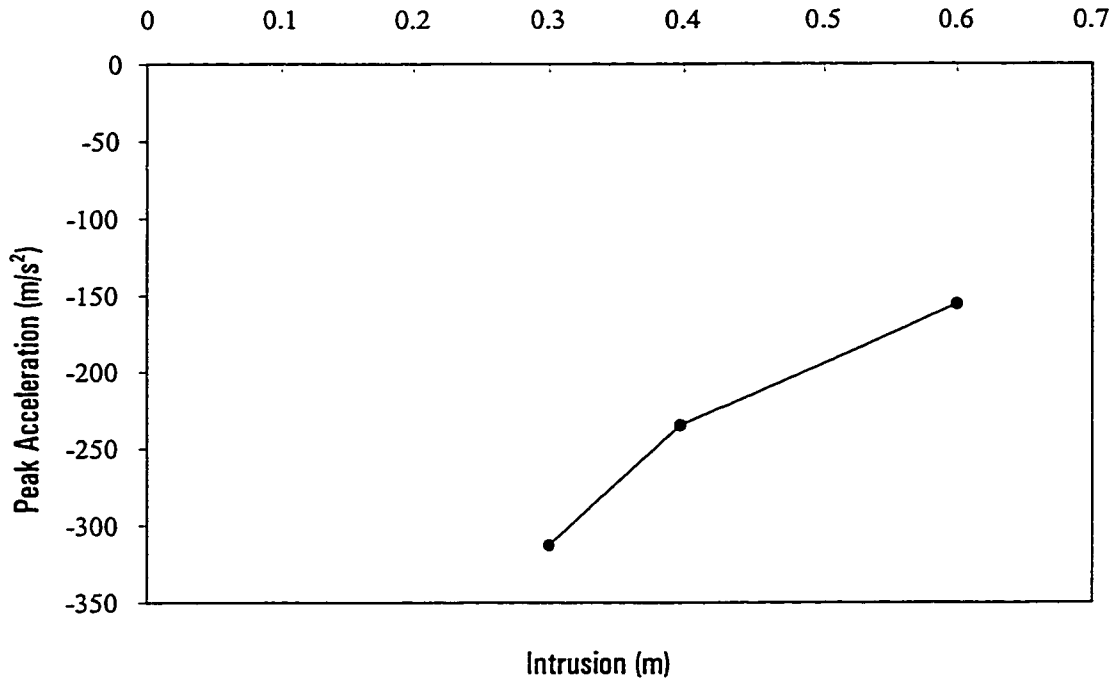

Figure 3.28: Variation of peak acceleration with intrusion of a car mass impacting damped guard with optimal parameters.

Figure 3.29 illustrates the response characteristics of the proposed optimal guard for the three different values of constraints (q_1, q_2), under impact at speed of 50 *km/h*. The results show that the drop arms re-impact the car mass, when $q_1 = 0.1$ (maximum intrusion < 0.3 *m*). The resulting peak acceleration of the car mass at the time of re-impact, however, lower than the initial peak acceleration. The results of the optimization studies performed with $q_1 = 0.15$ yields an increase in the maximum intrusion by 33%, $(x_c)_{max} = 0.398$ *m*, and a reduction in peak acceleration by 27%, $(\ddot{x}_c)_{max} = 235.4\ m/s^2$. The results presented in Table 3.3 and Figure 3.29 further show that soft stops are required to limit the peak acceleration response, when the constraint on the peak intrusion is relaxed. Stiff bump stops, however, are necessary to limit the maximum intrusion to a lower magnitude. The normalized dissipated energy tends to decrease when the permissible maximum intrusion is increased.

The results of the optimization study clearly reveal that the performance characteristics of the damped guard are strongly influenced by the compression mode damping. The high rebound mode damping, which the conventional automotive dampers provide, tends to determine the performance in a significant manner. The results of the optimization study further reveal that a damper design with two-stage compression and single-stage rebound damping, with $1 \leq p \leq 1.5$, is desirable.

3.5.1 Performance Characteristics of the Optimal Guard under Oblique Impact

The optimization problem, described in Equation (2.41), can be solved to determine optimal parameters of the proposed guard at different angles of impact and yaw velocity. Since a direct impact represents the most severe response, the optimal parameters of the

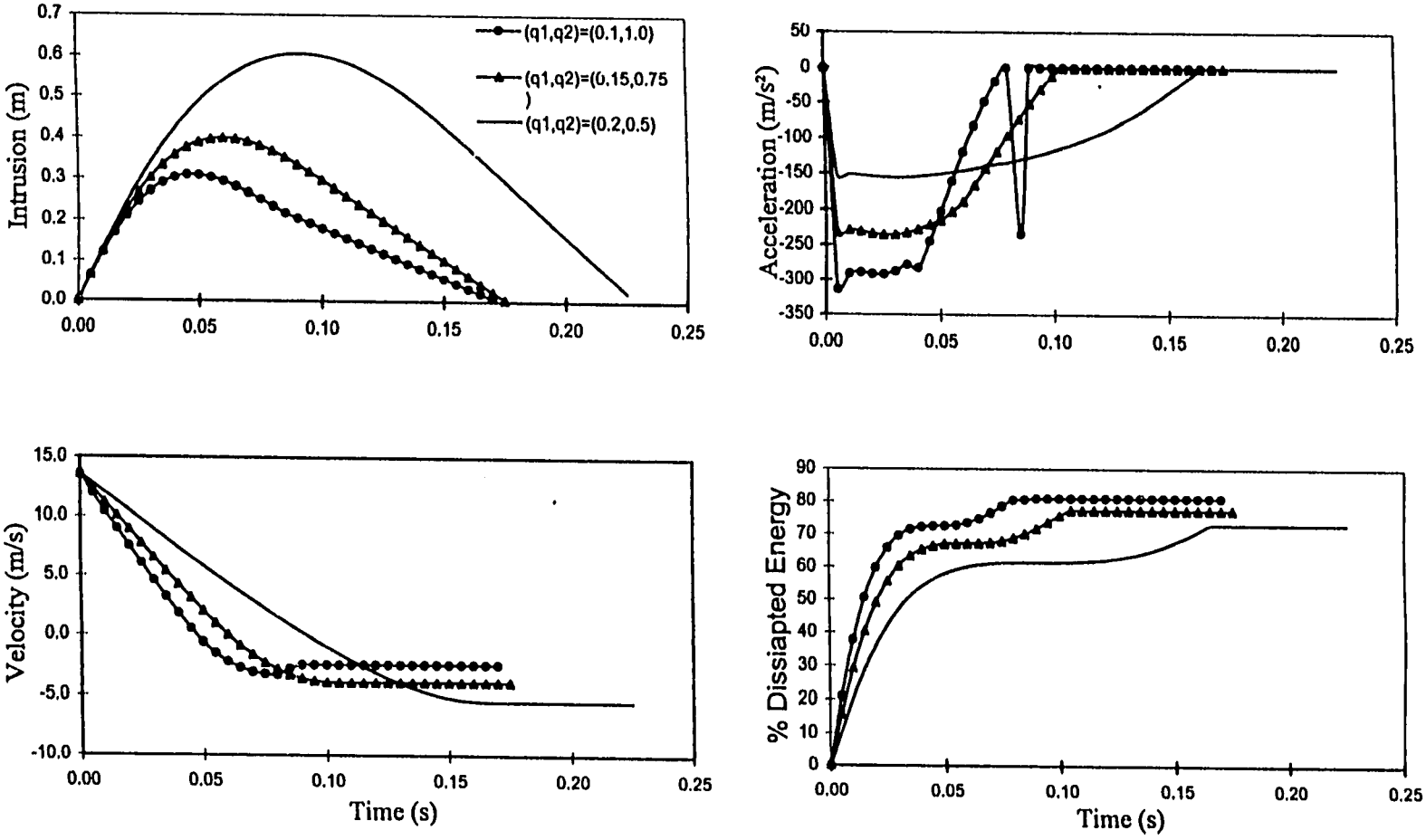

Figure 3.29: Performance of the proposed guard with optimal parameters.

damped guard are derived for the direct impact alone. The performance characteristics of the optimal guard, however, are examined under oblique impacts at different impact angles. The performance characteristics are evaluated for the optimal parameters, corresponds to $(q_1, q_2) = (0.15, 0.75)$, under different angles of impact.

The variations in different performance variables obtained under various oblique impacts with a damped guard with optimal parameters for constraint set $(q_1, q_2,)$: (0.15, 0.75) are illustrated in Figure 3.30. The effects of optimized parameters on the performance variables can be readily seen in the figure by comparing the results obtained using arbitrary values of damper parameters, illustrated in Figure 3.22. The variations in the performance variables for the two guard parameters are further summarized in Table 3.4. The two figures and Table 3.4 show that, the performance measures in-general, increase at impact angles, $\phi_0 < 30°$ and decrease for $\phi_0 > 30°$, when the optimal guard parameters are used.

Table 3.4: Comparison of performance measures for guard with optimal parameter 'Opt 2' and arbitrarily selected values.

Impact angle (Degrees)	Peak intrusion (m)		Peak acceleration (m/s^2)		% energy dissipated	
	Optimum	Arbitrary	Optimum	Arbitrary	Optimum	Arbitrary
0	0.39	0.42	235	235	82	80
15	0.26	0.33	215	230	46	65
30	0.31	0.37	202	210	71	70
45	0.32	0.26	175	165	55	32
60	0.18	0.15	113	110	17	12
75	0.08	0.07	56	51	3	2.5

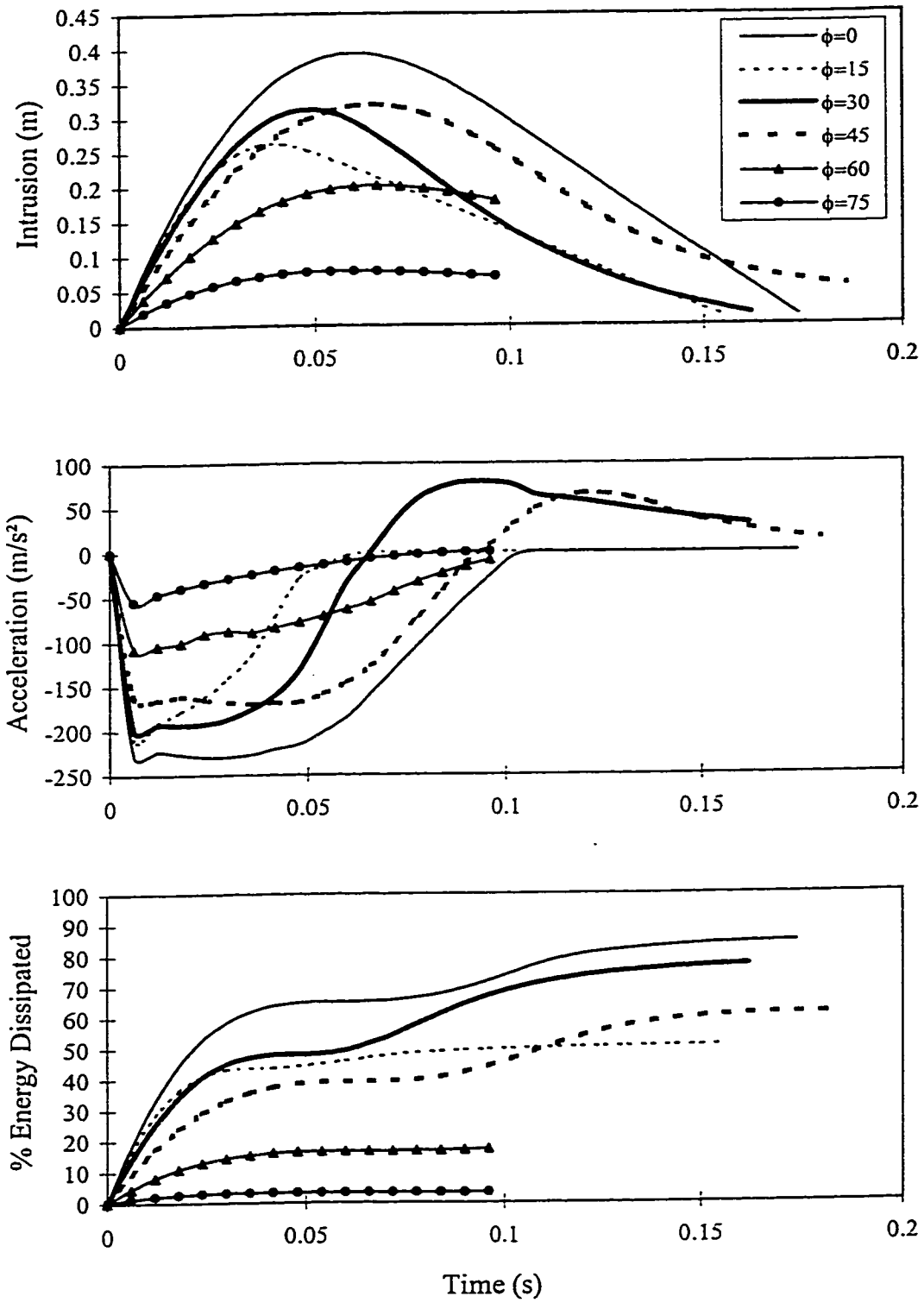

Figure 3.30: Influence of variations in the impact angle on the performance of optimal under-ride guard ($v_0 = 50$ *km/h*, $\dot{\phi}_0 = 0$ *rad/s*).

Some of the entries in Table 3.4, however, reveal certain discrepancies. For example, the difference in the performance variables under a direct impact is minimal. While the guard with arbitrary parameters resulted in a peak intrusion of 0.42 *m*, the guard with optimal parameters yields a peak intrusion of 0.39 *m*. A small reduction in the total impact duration can also be observed by the comparison of two figures. For a direct impact, the magnitude of energy absorbed is observed to increase by a small amount while the peak acceleration response remained unchanged. A high reduction in the amount of energy dissipation from 65% to 46% can be observed for an impact angle of $\phi_0 = 15°$. The peak values of intrusion and acceleration response at different angles of impact, however, are observed to be within the safe level recommended by the HIC. It should be noted that the sudden changes in the acceleration response for the guard with optimal parameters, shown in Figure 3.30 are due to the non-linearity associated with the optimal guard.

3.6 RELATIVE PERFORMANCE CHARACTERISTICS OF THE DAMPED AND CONVENTIONAL GUARDS

The performance characteristics of the optimal damped guard, corresponding to limit constraints $q_1 = 0.15$ and $q_2 = 0.75$ are compared with those of the conventional guards to illustrate the performance potentials of the proposed guard. The response characteristics of the guards in terms of the peak intrusion and peak acceleration are compared as a function of initial impact speed, as illustrated in Figure 3.31. From the figure it is clear that damped guard with optimized parameters yield acceleration levels comparable to the design B of conventional guard, while limiting the intrusion to a safer level.

The results clearly show that the peak acceleration response under impact with stiff conventional guard is considerably higher than that encountered under impact with

the damped and softer conventional guards, irrespective of the impact speed. While the peak acceleration response of softer conventional guard is similar to that encountered with the proposed damped guard, the conventional guard yields excessive intrusion of the car mass.

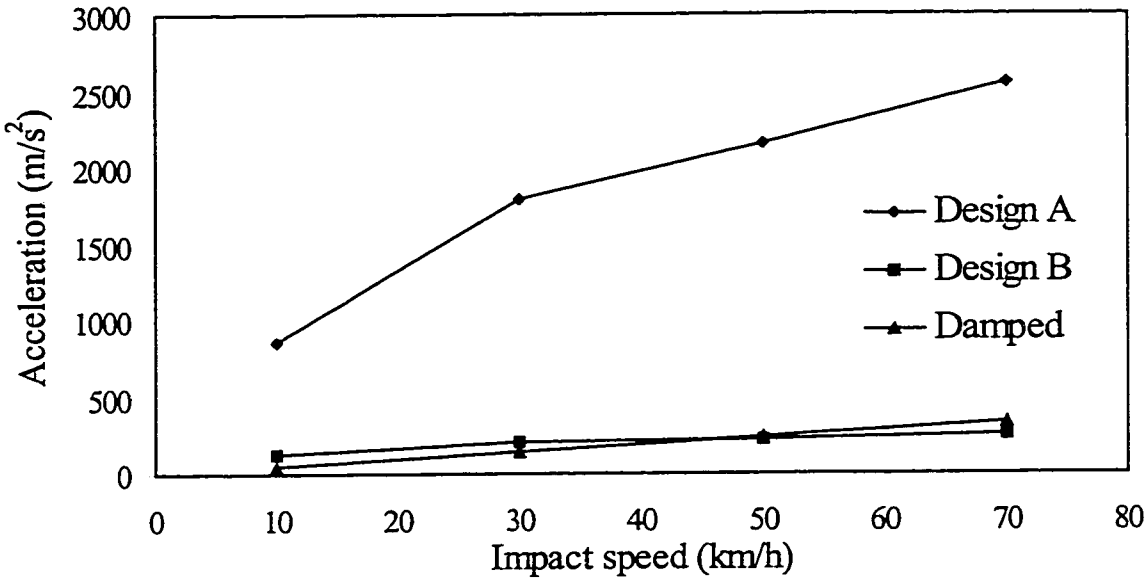

Figure 3.31: Comparison of peak acceleration levels for the conventional and proposed under-ride guards.

3.7 SUMMARY

The energy dissipation behavior of a flexible under-ride guard impacted by a rigid car body is investigated using the Hardware-in the-Loop test and simulation technique. The analytical model of the under-ride guard is analyzed using SIMULINK software interfaced with a hydraulic damper using the ADC, DAC and DSP hardware. The HIL

tests are performed and the results are compared with those derived from the analytical model to demonstrate its validity.

The concept of damped under-ride guard proposed in Chapter 2 was analyzed to derive the performance benefits. A comprehensive parametric study was conducted to determine the influence of various parameters such as damping coefficients, stiffness constants, angle and speed of impact and the contact surface friction properties, on the performance of damped under-ride guard. The guard parameters are optimized for various constraint sets based on the HIC and the results are compared with those of the conventional guards obtained from finite element analysis.

CHAPTER 4

LUMPED-PARAMETER AND FINITE ELEMENT IMPACT MODELS OF AUTOMOBILE

4.1 INTRODUCTION

A concept of an energy dissipating and flexible under-ride protection system for the heavy vehicles was proposed and analyzed in Chapter 2, to minimize the highway safety risks associated with the car-to-heavy vehicle collisions assuming the car as a rigid body. The energy dissipation properties of the guard were evaluated under direct and oblique impacts at different initial forward speeds, yaw angles and velocities. The crashworthiness of an automobile, however, is strongly dependent upon its energy absorption properties associated with plastic deformations of various structural members. The automotive bumpers comprising crush elements absorb part of the energy in a crash situation by plastic deformations, while other structural members further absorb certain amount of crash energy. The energy absorption properties of the car structure thus need to be included in the performance analysis of the characterization of the damped under-ride guard. The rigid mass representation of the automobile does not permit the analysis of energy absorption during a car truck collision. A large number of finite element based programs have been developed to study the crashworthiness of automobiles [25-30].

Although finite element techniques are considered most appropriate to study the energy absorption and dynamic resistance of the automobile bumper and various structural components using elastic-plastic analysis, such models are known to be

cumbersome and extremely demanding on the computing resources and interpretations. Alternatively lumped parameter (LP) models of the automobiles have been proposed to predict the acceleration transmitted to the occupant compartment during a barrier impact in a relatively simpler manner [16-21,119]. Kamal [21,119] proposed a three-degree of freedom (dof) non-linear lumped parameter model of an automobile using static characteristics of various components and dynamic magnification factors. In this chapter, a four-dof lumped parameter model of an automobile is developed. The Nonlinear resistance properties of different structural parts identified from the literature are integrated into the model. The proposed model is analyzed under impacts with conventional and damped under ride guards. In view of the excessive severity of the direct impacts, the lumped parameter model is developed for direct impacts only. The dynamic response characteristics of different lumped masses subject to direct impacts at different velocities are analyzed. The relative performance potentials of the damped guard are analyzed by comparing its performance measures with those of a conventional guard design. A detailed finite element model of the car structure is further developed and an elastic-plastic analysis of the car-to-under-ride guard is performed. The results obtained using the rigid body, lumped parameter model and the finite element analysis are discussed to illustrate the relative merits of the methods.

4.2 LUMPED PARAMETER MODEL

In a vehicle impact simulation, the deformations of certain components are of special interest. For example, excessive deformations of dash and A-pillar result in steering column deformations into the passenger space. An effective simulation model, from a

design point of view therefore must incorporate all the essential elements describing distinct substructures of the vehicle. Kamal [119] proposed such a model of a passenger car, with a front engine rear wheel drive and body-over-frame construction.

In a vehicle collision, the total kinetic energy of the vehicle is absorbed, except for a small portion in rebound due to plastic deformation. At the same time it is desirable that the passenger compartment retains its structural integrity, undergoing only limited plastic deformation. The front end structure experiences deformations of the order 0.8 m in a time interval of 0.1 s. Local strain rates must be appropriately incorporated in such models which may vary between $1/s$ and $100/s$. The structural problem to be solved in a vehicle impact is that of determining the dynamic forces and the deformations for the frontal structure, which are made of shells, beams, panels and irregular bars. The basic concept behind the simulation technique is to use the static force-deformation characteristics of the vehicle structural components to define the impact response under different conditions, such as impact velocity, mass distribution and geometric configuration. The static force-deformation characteristics can be obtained from either crush tests data, if available. Dynamic magnification factors are then incorporated to account for the high rate of deformations during a crash. The following simplifying assumptions are made in formulating the simulation model:

1. Structural integrity of the passenger compartment is maintained through out the impact.

2. The vehicle is symmetrical about its central plane.

3. Pitch, yaw and roll motions of the vehicle during an impact are considered negligible.

4. The mode of deformation of the structural components under static loading is similar to that under dynamic loading, assuming that the inertia force of a

component is considerably smaller than its collapse strength. It has been established that this assumption holds true for the automobile fore-structure [119].

5. Each resistance in general is considered to be inelastic while its loading and unloading paths are assumed to be inelastic.

6. The resisting force of a structural component is a function of deformation and deformation rate.

7. A conventional rigid guard is represented by a fixed and undeformable vertical barrier due to excessive inertia of the heavy vehicle.

A physical model of the crushable front end of the car structure is illustrated in Figure 4.1. The passenger compartment is considered as a lumped mass owing to assumption 1. The engine, and suspension and cross members, form other two lumped masses, since they are structurally stronger than the other deformable components of the vehicle. The bumper is also modeled as a lumped mass to transfer the impact forces to the structural elements. It should be noted that the mass due to transmission is included in the engine mass. The four lumped masses are connected by eight nonlinear springs, which represent, torque box, front frame, driveline, sheet metal, firewall, radiator, engine mount and transmission mount, as shown in the figure. The physical clearance between the sheet metal and the barrier, firewall and the engine, and radiator and engine are represented by appropriate clearances.

The resistance in the automobile fore-structure were selected by examining the load path from the rigid barrier to the lumped masses. The upper load path is from the barrier wall (or under-ride guard) to the body mass through the sheet metal (F_4), which covers the power plant, wheels and suspension. The lower load path is through the frame (F_2, and F_1). The front part of the engine is mounted on through the cross member in the mid-span of the frame rubber mounts (F_7), while the rear part is coupled to the

transmission and mounted on the underbody (m_{c1}) through mounts (F_8). When the vehicle impacts a barrier, the sheet metal and the frame crush between the barrier and the body. Components of the engine inertia forces are transmitted to the body and the frame through the transmission and engine mounts respectively. The engine inertia, during the early part of the impact, therefore increases the loading of the front frame and unloading of the torque box. This state continues until the engine crushes the radiator (F_6) and comes to a stop against the radiator. The body then crushes the drive-line and transmission mount against the engine until the latter contacts the firewall. The body may approach rest position after the fore-structure is reduced approximately to the length of the engine.

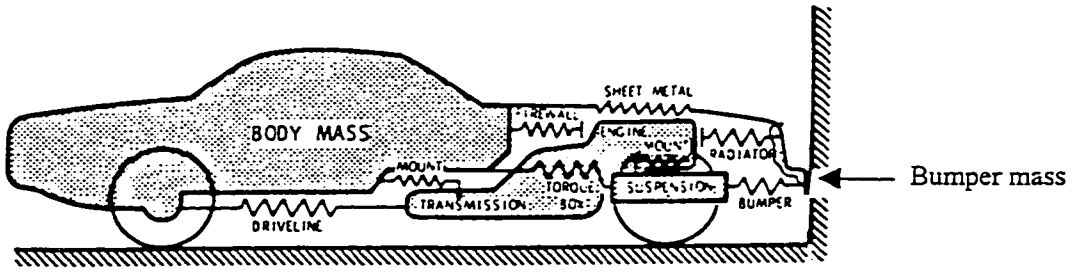

Figure 4.1: Physical description of the crushable front end of an automobile.

4.2.1 Model Description

A four-dof lumped parameter model (LP) of the automobile is developed as shown in Figure 4.2. The automobile is represented by four lumped masses: m_{c1} due to the car body, m_{c2} due to the engine mass, m_{c3} due to the cross-member and suspension mass and m_{c4} due to bumper and accessories. It should be noted that the mass m_{c4} is relatively small in magnitude, which is incorporated to characterize the impact force and the momentum transfer during the impact with the under-ride guard. The four masses are connected by eight non-linear springs with suitable clearances, as shown in the Figure. An impact between the automobile and the damped under-ride guard can be analyzed by combining the LP models of the automobile and the damped guard (described in Chapter 2). Figure 4.3 illustrates the coupled model of the car and the guard under direct impact.

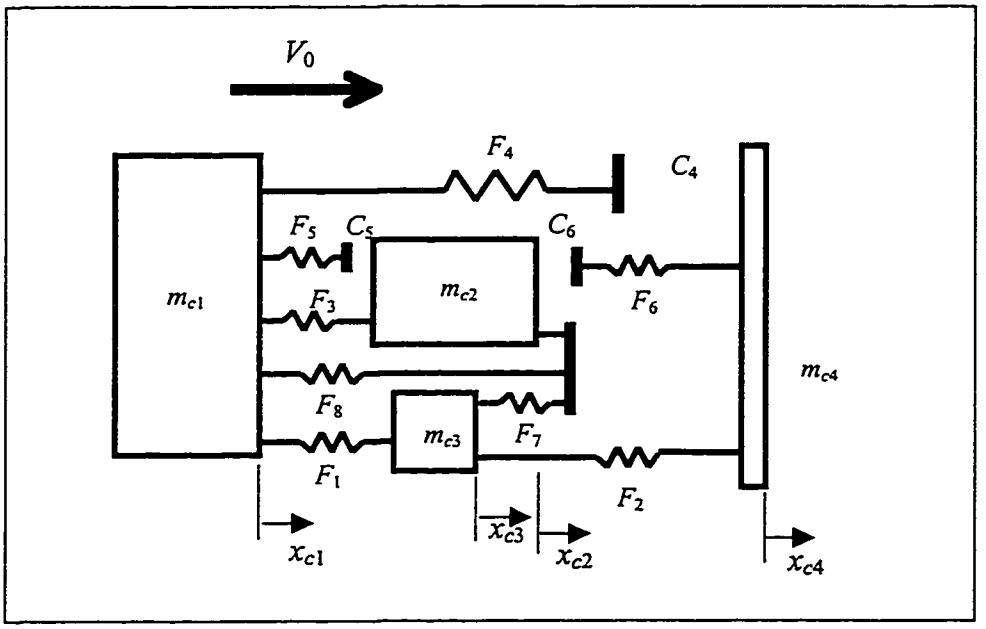

Figure 4.2: A lumped-parameter model of an automobile.

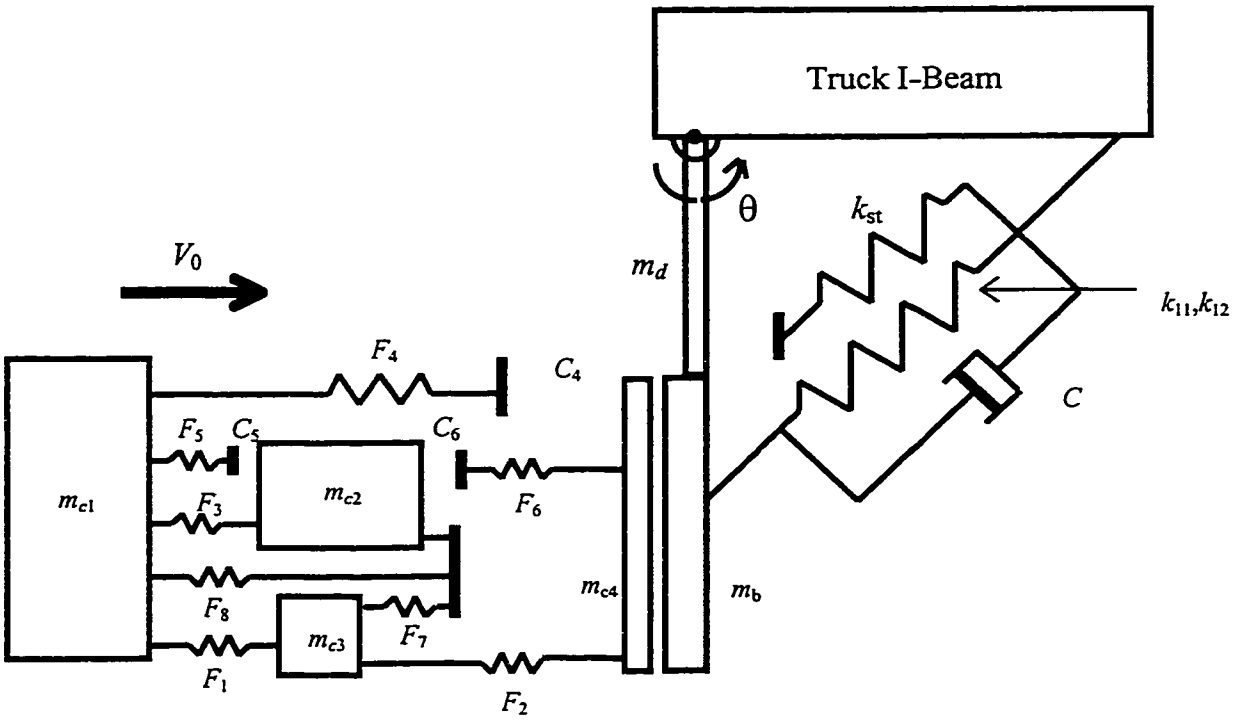

Figure 4.3: Lumped parameter car models of the automobile and the proposed under-ride guard.

In the impact simulation model, illustrated in Figures 4.2 and 4.3, F_1 represents the resistance due to cross member connected to the side rail on which the engine is mounted and is referred to as the torque box. The resistance due to portion of the vehicle consisting of the front frame structure and bumper forward of the spring mounts is represented by F_2. The resistance due to drive-line is described by the force-deflection characteristics of a rear-wheel drive, when the driveshaft push rearward, which transmits load through the driveshaft, rear axle housing and rear-suspension into the frame. The drive-line is represented by a nonlinear resistance F_3 in the simulation model.

For a framed vehicle, the sheet metal resistance (F_4) includes the assembly of fenders, hood, grille and other attached parts above the frame and forward of the body. The sheet metal does not contact the barrier in the initial stages of impact due to the physical clearance, shown in Figure 4.1, which is represented by a clearance C_4 in the model illustrated in Figure 4.2. The firewall is located at a distance of C_5 from the engine and is directly connected to the body and it contacts the engine and the accessories, as the impact event progresses. The resistance offered by the radiator and the grille, when the engine body moves forward in an impact event, is assumed to be F_6. The physical clearance between the radiator and the engine mass is shown as a clearance C_6 in Figure 4.2. The resistances F_7 and F_8, respectively represent the rubber mounts on which the engine and transmission are mounted. It should be noted that the clearance C_4 and C_5 are constant for a given automobile. The clearance C_6 between the radiator and the engine is computed dynamically since the motion of the engine mass is constrained to a certain maximum value.

4.2.2 Equations of Motion

The development of an analytical model of the damped guard and the car structure impact involves consideration of three sequential phases considered in Chapter 2: (i) the application of the principle of impulse and momentum to determine the velocity of the combined car bumper mass and under-ride guard bumper beam masses, immediately after the impact; (ii) dynamic analysis of the coupled system for the contact duration; and (iii) dynamic analysis of uncoupled models after the loss of contact which may occur either during compression or rebound stroke of the guard.

The principle of impulse and momentum is applied in the first phase of the analysis to determine the velocity of the bumper beam immediately after the impact, while the car bumper mass (m_{c4}) is assumed to be in contact with the under-ride guard beam mass. The different forces and momentum acting on the bumper mass and the under-ride guard illustrated in Figure 4.4 are similar to those described earlier in Figure 2.5, with the exception of momentum $m_{c4}\ddot{x}_{c4}$ due to the car bumper mass. Equating the moment of momentum about the hinge point O just before the impact with that after the impact, while assuming negligible deflection of the bumper at the point of impact, yields:

$$m_{c4}\dot{x}_{c4,0}l = m_{c4}\dot{x}_{c4,1}l + m_b\dot{x}_{b1}l + m_d\frac{\dot{x}_{b1}}{2}\frac{l}{2} + \frac{1}{12}m_d l^2\frac{\dot{x}_{b1}}{l} \tag{4.1}$$

where $\dot{x}_{c4,0}$ and $\dot{x}_{c4,1}$ are velocities of the car bumper mass before and just after the impact, respectively. It should be noted that the velocity of the car bumper mass, $\dot{x}_{c4,0}$ is equal to the approach velocity of the car, v_0. While the velocity of the bumper beam mass of the damped guard at the contact point before the impact point is zero, its velocity just after the impact, is represented by $\dot{x}_{b1} = \dot{x}_{c4,1}$. Owing to the flexibility of the under-ride guard along its rotational degree of freedom, the impact is considered to be perfectly plastic. The car bumper mass and the point of contact on bumper beam thus experience identical velocities, given by,

$$\dot{x}_{c4,1} = \frac{m_c\dot{x}_{c4,0}}{\left[m_c + m_b + \frac{m_d}{3}\right]} \tag{4.2}$$

The equations of motion of the automobile and the under ride guard models for the second phase of impact analysis are derived using the force balance. Both models are subject to the contact force F_x acting along the line of impact. The equation of motion for

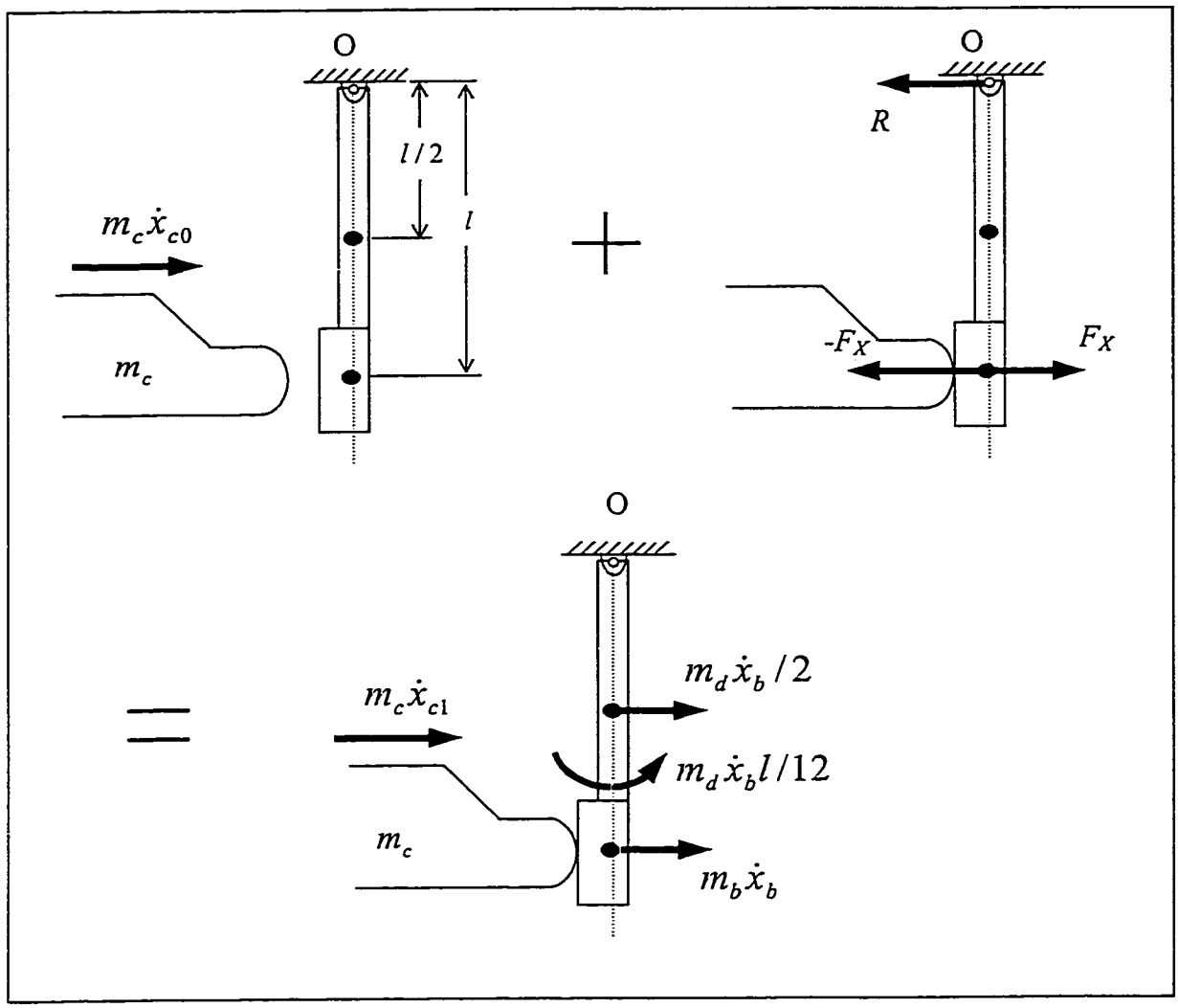

Figure 4.4. Forces and momentum just before and after the impact.

the under-ride guard is identical to that derived in Chapter 2, with the exception of the momentum due to the car bumper mass $m_{c4}\dot{x}_{c4,0}$. The under ride guard, however, is subject to the component of F_x along the line of contact, which is a function of the angular deflection of the guard. The equation of motion for the under-ride guard alone is derived using Lagrange's energy approach and is expressed as:

$$\left\{m_b + \frac{m_d}{3}\right\} l^2\ddot{\theta} + l_1 F_d + \left(m_b + \frac{m_d}{2}\right) gl\sin\theta + F_k \frac{\partial S_1}{\partial \theta} + F_{st} \frac{\partial S_2}{\partial \theta} + k_t\theta = \frac{F_x l'}{\cos\theta} \tag{4.3}$$

The equations of motion for the four-dof lumped parameter model of the car can be readily derived as:

$$\begin{aligned} m_{c1}\ddot{x}_{c1} &= -F_1 - F_3 - F_4 - F_5 + F_8 \\ m_{c2}\ddot{x}_{c2} &= F_3 + F_5 - F_6 + F_7 - F_8 \\ m_{c3}\ddot{x}_{c3} &= F_1 - F_2 + F_7 \\ m_{c4}\ddot{x}_{c4} &= F_2 + F_4 + F_6 + F_x \end{aligned} \tag{4.4}$$

where, $F_i = F_i(\delta_i, \dot{\delta}_i)$, i = 1,2,....8, are the dynamic nonlinear resisting forces of the various structural components, which are functions of the instantaneous deflections, δ_i and rates of deflections $\dot{\delta}_i$. The deformations of different springs δ_i, are defined as:

$$\delta_1 = x_{c1} - x_{c3} \qquad \delta_2 = x_{c3} - x_{c5} \qquad \delta_3 = x_{c1} - x_{c2}$$
$$\delta_4 = x_{c1} - x_{c4} - C_4 \qquad \delta_5 = x_{c1} - x_{c2} - C_5 \qquad \delta_6 = x_{c2} - x_{c4} - C_6$$
$$\delta_7 = x_{c2} - x_{c3} \qquad \delta_8 = x_{c2} - x_{c1}$$

where x_{c1}, x_{c2}, x_{c3} and x_{c4} are the displacements of the body, engine, suspension and car bumper masses, respectively. The quantities C_4, C_5 and C_6 are the physical clearances between the masses and the sheet metal, firewall and the radiator.

Equations (4.3) and (4.4) define the equations of motion of the damped guard and the car during the second phase of impact with six unknown response variables (x_{c1}, x_{c2}, x_{c3}, x_{c4}, θ and F_x). The contact force, however, can be eliminated using the velocity constraint at the contact point, to yield equation of motion for the coupled car and under-ride guard structures. The velocity of the car bumper mass can be represented in terms of the angular motion of the under-ride guard, as described earlier in Equation (2.4), as:

$$\dot{x}_{c4} = \frac{l\dot{\theta}}{\cos^2\theta} \tag{4.5}$$

The acceleration of the car bumper mass can be obtained from time differentiation of Equation (4.5), as:

$$\ddot{x}_{c4} = \frac{l}{\cos^2\theta}\left[\ddot{\theta} + 2\dot{\theta}^2 \tan\theta\right] \tag{4.6}$$

Elimination of reaction force from Equation (4.3) using Equations (4.4) and (4.6) yields:

$$\left\{\frac{m_{c4}}{\cos^4\theta} + m_b + \frac{m_d}{3}\right\} l^2\ddot{\theta} + 2m_{c4}l^2\left(\frac{\sin\theta}{\cos^5\theta}\right)\dot{\theta}^2 + l_1F_d + \left(m_b + \frac{m_d}{2}\right)gl\sin\theta + F_k\frac{\partial S_1}{\partial\theta} + F_{st}\frac{\partial S_2}{\partial\theta} + k_t\theta - \frac{(F_2 + F_4 + F_6)l}{\cos^2\theta} = 0 \tag{4.7}$$

Equations (4.4), (4.6) and (4.7) yield the equations of motion of the car and the under ride in terms of x_{c1}, x_{c2}, x_{c3}, and θ, as follows:

$$\begin{aligned}
&m_{c1}\ddot{x}_{c1} + F_1 + F_3 + F_4 + F_5 - F_8 = 0\\
&m_{c2}\ddot{x}_{c2} - F_3 - F_5 + F_6 + F_7 + F_8 = 0\\
&m_{c3}\ddot{x}_{c3} - F_1 + F_2 - F_7 = 0\\
&\left\{\frac{m_{c4}}{\cos^4\theta} + m_b + \frac{m_d}{3}\right\} l^2\ddot{\theta} + 2m_{c4}l^2\left(\frac{\sin\theta}{\cos^5\theta}\right)\dot{\theta}^2 + l_1F_d\\
&\quad + \left(m_b + \frac{m_d}{2}\right)gl\sin\theta + F_k\frac{\partial S_1}{\partial\theta} + F_{st}\frac{\partial S_2}{\partial\theta} + k_t\theta - \frac{(F_2 + F_4 + F_6)l}{\cos^2\theta} = 0
\end{aligned} \tag{4.8}$$

The above equations are solved using the initial conditions:

$$\begin{aligned}
&x_{c1}(0) = x_{c2}(0) = x_{c3}(0) = \theta(0) = 0\\
&\dot{x}_{c1}(0) = \dot{x}_{c2}(0) = \dot{x}_{c3}(0) = v_0; \quad \dot{\theta}(0) = \dot{x}_{b1}/l
\end{aligned} \tag{4.9}$$

The response characteristics of the car bumper mass are then obtained upon substituting for the angular motion of the guard in Equations (4.5) and (4.6).

4.2.3 Characterization of Nonlinear Resistance

The dynamic force-displacement characteristics of the nonlinear springs considered in the car model are represented as functions of deflections and rates of deflection $(\delta, \dot{\delta})$ [21,119]. During the impact process, the crushable components represented by non-linear springs in the model may undergo plastic deformations. The mathematical characterization of the plastic deformation of such springs is however highly cumbersome. Alternatively the force-displacement characteristics of the components may be derived from static crush tests performed on specific components. The measured static force-deflection characteristics of the torque-box, front-frame, drive-line, front end sheet metal, firewalls, radiator and engine mounts of an automobile have been reported in literature [119].

It has been further proposed that the resistance under dynamic load conditions attributed to the strain rate effect can be estimated from the static crush test data. For barrier impacts in the speed range of 0-56 *km/h*, as proposed in the FMVSS [3], the strain rate effects can be incorporated through a dynamic load magnification factor. A load magnification factor in the specified speed range of 0.623 % per *km/h* has been proposed [119]. It is recognized that the static crush data and the load magnification factor for the modern lightweight designs may differ from the repeated data. In view of complexities associated in performing such crush tests, the components are characterized using the reported data in order to derive the relative performance benefits of a damped guard.

The ability to accurately predict vehicle-barrier impact behavior is strongly dependent on the force-deflection characteristics of the various components derived from their respective crush test data. The force deflection characteristics of different structural components of an automobile have been established using slow-speed crusher [119]. The components were subject to loading and plastic deformations, and corresponding force-deflection characteristics of the eight components are illustrated in Figures 4.5.to 4.8.

The torque box comprising the cross-members connected to the side rails was statically loaded at its extremities and the resulting force-deflection characteristics were measured as illustrated in Figure 4.5. The results reveal elastic and plastic region before the final crush occurs at a deflection exceeding 300 *mm*. The elastic limit is observed to be approximately 15 *mm*, with a maximum load of 180 *kN*. The resistance due to front frame structure and bumper, forward of the spring moments was measured by constraining it from sliding vertically on the crusher ram, and the tests were conducted at speeds less than 4 *mm/s*. The force-deflection properties of the front structure, shown in Figure 4.5, revealed insignificant elastic region, and more or less a continuos crush up to 630 *mm* with a maximum load of 440 *kN*. The force-deflection characteristics describing the resistance F_3 due to driveline (Figure 4.5) reveals a 250 *mm* crush with maximum load of 80 *kN*. The resistance F_4 due to the sheet metal, including the assembly of fenders, hood, grille and other attached parts above the frame and forward of the body, is derived from the measured from the static force-deflection properties shown in Figure 4.6. Since it is very easy to get improper failure such as buckling of the fenders at the front wheel

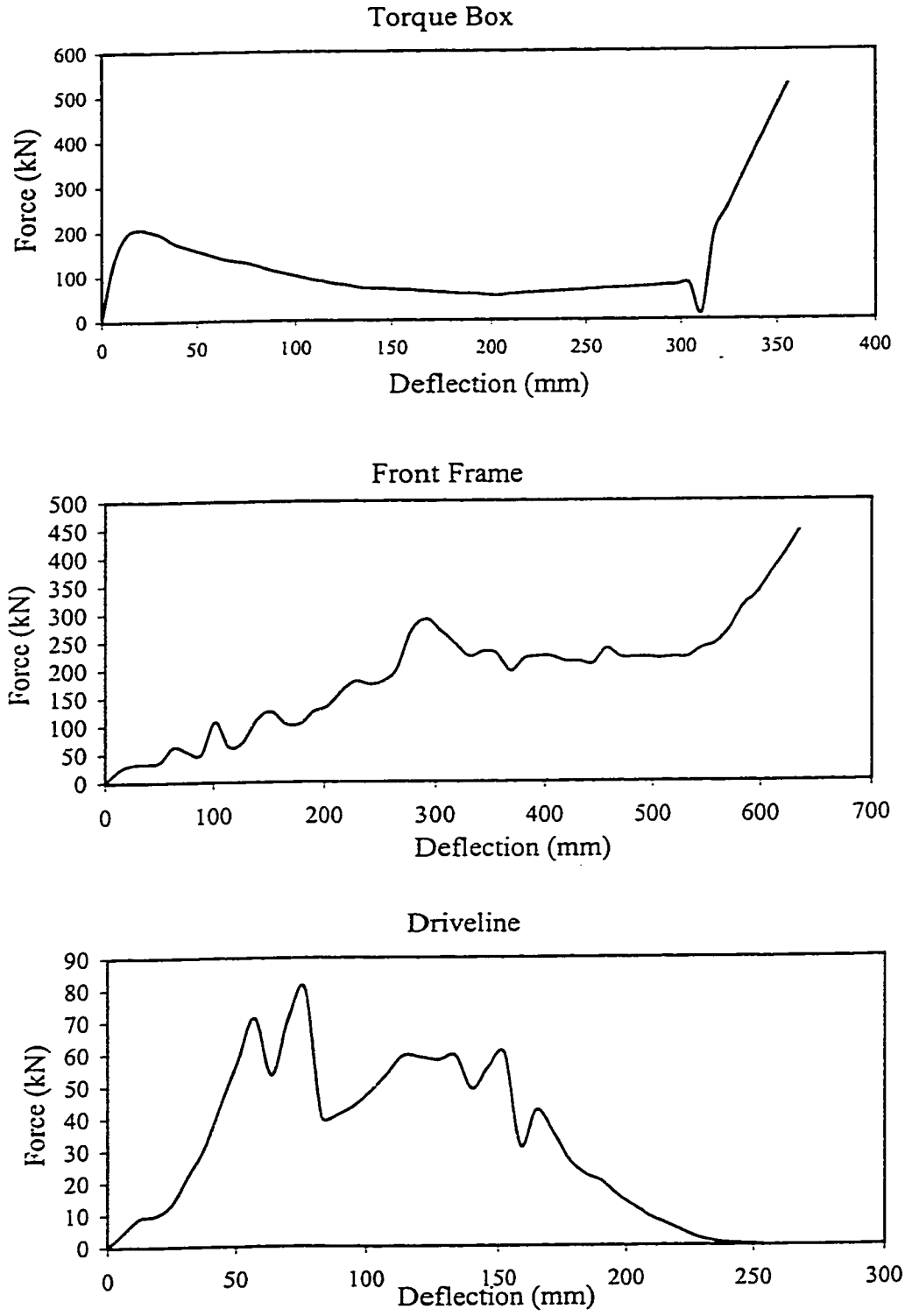

Figure 4.5: Measured static force-deflection characteristics of the torque box (F_1), front frame (F_2) and drive-line (F_3) [119].

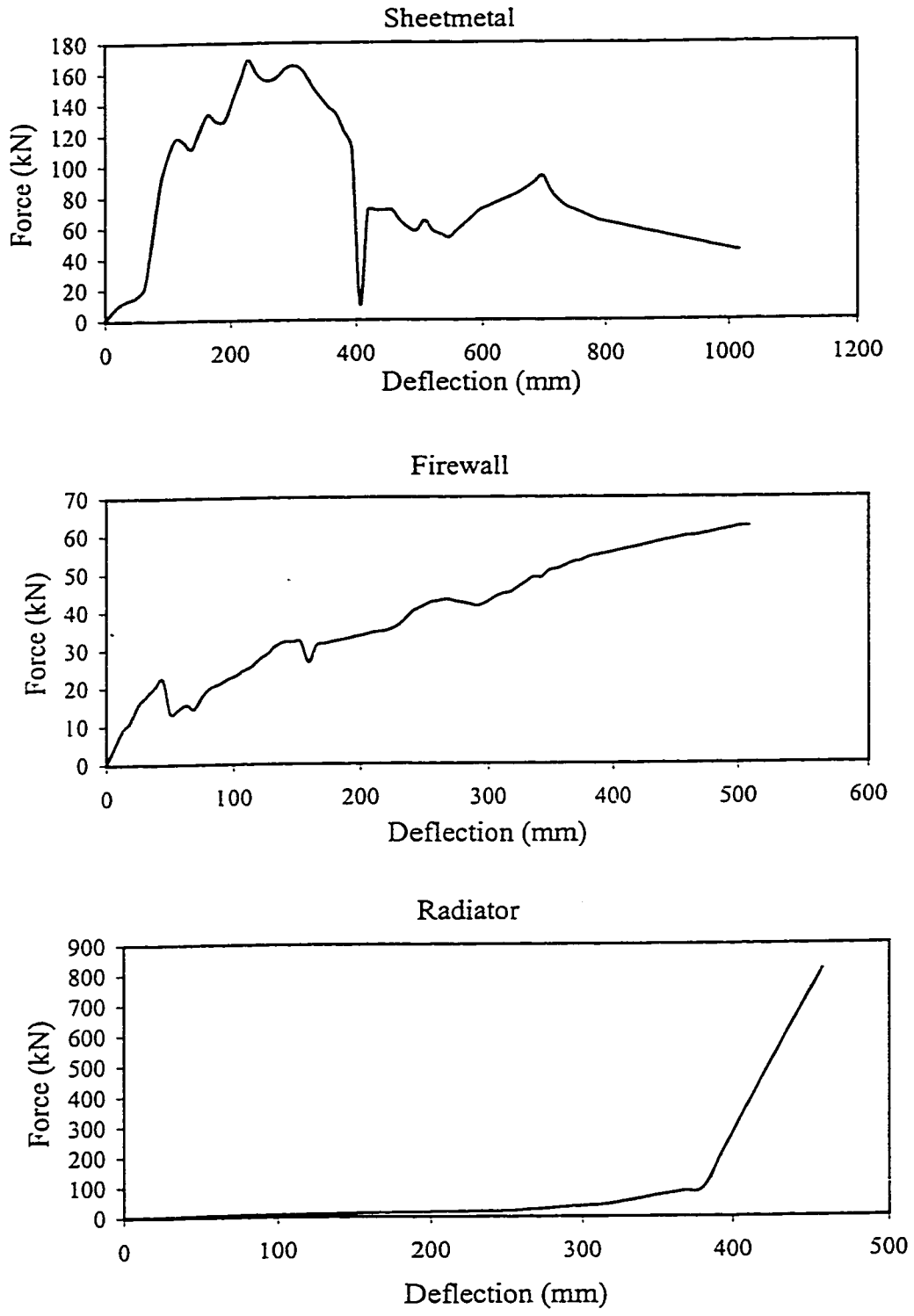

Figure 4.6: Measured static force-deflection characteristics of the sheet metal (F_4), firewall (F_5) and radiator (F_6) [119].

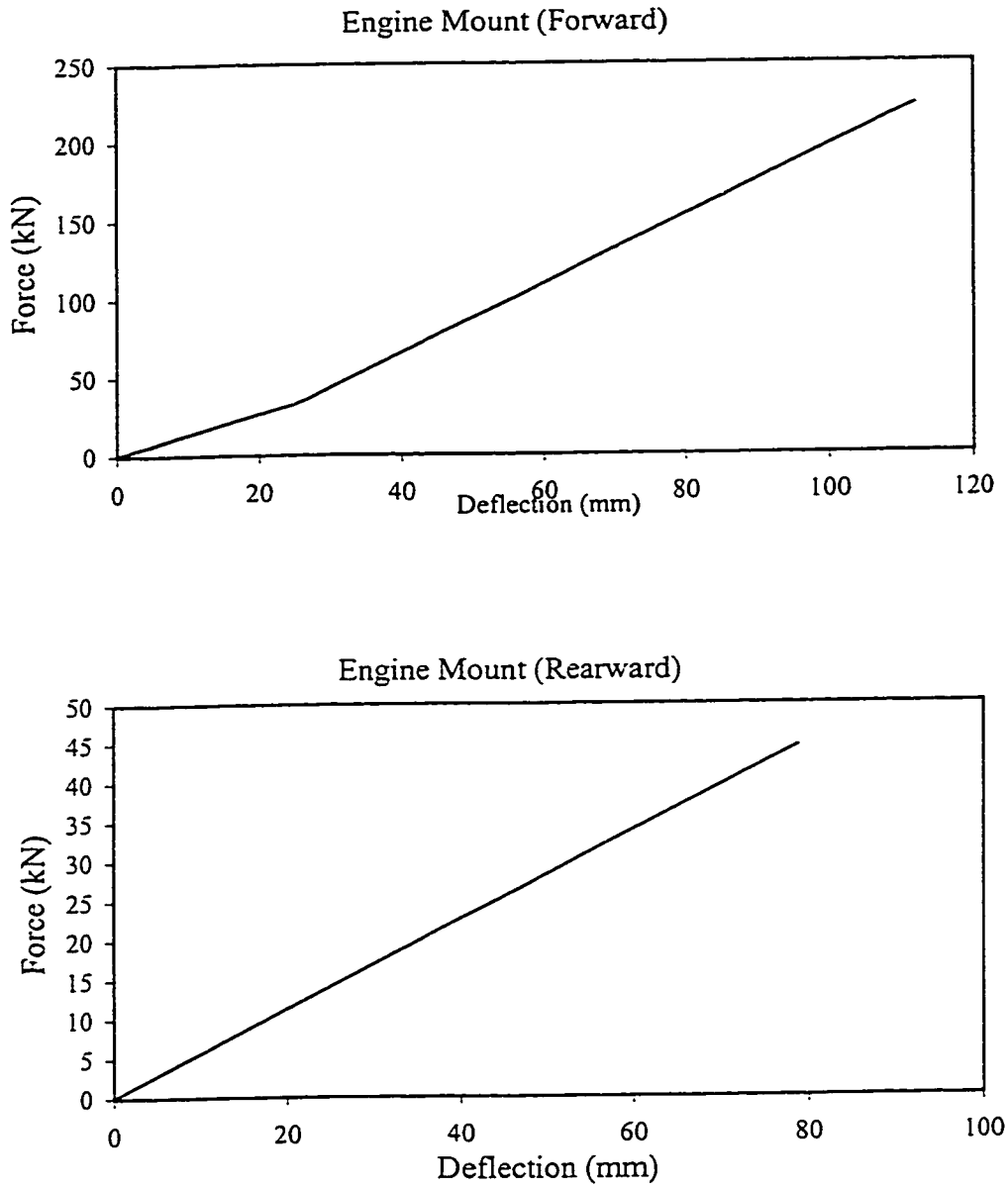

Figure 4.7: Measured static force-deflection characteristics of the engine mounts (F_7), in the forward and rearward directions [119].

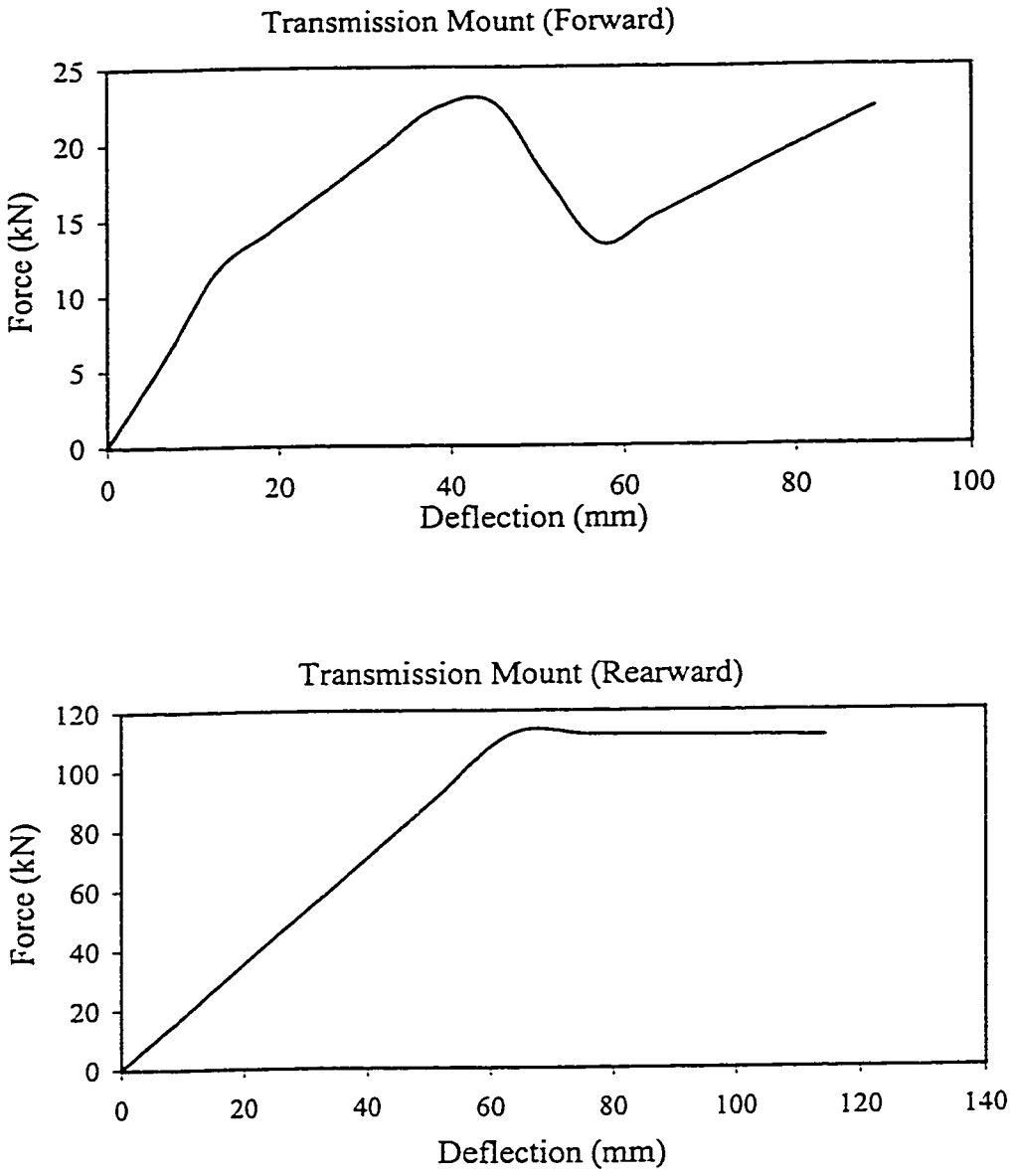

Figure 4.8: Measured static force-deflection characteristics of the transmission mounts (F_z), in the forward and rearward directions [119].

opening, the sheet metal was run in conjunction with a frame and the frame effects were subtracted from the measured frame force levels. The sheet metal revealed a total crush of more than 1 m and a maximum load of 166 kN. The contact between the body and the engine and if accessories may occur due to excessive deformations in the later stages of collisions. The firewall crush force determined by pushing the engine to the body revealed relatively weaker resistance (F_3) of the firewall with a maximum load of 60 kN. As the front of the vehicle crushes during an impact, the engine front penetrates the radiator and the grille. The test was performed after the sheet metal test, using the crushed front sheet metal assembly. The radiator revealed almost negligible resistance until total crush, where the resistance increased to 800 kN during the final stage.

The force-deflection properties of the engine and transmission mounts, illustrated in Figures 4.7 and 4.8 respectively, were obtained by loading the components in the fore-aft direction. The mount resistances are capable of crushing in both forward and rearward directions while the engine mounts reveal nearly linear force-deflection characteristics, the transmission mounts reveal linear elastic and plastic regions in both forward and rearward directions.

The solution of Equation (4.8) to derive the impact response of the automobile requires appropriate characterization of the dynamic forces developed during the crash. These dynamic forces depend upon the rate of deflection of the components. Figure 4.9 illustrates a generalized load path of a resistance in the F-δ plane. In the Figure S_i represents the slope of the curve corresponding to loading, unloading and reloading conditions in the elastic regime, and δ_i^R is the residual deformation upon rebound. A series of loading zones may be identified from the load path curve of a specific

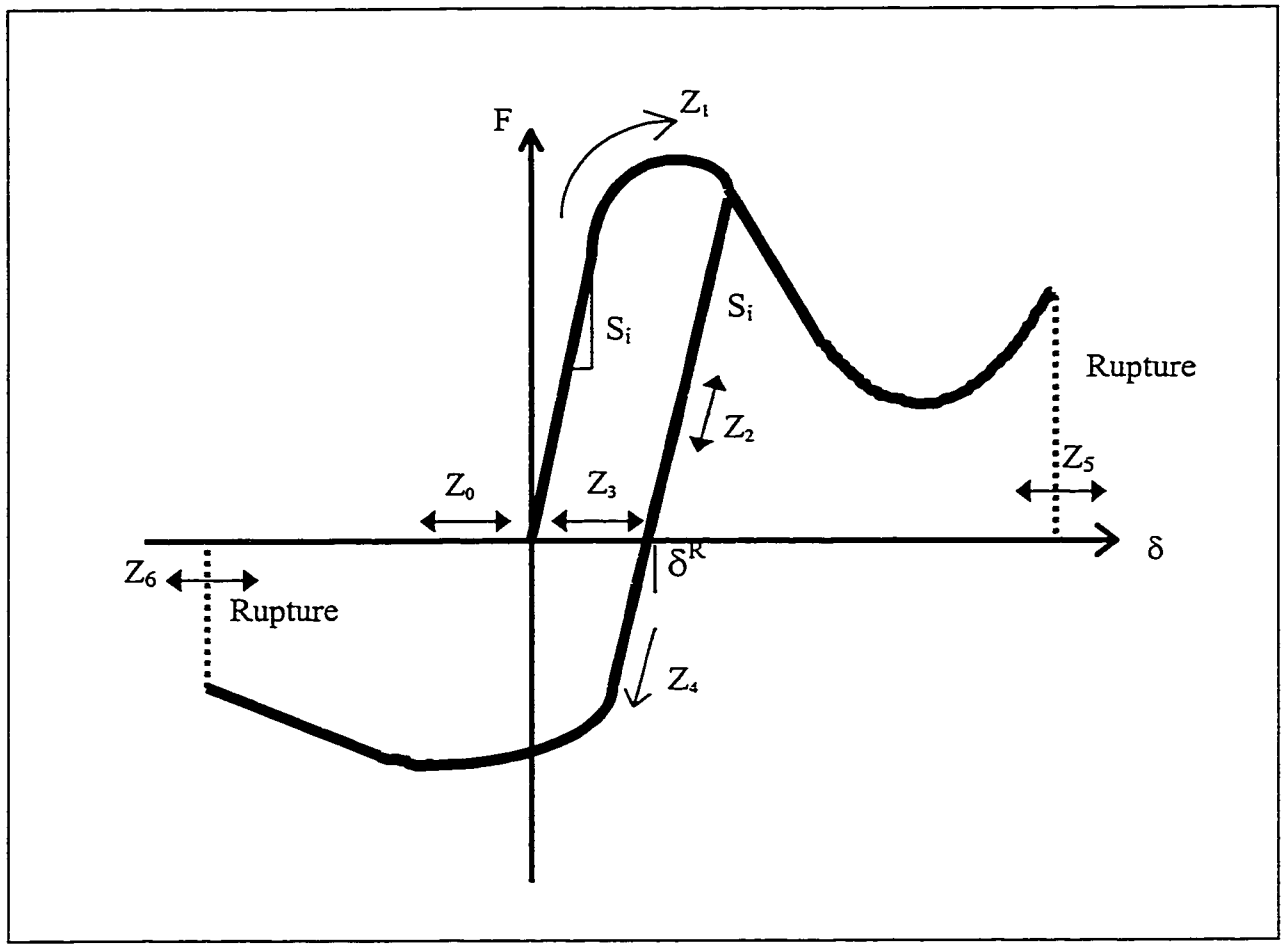

Figure 4.9: Generalized load path of a resistance.

component. A total of seven possible "load-zones" have been identified and used in the present analysis. The different zones, referred to as Z_i (i = 0,6) are described below in terms of the deformations:

Z_0 = Displacement with no resistance in the initial phase of motion;

Z_1 = Displacement under loading in the "forward" direction;

Z_2 = Displacement during elastic unloading (downward) and reloading (upward);

Z_3 = Post-rebound displacement with no resistance;

Z_4 = Displacement with loading in the opposite direction following complete unloading;

Z_5 = Displacement with no resistance following rupture in the forward direction;

Z_6 = Displacement with no resistance following rupture in the rearward direction.

The load path characteristics of various structural components however, do not pass through all of the above zones. The measured F-δ characteristics of various components used in the model have been represented into two groups, based on their loading zones [119]:

Group I: This group consists of torque box, front frame, drive line, sheet metal, firewall and radiator resistance and the load path curves may pass through zones Z_0, Z_1, Z_2, $Z_3$and Z_5, depending upon the magnitude of deflection.

Group II: This group consists of engine mounts and transmission mounts resistance where the load path curves may pass through zones Z_0, Z_1, Z_2, Z_3, Z_4, Z_5 and Z_6. Once the resistance approaches zone Z_5 or Z_6, the component will remain in the respective zone for the rest of impact process.

The dynamic forces due to various resistances can be evaluated from the measured static load path curves by integrating a dynamic load magnification factor. The dynamic forces associated with different loading of the generalized load path curve can be expressed as:

$$\begin{aligned} F_i &= (1 + K_i\dot{\delta}_i) f(\delta_i) && \text{for zone } Z_1 \\ F_i &= (1 - K_i\dot{\delta}_i) \bar{f}(\delta_i{}^R - \delta_i) && \text{for zone } Z_4 \\ F_i &= (\delta_i - \delta_i{}^R) S_i && \text{for zone } Z_2 \\ F_i &= 0 && \text{for zones } Z_0, Z_1, Z_5 \text{ and } Z_6 \end{aligned} \tag{4.10}$$

where $f(\delta_i)$ and $\bar{f}(\delta_i)$ are the static force-displacement relationship in the forward and rear directions, respectively and K_i is the dynamic magnification factor.

The impact between the car and the under-ride guard is analyzed by generating the dynamic forces from the measured static-force deflection data. The force-deflection characteristics of non-linear spring, shown in Figures 4.5 to 4.8 are initially descretized to formulate the look up tables. The equations of motion of the combined car-guard system (Equation 4.8) are solved to determine the deflection response of each spring as a function of time, and the corresponding instantaneous 'zone' of the springs in the generalized force-deflection curve is identified. The resistance offered by each spring is then computed in the corresponding 'zone' using Equation (4.10). The instantaneous deflection and velocity of the corresponding spring is used to evaluate the dynamic force along with the magnification factor. The force generated by each spring at time t_i is used compute the deflection of each spring corresponding to t_{i+1}.

4.2.4 Impact with Rigid Under-ride Guard

The lumped parameter model of the automobile may be analyzed to evaluate the response behavior under direct impact with a rigid under-ride guard. Assuming perfectly plastic impact the model of the car impacting a rigid under-ride guard may be further simplified, as shown in Figure 4.10. The resulting model is similar to the one proposed by Kamal [21,119], where the relatively small mass due to the bumper m_{c4} is considered negligible in relation to the fixed barrier. During the impact, the bumper mass, m_{c4}, will be part of the rigid structure (assuming perfectly plastic impact). The dynamic response of the LP model can be derived from Equation (4.8).

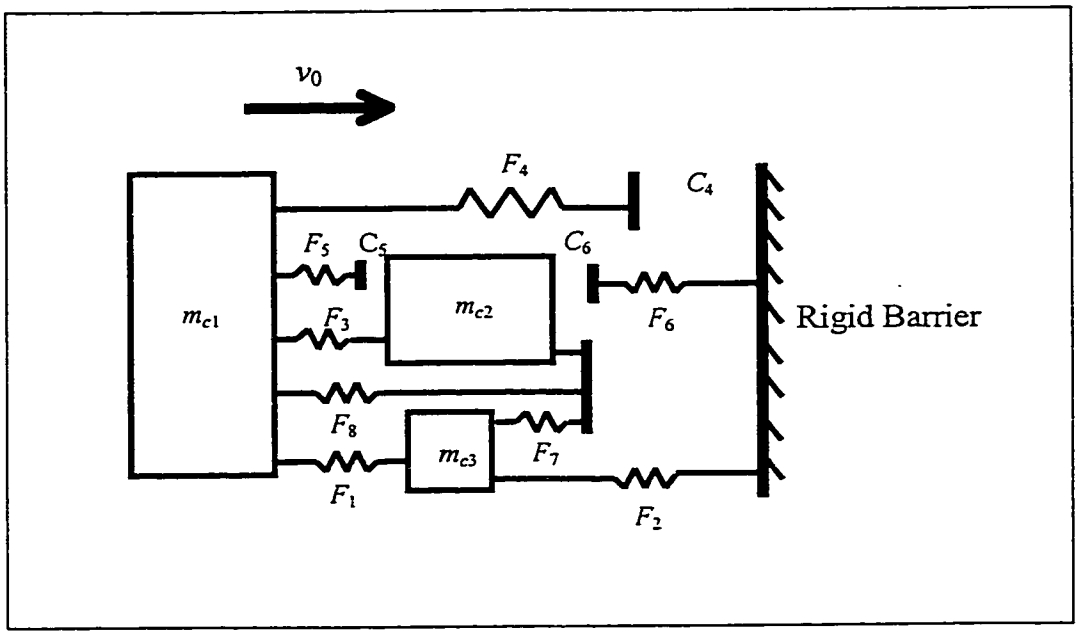

Figure 4.10: LP model of a car impacting a rigid barrier.

4.3 FINITE ELEMENT MODEL OF THE CAR-TO-UNDER-RIDE GUARD IMPACT

In order to gain further insight into the car-to-under-ride guard impact, the analysis is performed using the finite element software DYNA3D [31]. A finite element model of a modern light weight 1000kg car, developed by Ray [120], was used to analyze the impact with rigid and damped under-ride guards. The dimensions, masses and material properties of different structural components of the vehicle are assumed as outlined in the reference [120]. While the material properties and the dimensions of the vehicle in the LP model are quite different from that used in the finite element model, the total mass of the vehicle is assumed to be 1000 kg in both models.

The finite element model of the car consists of beam, shell and brick elements. The model consisted of 32 different components, where each component is identified by a material number. A different material number for each component facilitates the computation of average kinematic and dynamic motion for the corresponding component in the TAURUS post-processor, as described in Section 2.2.3. Finite element models of the rigid and the damped under-ride guards were developed and integrated with that of the car in [120]. The resulting coupled model of the car under-ride guard comprising 6220 nodal points, which were approximately connected to form 854, solid hexahedron elements, 88 beam elements and 4565 4-node shell elements, Figure 4.11 illustrates the finite element models of the car impacting rigid and damped under ride guards. The suspension, axles and hood reinforcements were represented by beam elements with appropriate material properties. While the suspension elements were assumed to be made of elastic-plastic beam elements (DYNA material model 19), the remaining beam elements were assumed to be rigid in nature. The strain rate effects of there beam elements are assumed to be negligible. Most of the body parts, bumper, horns to the core support and to bumpers, the engine cradle, engine mounts, frame rails, radiator, core support and the wheels, were represented by two-dimensional, 4-node shell elements.

All the above components are considered to be made of steel and are strain rate sensitive. The effects of strain rate on the crushing behavior of steel summarized in Table 4.1 [103]. The results show that the yield strength of the material increases with the strain rate in a non-linear manner. The elastic-plastic strain rate sensitive material model, available in the DYNA3D material library (material 19), was used to incorporate the effects for the shell elements. The windows and the windshield are modeled as 4-node

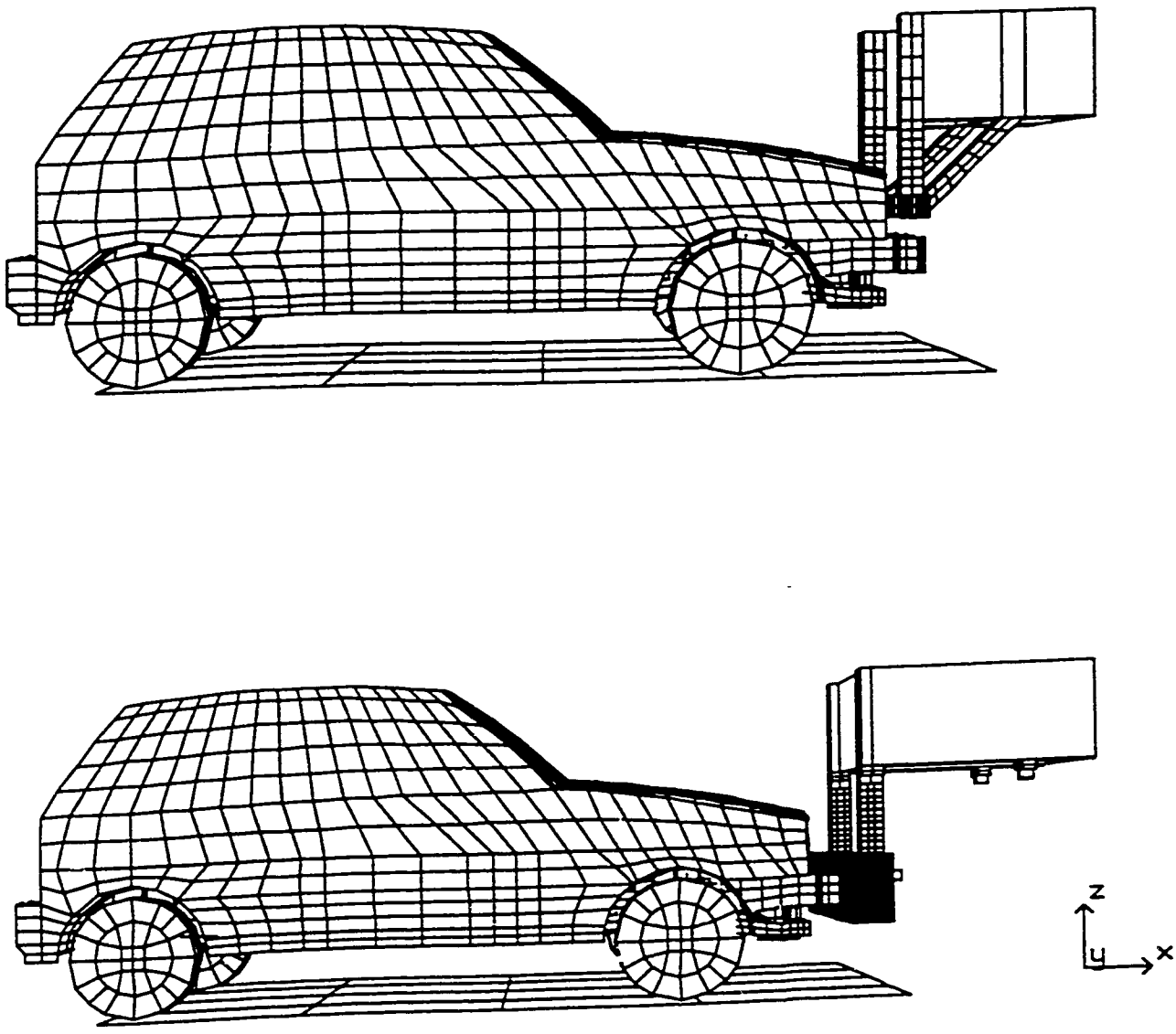

Figure 4.11: Finite element model of the car-to-under-ride guard impact analysis.

shell elements using material model 3 with appropriate properties of glass. The windows and the windshield, however, are assumed to be insensitive to rate of strain. Three-dimensional brick elements are used to represent the engine, rubber tire and steel wheel rim. An acceleration box was introduced at the center of gravity (c.g.) of the car, in order to derive an estimate the acceleration level experienced by the car c.g or the occupant. The acceleration box is also modeled using a three dimensional brick element while the drop arms and the bumper beams of the proposed under-ride guard are modeled using shell elements, discrete spring-mass-damper elements were used to incorporate the spring-damper attachments of the under-ride guard. The material properties of different components of the model are illustrated in Table 4.2 and the vehicle dimensions used in the model are given in Table 4.3.

Table 4.1: Effect of Strain Rate on Steel [103].

Strain rate ($1/s$)	0.001	0.01	0.1	1.0	10	100	1000
Yield stress (MN/m^2)	273	298	322	372	471	570	694

Table 4.2: Material Properties Used in the Finite Element Model.

Property	Material		
	Sheet metal (steel)	Radiator	Glass
Modulus of Elasticity (GPa)	200	30	80
Poisson Ratio	0.33	0.33	0.33
Yield Stress (MPa)	207	20	-
Tangent Modulus (MPa)	200	30	-
Density (kg/m^{-3})	7860	1860	2200

Table 4.3: Properties and Dimensions of the Vehicle and Under-ride Guard.

Modulus of elasticity (MPa):	
Front shock	1.0
Rear shock	2.0
Tire	1.0
Masses of major components (kg):	
Engine	170
Body	230
Ballast mass	240
Floor	12
Box at cg	10
Single tire	5
Rim	5
Major Dimensions (mm):	
Maximum width of the body	1625
Track width	1525
Wheel-base	2290
Length of the car	3350
Total maximum height of the vehicle	1420
Dimensions of the Under-ride Guard (mm):	
Height of UG above ground	300
Bumper beam length	1400
Bumper beam height	300
Bumper beam width	87.5
Length of drop arm	400
Drop arm width	87.5
Drop arm thickness	6.0

The interactions between the vehicle components and the under-ride guard during an impact are modeled using different 'slide surface' algorithm available in DYNA3D. The main contact between the vehicle and the under-ride guard is defined using the 'sliding only' (type 1) option of the sliding surfaces, which is a nodal constraint formulation. A penalty function approach was used and the under-ride guard elements are defined as master side. The contacts between various vehicle components are defined

using appropriate slide surface definitions, which are illustrated in Table 4.4. The surface friction affects were included in the model by defining friction coefficients along with the slide surface definitions. The static and kinematic friction coefficients for all the surfaces are assumed to be 0.33 and 0.3, respectively.

The finite element models of the car and the guard are analyzed using DYNA3D and the time histories of the average model deflections are extracted for further post processing of data. By defining each component as a material number, the averaged deflections, velocity and accelerations of each component are readily available in the post-processor, as described in Section 2.2.3.

Table 4.4: Slide Surface Definitions used in the FE Model of the car-under-ride guard impact analysis.

Contact surfaces (m – master, s – slave)	Slide surface type
Under-ride guard (m) - car components (s)	Sliding with separation and friction
Bumper (m) – radiator front (s)	Sliding with separation and friction
Radiator (s) – engine (m)	Sliding with separation and friction
Top radiator and engine (s) – hood (m)	Sliding with separation and friction
Engine-radiator (s) – frame (m)	Sliding with separation and friction
Engine (s) – fender (m)	Sliding with separation and friction
Bottom of engine (m) – cradle (m)	Sliding with separation and friction
Bumper self contacting	Single surface
Lower core support self contacting	Single surface
Horn self contacting	Single surface
Fender (m) – frame (s)	Tied with failure
Accelerometer box (m) – floor (s)	Single surface
Fender (m) – wheels (s)	Sliding with separation and friction
Radiator top (s) – upper core bottom (m)	Sliding with separation and friction
Vehicle – ground	Stonewall

4.4 PERFORMANCE MEASURES

The car-truck collision analyses are performed using the lumped parameter and the finite element models of the automobile to account for the energy absorbed due to deformations of the structural components. The analyses are performed with both the conventional rigid and the proposed damped guards, and the dynamic response characteristics are evaluated in terms of the performance criteria defined in Chapter 2.

4.4.1 Analysis using LP Model

In case of lumped parameter model of the car, the discrete masses and resistance represent the various structural components. The degree of under-ride or the intrusion is derived from the instantaneous coordinates of the bumper mass (m_{c4}), while the peak acceleration measure is expressed in terms of the acceleration response of the body mass. While the energy dissipated by the damped guard is derived from Equation (2.39), the energy absorbed by the structural members is evaluated from the respective force-displacement relations presented in Figures 4.5 to 4.8. The performance measures employed to assess the performance of the damped guard in conjunction with the lumped parameter model are summarized below.

Magnitude of intrusion: The magnitude of intrusion of the automobile is derived from displacement of the bumper mass (m_{c4}) beyond its zero-displacement position, x_{c4}. For convenience of analysis, the peak magnitude of intrusion, $(x_{c4})_{max}$, is normalized with respect to the wheel-base of the car (L), such that:

$$\mu_d = \frac{(x_{c4})_{max}}{L} \tag{4.12}$$

Peak Acceleration: The peak acceleration encountered during an impact is expressed in terms of the acceleration response of the occupant compartment, i.e., the car body mass acceleration, normalized with respect to acceleration related to HIC, 32g, such that:

$$\mu_a = \frac{(\ddot{x}_{c1})_{\max}}{32g} \tag{4.13}$$

Dissipated Energy: The energy dissipated by the damped guard is evaluated using Equation (2.39), and is normalized with respect to the sum of initial kinetic energy due to various lumped masses:

$$\mu_e = \frac{pcl_1 \int \dot{\theta} \cos^2(\psi - \theta) d\theta}{0.5 \sum_{i=1}^{4} m_{ci} v_0{}^2} \tag{4.14}$$

This performance measure is further enhanced to include the energy absorbed due to deformations of various members, evaluated from the measured force-deflection characteristics of the components.

The analyses are performed using the mass parameters of a modern light weight automobile with total mass of 1000 kg. It should be noted that the measured force-deflection characteristics have been reported for a relatively heavier automobile (mass=1625 kg) [119]. While a smaller car with modern materials will have different force-deflection characteristics, laborious and expensive experiments are required to obtain the data. The present analyses is thus performed using this reported data, while the vehicle mass is proportionally distributed to derive the lumped masses as: $m_{c1} = 750\ kg$, $m_{c2} = 170\ kg$, $m_{c3} = 70\ kg$ and $m_{c4} = 10\ kg$.

4.4.2 Analysis using FE Model

In the case of finite element model of the car, beam, shell and solid brick elements of varying size and properties represent the various structural components. The degree of under-ride or the intrusion is derived from the averaged instantaneous coordinates of the under-ride guard in X direction. The DYNA 3D software further computes the average deflections of the entity, identified in terms of the material number, along the X, Y and Z directions. The magnitude of intrusion is thus taken as the average deflection of the guard bumper beam along the X-axis. The peak acceleration measure is expressed in terms of the acceleration response of the acceleration block located at the c.g. of the car body, hereafter referred to as the 'c.g. block'. The energy dissipated by the damped guard is derived from the relative displacement and velocity of the spring-damper system along its axis in conjunction with the damping coefficients of the damper. The energy absorbed by individual structural members is evaluated from the internal energy plot option of the post-processor TAURUS. The total amount of energy absorbed can be evaluated by adding the energy absorbed by individual components over the impact duration.

4.5 IMPACT ANALYSIS USING LP MODEL

The impact analysis of the lumped parameter model is carried out for both rigid and damped guards at an initial velocity of 50 *km/h*. The results of the analysis are discussed below and analyzed to illustrate the relative performance potentials of the damped guard, and discussed below.

4.5.1 Conventional Rigid Guard

The impact of a car with the rigid under-ride guards can be conventionally analyzed as an impact between the car and a rigid barrier, as discussed in Section 4.2.4. The rigid barrier impact criteria proposed in the FMVSS code 571.204 [4] recommends the tests to be performed at a speed of 50 *km/h*. The analyses are thus performed at an impact speed of 50 *km/h*, while the influence of impact speed on the performance behavior of the guards has been illustrated in Chapter 3. Equations (4.8) are solved for an impact velocity of 50 *km/h*, and simulation is terminated when the total bumper force, the sum of forces due to non-linear springs, F_2, F_4 and F_6, approaches zero.

Figure 4.12 shows the time-histories of the displacement, velocity and acceleration response of the three lumped masses of the LP model impacting a rigid under-ride-guard, represented by a fixed barrier. It should be noted that the intrusion of the car mass subject to an impact with a rigid barrier is considered to be negligible. This confirms with the results of the FE analysis reported in Chapter 3, which revealed peak intrusion with a rigid guard of the order of 5 *cm*. The results show the response characteristics of three lumped masses representing the body (m_{c1}), engine (m_{c2}), and suspension and cross members (m_{c3}). While the displacement response characteristics of all the masses are observed to be quite similar, the engine mass exhibits slightly larger peak displacement due to rapid deformation of the radiator (F_6) and the front frame (F_2). The total crash event is observed to occur over a duration of 0.064 *s* when total bumper force approaches zero, and the peak displacements occur at 0.036 *s* for all the three lumped masses.

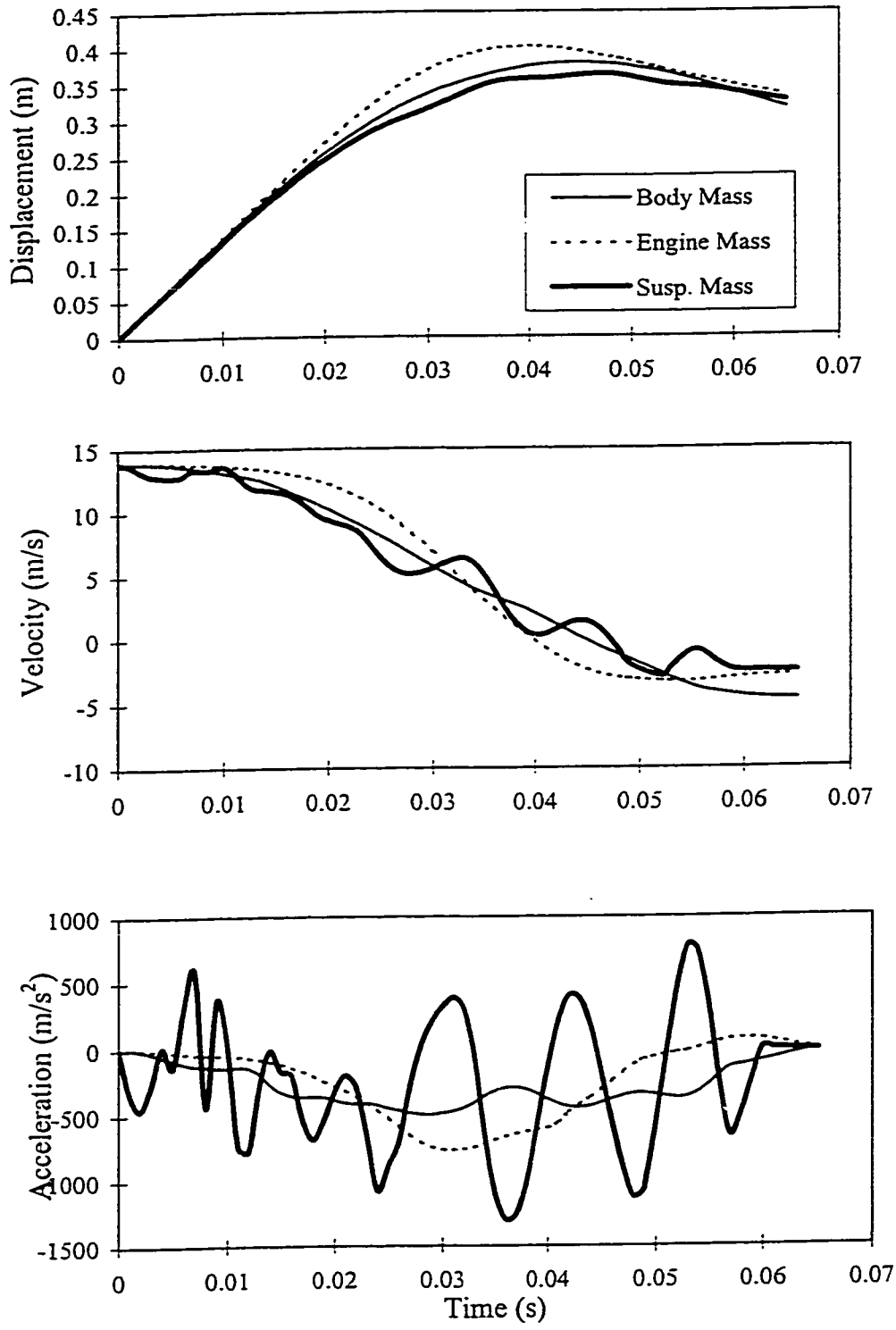

Figure 4.12: Displacement, velocity and acceleration responses of the lumped masses of the car under impact with a rigid barrier ($v_0 = 50$ *km/h*).

The velocity response characteristics of the lumped masses reveal gradual reduction in the velocity, while all the masses undergo rebound near 0.04 *s*. The acceleration response histories of the three masses, shown in Figure 4.12, reveal that the body-mass experiences a peak deceleration of 502 m/s^2 (51.2g). The suspension and the engine masses tend to have higher acceleration owing to their lower mass values. Further, the acceleration response of the suspension mass is observed to be more oscillatory as compared to those of the body and engine masses. The oscillations in the acceleration response are attributed to higher natural frequency of the suspension assembly mass. Although, the peak acceleration response of the suspension mass is very large, the objective is to minimize the acceleration experienced by the body mass. The peak acceleration of the body mass of the car impacting a rigid barrier is observed to be considerably larger than the head injury criteria, which further emphasizes the necessity of an energy dissipating absorption mechanism.

During an impact with a rigid barrier, the crushing of structural members of the car is associated with absorption of certain portion of the kinetic energy of the car. In the LP model the non-linear springs represent the energy absorbing members of the car. The energy absorption characteristics of the eight non-linear springs during the impact is illustrated in Figure 4.13. The energy absorption characteristics of different springs show that major part of the crash energy is absorbed by the plastic deformations of the front frame (F_2), which includes the bumper, and the sheet metal (F_4). The front frame absorbs more than 57% of the total kinetic energy (96.5 kJ) of the car. While the next major contribution towards energy absorption is from the sheet metal (28% of the total kinetic energy), the remaining components (F_1, F_6, F_7 and F_8) absorb smaller fractions of the

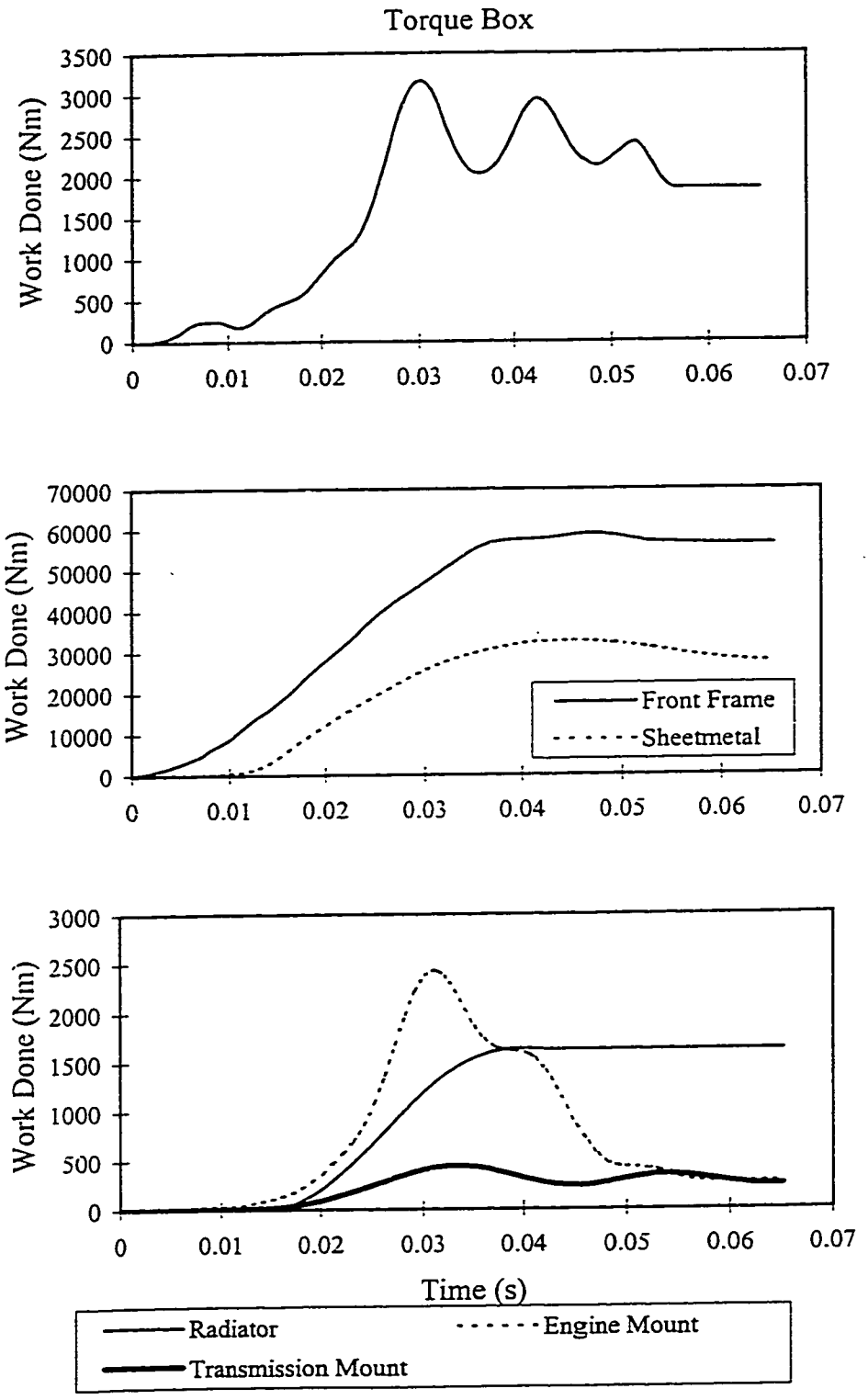

Figure 4.13: Amount of plastic work done (energy absorbed) by different components of the LP model subject to an impact with rigid barrier ($v_0 = 50$ *km/h*).

initial energy. It is interesting to note that drive-line and the firewall do not absorb any energy when the initial speed of the car is 50 *km/h*. The energy absorbed by these two members, increased slightly when the initial impact speed was increased to 60 *km/h*. The energy absorbed by the fire wall (F_3) and the drive line (F_5) is insignificant due to small relative deflections between the engine and body masses, and clearance C_6. The incapability of energy absorption by the firewall and the drive-line is further attributed to the unidirectional force-displacement characteristics of the components. These springs are assumed to be capable of energy absorption while compressed, but no work is done during extension. A comparison of the displacement response of the car body and the engine masses, shown in Figure 4.12, reveals that the engine mass displaces more than the body mass. The drive-line and the firewall members are thus subjected to extension resulting in zero or insignificant energy absorption.

Figure 4.14 illustrates the total amount of plastic work done by different components and the total bumper force of the car subject to a rigid barrier impact at a speed of 50 *km/h*. The results show that almost entire kinetic energy (96.5 kJ) of the car is converted as plastic work, which may represent higher risk of occupant casualty. The total bumper force or the contact force approaches a peak value of 510 *kN*, which occurs slightly before the masses experience peak displacements. The total contact force then gradually reduces to zero at the end of the crash event.

4.5.2 Damped Guard

The impact analysis of the lumped-parameter model of the automobile with the damped under-ride guard is evaluated under-direct impact at 50 *km/h*. Equations (4.8) are solved

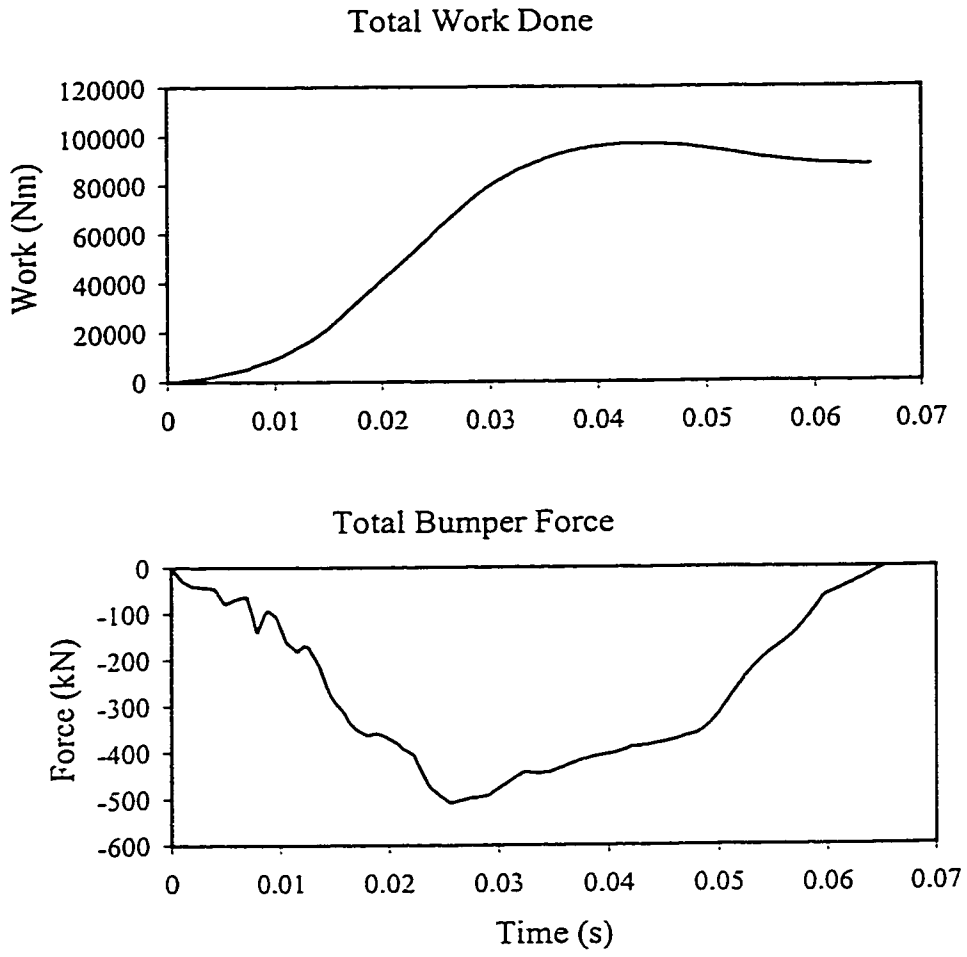

Figure 4.14: Total amount of plastic work done (energy absorbed) by different components and the total bumper force of the LP model subject to an impact with rigid barrier ($v_0 = 50$ *km/h*).

to determine the response characteristics of the lumped-parameter models of the car and the damped guard. A comprehensive parametric study is carried out to study the influence of various parameters of the damped guard on the response characteristics, expressed in terms of the performance measures.

The results of the parametric study revealed trends similar to those observed with rigid representation of the car, presented in Section 3.4.2. The results further demonstrated that the magnitude of intrusion and the acceleration response of the car body mass are strongly related to the stiffness and damping properties of the guard. A heavily damped guard with stiff spring resulted in low intrusion and high acceleration of the body mass, while a lightly damped and soft guard revealed excessive under-ride with lower transmitted acceleration. Since the important trends observed from the parametric study conform with those described in Section 3.4.2, the results of the parametric study are not presented. An optimal design of the damped guard, however, is attempted to achieve optimal performance under impact with the lumped parameter model of the car. A design optimization study was performed to minimize the weighted function of performance variables, defined in Equation (2.41), to identify the optimal parameters of the guard. The peak intrusion and acceleration terms in the objective function, however, are replaced with the modified performance measures described in Equations (4.12), (4.13) and (4.14). In view of the strong and conflicting dependency of the guard performance in terms of magnitude of intrusion and the peak acceleration, the optimization is performed using different limiting constraints imposed on these measures. The constrained optimization function is thus defined as:

$$U(\bar{x}) = \text{ minimize}\left[\alpha_1\mu_d + \alpha_2\mu_a + \alpha_3\frac{1}{\mu_e}\right] \tag{4.15}$$

Subject to:

$$g_1(\bar{x}) = q_1 - \mu_d \geq 0$$

$$g_2(\bar{x}) = q_2 - \mu_a \geq 0$$

where $\bar{x}$ is a vector of design variables, given by:

$$\bar{x} = \{\xi_c \;\; n_c \;\; v_c \;\; p \;\; n_e \;\; v_e \;\; k_{11} \;\; k_{12} \;\; k_{st}\}^T$$

q_1 and q_2 are the limiting values of magnitude of normalized intrusion of the bumper mass m_{c4} and peak normalized acceleration of the car body mass m_{c1}. The constrained optimization problem in Equation (4.15) is solved using a nonlinear programming technique for three different target values for the constraints $\{q_1, q_2\}$: {0.1, 1.0}, {0.15, 0.85}, {0.2, 0.75}. It should be noted that the above limiting values differ from those utilized for the optimization study in conjunction with rigid mass representation of the car (Section 2.6.2). The car body, in general, experience acceleration levels, which are considerably larger than that encountered by a rigid mass. The higher acceleration of the body mass is attributed to plastic deformations of the structural components, which tend to transfer the energy to the lumped masses. Higher acceleration limits are thus chosen when the normalized intrusion limit is relaxed to 0.15 and 0.2.

Table 4.5 illustrates the optimal parameters of the damped guard, subject to a direct impact with the LP model of the car at a speed of 50 *km/h*, corresponding to three sets of limit constraints. The results show that a very high compression and rebound stroke damping is required, when the maximum intrusion is limited to 0.45 *m* (q_1 = 0.1 and 0.15). The relaxation in the intrusion to 0.6 *m*, however, allows the solution to

converge near the compression mode damping coefficient of 0.4. The results further show that multiple stages in compression and rebound damping are not necessary, as evident from unity values of n_e and n_c. While a high rebound mode damping ($p = 1.39$) is required to limit the maximum intrusion to 0.3 m ($q_1 = 0.1$), the asymmetry factor reduces to 0.24 when peak intrusion limit is relaxed to 0.6 m ($q_1 = 0.2$). The results of the optimization study contradict considerably with those obtained for the guard subject to an impact with a rigid mass. The relatively lower acceleration response of the rigid mass requires lightly damped guard with compression mode damping coefficient ranging from 0.35 to 0.5 in order to meet the selected limits (q_1, q_2). The damped guard tends to limit the high acceleration response of the lumped car body mass by converging to relatively high damping. The peak acceleration is further limited by relaxing the peak intrusion of the bumper mass. The peak intrusion, however, is limited by converging towards stiffer bump stops and higher values of cubic stiffness coefficient, specifically for the constraint limits, $q_1 = 0.2$ and $q_2 = 0.75$.

Table 4.5: Summary of Optimal Design Parameters of the Damped Under-ride Guard using LP Model ($v_0 = 50$ *km/h*).

Design Variable	Constraint (q_1, q_2)		
	(0.1, 1.0)	(0.15, 0.85)	(0.2, 0.75)
ξ_c	0.86	0.9	0.39
n_e, n_c	1.0, 1.0	1.0, 1.0	1.0, 1.0
v_e (*m/s*)	3.0	3.0	3.0
P	1.39	0.82	0.24
k_{11} (*MN/m*)	2.975	1.512	0.939
k_{12} (MN/m^3)	2.638	2.459	2.712
k_{st} (*MN/m*)	1.44	2.337	0.878

The results show that the damping required to limit the intrusion to a particular value is much higher in the case of optimization using LP model. The higher value of damping in the case of LP model may be attributed to the smaller kinetic energy of the body in contact with the under-ride guard. There is no direct contact between the car body mass and the under-ride guard, and the energy is transmitted through the springs representing different parts of the car. The non-linear springs are crushed due to the relative motion between the masses and the deformation of the spring results in either temporary storage of the energy or absorption due to plastic deformation. The stored energy is being transmitted back to the three lumped masses and the motion of the masses is dependent on the combined effect of the force transmitted from the car-body spring and the under-ride guard.

The performance measures of the optimal design of the guard subject to the three tests of limiting constraints are compared with those obtained with the conventional guard as illustrated in Table 4.6. Three optimal designs are referred to as 'Opt 1', 'Opt 2', 'Opt 3', corresponding to (q_1, q_2), equal to (0.1,1), (0.15,0.85) and (0.2,0.75) respectively. It can be observed that the optimization using LP model resulted in higher minimum acceleration level for a particular value of intrusion. While the single degree of freedom model resulted in an acceleration of 158 m/s^2 (for a maximum intrusion of 0.6 m), the optimization using LMS model resulted in 235.1 m/s^2 for the same amount of intrusion of the bumper mass. The comparison of the performance measures illustrated in Table 4.6, clearly demonstrates the potential performance benefits of the damped guard. The intrusion of the bumper mass under the optimal guard can be limited at the expense of high acceleration of the car body. The peak acceleration transmitted to the car body is 312

m/s^2, when the peak intrusion is limited to 0.295 m. This acceleration level is considerably lower (38%) than the 502 m/s^2 encountered under a rigid barrier impact. The peak acceleration levels of the car body mass reduce to 266 m/s^2 and 235 m/s^2, when the intrusion limits are relaxed to 0.45 m and 0.6 m, respectively. The final rebound velocities of the car body mass impacting the optimal damped guards tend to be considerably larger than that obtained under rigid guard impact. The increased rebound velocity with the damped guard is attributed to energy stored and relaxed by the flexible guard.

Table 4.6: Performance Comparison of the Optimized Damped Guard and Rigid Guard using LP Model ($v_0 = 50$ *km/h*).

Performance Variable	Opt 1	Opt 2	Opt 3	Rigid Barrier Guard
Maximum intrusion (m)	0.295	0.449	0.596	-
Final velocity (m/s)	-6.69	-8.38	-10.88	-3.8
Peak acceleration (m/s^2)	-312.45	-265.8	-235.1	-502
Normalized dissipated energy (%)	48.2	46.6	20.6	-
Total plastic energy of springs (%)	44.7	29.6	31.6	91.2
Total Energy (%)	92.9	76.2	52.2	91.2

The results further show that the damped guard dissipates a significant portion of the initial kinetic energy. A relatively smaller fraction of the KE is absorbed through deformations of the structural components of the automobile. The damped guard tends to dissipate 46-48% of the total energy, when the peak intrusion is limited to 0.45 m. An impact with a rigid guard/barrier yields absorption of 91.2% of the total energy through plastic deformations of the members. The absorbed energy reduces to only 44.7% with the damped guard with peak intrusion limited to 0.295 m. The component of the energy

absorbed with the damped guard reduces to approximately 30%, when the bumper mass is permitted to under-ride by 0.45 *m* to 0.6 *m*.

The total bumper force, percentage of energy dissipated by the under-ride guard damper and the percentage of energy absorbed by the car body parts for the three optimal designs due to different guard designs are shown in Figure 4.15. A comparison of the total bumper forces that due to different damped guard designs that due to impact with rigid under-ride guard (Figure 4.14) clearly reveals that the damped guards yield considerably lower bumper forces. While a 25% reduction in total bumper force can be achieved by allowing 0.3 *m* intrusion of the car, a 0.6 *m* intrusion would result in 50% reduction in the bumper force. While part of the kinetic energy of the car is dissipated by the damper a portion of the energy is absorbed due to plastic deformation of the various components of the automobile. The amount of energy absorbed and dissipated, however, depends on the set of constraints selected to achieve an optimal design. While a total of 92% energy is absorbed when the intrusion is limited to 0.3 *m*, only 52% of the kinetic energy is used when the intrusion constraint is increased to 0.6 *m*. A lower amount of energy expended in the impact process indicates that the vehicle masses retain higher velocity and kinetic energy.

The displacement, velocity and acceleration response characteristics of the car body, engine, suspension, and bumper masses during an impact with optimal design of the under-ride guard are further compared in Figures 4.16–4.19. The displacement and velocity response characteristics of the different masses exhibit similar trends for all three optimal designs. The displacement response reveals that the car body mass approaches

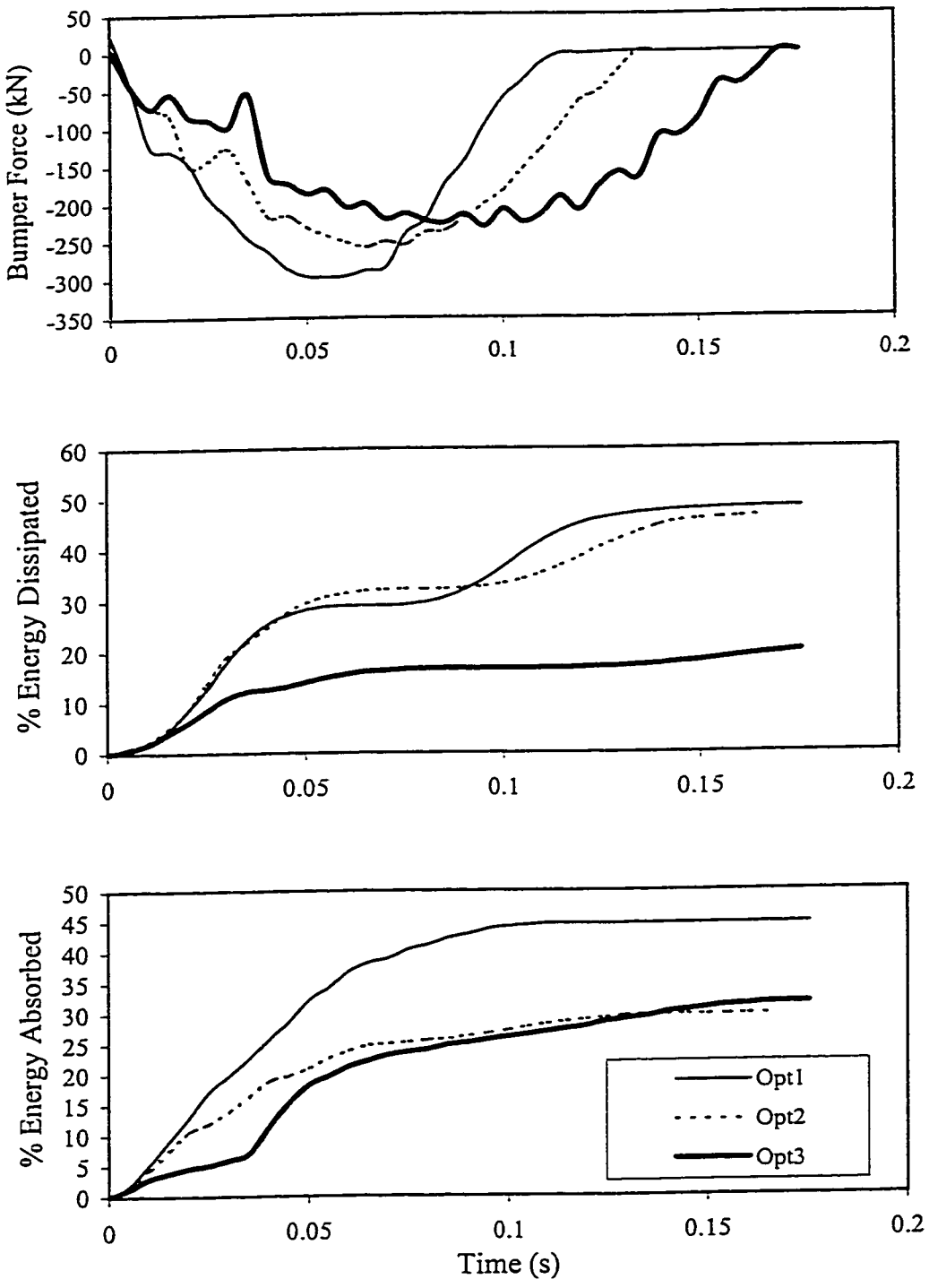

Figure 4.15: Total bumper force, energy absorbed and dissipated obtained by the LP model of the car subject to an impact with optimum damped guard ($v_0 = 50$ *km/h*).

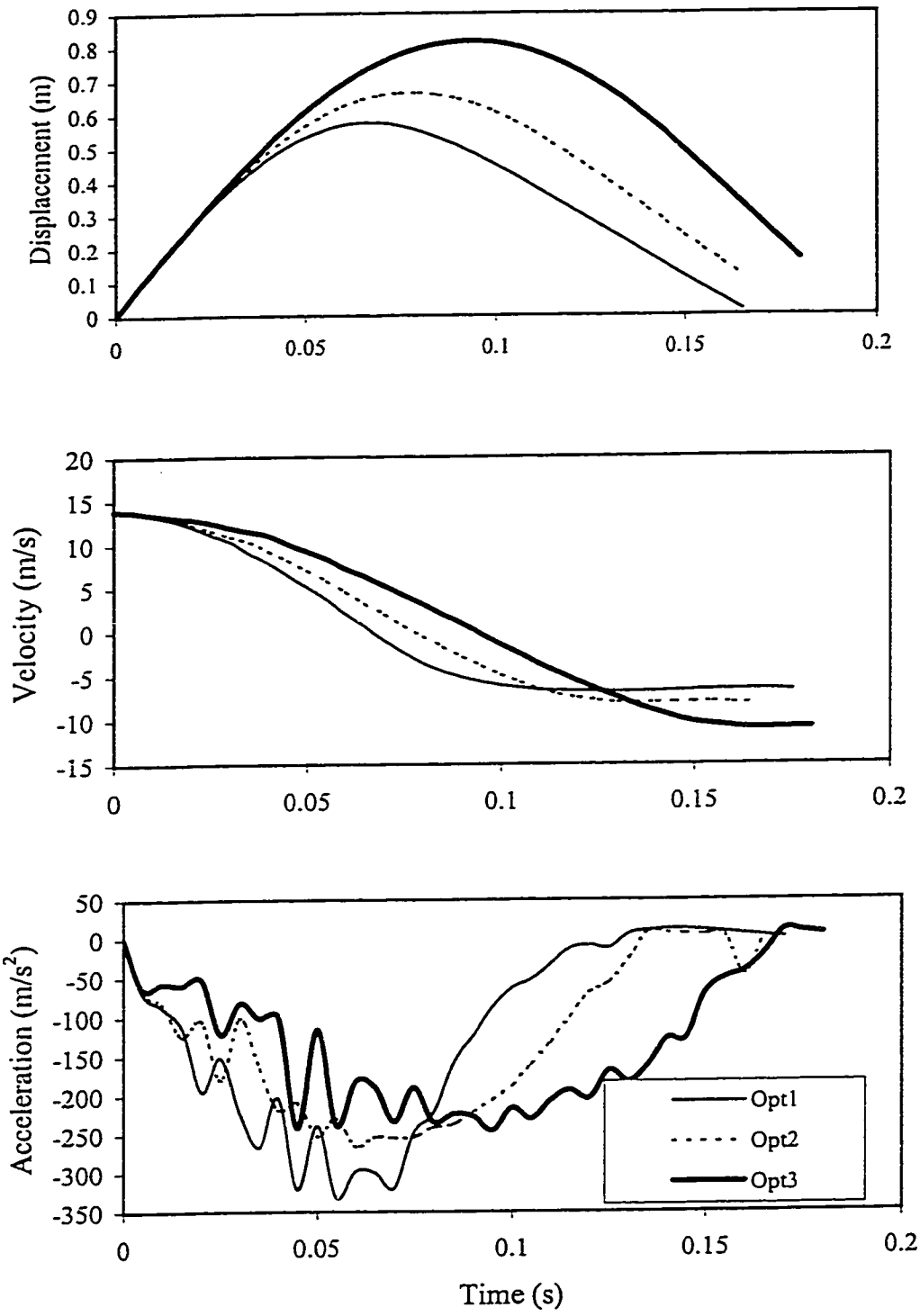

Figure 4.16: Displacement, velocity and acceleration responses of body mass in the LP model of the car subject to an impact with optimum damped guard ($v_0 = 50$ *km/h*).

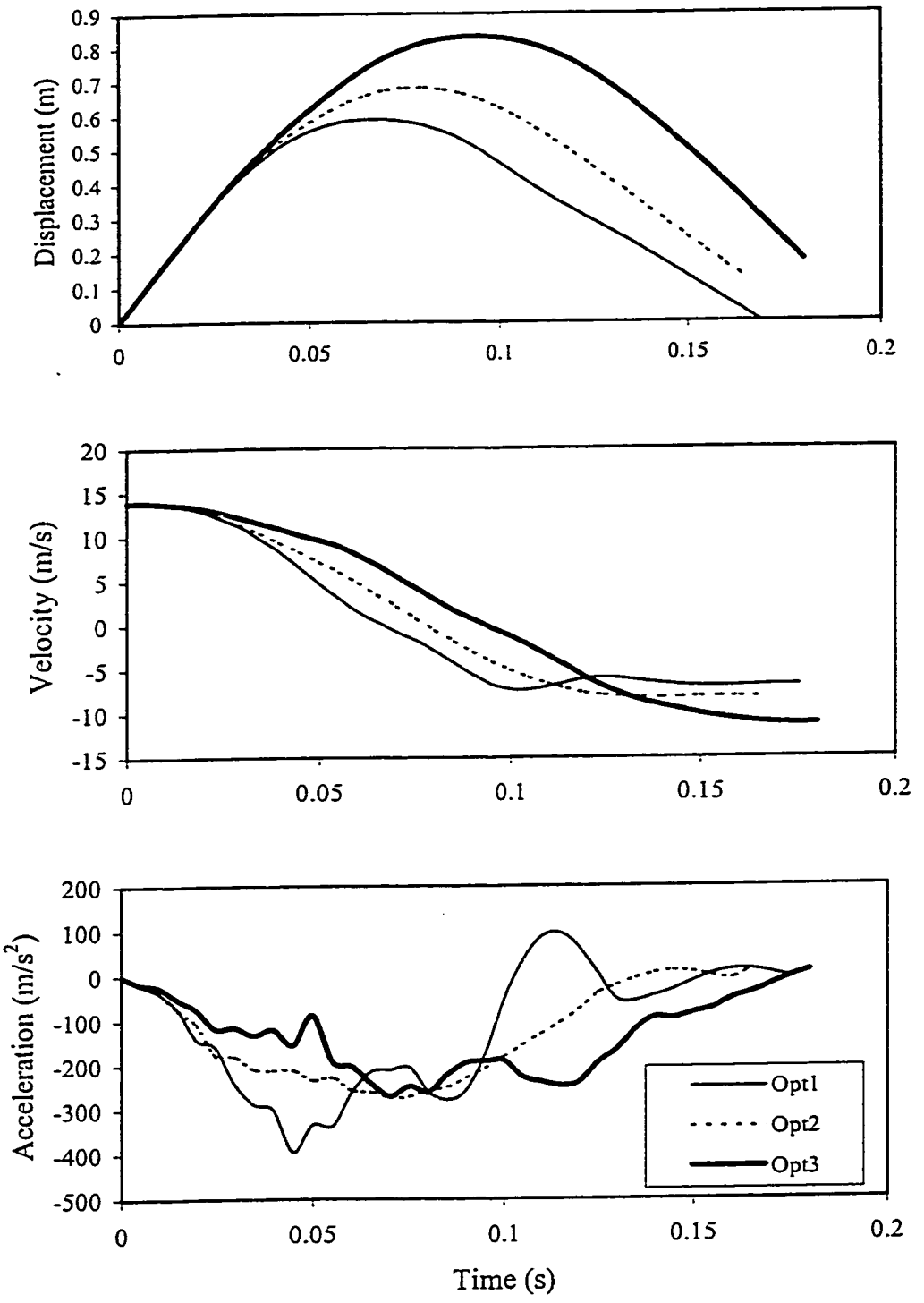

Figure 4.17: Displacement, velocity and acceleration responses of engine mass in the LP model of the car subject to an impact with optimum damped guard (v_0 = 50 *km/h*).

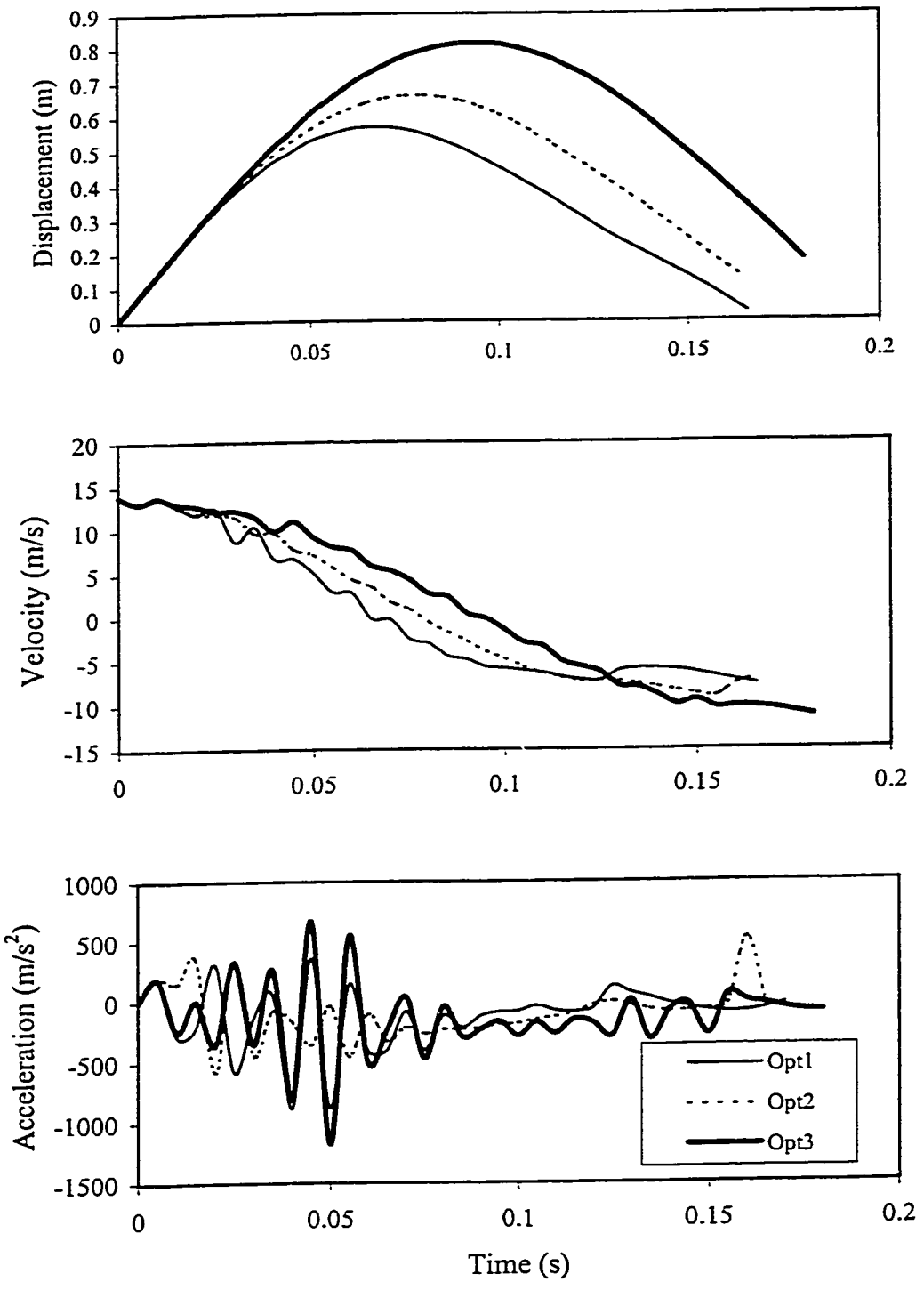

Figure 4.18: Displacement, velocity and acceleration responses of suspension mass in the LP model of the car subject to an impact with optimum damped guard ($v_0 = 50$ *km/h*).

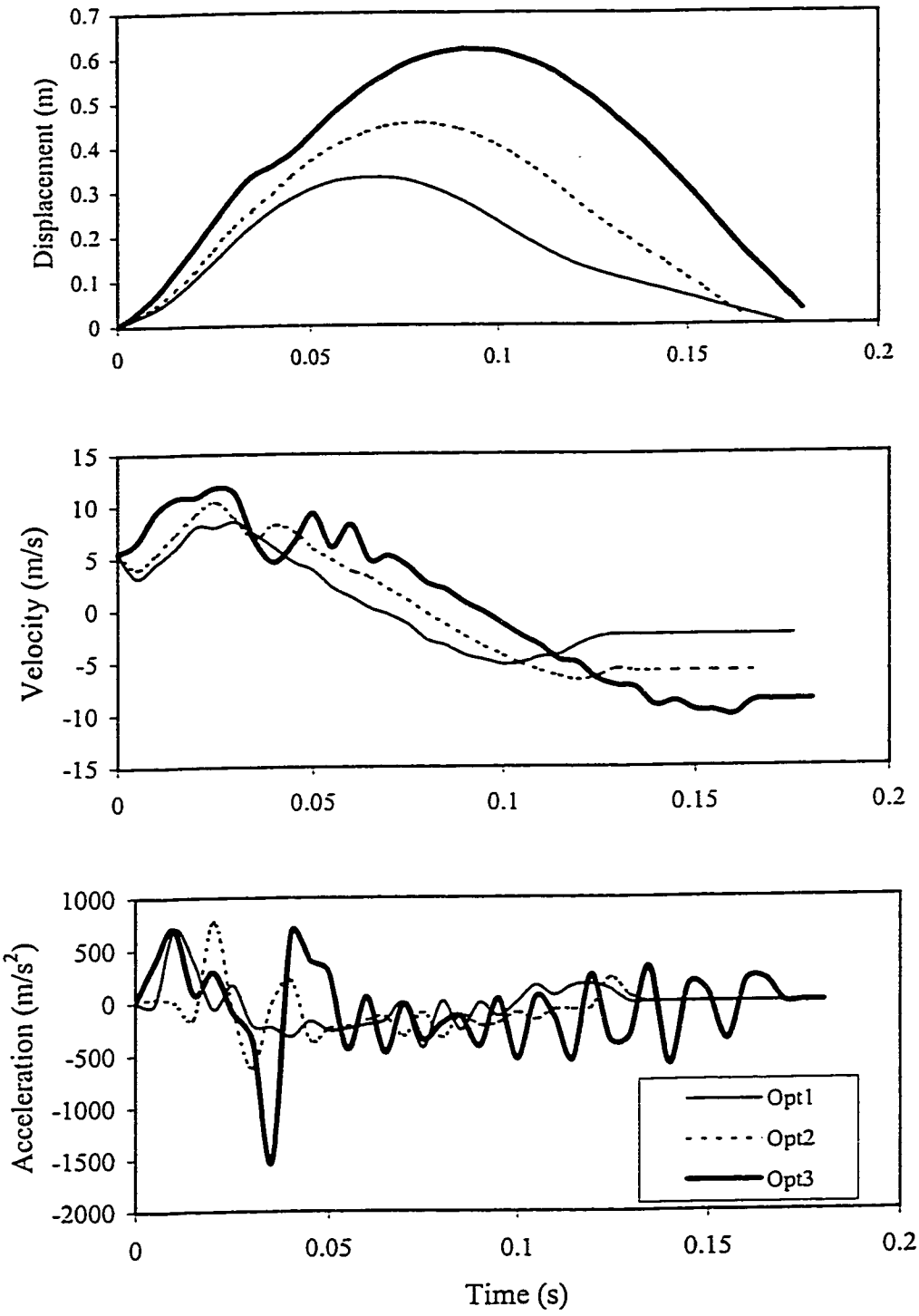

Figure 4.19: Displacement, velocity and acceleration responses of bumper mass in the LP model of the car subject to an impact with optimum damped guard (v_0 = 50 *km/h*).

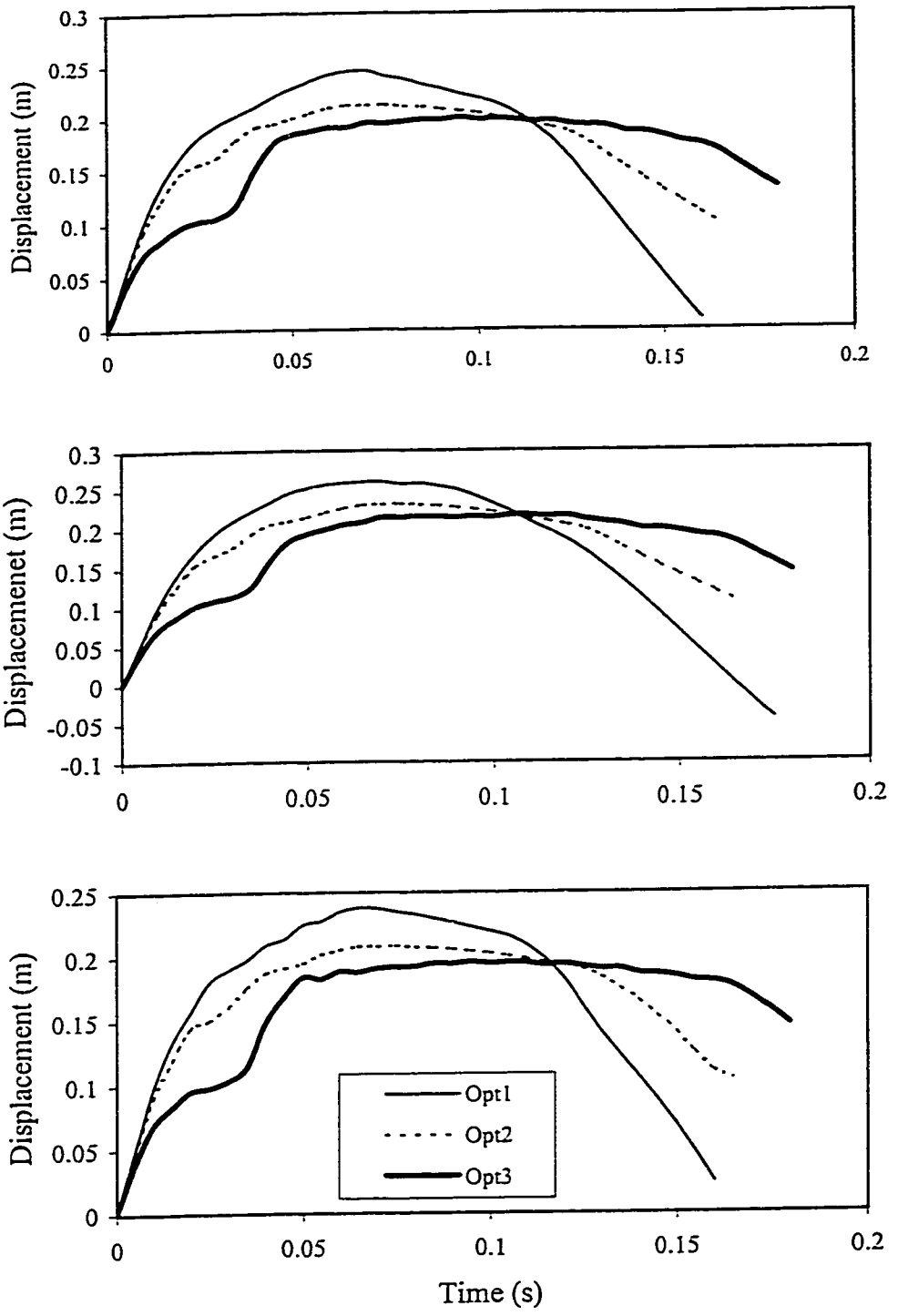

Figure 4.20: Relative displacement responses of body, engine and suspension masses withy respect to the bumper mass in the LP model of the car subject to an impact with optimum damped guard ($v_0 = 50$ *km/h*).

the original position with the Opt1 design, while the designs Opt2 and Opt3 lead to loss of contact prior to approaching the original position. A comparison of peak acceleration levels of the four lumped masses reveals that the car bumper mass experiences highest acceleration, while the car body mass experiences the least. This is attributed the higher inertia of the car body mass. Figure 4.20 illustrates the crush of various structural members in terms of relative deflection between the lumped masses. The results show similar degrees of crush of similar members.

4.6 IMPACT ANALYSIS USING FE MODEL

The car-truck collision analysis is further carried out using the FE model of the car coupled with FE models of both rigid and damped guards. The results of the analysis, presented in terms of the performance measures discussed in Section 4.4, are discussed to illustrate the relative performance potentials of the damped guard.

4.6.1 Conventional Rigid Guard

Finite element analysis of the impact between a modern light weight car and rigid under-ride guard model is performed using DYNA3D for an impact velocity of 50 *km/h*. The car was modeled using beam, shell, and brick elements as discussed earlier, while the under-ride guard mainly consisted of shell elements. The analyses were performed for a duration of 120 *ms,* when the car velocity was observed to approach a nearly constant value. Figure 4.21 illustrates the crushing of the car in a qualitative manner at four different instants during the impact. The figure reveals considerable deformation of the front end

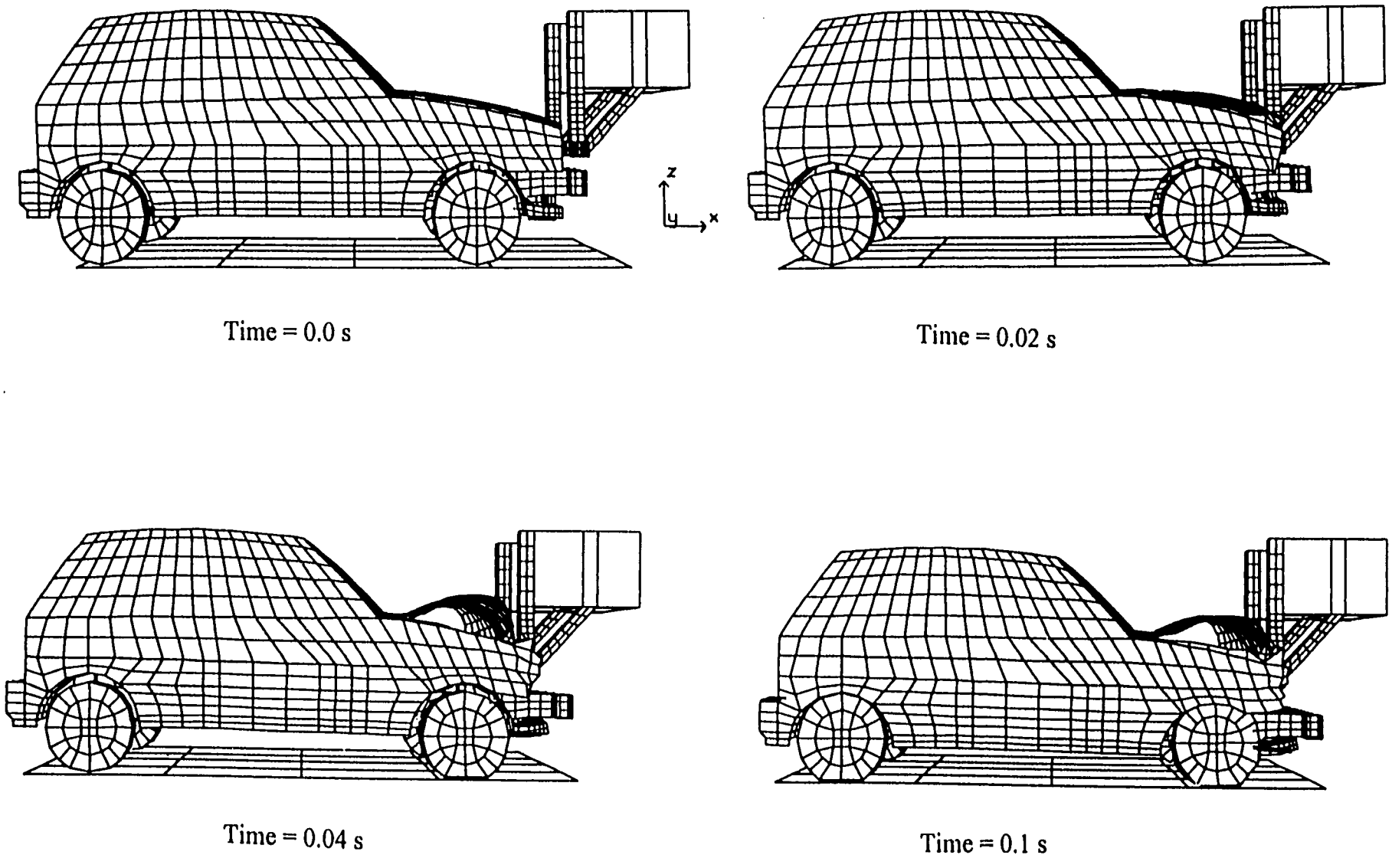

Figure 4.21: Crushing of car structure at different instants during an impact with a rigid under-ride guard ($v_0 = 50$ *km/h*).

of the car impacting the conventional rigid guard. The rear section of the car tends to lift up and nosedive under the rigid under-ride guard. Figure 4.21 further illustrates the structural integrity of the rigid under-ride guard at the end of impact. The results obtained from the DYNA3D analysis are post-processed in TAURUS to yield different performance measures. The kinematics of the vehicle components subject to severe plastic deformations is further studied and the overall energy absorbed by the structural members is computed.

The displacement, velocity and acceleration response characteristics of different components of the car and the rigid under-ride guard along the X-axis during a 50 *km/h* impact are illustrated in Figure 4.22. The results show the response characteristics of sheet metal, car bumper, engine cradle, engine block, under-ride guard bumper and car c.g. block. While different components of the car body experience different magnitudes of displacement, velocity and acceleration, the passenger casualty can be approximately assessed in terms of the kinematics and dynamics of the c.g. block of the car.

The displacement response reveals that the car bumper and the c.g. block experience similar values of peak displacement. It should be noted that the car bumper does not make any contact with under-ride guard due to difference in the ground clearance, while the c.g.-block undergoes displacement due to crushing of various structural elements. The displacement response of car bumper yields the amount of car intrusion under the guard. The peak displacement of the car c.g. is observed to be approximately 0.4 *m* for the selected geometry and properties. While the displacements of

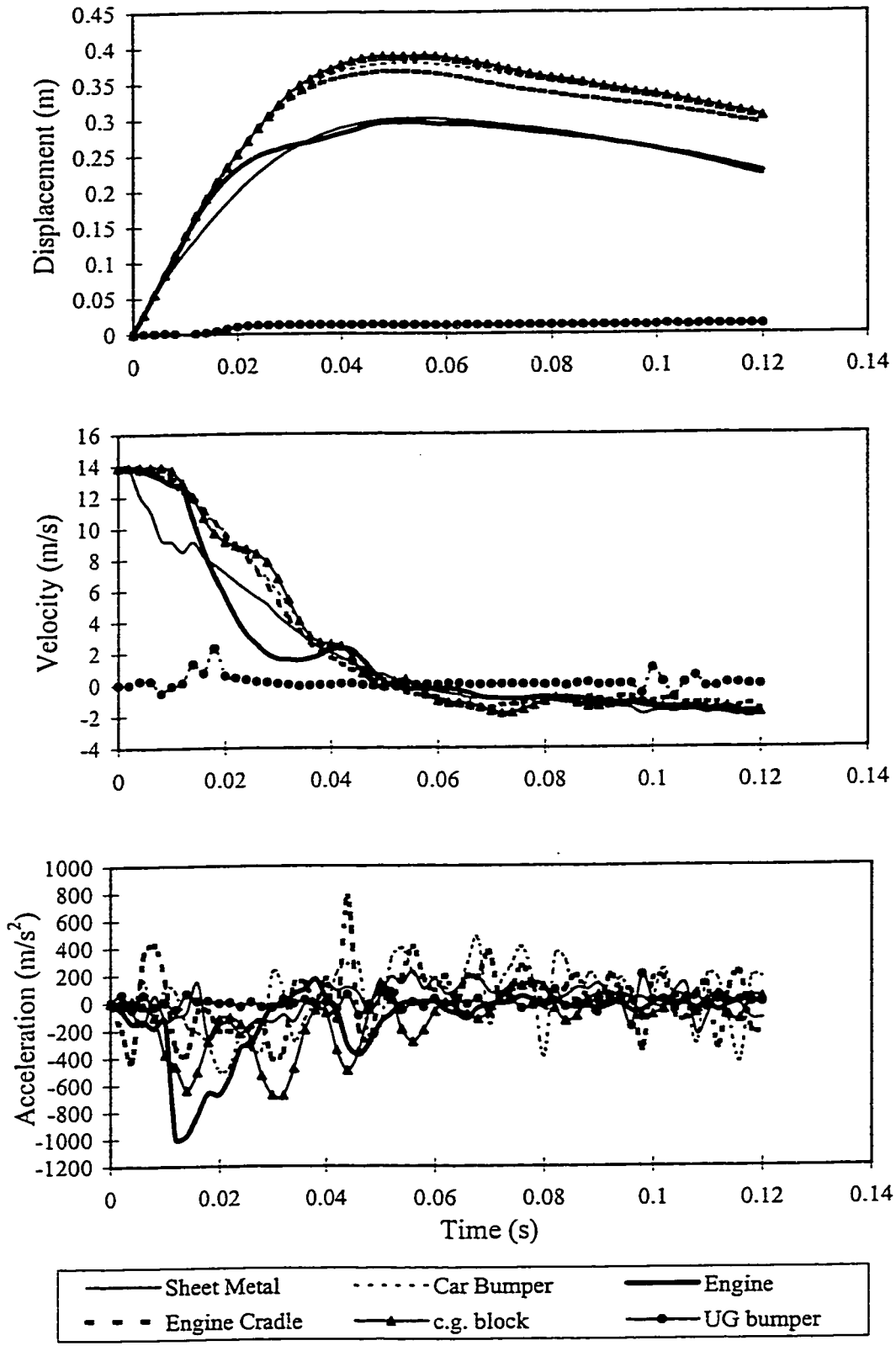

Figure 4.22: Displacement, velocity and acceleration responses of different components of the FE model of car under an impact with a rigid under-ride guard (v_0 = 50 *km/h*).

other components of the car are observed to be less than 0.4 *m*, the rigid under-ride guard experiences only 0.02 *m* peak displacement. The displacement response of the crushable car parts, such as radiator, sheet metal in the Y and Z directions are illustrated in Figure 4.23. The results clearly show that the deflections along these directions are considerably smaller when compared those along X direction. The rigid under-ride guard exhibits negligible displacements along Y and Z axes. The deflections of various structural elements along the Y-axis are also observed to be quite small. The car bumper, engine cradle, engine, c.g. block, and sheet metal components exhibit considerable levels of vertical displacements, which is mostly attributed to the nose diving of the car under the rigid guard. The car bumper is observed to yield a maximum of 18 cm vertical displacement at t = 0.075 *s*.

The longitudinal velocity response characteristics, illustrated in Figure 4.22, reveal that the component velocities approach zero near t = 0.05 s, where the displacement response is observed to be maximum. The vehicle then rebounds due to the transfer of energy stored in the under-ride guard, and most components approach a velocity of approximately –1.8 *m/s* during later stages of the impact. The velocity response of the under-ride guard bumper is observed to be considerably small, and it approaches zero velocity during the later stages of the impact.

The longitudinal acceleration response characteristics reveal that the car c.g. block experiences a peak acceleration of –710 m/s^2, which is considerably higher than the HIC. The engine and its cradle, and the bumper also experience higher values of peak acceleration along the X-axis as shown in figure 4.23.

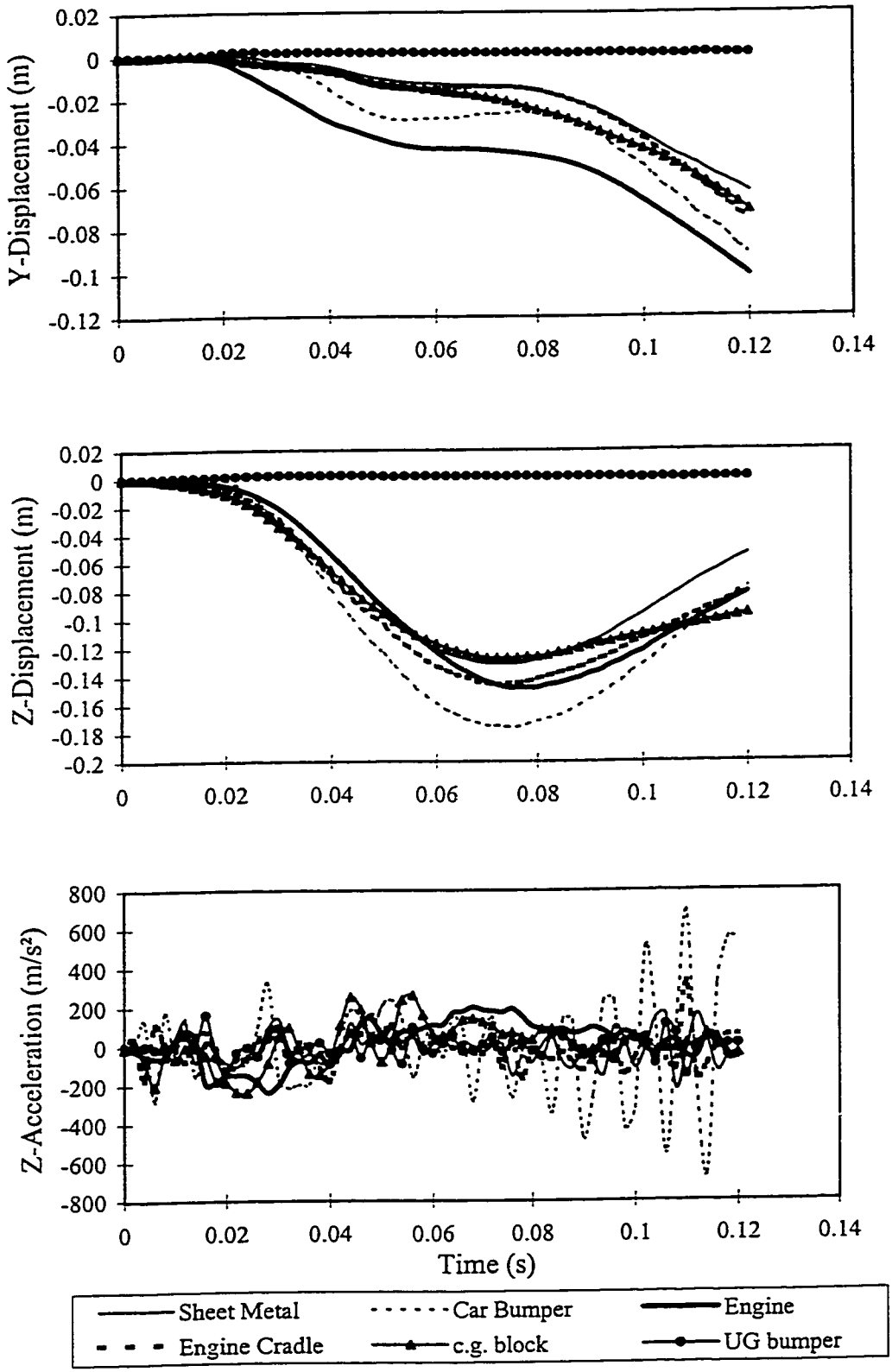

Figure 4.23: Displacement and acceleration responses of different components of the FE model of car along Y and Z axes, under an impact with a rigid under-ride guard ($v_0 = 50$ *km/h*).

4.6.2 FE Analysis of the Damped Guard

Discrete non-linear spring-damper elements are used to model the proposed under-ride guard in DYNA3D. The damping and stiffness properties are selected to yield minimum acceleration at the c.g block. The analyses are performed for three sets of damping coefficients and spring stiffness values that are optimally obtained using the LP model, and presented in Table 4.5. The response characteristics of the car and under-ride guard components are evaluated for the three optimal designs of the under ride guards. The performance measures derived for the three sets of optimal guard parameters are compared with those of impact with a rigid under-ride guard. Figure 4.24 illustrates the crushing of the automobile during impact with the damped under-ride at four different time instances. The results are presented for impact with the 'Opt 2' design of the damped guard (q_1= 0.1 and q_2 = 1.0). A comparison of Figure 4.24 with 4.21, which illustrates the impact of car with a rigid under-ride guard, reveals that the automobile undergoes considerably less deformations when impacted with the proposed under-ride guard. The front tires, hood and the bumpers of the automobile incur severe damage under impact with a rigid under-ride guard, while impact with a damped under-ride guard reveals in minimal damage to these components.

Figure 4.25 illustrates the displacement, velocity and acceleration responses of different components of the car along the X-axis during impact with the damped under-ride guard at a speed of 50 *km/h*. The response characteristics represent the impact behavior for the 'Opt 2' design of the damped guard. The response characteristics of the

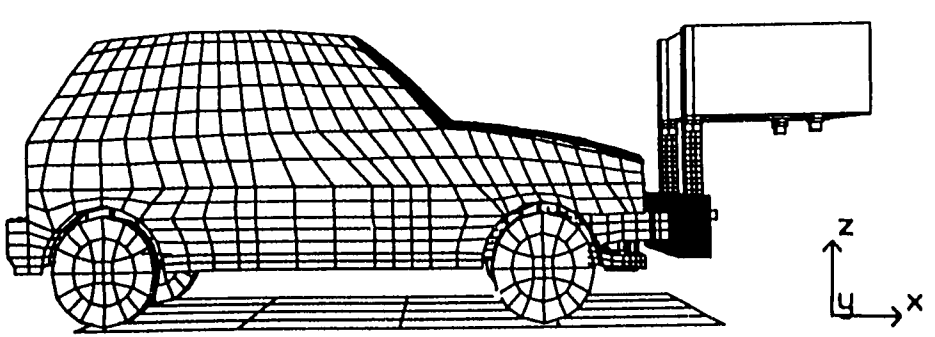

Time = 0.0 s

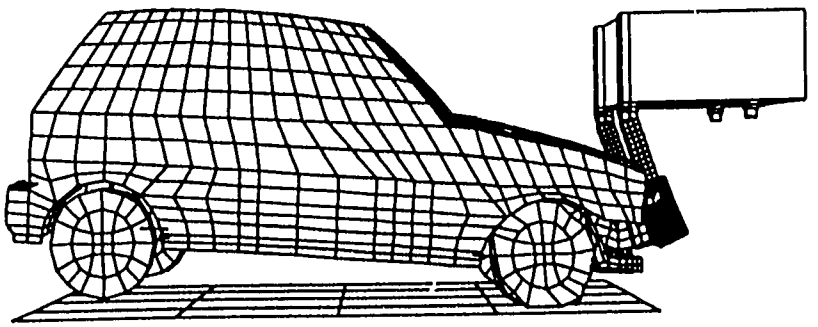

Time = 0.1 s

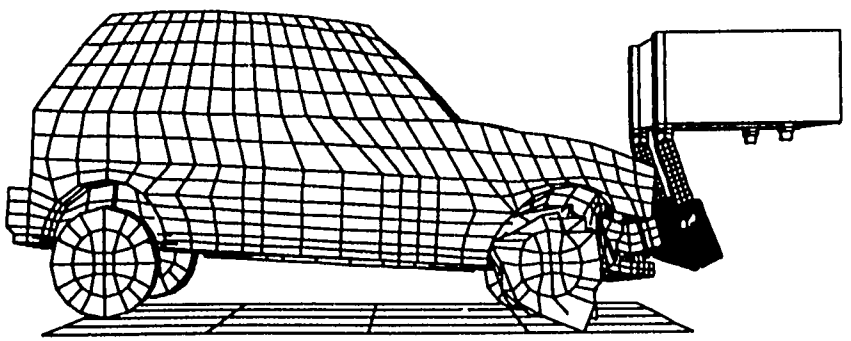

Time = 0.2 s

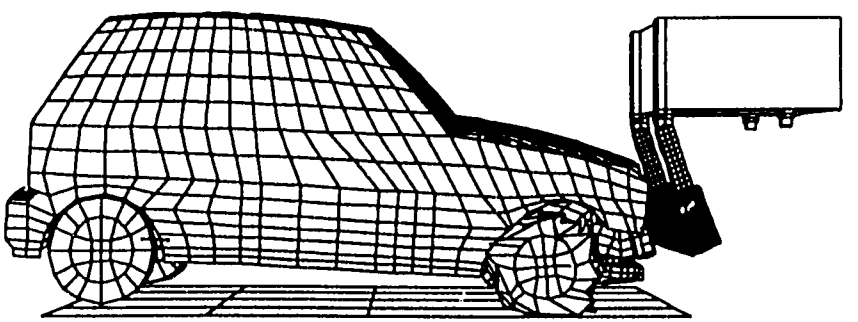

Time = 0.3 s

Figure 4.24: Crushing of car body at different instants during an impact with damped under-ride guard (v_0 = 50 *km/h*)

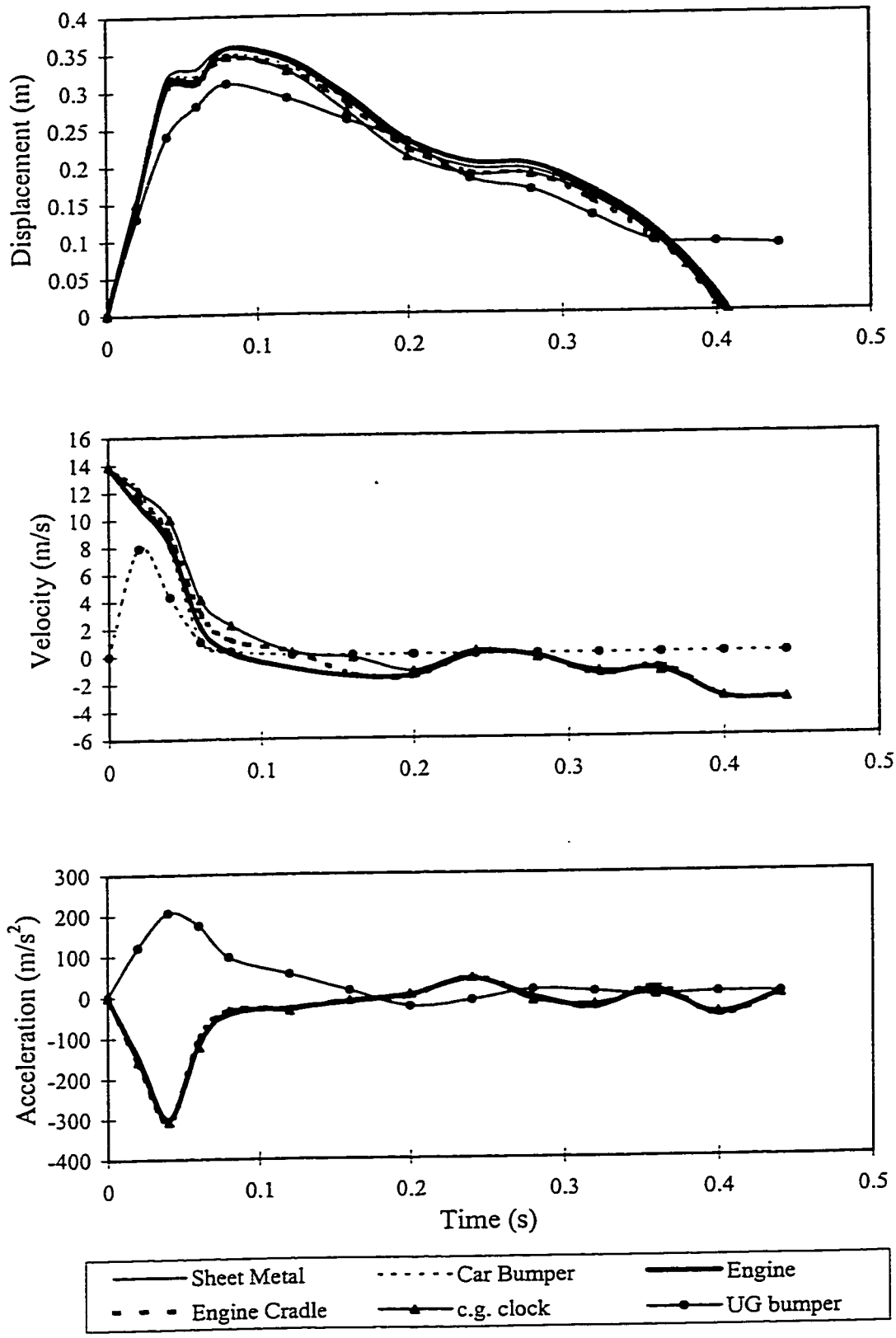

Figure 4.25: Displacement and acceleration responses of different components of the FE model of car along X axis, under an impact with Opt2 design of damped under-ride guard ($v_0 = 50$ *km/h*).

sheet metal, car bumper, engine block, engine cradle, c.g. block and the under-ride guard bumper are plotted for the duration of impact. The displacement response characteristics reveal almost equal magnitudes of displacement of the different selected components, which may be attributed to the minimum damage caused to the vehicle. The c.g. block and other car components are observed to have a peak displacement of 0.36 m at $t = 0.09$ s. The peak displacement of the under-ride guard in the X-direction, however, is limited to 0.31 m. The difference in the peak displacements of the car bumper and the under-ride guard may be attributed to the rotation of the under-ride guard with respect to the hinge. While the car body tends to either travel parallel to the ground or with a slight nose-dive at the front end, the under-ride guard tends to move upwards in the Z-direction due to rotation.

The nose diving of the front end of the car and the displacement of the guard bumper in the positive Z-direction are revealed in the Figure 2.26, which illustrates the response of different components in the Y and Z directions. The displacement response of the car components is observed to be considerably smaller in the Y-direction as compared to that in the X-direction. The vertical displacement response of the under-ride guard bumper beam is close to that observed in the X-direction, which may be attributed to the spring-damper mounting angle with the horizontal I-beam of the truck. The displacement response of the different components of the car further reveals that after the impact the car is pushed back to the mean position by the under-ride guard. In the mean time the car acquires a rebound velocity of –3.35 m/s. The velocity response of the components in the X-direction are observed to be nearly equal for the duration of impact and rebound.

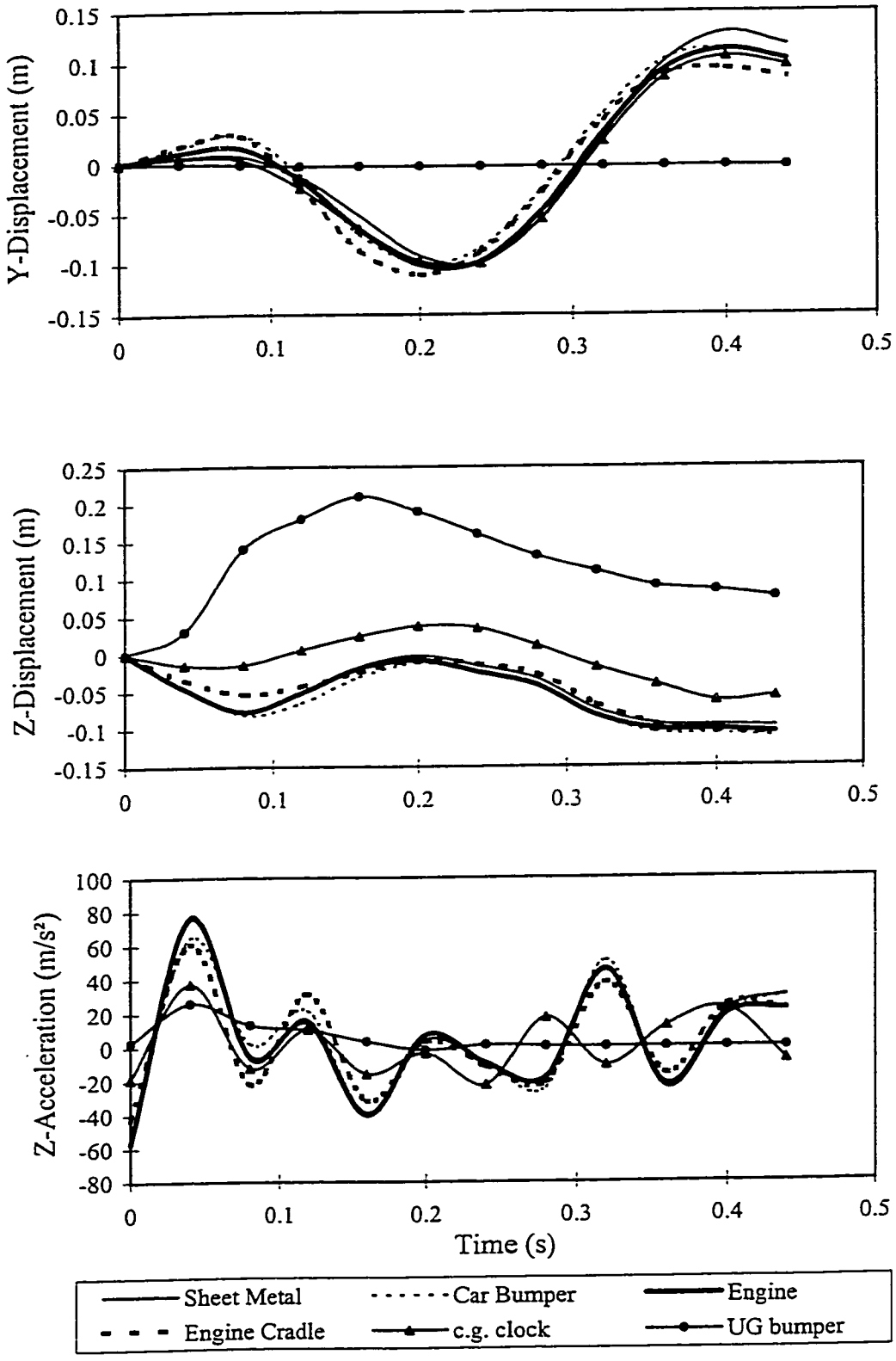

Figure 4.26: Displacement and acceleration responses of different components of the FE model of car along Y and Z axes, under an impact with Opt2 design of damped under-ride guard ($v_0 = 50$ *km/h*).

The displacement response of the car components and the under-ride guard can further be utilized to determine the time at which loss of contact occurs between the two impacting masses. In Figure 4.25, at $t = 0.37\ s$, a cross over between the displacement response of the car components and the under-ride guard can be observed, which is attributed to the loss of contact between the two impacting masses.

The acceleration response of the components in the X-direction reveals that, all the selected components experience nearly equal acceleration variations. A peak acceleration of nearly $-307\ m/s^2$ is observed at $t = 0.05$ s for all the components. The use of damped under-ride guard yields a much lower acceleration level when compared to that of rigid under-ride guard. While an impact between car and rigid under-ride guard resulted in a peak acceleration level of $-710\ m/s^2$ (Figure 4.22), the proposed guard with the optimized parameters, reduced the c.g. acceleration level to $-307\ m/s^2$ (Figure 4.25). The acceleration levels in the Y and Z directions at the c.g. are also observed to be lower than the respective peak levels obtained with the rigid under-ride guard impact.

Table 4.7 further summarizes the performance variables for the rigid and damped under-ride guards obtained using finite element analysis of the car model. The energy dissipated by the under-ride guard damper is evaluated using the relative displacement and velocity of the spring-damper unit with respect to the rigid frame of the truck. The resultant velocity and displacement of the spring-damper unit is obtained by vector addition of the respective quantities along the X and Z directions at each time interval, shown in Figure 4.25. The total energy absorbed by the structural members is obtained directly from the DYNA3D post-processor, which estimates the total internal energy by

summing the energy absorbed by individual components. The energy absorption can also be estimated by subtracting the kinetic energy of the car at the end of the impact event and the energy dissipated by the damper from the total initial kinetic energy. The respective kinetic energies can also be evaluated easily from the velocity responses (Figure 4.25) that can be extracted from the database available by the DYNA3D post-processor.

Table 4.7: Performance Comparison of the Optimized Damped Guard and Rigid Guard using Finite Element Model ($v_0 = 50$ *km/h*).

Performance Variable	Opt 1	Opt 2	Opt 3	Rigid Barrier Guard
Maximum intrusion (*m*)	0.265	0.31	0.49	0.03
Final velocity (*m/s*)	-2.0	-3.35	-4.0	-1.8
Peak acceleration (m/s^2)	-307.0	-301.1	-264.9	-720.0
Normalized dissipated energy (%)	45.0	43.6	17.2	-
Total plastic energy of springs (%)	50.8	44.8	66.2	96.6
Total Energy (%)	95.8	88.4	83.4	96.6

While the damped and rigid guards yield almost equal displacements of the car c.g. (0.36 m), the damped guard yields considerably lower peak acceleration level of the car c.g. Almost entire kinetic energy is converted to plastic energy by different structural members when the guard is made of rigid elements. On the other hand damped guard dissipates up to 45 % of the initial kinetic energy of the car. The remaining energy is absorbed by different structural members by plastic deformation. However, in the case of

damped guard only the front end of the car incurs plastic deformations resulting in relatively lower risk of passenger casualty.

Comparison of performance measures obtained using finite element analysis of automobile impact with under-ride guards with three sets of optimal parameters is further illustrated in Table 4.7. From the table, it can be observed that, a guard with optimal parameter 'Opt 1' yields minimum intrusion (0.265 *m*) and rebound velocity (2.0 *m/s*) as compared to the intrusion (0.49 *m*) and rebound velocities (-4.0 *m/s*) of the guard with optimal parameter 'Opt 3'. The optimal guard with parameters 'Opt 3', however, yields minimum peak acceleration (265 m/s^2) as compared to that obtained by 'Opt 1' (307 m/s^2). The energy absorbed and dissipated during impacts with different sets of optimal and rigid guards are further compared in Table 4.7. The guard with parameters of 'Opt 1' dissipates maximum energy as compared to the 'Opt 2' and 'Opt 3' due to high values of damping coefficients. The total amount of energy dissipated/absorbed is also observed to be lower with the optimal sets, the 'Opt 1' design yielding a maximum total energy of 95.5 %, which is comparable to the energy absorbed by plastic deformation in the case of rigid body impact (96.6%).

4.7 SUMMARY

Lumped parameter and finite element models of the automobile under ride guards are developed to evaluate the relative performance potentials of the damped under-ride guard. The response characteristics of different components of the car and under-ride guard are evaluated under direct impacts with the damped and the rigid under guards at 50 *km/h*.

While a finite element model provides a good estimate of the performance characteristics of the under-ride guard and the crash behavior of the vehicle, the lumped parameter model provides the relative performance analysis in a convenient manner. The lumped parameter model thus offers a good compromise between the complexity, cost and the accuracy. A design optimization study is undertaken to determine optimal guard parameters in order to minimize the weighted function of different performance indices. The results of the studies clearly show that an optimal damped guard can reduce the magnitude of transmitted acceleration, while limiting the peak intrusion to an acceptable level. The damped guard further reduces the deformation of the car structure by dissipating part of the kinetic energy. Composite materials crush elements are further explained in the following chapters in order to enhance the energy absorption capabilities of the automobile.

CHAPTER 5

DEVELOPMENT OF CRUSH ELEMENTS

5.1 INTRODUCTION

The theoretical and experimental studies presented and the results discussed in the previous chapters showed that although proposed damped under-ride guard reduces the magnitude of peak acceleration and the intrusion considerably, the values are still higher than that recommended by the head injury criteria (HIC). Other means of crash energy handling is thus essential to meet the HIC in a car-truck rear-end collision. Further more, an improved front-end crash energy management system for the passenger car would be useful in other crash situations, such as, car-to-car impact.

Vehicle structures are designed to absorb crash energy through plastic deformation of structural components, while maintaining structural integrity of the passenger compartment. The structures of a passenger car, designed for normal service loads, do not exhibit sufficient energy absorbing capacity to dissipate the kinetic energy, developed in a 48 *km/h* frontal barrier crash test as recommended in FMVSS [3] in a controlled manner. The passenger compartment may thus deform considerably posing high risks of fatality and injuries among the occupants. With the current trends of shortening the vehicle front end, the traditional approach to crashworthiness improvement may need to be re-evaluated.

Alternatively, add-on crash energy absorbers (crush elements) can be used in the front end of the car to absorb a considerable portion of the crash energy during an

accident. The energy absorbers are tailored for a specific vehicle mass or energy level such that the total vehicle crush and the passenger compartment deformation would not exceed their respective allowable levels. Additional factors such as the loading direction, packaging functional clearances, service accessibility etc. must also be considered when designing actual energy absorbing devices. It is essential to select devices, which are lightweight and of high specific energy absorption capacity so that they do not add excessive mass to the vehicle. Many metallic and non-metallic energy absorbers have been tried in the past. A brief review of the relevant literature was discussed in Chapter 1.

In the present study, the fabrication and experimental studies for the development of crush elements is discussed in detail. Circular tubes of three different material types, namely, Kevlar/epoxy, graphite/epoxy, and glass/epoxy, tailored to the required size are fabricated in the laboratory. The tubes are tested under static and dynamic loading conditions for the assessment of energy absorption capability at various impact speeds. The results are compared and suggestions for the selection of material type for the energy absorbers are given at the end of the chapter.

5.2 CRUSH ELEMENT ENERGY ABSORBERS

The energy absorption capability of the crush elements depends upon factors such as, its dimensions, shape, material type and the crush force. The composite material crush elements are designed to meet the acceleration level requirements specified by the HIC and its is evaluated in terms of a performance indicators defined below.

5.2.1 Design Considerations

The crush element fixed to the front end of the car is required to absorb as much energy as possible while being crushed in a controlled manner. A catastrophic failure of the energy-absorbing member should be avoided. The peak and average crush forces of the energy absorbing member are limited due to the HIC, since excessive force would result in very high magnitudes of transmitted acceleration at the passenger compartment. Thus materials with very high magnitudes of peak and average crush force should be avoided while selecting the crush elements. While, increasing the cross sectional area and volume of the crush element would result in higher energy absorption, these quantities are limited by the space availability at the front end of the car. Thus the dimensions and the material selection of the energy absorbers are very critical. The following tube dimensions are selected to satisfy the space and HIC requirements for a 1000kg-model car.

- The average crush force may not exceed 30 *kN*
- The maximum length of the composite crush element is limited to 230 *mm*.
- The inner diameter of the tube is selected as 50 *mm*.

With the length and thickness of the tube fixed, the amount of energy depends on the material type and the wall thickness of the tube. These quantities are selected based upon the performance indicators of the composite energy absorbers discussed below.

5.2.2 Performance Indicators

The performance of composite tubes in a crash situation is measured in terms of two quantities, namely, specific sustained crushing stress (SSCS) and specific energy absorption. The specific sustained crushing stress is defined as the sustained crushing

load (average crushing load) divided by the product of the cross sectional area and the density of the material. The specific energy absorption of a composite tube is defined as the energy absorption in Joules per unit volume of the crushed material. Other quantities used for the comparison of performance of the crush elements are the peak and average load to crush the material and the plastic behavior of the tubes under impact load.

5.3 FABRICATION OF COMPOSITE CRUSH ELEMENTS

The required number of composite tubes was fabricated using an AUTOCLAVE. While the graphite/epoxy tubes were fabricated using unidirectional fiber prepegs laid up in $0_2/90_2$ sequence, the glass/epoxy and Kevlar/epoxy tubes were made of 0/90 fabrics impregnated with epoxy. The lay up sequence, number of layers, thickness of each tube and other details of each test samples are listed in Table 5.1.

Different curing cycles were used for different materials. The cure cycle for the Newport NCT-301 graphite/epoxy composite is as follows. The steel mandrel layed-up with 20 layers of graphite/epoxy prepegs, bagged and vacuumed was kept in the autoclave and the temperature of the autoclave was raised to 104°C while the pressure was maintained at 0.34 MPa. The temperature was maintained at 104°C for 15 minutes before raising to 140°C which is the final curing temperature. The graphite composite sample was allowed to cure for 1 hour under 0.34 MPa and 140°C. At the end of curing, the autoclave was allowed to cool down to 65°C under vacuum with the pressure maintained at 0.34 MPa. Once the temperature reached 65°C the pressure and vacuum were released and the

Table 5.1: Design Details of the Composite Tubes.

Material	ID No.	No. Of Layers	Wall thickness (mm)	Lay-up sequence
Kevlar/epoxy	1	10	3.0	0/90 fabric
	2	10	2.4	0/90 fabric
	3	10	2.6	0/90 fabric
Graphite/epoxy	1	12	1.6	$3(0_2/90_2)$
	2	12	1.6	$3(0_2/90_2)$
	3	12	1.6	$3(0_2/90_2)$
Glass/epoxy	1	10	2.00	0/90 fabric
	2	10	1.75	0/90 fabric
	3	10	1.75	0/90 fabric

Table 5.2: Material Properties of the Composite Tubes.

	E_x (GPa)	E_y (GPa)	G_{xy} (GPa)	ν_{xy}	ν_{yx}	σf_{xt} (MPa)	σf_{xc} (MPa)	σf_{yt} (MPa)	σf_{yc} (MPa)	σf_{xy} (MPa)	Specific gravity
Graphite/epoxy	181	10.3	7.17	0.28	0.3	1500	1500	40	246	68	1.541
Kevlar/ epoxy	24	22	21	0.27	0.3	415	152	345	125	42	1.400
Glass/ epoxy	20	20	--	0.26	0.3	310	345	310	345	445	2.100

mandrel was taken out after the autoclave further cools to room temperature.

The cure cycles for the glass/epoxy (CMS532-18, Style 181) and Kevlar/epoxy (CMS532-01, Type 1, and Class-1) were much simpler. The temperature was raised to 125°C once the bagged sample was inside the autoclave and the pressure level was brought to 0.38 MPa. The minimum linear heat-up rate was 0.5/minute with a maximum of 4°C/minute. The samples were allowed to cure for 1.5 hours before starting the cooling cycle. The autoclave is allowed to cool down to 65°C under the pressure at a linear maximum cool rate of 4°C/minute. When the autoclave pressure reached 0.068 MPa the vacuum was vented to atmosphere. The cure cycles for the three materials are illustrated in Figure 5.1.

5.4 ASSESSMENT OF ENERGY ABSORPTION

The energy absorbers developed were tested under static and dynamic loading conditions measuring the crushing force and displacement in real time. While a universal MTS machine with a maximum loading capacity of 100 *kN* was used for loading the tubes under static conditions, the dynamic behavior of the tubes was assessed using a drop weight test machine, designed and built in the laboratory. The measured data were then processed to estimate the energy absorption capacity of the tubes.

5.4.1 Experimental Setup

The force-deflection characteristics of the crush elements were determined under static and dynamic conditions using separate experimental setups and are discussed below.

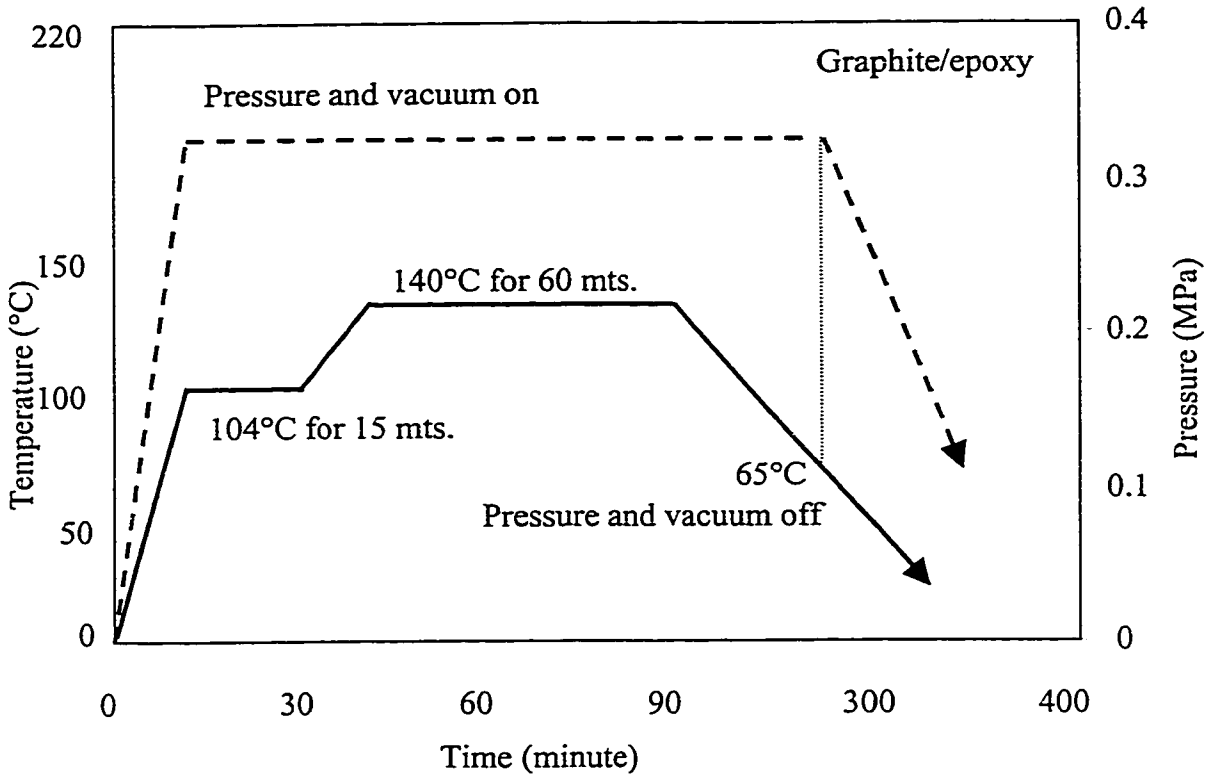

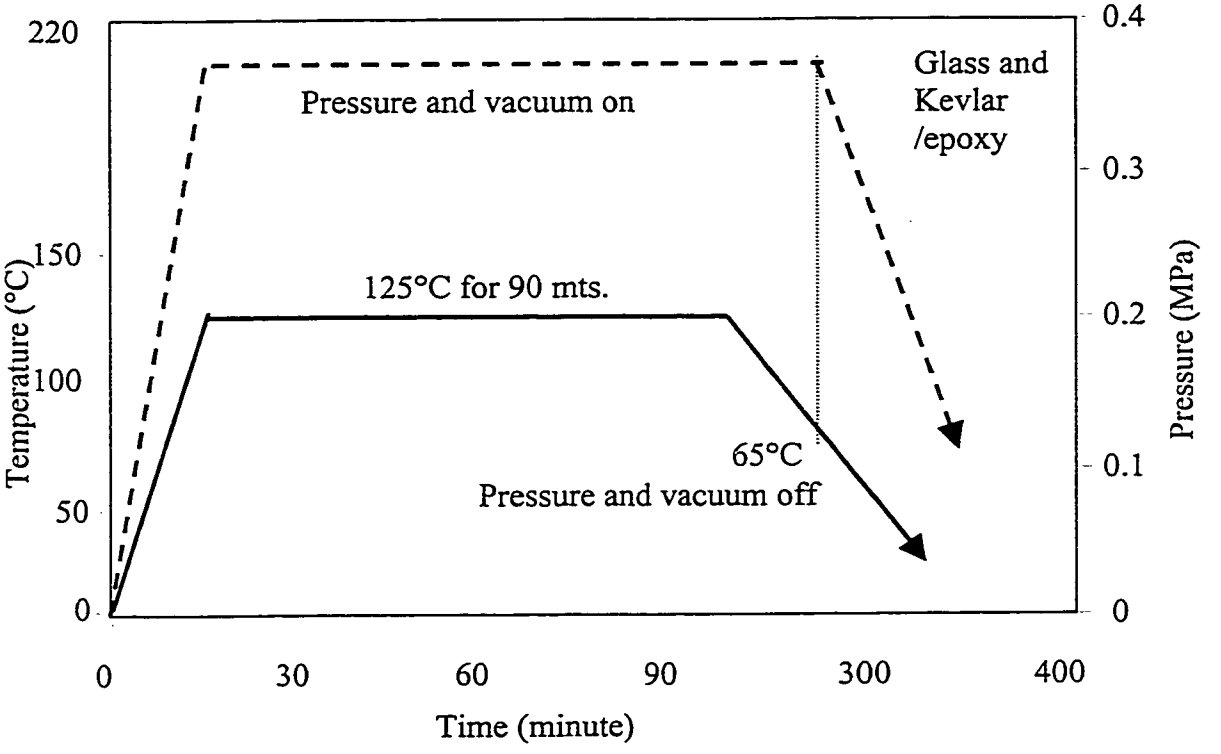

Figure 5.1: The cure cycle for the three materials.

STATIC TEST ON THE CRUSH ELEMENTS

The performance of the energy absorber samples at the static load conditions was obtained by applying quasi-static loads in an MTS machine. A 318 series MTS machine with a maximum capacity of 100 *kN* and flow rate of 0.0833 liters/s was used for the experiment. Since the motion of actuator is controlled by the closed loop control system integrated with the MTS machine, the displacement measurements were readily available. The load acting (static crush force) on the tube was measured using the force transducer that is attached to the MTS machine. The force and displacement data were transferred to the computer for further processing.

IMPACT TEST ON THE CRUSH ELEMENTS

The behavior of the crush elements under the dynamic loading conditions was assessed by conducting impact tests on the test samples using a drop-weight impact test machine developed in the laboratory. The drop-weight machine consisted of a falling mass on two vertical guide rails made of high strength, 25 *mm* diameter steel columns. The steel columns were fixed to a 25 *mm* base plate through cap screws from the bottom. The base plate was provided with leveling screws at four corners. The momentum and hence the impact force could be varied by selecting different drop height (0-3.5 *m*) and falling-mass blocks (15-45 *kg* in steps of 5 *kg*). A 102 *mm* C-channel was provided at the rear-end to support the whole structure as well as the top-plate on to which the guide rails are fixed. The falling mass blocks are held secured together using an eyebolt. The falling mass could be lifted to the required height using a bi-directional air motor and gear-pulley arrangement mounted on the top-plate. A 3.175 *mm* gauge cable connected to the falling

mass through eyebolt was used to lift the falling mass. Latching and releasing mechanisms were added to the set-up along with a locking mechanism for the safety purpose. Dampers were attached to the base plate to stop the falling mass from dropping beyond the required crush distance to protect the measuring instrumentation. A 100 *kN* capacity load cell was attached to the base plate and the test piece holding arrangement was connected to the load cell through studs. The schematic and photograph of drop weight test machine are respectively illustrated in Figure 5.2 and 5.3.

The crush force was measured using the calibrated load cell. The displacement of the falling mass during the crush process was measured using two different methods. In the first method, a cadmium sulfide photo detector attached to the falling mass was used as the motion detector with halogen-quartz light source. The light source was kept independent of the test machine to prevent the dynamics of impact affecting the intensity of light source due to directional changes since the motion-detector is very sensitive to the variation in the intensity. In the second method, a linear motion position transducer (by Longfellow) was attached to the falling mass. The core of the transducer was allowed to move along with the falling mass and hence used as a displacement sensor.

5.5 RESPONSE CHARACTERISTICS OF THE CRUSH ELEMENTS

The response characteristics of the different crush elements are studied using the performance indicators defined in Section 5.2. The force-deflection response of the composite tubes obtained from the static and dynamic tests on different crush elements are processed to obtain the performance criteria values.

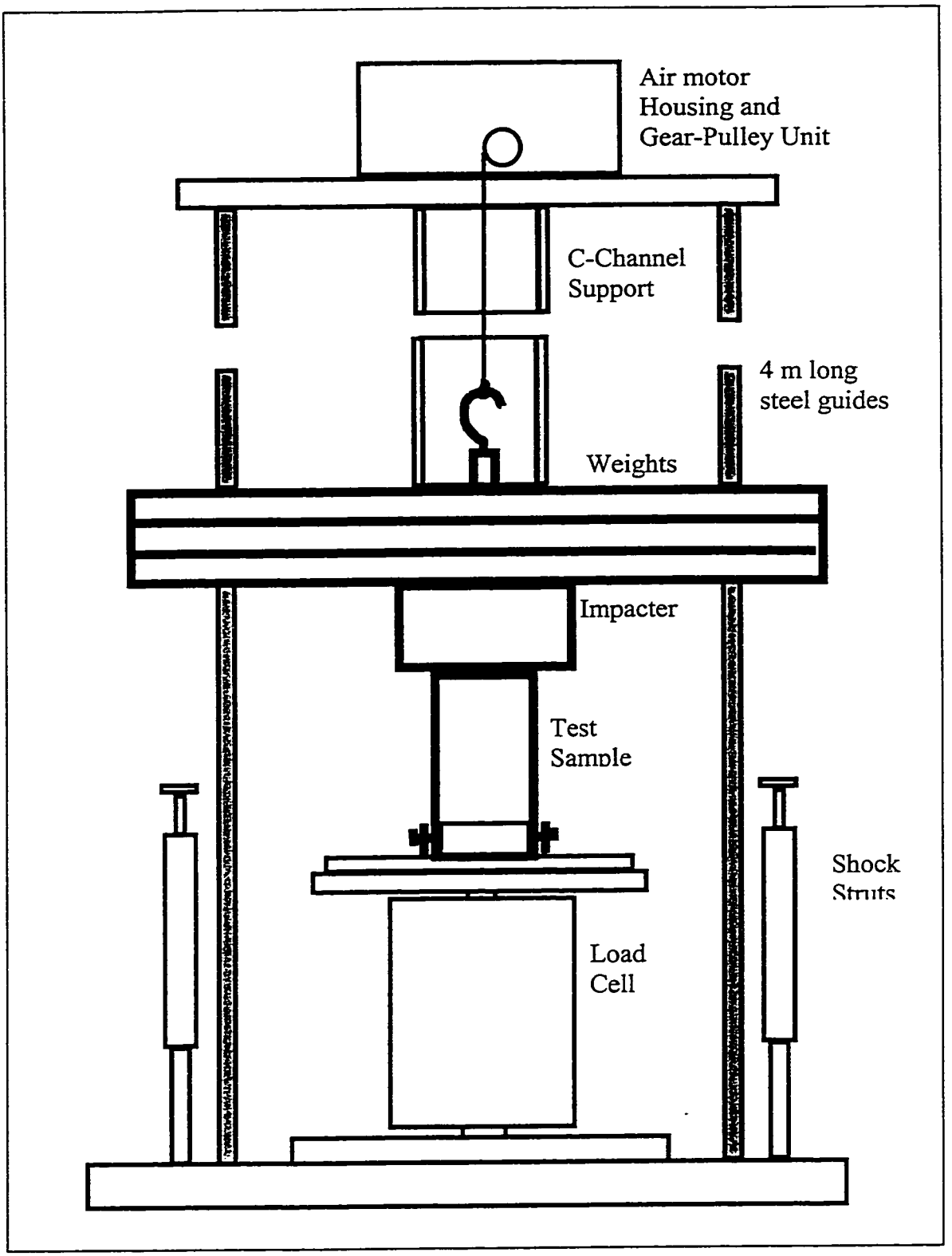

Figure 5.2: Schematic of the drop weight impact test machine.

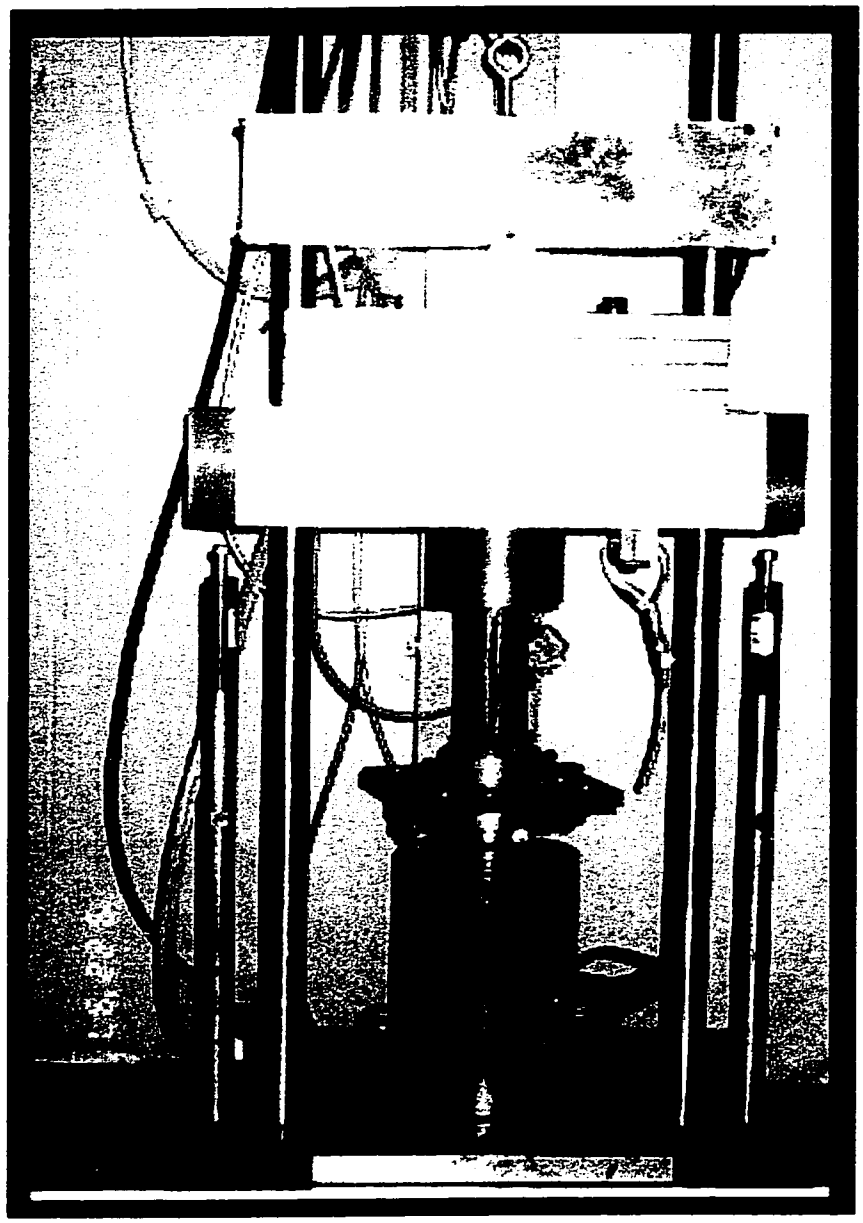

Figure 5.3: Photograph of the drop weight test setup.

5.5.1 Force Deflection Characteristics

The force-deflection characteristics of the glass/epoxy, graphite/epoxy and Kevlar/epoxy tubes under static (4 mm/minute) and impact (v_0 = 6.26 *m/s*) loads are illustrated in Figures 5.4 and 5.5, respectively. The peak and average crushing loads for the three types of tubes are observed to be varying over a wide range. While a direct comparison of the peak and average loads is not possible owing to the different tube thickness, the performance of each tube can be compared using the indicators defined earlier. The force-deflection characteristics illustrated in Figure 5.4 reveal the general crushing trend for the three types of tubes. It can be observed that, for both glass/epoxy and graphite/epoxy tubes the peak load is much larger than the average load, whereas the Kevlar/epoxy tube does not reveal a distinguished peak load. The peak load identifies the initial failure of the tube. From the figures, it can be noticed that graphite/epoxy tube loses its load carrying capacity tremendously (average load is 29% of the peak load) after the failure initiation. While the reduction in load carrying capacity is almost 50% in the case of glass/epoxy tube, the Kevlar/epoxy tube maintains the same load carrying capacity through out the crush length.

The discrepancy in the reduction of load carrying capacity, after the failure initiation, in the above three types of tubes is due to the difference in material characteristics. Brittleness and the unidirectional tube lay-up are the reasons that contribute to considerable reduction in load carrying capacity of the graphite/epoxy tube, once the failure is initiated. On the other hand, Kevlar fibers are more ductile and the tubes are made of fabric type of fibers and these can be used to explain why the load

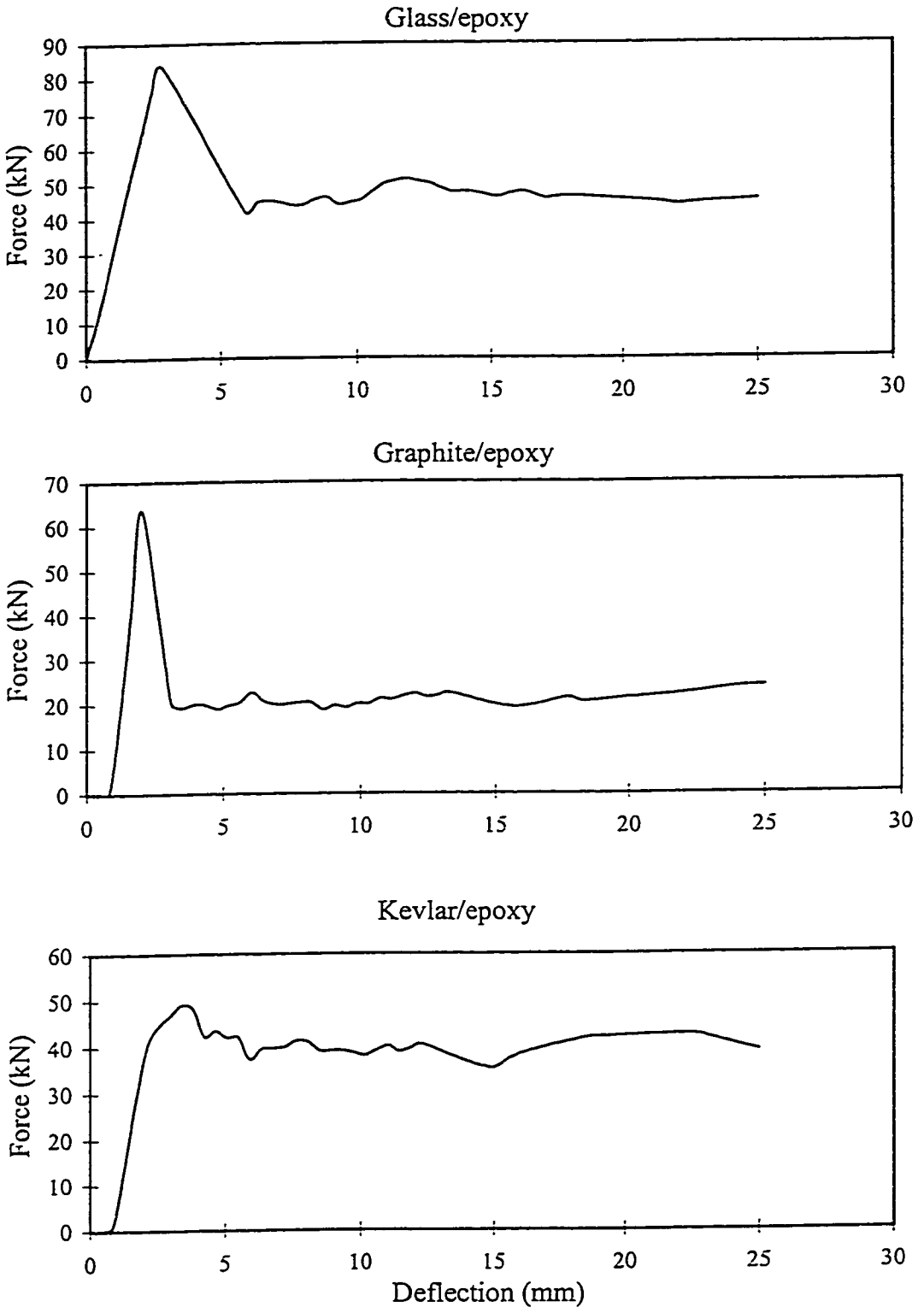

Figure 5.4: The static force-deflection characteristics of the crush tubes.

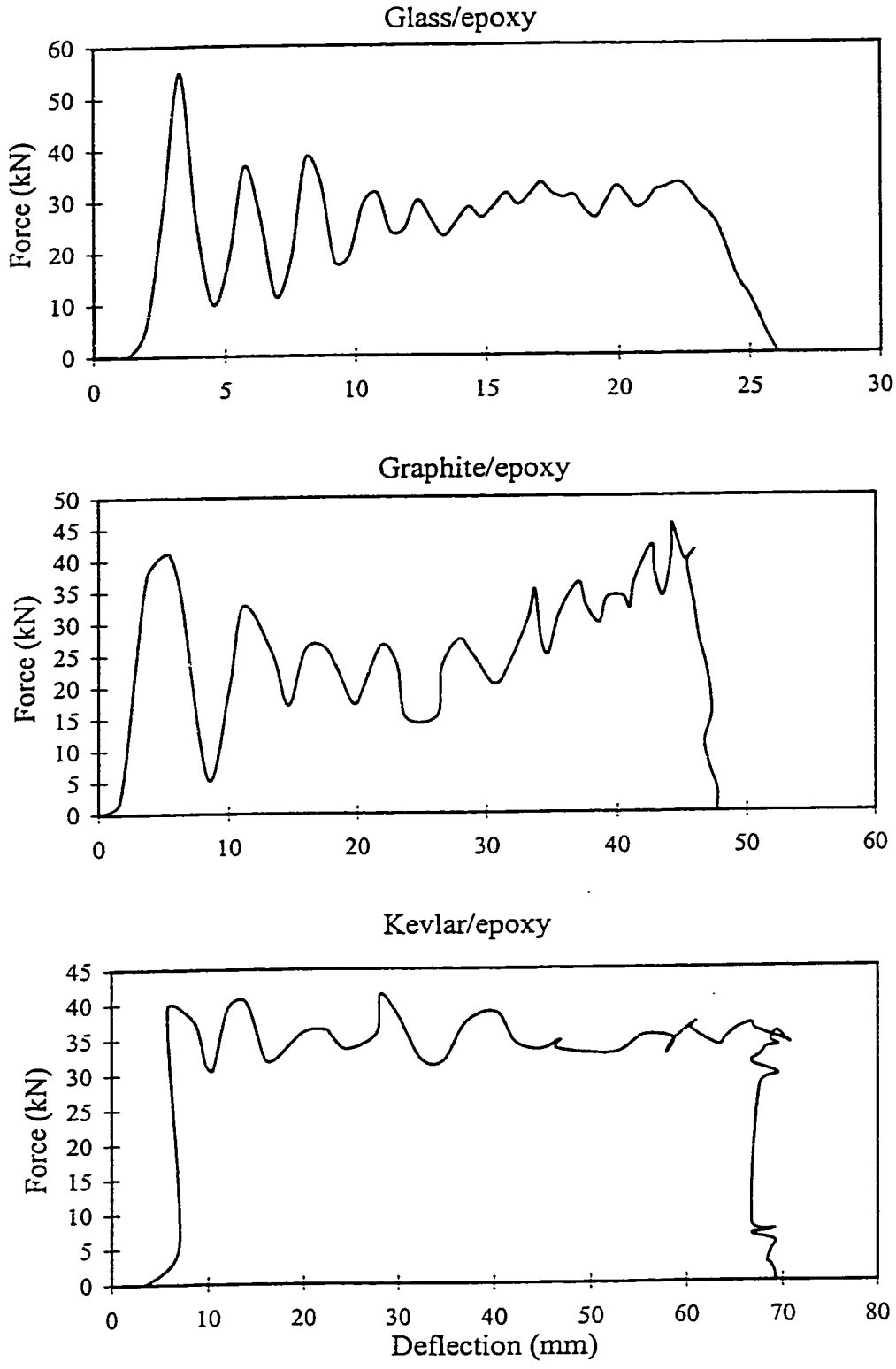

Figure 5.5: The dynamic force-deflection characteristics of the crush tubes ($v_0 = 6.26$ *m/s*).

carrying capacity remains almost at the same level after the failure initiation. A discussion on the macroscopic and microscopic failure observations is given in detail in Section. 5.6.

The load-deflection curves of the three tubes under impact load are observed to be quite different from that under static load, except for the initial stage. While the glass and graphite/epoxy tubes revealed a peak load at the beginning of the impact, Kevlar tube experienced similar load through out the impact. All the three tubes, however, revealed increased amount of waviness under impact load as compared to those obtained under static load. While the glass/epoxy tube crushed through 26 mm, the crush distance for graphite/epoxy and Kevlar/epoxy tubes are observed to be 48 mm and 70 mm, respectively. The increased crush distance in the case of Kevlar/epoxy tube may be attributed to its ductile nature.

5.5.2 Energy Absorption Characteristics of the Crush Elements

The force-deflection characteristics of each crush elements under static and dynamic loading conditions obtained from the experiments are used to assess the energy absorption behavior the crush elements. The average crush force, amount of energy absorbed, SSCS and the specific energy for the three tubes under static loading condition are evaluated as described in Section 5.2.2 and are illustrated in Table 5.3. It can be observed that the SSCS is least for the graphite/epoxy tube and maximum for Kevlar/epoxy tube. On the other hand, glass/epoxy has the highest specific energy, while Kevlar/epoxy is observed to have the least.

The energy absorption data for the three types of tubes, under dynamic load conditions are illustrated in Table 5.4. The dynamic load was generated by dropping 35 kg of mass from a height of 2 *m* in the drop weight impact-testing machine. Neglecting friction in the guides of the falling mass, the impact velocity can be calculated as 6.26 *m/s*. The tests were also conducted at different impact speeds, but since the measured data were considered invalid, the results for those cases have been omitted. While a 1 *m* drop had failed to crush the tubes, in the case of 3 *m* height drop, the falling mass bounced after the impact, thus resulting in invalid displacement measurement.

Table 5.3: Energy absorption Characteristics of the three tubes obtained from static test.

Material	Crush Distance (mm)	Average Crush Force (N)	Energy Absorbed (J)	SSCS $x10^3$(J/kg)	Specific Energy $x10^6$ (J/m^3)
Graphite/epoxy	31	20147	693	102.5	175.2
Glass/epoxy	33	46285	1538	108.0	228.5
Kevlar/epoxy	30	39100	1148	115.1	157.7

Table 5.4: Energy absorption Characteristics of the three tubes obtained from impact test ($h = 2$ *m*, $v = 6.26$ *m/s*).

Material	Crush Distance (mm)	Average Crush Force (N)	Energy Absorbed (J)	SSCS $x10^3$(J/kg)	Specific Energy $x10^6$ (J/m^3)
Graphite/epoxy	44	29487	1209	152.6	215.3
Glass/epoxy	38	26266	1295	89.4	243.8
Kevlar/epoxy	71	34691	2843	118.3	191.1

Under dynamic loading conditions, the energy absorption behavior of the three materials is observed to be different from the static case. Hence the effect of strain rate is

different for the three materials. The force-deflection curves for the three types of tubes under impact load are illustrated in Figure 5.5. The dynamic conditions tend to increase the average load carrying capacity of the graphite/epoxy tube as compared to the static case, with the lay-up sequence selected in this study. The higher load carrying capacity in turn increases the SSCS of the graphite tube as observed from the Table 5.3. It can be observed that the Kevlar/epoxy tube shows a slight increase in the energy absorption capacity under dynamic load. An explanation for the discrepancy in the amount of energy absorbed by different tubes is attempted under the section on macroscopic crushing modes and microscopic observations.

5.6 FAILURE MODES OF THE CRUSH ELEMENTS

The discrepancy in the energy absorption characteristics of the three types of crush elements under static and dynamic loading conditions, discussed earlier may be attributed to the failure mechanisms involved in each tube. Attempt is made to explain the discrepancy observed in the measured energy absorption properties of the crush elements. The mechanism involved in the failure of each tube may be explained well by discussing the macroscopic and microscopic observations that are explained below.

5.6.2 Macroscopic Observations

Figures 5.6 to 5.8 respectively illustrate photographs of crushed tubes under static and dynamic loads. Many differences can be observed in crushing pattern of the three tubes under static and dynamic loading conditions. The crushing pattern was both function of

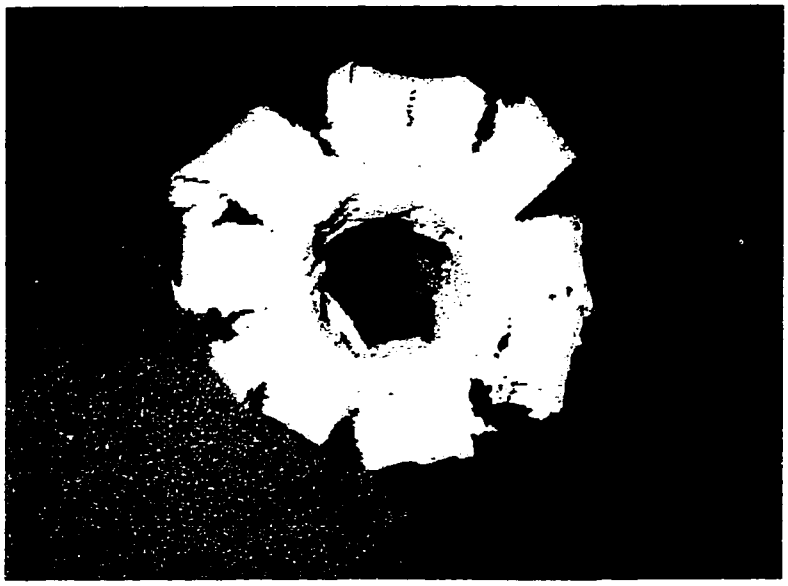

(a)

(b)

Figure 5.6: Crushed glass/epoxy tubes (a) static and (b) dynamic loads.

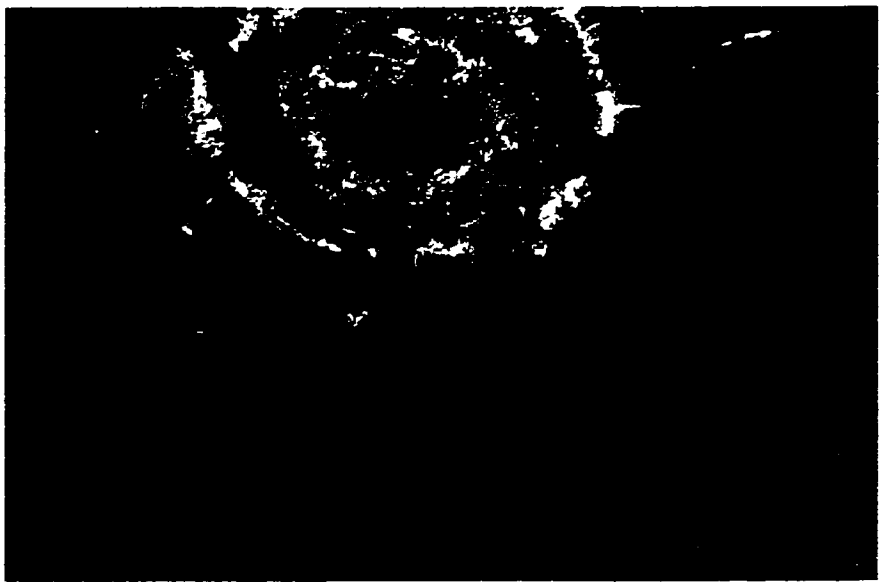

(a)

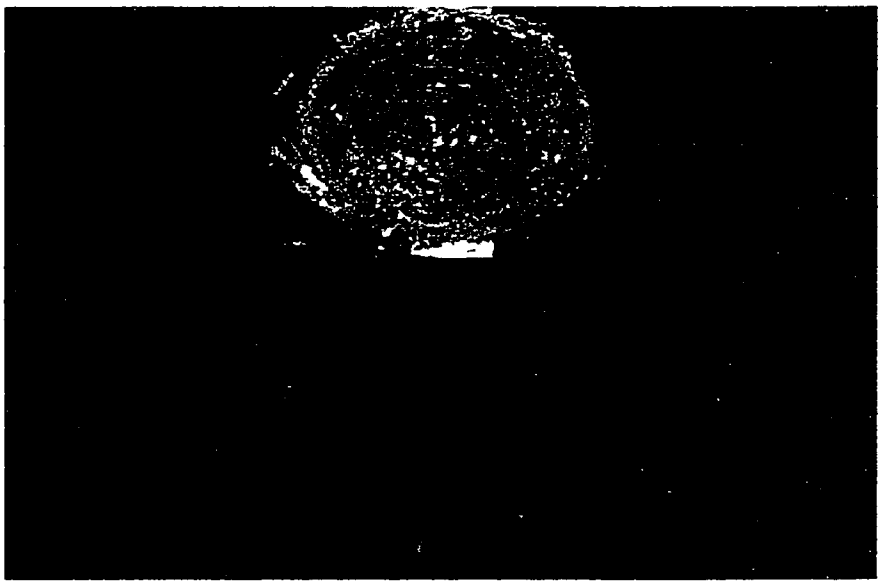

(b)

Figure 5.7: Crushed Graphite/epoxy tubes under (a) static and (b) dynamic loads.

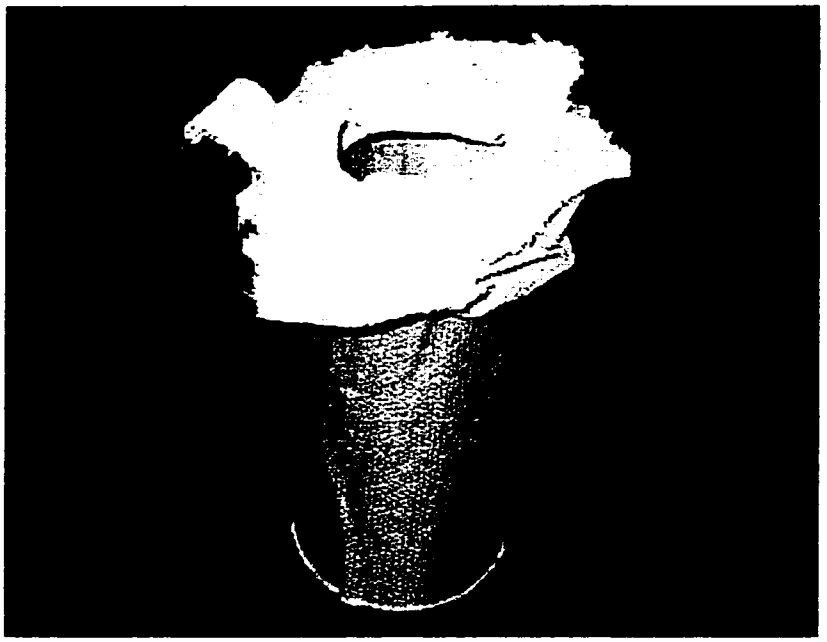

(a)

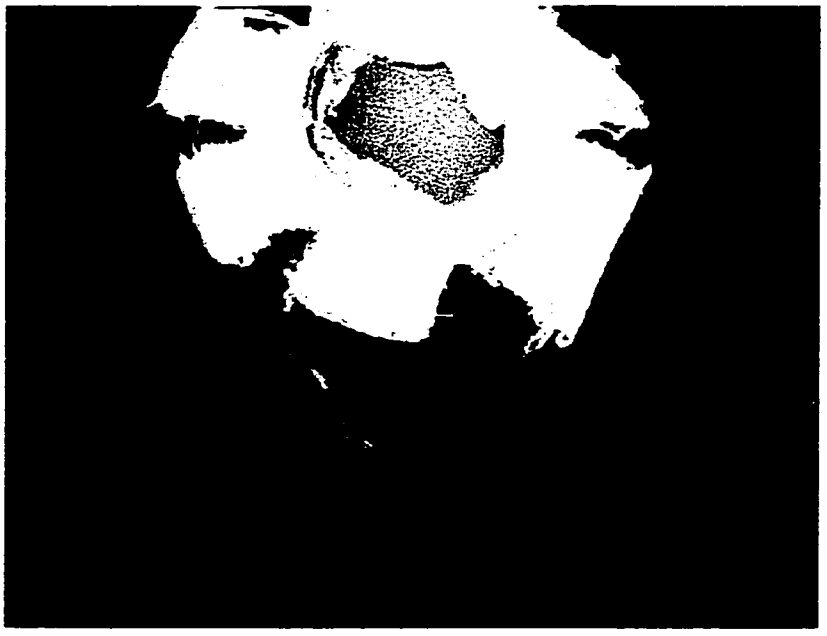

(b)

Figure 5.8: Crushed Kevlar/epoxy tubes under (a) static and (b) dynamic loads.

the type of load and the material. The basic crushing action observed in the case of glass/epoxy tube, was formation of an angular wedge between the layers and bending of layers inward and outward. In both static and dynamic crushing, the inward and outward fronds (flower petal nature-here onwards referred to as fronds) were split into several strips owing to the curvature of the tube. Large delaminations were apparent on both outward and inward fronds, however, the layers were still intact. The splitting of fronds also involves fiber breakage and pullout in the hoop direction of the tube. While the outward fronds looked to be same in both static and dynamic crushing, the formation of inward fronds varied with the type of loading. The inward fronds were uniform and completely bent inward under static load, probably due to the time factor. On the other hand, under dynamic load the crushing process does not have enough time for the formation of a uniform inward frond and the splits are observed to be randomly oriented. This probably shows that under dynamic conditions the tubes were more brittle and hence have lower energy absorption capacity. Further, resin powders could be seen all around the crushed site for the dynamically crushed glass tubes.

A statically crushed graphite/epoxy tube showed the formation of inward and outward fronds. However, the fronds were not strong and split into many parts. The fronds longer than certain length appeared to be broken owing to the brittle nature of the graphite fibers. Delamination and fiber breakage are the other modes of failure observed under static load conditions. Complete local crushing involving delamination, splitting, fiber breakage occurred when the graphite tube was crushed dynamically as seen in Figure 5.7. Interestingly, there were not any outward fronds formed and the more breakage of the inward fronds were observed to form a cover for the tube. Larger

quantities of resin and fiber powders were observed around the crushed site inferring a complete crushing of outward bent layers to form powders. The increase in the total energy absorbed by the graphite tube under dynamic load is probably due to the complete breakage as explained above.

Unlike glass and graphite tubes, Kevlar/epoxy tube crushed under static load did not form inward fronds, but outward fronds exist. The major failure mechanism responsible for the failure of Kevlar tube is local buckling. Under continued crushing (load) the buckled part of the tube seemed to be spread outward and finally splitting into three or four splits once the hoop stress exceeds the strength of the fibers in the hoop direction. The failure mechanism under dynamic load was similar to static load, however with the formation of more number of splits. The main failure mechanism once again was observed to be local buckling. The slight increase in the amount of energy absorption in the case of dynamically crushed tube can be attributed to the formation of more number of splits.

5.6.2 Microscopic Observations

Both statically and dynamically loaded tubes of the three types discussed in this study crushed from one end of the tube while the other end appeared to be undamaged. In order to assess the extent of damage, the crushed tubes were sectioned at different depths from the crushed end. No damages were apparent on these sections to the bare eyes. The sectioned surfaces were polished on a grinding wheel with sandpaper of different grit sizes (200, 400 and 600) to observe any micro failures. Figures 5.9 to 5.15 show

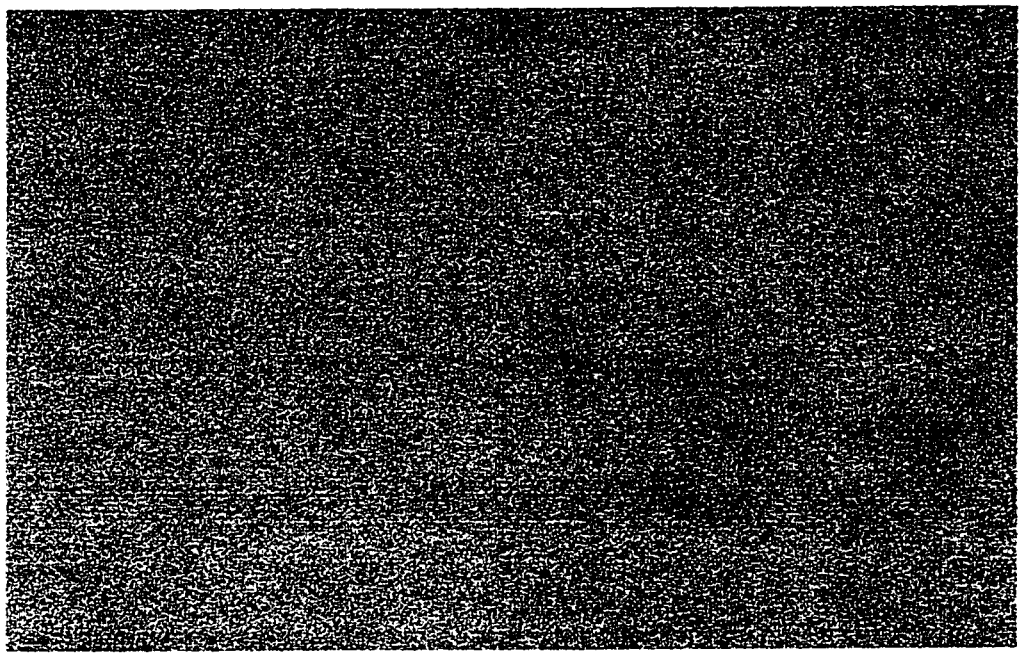

(a)

(b)

Figure 5.9a: Photograph showing the cross sections of (a) glass/epoxy and (b) Kevlar/epoxy tubes crushing before.

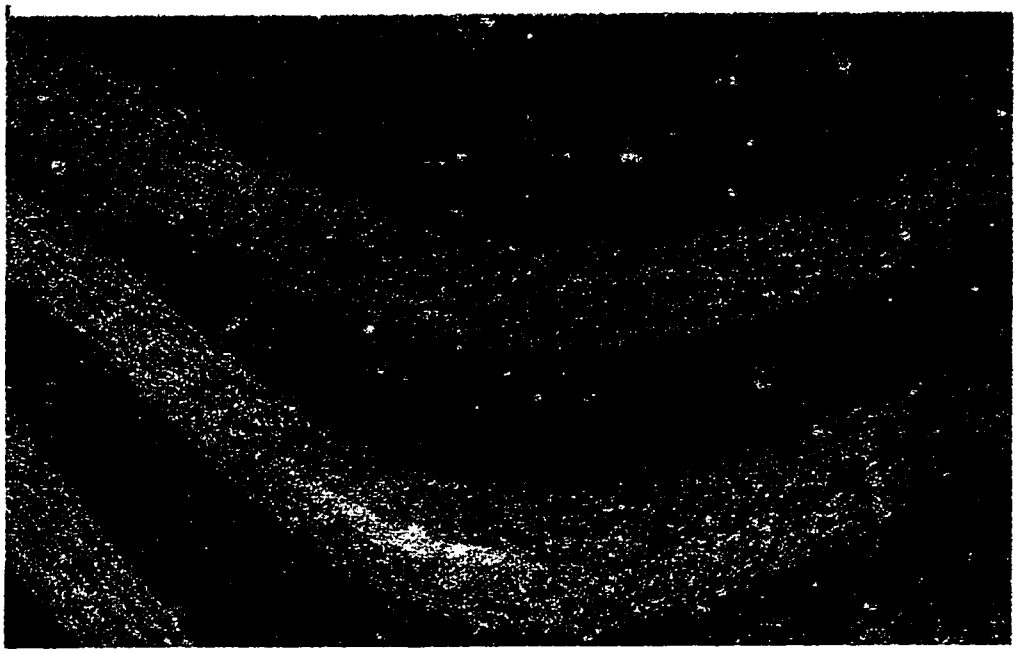

(a)

(b)

Figure 5.9b: Photograph showing the cross sections of graphite/epoxy before crushing at (a) folding and (b) regular location.

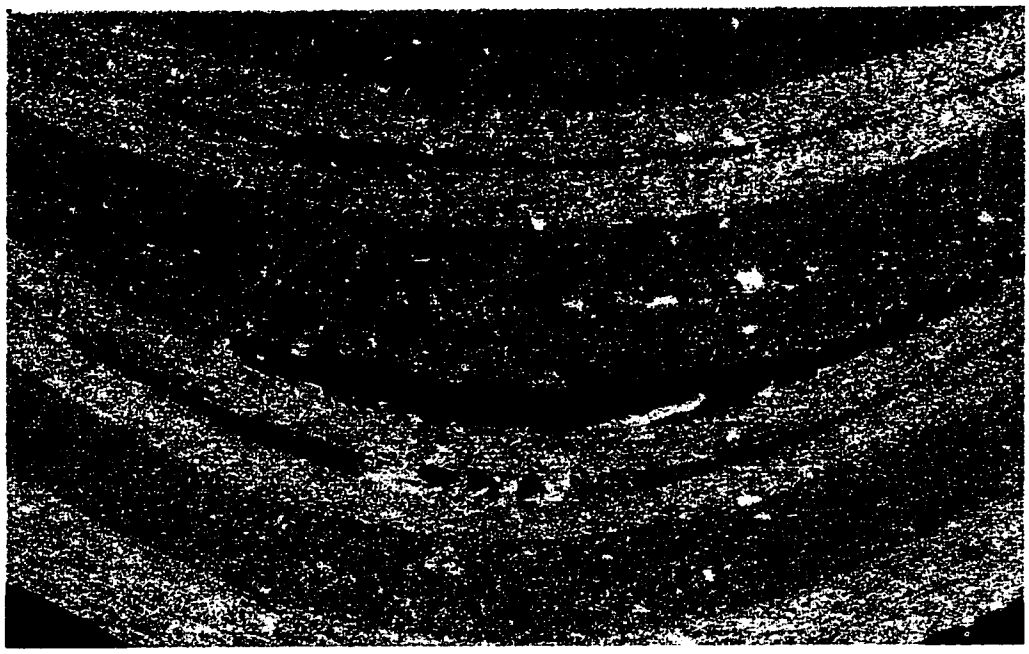

(a)

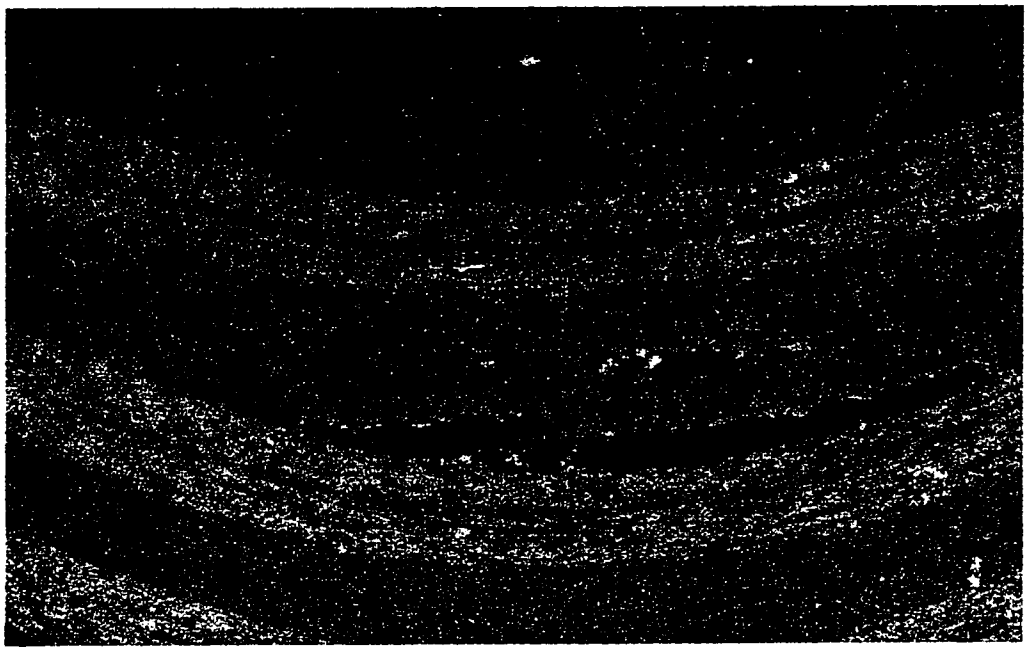

(b)

Figure. 5.10a: Surface cracks on graphite/epoxy tube at sections (a) 10 mm and (b) 30 mm below the crushed surface at a folding under static load.

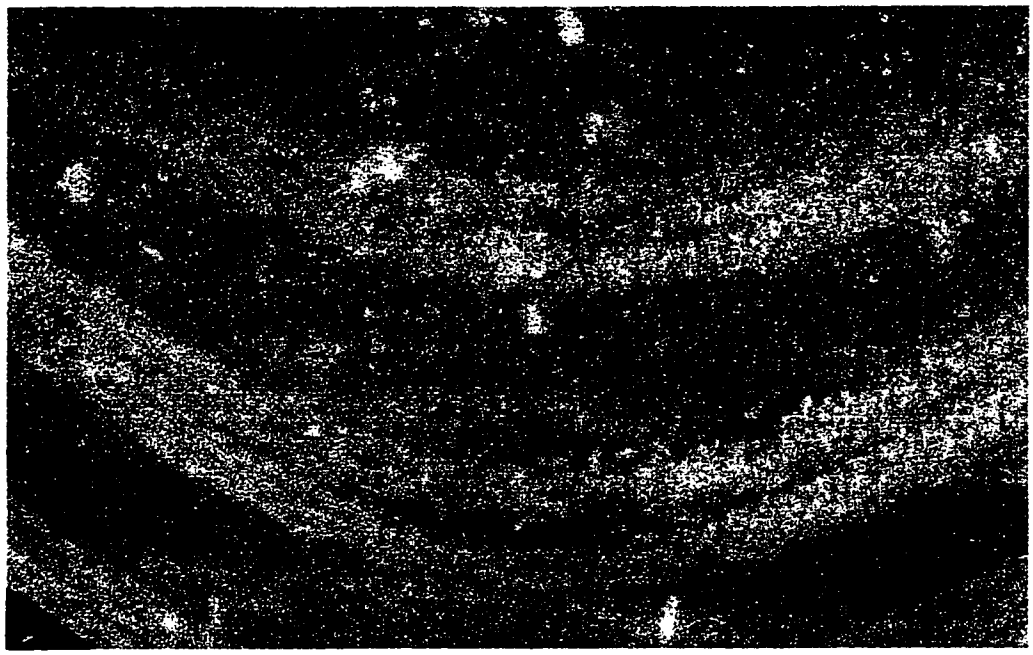

(a)

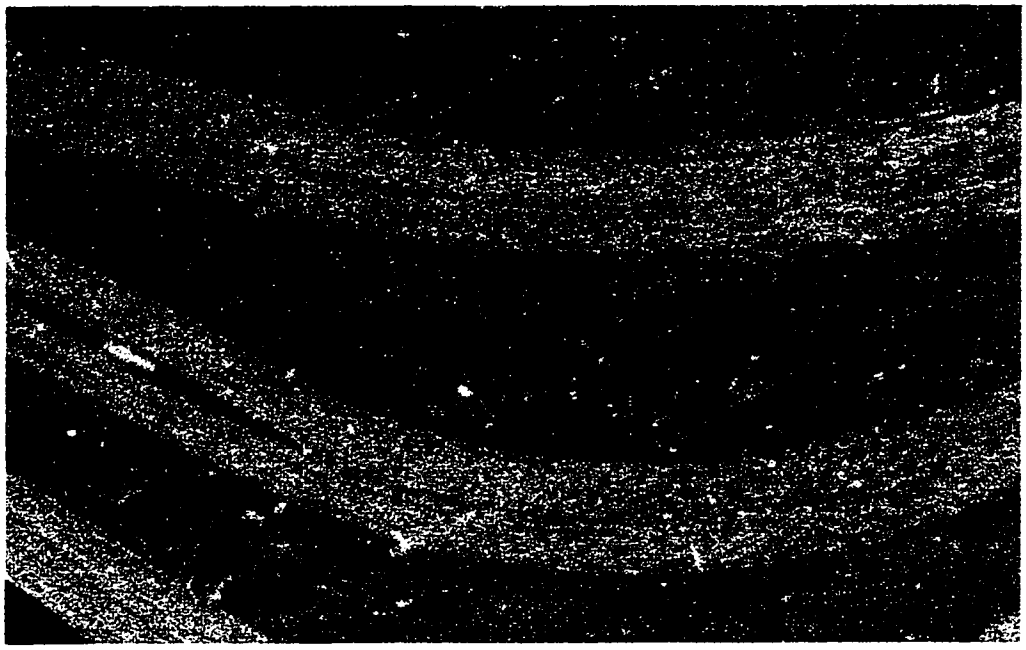

(b)

Figure. 5.10b: Surface cracks on graphite/epoxy tube at sections (a) 50 mm and (b) 70 mm below the crushed surface at a folding under static load.

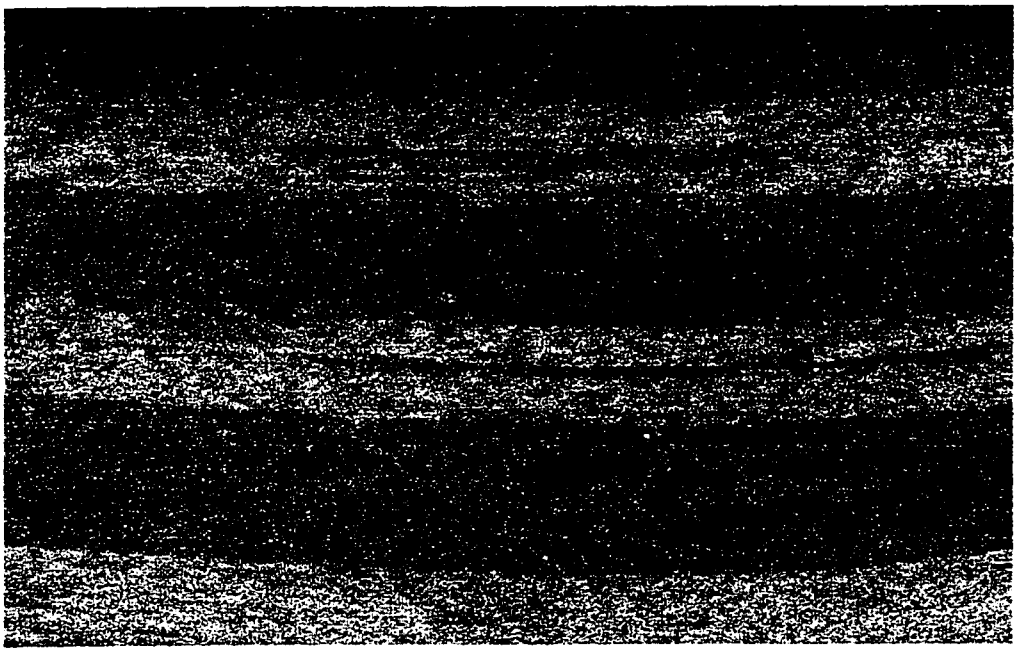

(a)

(b)

Figure 5.11a: Surface cracks on graphite/epoxy tube at sections (a) 10 mm and (b) 30 mm below the crushed surface at a regular location under static load.

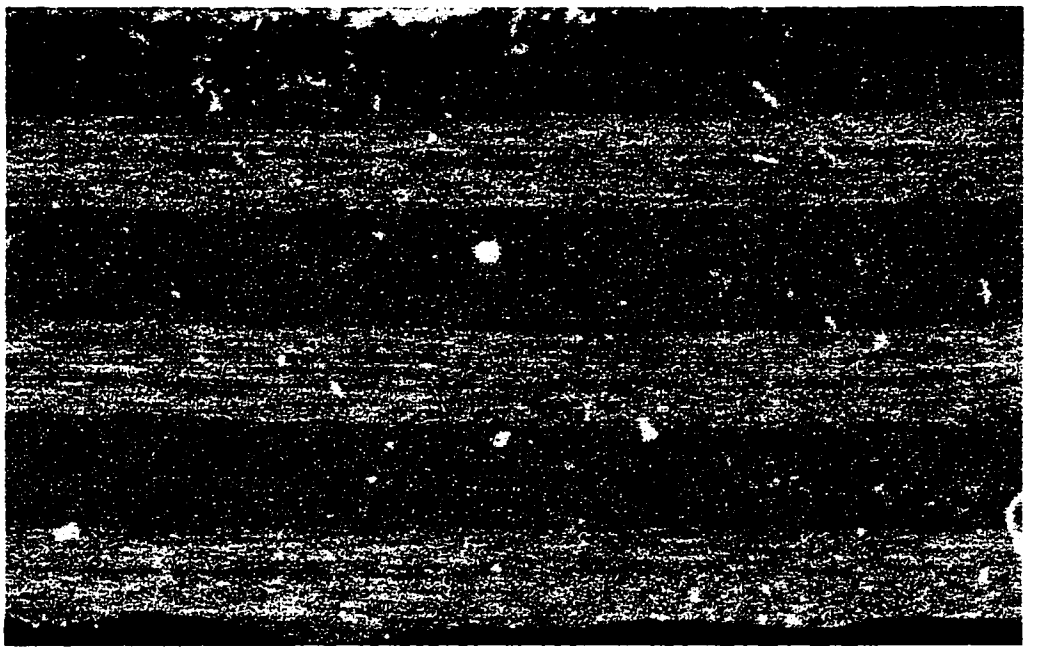

(a)

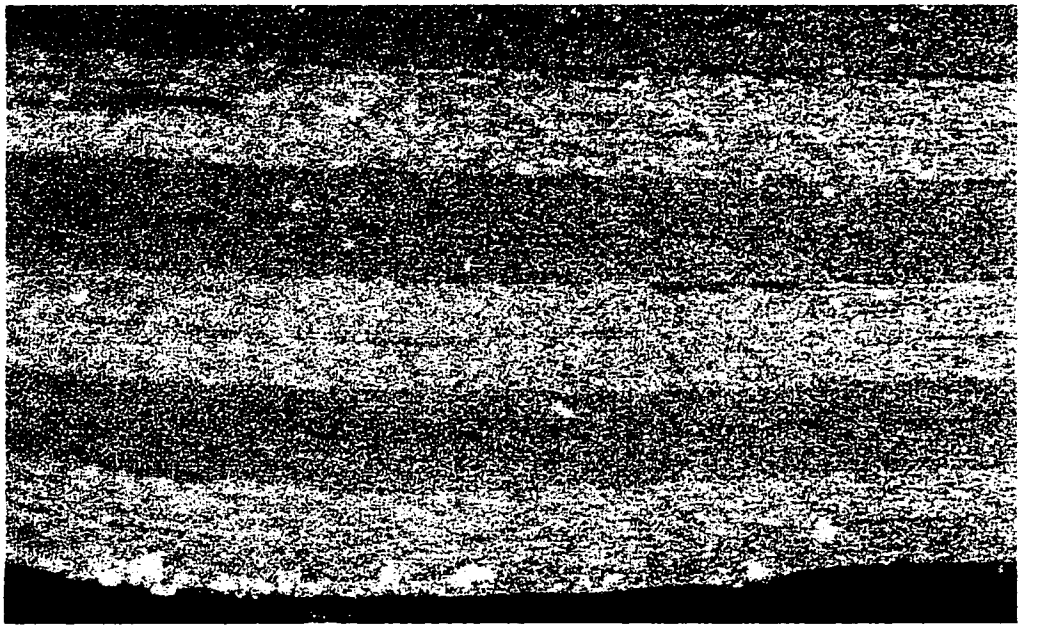

(b)

Figure 5.11b: Surface cracks on graphite/epoxy tube at sections (a) 50 mm and (b) 70 mm below the crushed surface at a regular location under static load.

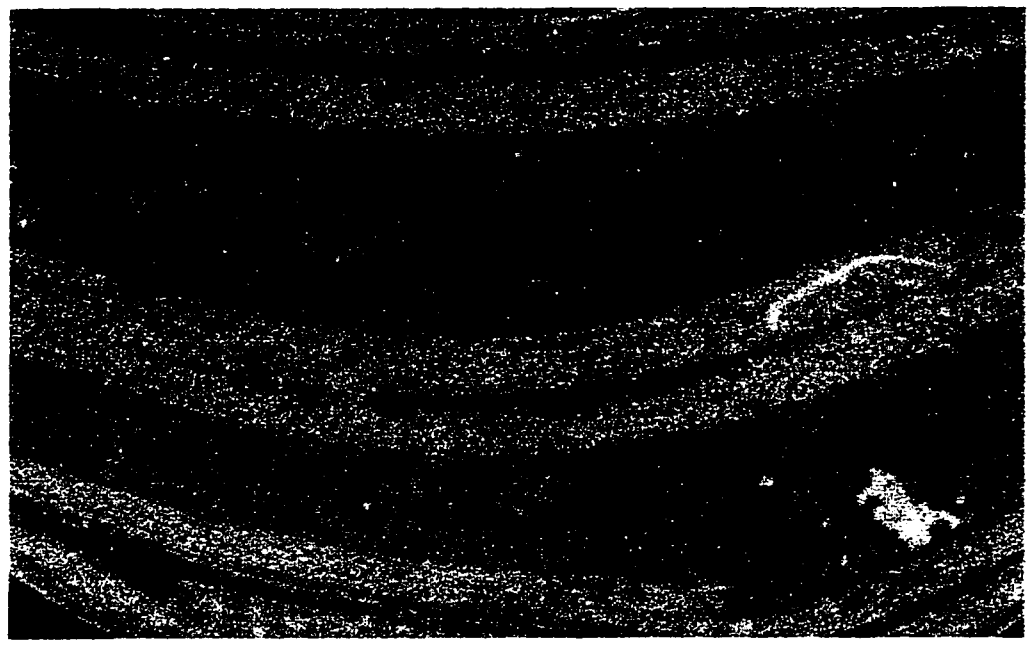

(a)

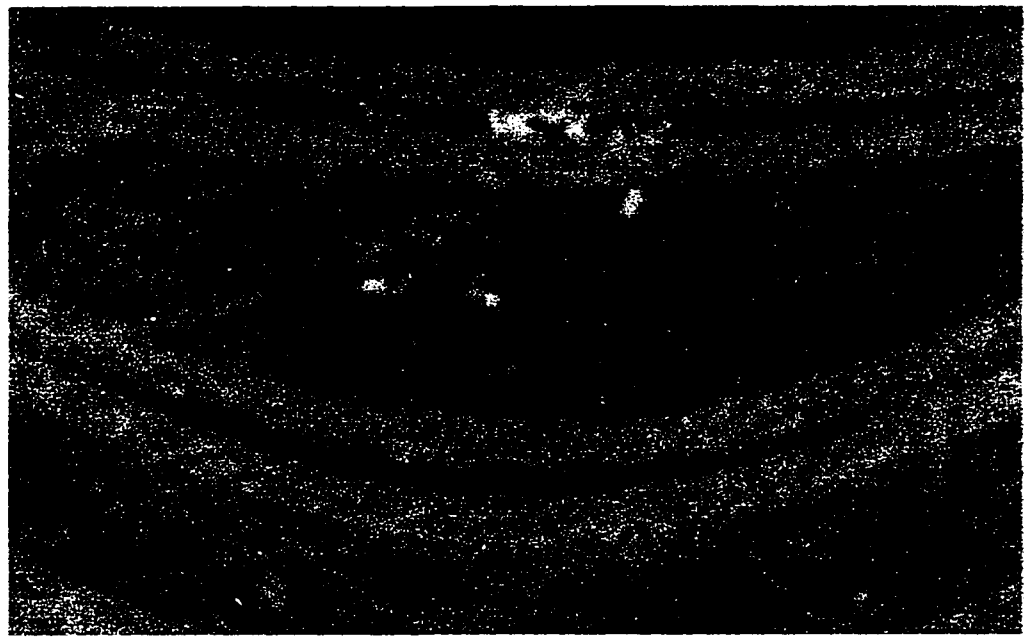

(b)

Figure 5.12a: Surface cracks on graphite/epoxy tube at sections 10 mm and 30 mm below the crush under dynamic load (at a folding).

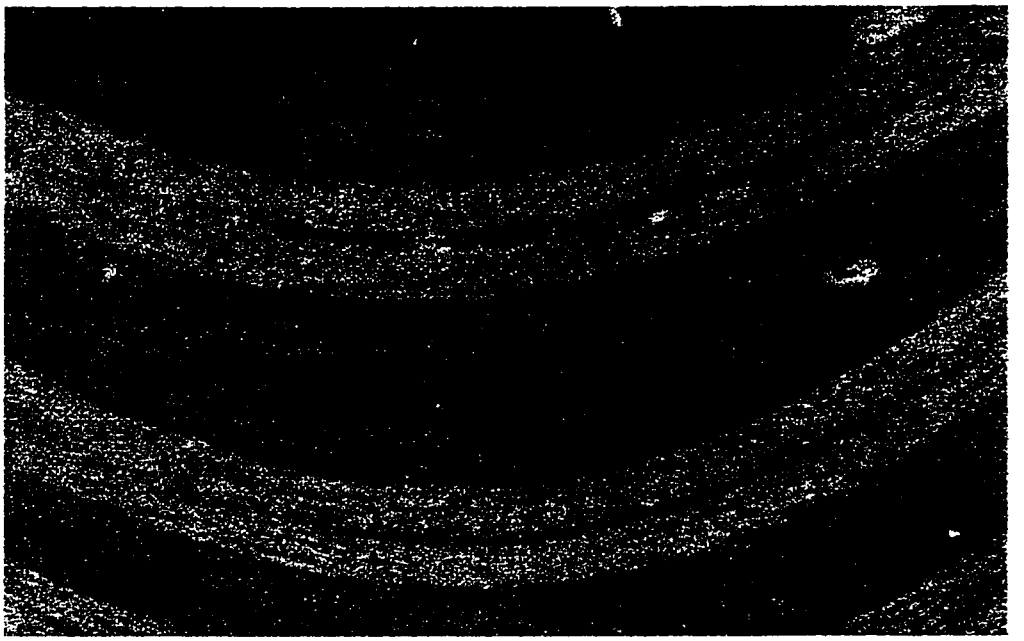

(a)

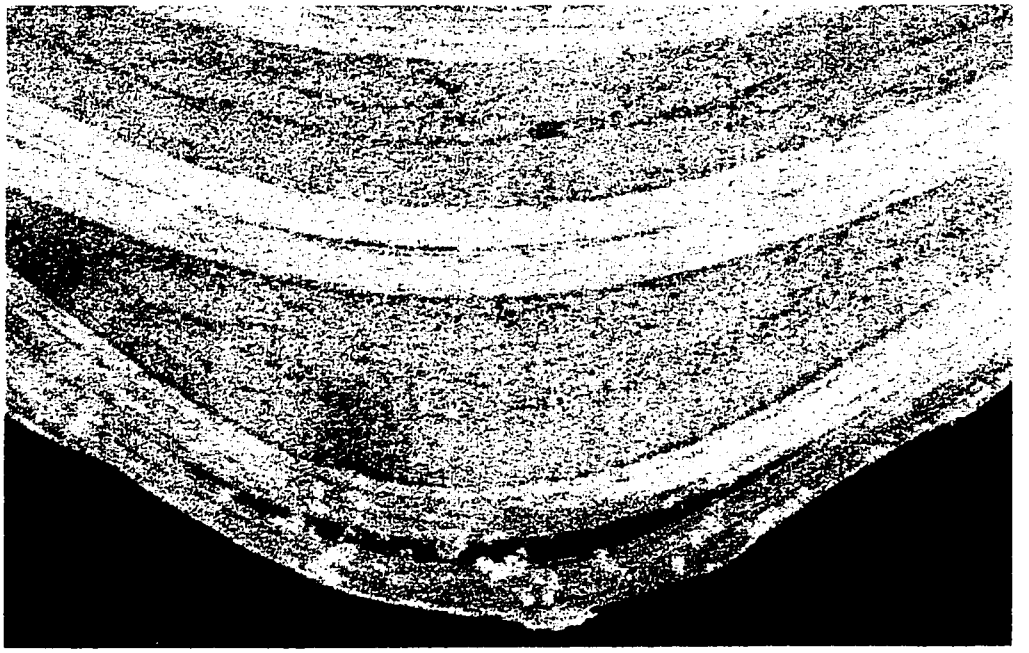

(b)

Figure 5.12b: Surface cracks on graphite/epoxy tube at sections 50 mm and 70 mm below the crush under dynamic load (at a folding).

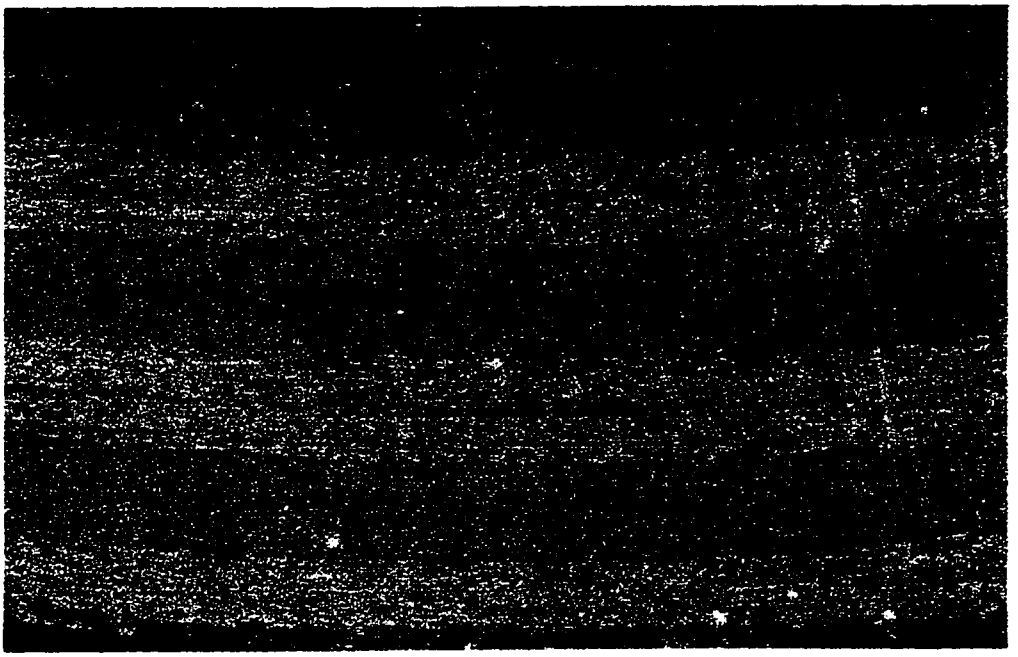

(a)

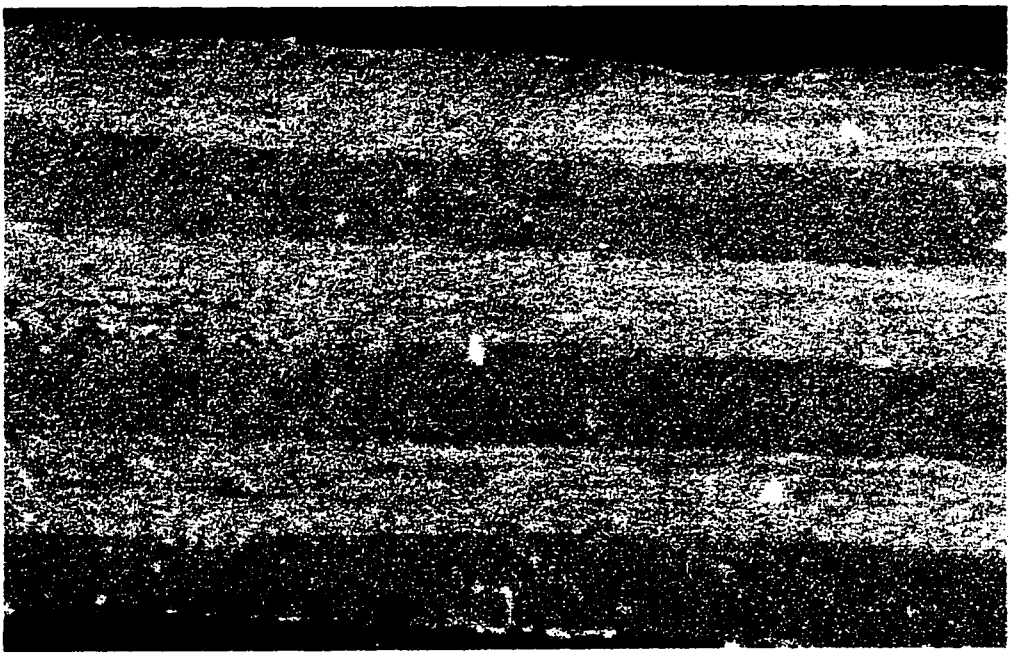

(b)

Figure 5.13a: Surface cracks on graphite/epoxy tube at sections (a) 10 mm and (b) 30 mm below the crushed surface at a regular location under impact load.

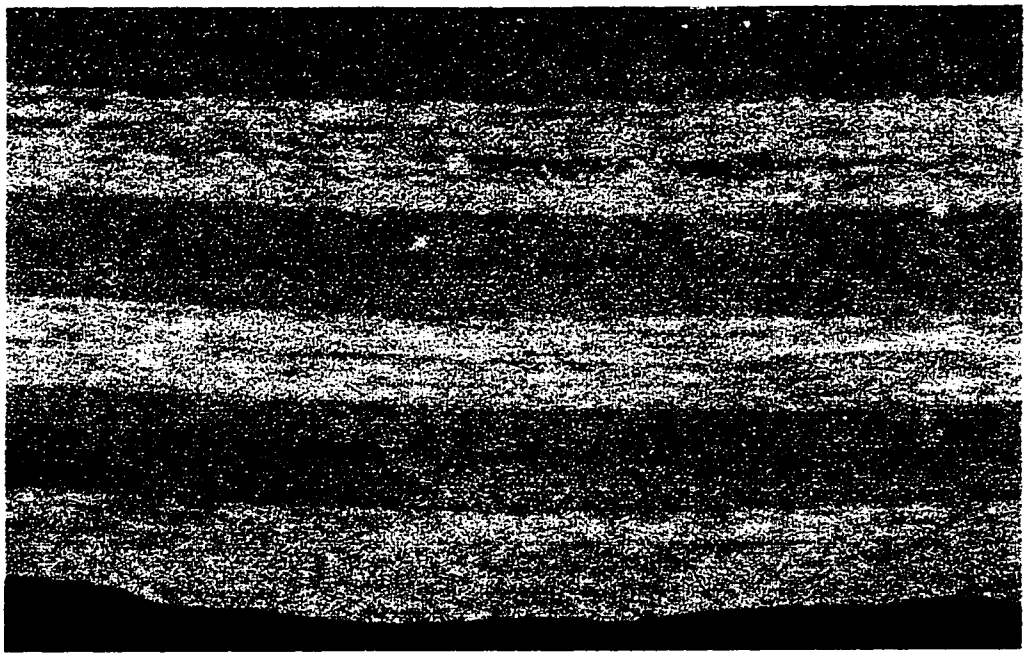

(a)

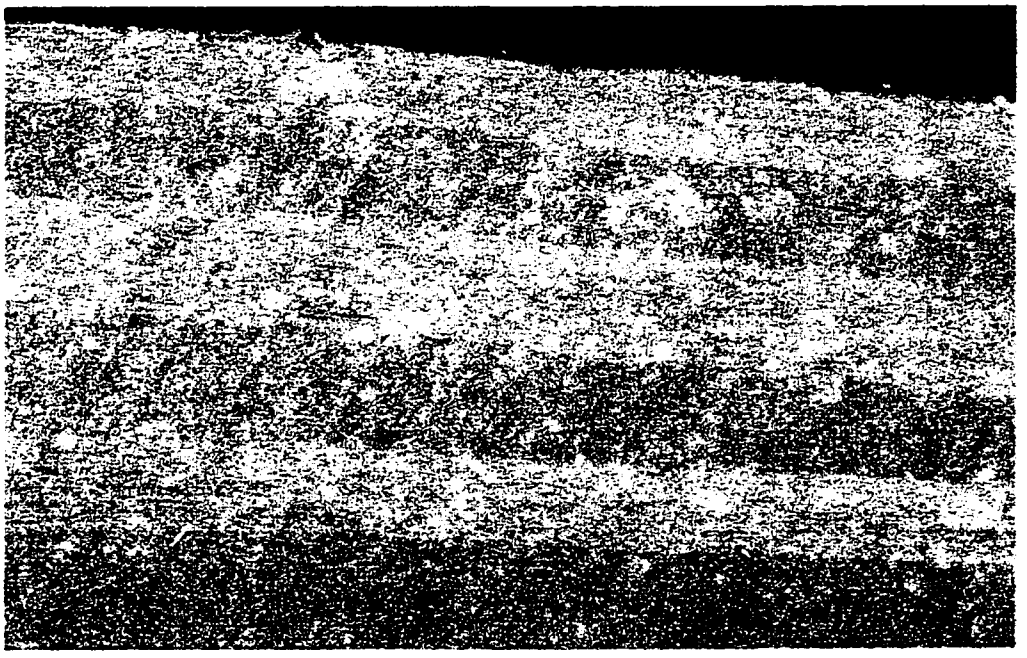

(b)

Figure 5.13b: Surface cracks on graphite/epoxy tube at sections (a) 50 mm and (b) 70 mm below the crushed surface at a regular location under impact load.

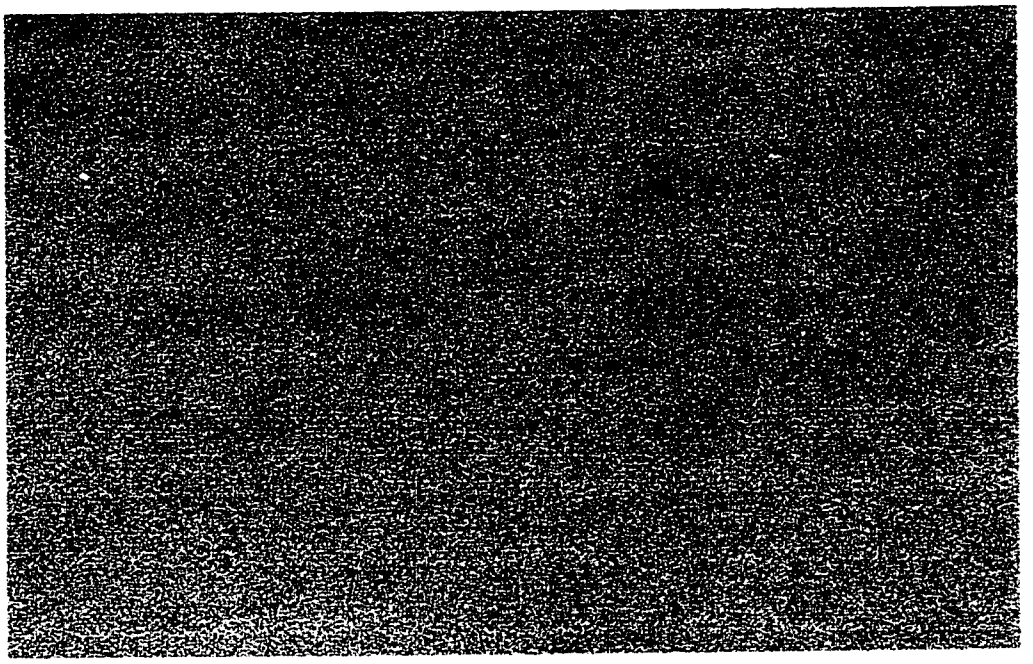

(a)

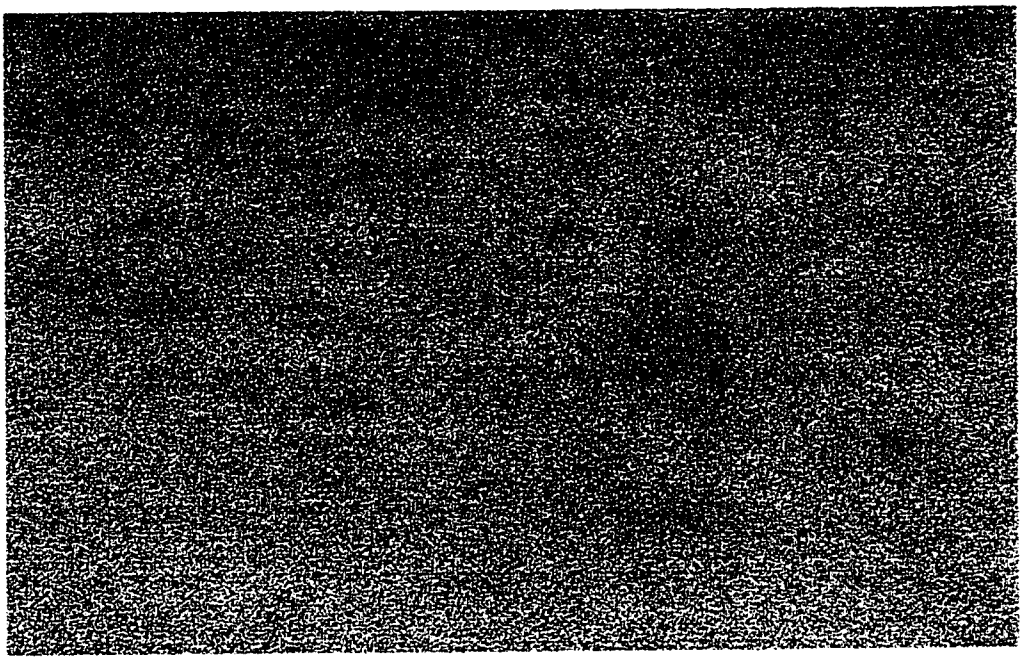

(b)

Figure 5.14: Cross-sections at 10 mm below the crush, for glass/epoxy tubes crushed under static and dynamic loads.

(a)

(b)

Figure 5.15: Cross sections at 10 mm below the crushed surface for Kevlar/epoxy tube under (a) static and (b) impact loads.

microphotographs of polished surfaces at different locations for the three types of tubes under static and dynamic loads.

Photographs of typical cross-sections of the glass/epoxy, kevlar/epoxy and graphite/epoxy tubes fabricated for the experimental study are presented in Figure 5.9. It can be observed from Figure 5.9 that the surfaces of all the three materials were mostly flawless and the laminates are intact. However, some fiber foldings and extra resin concentrations were observed in the case of graphite/epoxy tube.

Figure 5.10 depicts the surface photographs for the graphite/epoxy tubes at sections 10mm, 30mm, 50mm and 70mm from the crushed end under static load at a folding (weak point) formed during manufacturing of the tube. A similar series of photographs taken at a non-folding location on the surface is shown in Figure 5.11. A comparison of the photographs at different sections shown in Figures 5.10 and 5.11 concludes that delaminations occur even at depths away from the crushing point. The amount of delamination, however, is more between 90° and 0° layers than between 90° and 90° and 0° and 0° layers. Delamination is also more at the folding which is a weaker point than a non-folding location. Comparison of length of delamination at different depths shows that, the amount of delamination varies with the depth, with a maximum at a location close to the crushing point. A similar series of photographs taken at different locations and depths of a dynamically crushed tube and presented in Figures 5.12 and 5.13 shows a lower amount of delamination. The discrepancy in the amount of delamination between dynamically and statically crushed tubes may be attributed to the lesser available time to propagate the failure from the crushing point to a larger depth.

The glass and Kevlar tubes did not show any micro failures as observed by the Figures 5.14 to 5.15. The surface after the crush at different sections is observed to be similar to that of the section before the crush, in both dynamic and static cases. Hence it can be concluded that the failure in glass and graphite tubes were a local phenomenon probably owing to the flexible nature of the fibers. From the above discussion it can be concluded that tubes made of materials, which are brittle in nature, such as graphite would propagate the failure to a larger extent. On the other hand flexible material property results in a local failure of the tube. Further, glass fibers being more brittle as compared to Kevlar fibers would fail in more number of modes.

Observations from the crush test discussed above showed that there are several modes of failure for each of the tubes. The major failure mechanisms of different materials are:

GRAPHITE/EPOXY

When the ultimate strength of the tube has reached it starts failing from one end. The load carrying capacity reduces by more than 65% in both dynamic and static loading cases, once the failure has initiated. Debonding and delamination seemed to be the cause of failure initiation from a weak point. Glass fibers having a good compression strength, probably would have sustained more load, if delaminations do not occur. The folding defect in the hoop direction of the tube is observed to be a weak point, with the fibers folded and the excessive resin concentrated at a point. Delamination was especially detected between the 0° and 90° layers of the tube thickness where the interlaminar stress is higher. With the continuation of load application on the specimen, inward and outward

fronds are formed at the crush location. Graphite fibers being weak in bending, the fronds tend to break once the bending stress on the fibers exceeds the bending strength. A higher strain rate causes powdering of the fibers and resin of the bent lamina. While a static load causes the propagation of delamination to a longer distance longitudinally, in the case of dynamic load the propagation of delamination is smaller. However, a complete failure of fronds results in higher energy absorption when the specimen is loaded dynamically.

GLASS/EPOXY

The main macroscopic crushing mechanism governing the axial crushing of glass/epoxy tube was observed to be formation of inward and outward fronds due to delamination and wedge formation. Fiber breakage of the fronds in the hoop direction and powdering of the fibers and resin are the other phenomena contributing to the energy absorption ability of the glass/epoxy tube.

KEVLAR/EPOXY

Local buckling is the main reason for the failure of Kevlar/epoxy tubes while loaded axially. The buckled tube deforms in the radial direction and when the hoop stress exceeds the strength, hoop breakage occurs. The hoop breakage to form strips was observed to be more in the case of dynamically loaded tube.

5.7 SUMMARY

The axial crushing behavior of glass/epoxy, graphite/epoxy and Kevlar/epoxy circular tubes under static and dynamic loads has been studied experimentally. Much information

has been gained from the measured load-deflection data of the three tubes. The strain rate of crushing is observed to have affect on the crushing behavior of the three types of tubes. While the total energy absorbed has increased under dynamic load in the case of graphite and Kevlar tubes the higher strain rate reduces the energy absorption capacity of the glass tube. A complete powdering action of the graphite tube under an impact load results in increase of energy absorption as compared to the static case. The brittle property of the graphite tube helps the powdering process. The Kevlar fibers are weak in compression and fail due to local buckling. The extra tearing action of the locally buckled Kevlar tube when impacted by a mass increases the energy absorption capacity of the tube. On the other hand, glass fibers being neither too brittle, nor ductile behave poorly under impact load. A selection of right material for the energy absorption tubes should be based on its energy absorption capacity under impact loads. From the above-discussed results, it can be concluded that, glass/epoxy tube is a poor selection as energy absorber. Further, the peak load for the glass/epoxy tubes under both static and dynamic cases was observed to be very high, which may result in transfer of higher force levels to the passenger cabin, when the tubes are used as crush elements. Both brittle (graphite) and ductile (Kevlar) material are desirable selection for the energy absorber due to their higher energy absorption capacity under dynamic load.

CHAPTER 6

LUMPED PARAMETER AND FINITE ELEMENT MODELS WITH CRUSH ELEMENTS

6.1 INTRODUCTION

The dynamics of a car-to-truck collision has been modeled and studied using rigid body, lumped parameter and finite element methods in the previous chapters. The results presented in Chapters 2 to 4 revealed considerable performance benefits of the energy dissipating under-ride guard in reducing the acceleration transmitted to the automobile passenger during a car-to-truck rear end collision. Optimization studies were performed to obtain the damper and spring parameters of the under-ride guard for best performance in terms of the acceleration transmitted and the allowed intrusion of the vehicle. The energy absorption characteristics of crush elements made of different composite materials are investigated in Chapter 5. From the results it was concluded that a glass/epoxy crush tube yields poor energy absorption, high peak loads under both static and dynamic loading. A glass/epoxy tube is expected to yield higher deceleration of the occupant compartment. Both brittle (graphite) and ductile (Kevlar) materials revealed enhanced energy absorption capabilities and performance under dynamic loads.

The results presented in the previous chapters showed that the peak acceleration transmitted to the passenger cabin of a 1000 kg automobile, considered in the study, either exceeds or is close to the Head Injury Criteria. Collisions occurring at relatively

higher speeds may lead to transmission of higher acceleration levels to the occupant compartment. Alternatively, crush elements may be incorporated in the front end of the structure to enhance its energy absorption properties. The crush elements coupled with the damped under-ride guard may lead to further reductions in the transmitted acceleration. The performance benefits of additional crush elements are investigated using both the lumped parameters and the finite element models of the automobile and the guards. The crush elements are represented by non-linear spring elements using measured force-displacement characteristics, discussed in Chapter 5. Impact analyses are performed for vehicle impacts with both conventional rigid and the energy dissipating under-ride guards, and the potential performance benefits are discussed in terms of the performance criteria defined in Chapter's 2 and 4.

6.2. MODEL DESCRIPTION

The effectiveness of composite material crush elements are evaluated by developing lumped parameters and DYNA3D models of the car-under-ride guard system, described in Chapter 4. The models described in Chapter 4, however, are modified in order to incorporate non-linear spring elements representing the crush elements. The measured force-deflection properties of composite tubes, presented in Chapter 5, are used to describe the non-linear spring elements of the models. The analyses are performed for the Kevlar/epoxy crush elements only, due to their enhanced energy absorption characteristics as discussed in Chapter 5. The analytical models, however, can be effectively applied to study the crash behavior in conjunction with different crush elements, such as graphite and glass/epoxy.

6.2.1 Lumped Parameter Model with Crash Elements

The lumped parameter model of the automobile with crush elements impacting the proposed under-ride guard is illustrated in Figure 6.1. The crush elements, connected between the bumper mass (m_{c4}) and the front frame are represented by a non-linear resistance F_{CE}. The attachments of the crush elements are represented by a small lumped mass m_{c5} The impact behavior of the car and under-ride guard is analyzed in three sequential stages as described earlier in Chapter's 2 and 4. While the equations of motion for the first stage of impact are identical to those derived in the previous chapters, the governing differential equations of motion during the second and third phase of impact differ due to additional crush elements and the degree of freedom. The equation of motion of the under-ride guard under the application of the contact force F_x is also identical to the equations presented in Equation 4.8. The equations of motion for the five degree of freedom lumped parameter model of the car can be readily derived as:

$$\begin{aligned} m_{c1}\ddot{x}_{c1} &= -F_1 - F_3 - F_4 - F_5 + F_8 \\ m_{c2}\ddot{x}_{c2} &= F_3 + F_5 - F_6 - F_7 - F_8 \\ m_{c3}\ddot{x}_{c3} &= F_1 - F_2 + F_7 \\ m_{c4}\ddot{x}_{c4} &= F_{CE} + F_4 + F_6 + F_x \\ m_{c5}\ddot{x}_{c5} &= F_2 - F_{CE} \end{aligned} \tag{6.1}$$

where F_1 to F_8 describe the various forces generated by the various structural elements as a function of the deformation δ_i. F_{CE} is the force developed due to the deformation of the crush element. The deformations of various structural elements are defined as:

$$\delta_1 = x_{c1} - x_{c3} \qquad \delta_2 = x_{c3} - x_{c5} \qquad \delta_3 = x_{c1} - x_{c2}$$
$$\delta_4 = x_{c1} - x_{c4} - C_4 \qquad \delta_5 = x_{c1} - x_{c2} - C_5 \qquad \delta_6 = x_{c2} - x_{c4} - C_6$$
$$\delta_7 = x_{c2} - x_{c3} \qquad \delta_8 = x_{c2} - x_{c1} \qquad \delta_{CE} = x_{c5} - x_{c4}$$

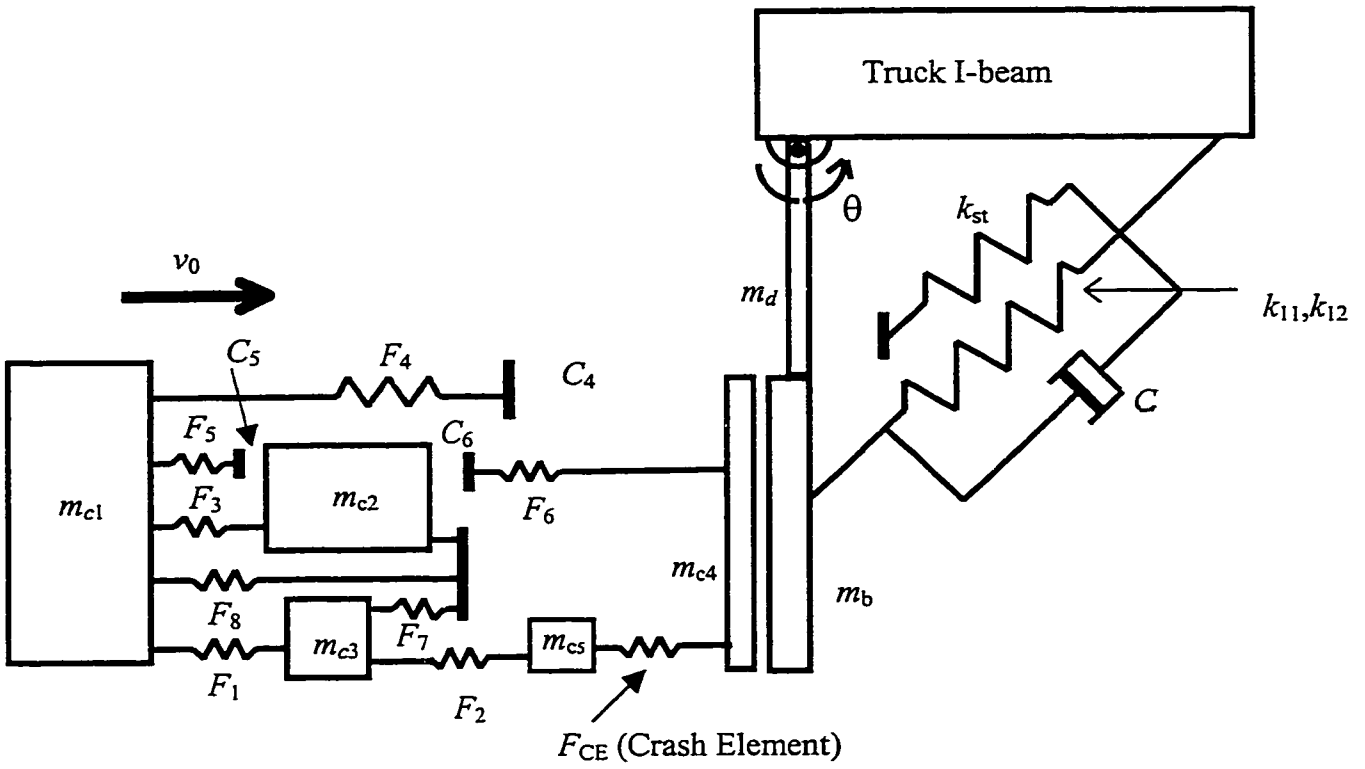

Figure 6.1: The lumped parameter model of the car with crush elements and the damped guard.

where x_{c1}, x_{c2}, x_{c3}, x_{c4} and x_{c5} are the displacements of masses due to car body, engine, suspension and cross member, car bumper and the attachment between front frame and the crush element, respectively. Equation (6.1) together with (4.8) represent the dynamic behavior of the coupled system in terms of seven unknown response variables (x_{c1}, x_{c2}, x_{c3}, x_{c4}, x_{c5}, θ and F_x). The contact force, however, can be eliminated using the velocity constraint at the contact point, to yield equations of motion for the coupled car and under-

ride guard structures. Following the approach used in Chapter 4, the complete set of equations of motion can be written as:

$$
\begin{aligned}
&m_{c1}\ddot{x}_{c1} + F_1 + F_3 + F_4 + F_5 - F_8 = 0 \\
&m_{c2}\ddot{x}_{c2} - F_3 - F_5 + F_6 + F_7 + F_8 = 0 \\
&m_{c3}\ddot{x}_{c3} - F_1 + F_2 - F_7 = 0 \\
&m_{c5}\ddot{x}_{c5} - F_2 + F_{CE} = 0 \\
&\left\{\frac{m_{c4}}{\cos^4\theta} + m_b + \frac{m_d}{3}\right\} l^2\ddot{\theta} + 2m_{c4}l^2\left(\frac{\sin\theta}{\cos^5\theta}\right)\dot{\theta}^2 + l_1 F_d \\
&\quad + \left(m_b + \frac{m_d}{2}\right) gl\sin\theta + F_k\frac{\partial\delta_1}{\partial\theta} + F_{st}\frac{\partial\delta_2}{\partial\theta} + k_t\theta - \frac{(F_2 + F_4 + F_6)l}{\cos^2\theta} = 0
\end{aligned}
\tag{6.2}
$$

subject to the following initial conditions:

$$
\begin{aligned}
&x_1(0) = x_2(0) = x_3(0) = \theta(0) = 0 \\
&\dot{x}_1(0) = \dot{x}_2(0) = \dot{x}_3(0) = \dot{x}_4(0) = v_0; \quad \dot{\theta}(0) = \dot{x}_b / l
\end{aligned}
\tag{6.3}
$$

The analyses are performed for different numbers of crush elements and the results are examined to identify a near optimal number of such elements.

6.2.2 Finite Element Model with Crash Elements

The Finite element model of the car described in Chapter 4 is further modified to incorporate the measured non-linear force-deflection characteristics of the crush elements. Two crash elements are connected between the car bumper and the firewall on both sides of the engine block. The attachments of the crush elements are modeled using brick elements defined having common nodes with the surface elements, representing the bumper and the firewall. Spring elements are defined between the brick elements on both sides of the engine to represent the crush elements. A load-curve input file is compiled

using measured force-displacement characteristics of the crush elements to perform the analysis using DYNA3D. Based on the results of the LP model, 3 and 4 crush elements were incorporated in the model with rigid and damped guards, respectively.

6.2.3 Crush Elements

The dynamic force-displacement characteristics of the crush element considered in the car model are represented as function of deflection and rate of deflection (δ,$\dot{\delta}$). During the impact process, the crush element may undergo plastic deformation. A mathematical characterization of the plastic deformation of such springs, however, is highly cumbersome. Alternatively the force-displacement characteristics of the crush elements derived from static tests can be used in conjunction with a dynamic magnification factor. This approach is similar to that used for the crushable components of the car structure. The measured data obtained under static and dynamic tests discussed in Chapter 5, at an impact speed of 6.25 *m/s* (22.5 *km/h*) are used to derive the dynamic magnification factor in the 0-22.5 *km/h* speed range. Although, the magnification factor may vary at higher impact speeds, in the present analysis it is assumed to remain linear in the 0-50 *km/h* speed range. The peak crush forces under static and dynamic loading conditions are used to estimate the magnification factor. The static crush test on Kevlar/epoxy crush elements revealed a average force of 39000 N, while the peak crush force at 6.25 *m/s* was observed to be 34000 N. A magnification factor was thus computed as -0.0205 % per *m/s* or -0.569% per *km/h*. It should be noted that force-deflection characteristics of the Kevlar crush elements are similar to those of the automobile components within the Group I, described in Section 4.2.3. The dynamic force due to the element is derived using

Equation (4.10), corresponding to the instantaneous deflection and the identified 'Zone', as described earlier in Section 4.2.3.

The car-truck collision analyses are performed using the lumped parameter and the finite element models of the automobile to account for the energy absorbed due to deformations of the structural components. The analyses are performed with both the conventional rigid and the proposed damped guards, and the dynamic response characteristics are evaluated in terms of the performance measures defined in Chapter 4.

6.3 IMPACT ANALYSIS USING LP MODEL

The impact analysis of the lumped parameter model with crush elements is carried out for both rigid and damped under-ride guards. The results of the analysis are discussed below to illustrate the relative performance benefits of damped guard. The results are further compared with those obtained without the crush elements to demonstrate the performance potentials of the crush elements.

6.3.1 Impact with Rigid Under-ride Guard

The impact of a car with a rigid under-ride guard is analyzed as an impact between the car and a rigid barrier, as discussed in Section 4.2.4. The analyses are performed at an impact speed of 50 *km/h* as recommended by the FMVSS for the barrier impact test. Equations (6.1) are solved for an impact velocity of 50 *km/h*, and simulation is terminated when the total bumper force, the sum of forces due to non-linear springs, F_{CE}, F_4 and F_6, approaches zero. The equations of motion are solved using different number of crush elements, while the dimensions and properties are retained as those discussed in Chapter

5. The results are examined in order to derive a near optimal number of crush elements leading to minimum levels of transmitted acceleration. From the results of the parametric study (not presented), it was concluded that the use of 4 crush elements can reduce the body mass acceleration level to 35g. The impact response characteristics presented thus correspond to the LP model comprising 4 crush elements.

Figure 6.2 illustrates the time-histories of the displacement, velocity and acceleration response of the four lumped masses of the LP model impacting a rigid under-ride-guard, represented by a fixed barrier. It should be noted that the intrusion of the car mass subject to an impact with a rigid barrier is considered to be negligible, which conforms with the results of the FE analysis reported in Chapter 3. The results show the response characteristics of four lumped masses representing the body (m_{c1}), engine (m_{c2}), suspension and cross members (m_{c3}), and crush element attachment (m_{c5}). While the displacement response characteristics of m_{c1}, m_{c2}, and m_{c3} are observed to be quite similar, the engine mass exhibits slightly larger peak displacement due to excessive deformations of the radiator (F_6). The total crash event is observed to occur over a duration of 0.074 s, when total bumper force approaches zero, and the peak displacements occur near $t \approx 0.05$ s for all the four lumped masses. While the engine mass reveals a maximum displacement of 0.45 m, the body mass experiences a peak displacement of 0.41 m. The relative displacement between the body mass and the suspension mass is observed to be close to zero, which reveals minimum crush of the drive-line. The peak displacement of the crush elements attachment mass (m_{c5}) increases gradually and approaches a peak value of 0.22 m. The displacement of 0.22 m corresponds with the maximum permissible deformation of crush elements.

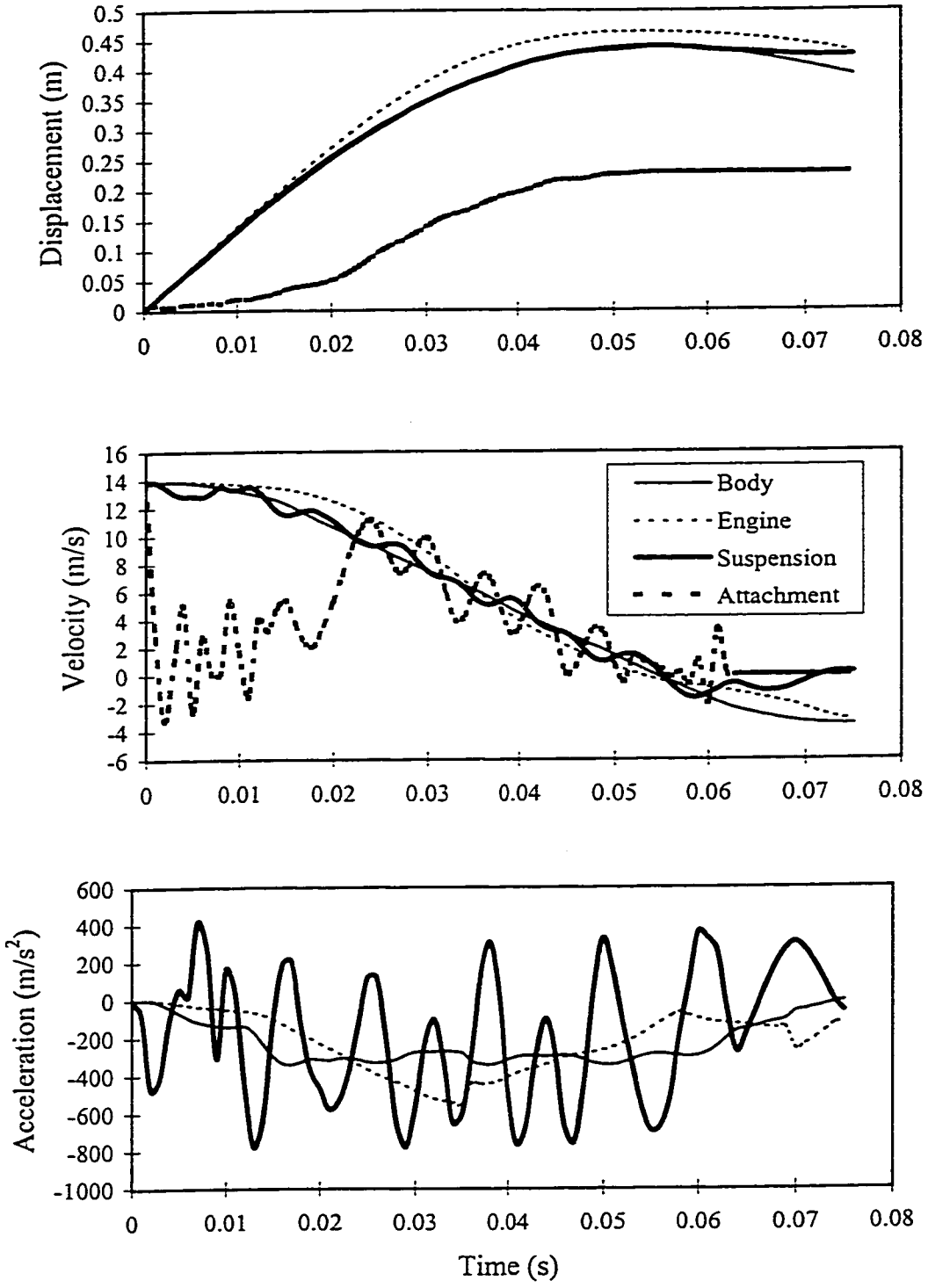

Figure 6.2: Displacement, velocity and acceleration response of the lumped masses of the car under impact with a rigid barrier.

The velocity response of the crush element attachment mass is observed to be oscillatory which may be attributed to its low numerical value, elastic behavior of the front frame and the elements in the early stages of impact, and localized buckling of the crush elements. The resulting acceleration response of m_{c5} is thus excessively high. This acceleration response is not represented in the figure. The velocity response characteristics of the lumped masses (m_{c1}, m_{c2} and m_{c3}) reveal gradual reduction in the velocity, while all the masses with the exception of m_{c5} undergo rebound near 0.05 s. The acceleration response histories of the three remaining masses, shown in Figure 6.2, reveal that the body-mass experiences a peak deceleration of 345 m/s^2 (35.1g) at $t = 0.038$ s. The suspension and the engine masses tend to encounter higher acceleration owing to their lower mass values. Further, the acceleration response of the suspension mass is observed to be more oscillatory as compared with those of the body and engine masses. These oscillations in the acceleration response are attributed to higher natural frequency of the suspension assembly mass. Although, the peak acceleration response of the suspension mass is very large, the objective is to minimize the acceleration experienced by the body mass. The peak acceleration of the body mass of the car impacting a rigid barrier is observed to be considerably larger than the head injury criteria, which further emphasizes the necessity of an energy dissipating absorption mechanism.

During an impact with a rigid barrier, the crushing of structural members of the car is associated with absorption of certain portion of the kinetic energy of the car. In the LP model the non-linear springs and the crush elements represent the energy absorbing members of the car. The energy absorption characteristics due to the front frame (F_2), sheet metal (F_4), radiator (F_6), engine and transmission moments (F_1 and F_8), non-linear

springs and the crush elements during the impact are illustrated in Figure 6.3. The energy absorption characteristics of different springs show that major part of the crash energy is absorbed by the plastic deformations of the front frame (F_2), which includes the bumper, and the sheet metal (F_4). The sheet metal absorbs more than 40% of the total kinetic energy (96.5 kJ) of the car, while the next major contribution towards energy absorption arises from the front frame (20% of the total kinetic energy). The crush elements absorb up to 17% of the total kinetic energy. It is interesting to note that driveline and the firewall do not absorb any energy under impact at a speed of 50 *km/h*, which is attributed to excessive clearances C_5 and stiffness of the driveline. A comparison of energy absorption by the different components of the car without the crush elements reveals that energy absorbed by most structural elements is considerably lower when crush elements are employed. The sheet metal, however, absorbs 40% of the total energy as compared to 28% in the case of car without crush elements. The front frame of the car with crush elements, on the other hand, absorbs lower amount of energy (20%) as compared to 57% in the case of car without crush elements. This is attributed to the energy absorbed by the crush elements which are located in the load path corresponding to the front frame.

Figure 6.3 further illustrates the total amount of plastic work done by different components of the car subject to a rigid barrier impact at a speed of 50 *km/h*. The results show that almost entire kinetic energy (96.5 kJ) of the car is converted as plastic work, which may represent higher risk of occupant casualty. However, since a part of the energy is absorbed by the crush elements, the damage to many structural parts can be expected to be relatively less.

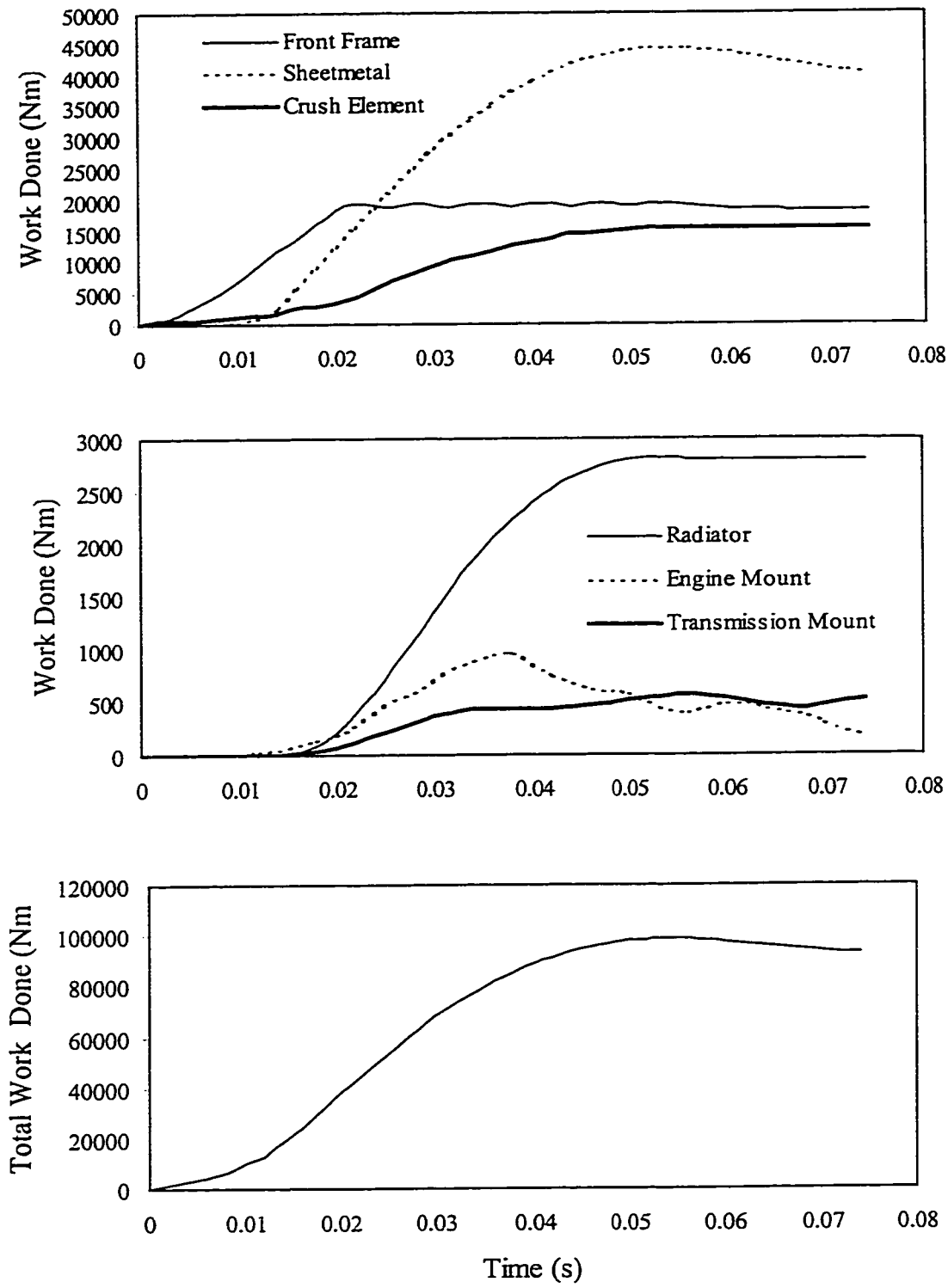

Figure 6.3: Energy absorbed by the different components of the LP model subject to an impact with a rigid barrier ($v_0 = 50$ *km/h*).

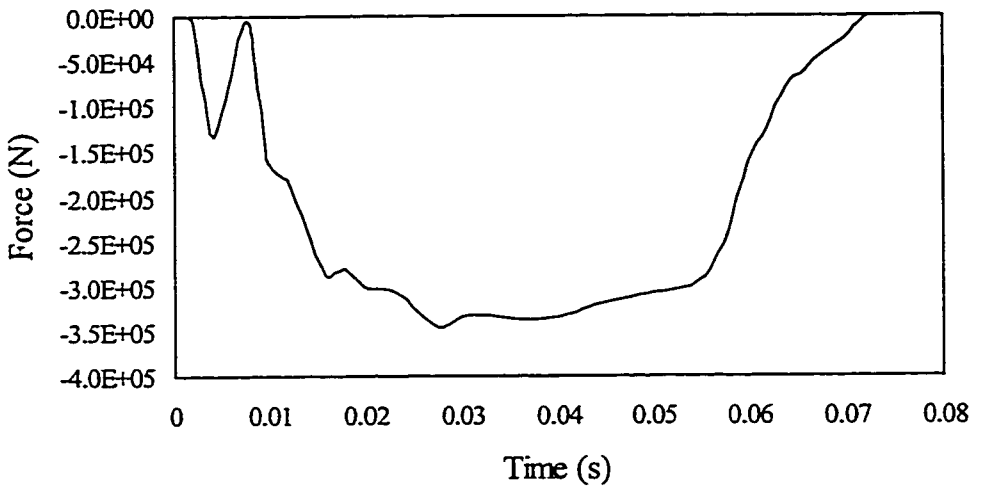

Figure 6.4: Total bumper force of the car (LP model) subject to an impact with a rigid barrier ($v_0 = 50$ *km/h*).

The total amount of bumper force of the car subject to a rigid body impact is illustrated in Figure 6.4. The total bumper force or the contact force approaches a peak value of 340 *kN*, which occurs slightly before the masses experience peak displacements. A comparison of total bumper force and the amount of energy absorbed by the model without the crush elements, (Figure 4.15), reveals that the total bumper force reduces considerably from 510 *kN* to 340 *kN*, when crush elements are introduced. The total contact force then gradually reduces to zero at the end of the crash event. The response characteristics of the LP model with and without the crush elements in terms of the performance measures are further compared in Table 6.1. The results clearly illustrate the potential benefits of the crush elements.

Table 6.1: Comparison of Performance Measures with and without the Crush Elements.

Performance Measure	Without crush elements	With crush elements
Peak body displacement (m)	0.35	0.41
Peak body acceleration (m/s^2)	502	340
Peak bumper force (kN)	510	347
Total energy absorbed (%)	97	98

6.3.2 Impact with Damped Under-ride Guard

The impact analysis of the lumped-parameter model of the automobile with the damped under-ride guard is evaluated under-direct impact at 50 km/h. Equations (6.2) are solved to determine the response characteristics of the lumped-parameter models of the car and the damped guard. A comprehensive parametric study is carried out to study the influence of various parameters of the damped guard on the response characteristics, expressed in terms of the performance measures.

The results of the parametric study revealed trends similar to those observed with rigid representation of the car, presented in Section 3.4.2. The results further demonstrated that the magnitude of intrusion and the acceleration response of the car body mass are strongly related to the stiffness and damping properties of the guard. An optimal design of the damped guard is thus attempted to achieve optimal performance under impact with the lumped parameter model of the car comprising crush elements. A design optimization study was performed to minimize the weighted function of performance variables, defined in Equation (2.4.1), to identify the optimal parameters of the guard. The peak intrusion and acceleration terms in the objective function, however, are replaced with the modified performance measures described in Equations (4.12),

(4.13) and (4.14). The optimization problem in Equation (4.15) is solved using a nonlinear programming technique for one set of limiting constraints $\{q_1, q_2\}$: {0.15, 0.85}.

Table 6.2 illustrates the optimal parameters of the damped guard, subject to a direct impact with the LP of the car at a speed of 50 *km/h* for the selected limit constraint. The results show that, a very high compression and rebound stroke damping is required, when the maximum intrusion is limited to 0.45 *m* ($q_1 = 0.15$). The results further show that multiple stages in compression and in rebound damping are not necessary, as evident from unity values of n_e and n_c. The results of the optimization study correlates reasonably well with those obtained in Chapter 4 in conjunction with LP model of the car without the crush elements.

Table 6.2: Summary of Optimal Design Parameters of the Damped Under-ride Guard using LP Model ($v_0 = 50$ km/h, $q_1 = 0.15$, $q_2 = 0.85$).

Design Variable	Parameter value
ξ_c	0.93
n_e, , n_c	1.0, 1.0
v_e (*m/s*)	2.0
p	0.5
k_{11} (*MN/m*)	1.206
k_{12} (MN/m^3)	2.938
k_{st} (*MN/m*)	2.789

The displacement, velocity and acceleration response characteristics of masses due to the engine, suspension, car bumper and the crush element attachments during an impact with the optimally damped under-ride guard parameters illustrated in Figures 6.5. In general all the lumped masses exhibit similar trends in response characteristics, while

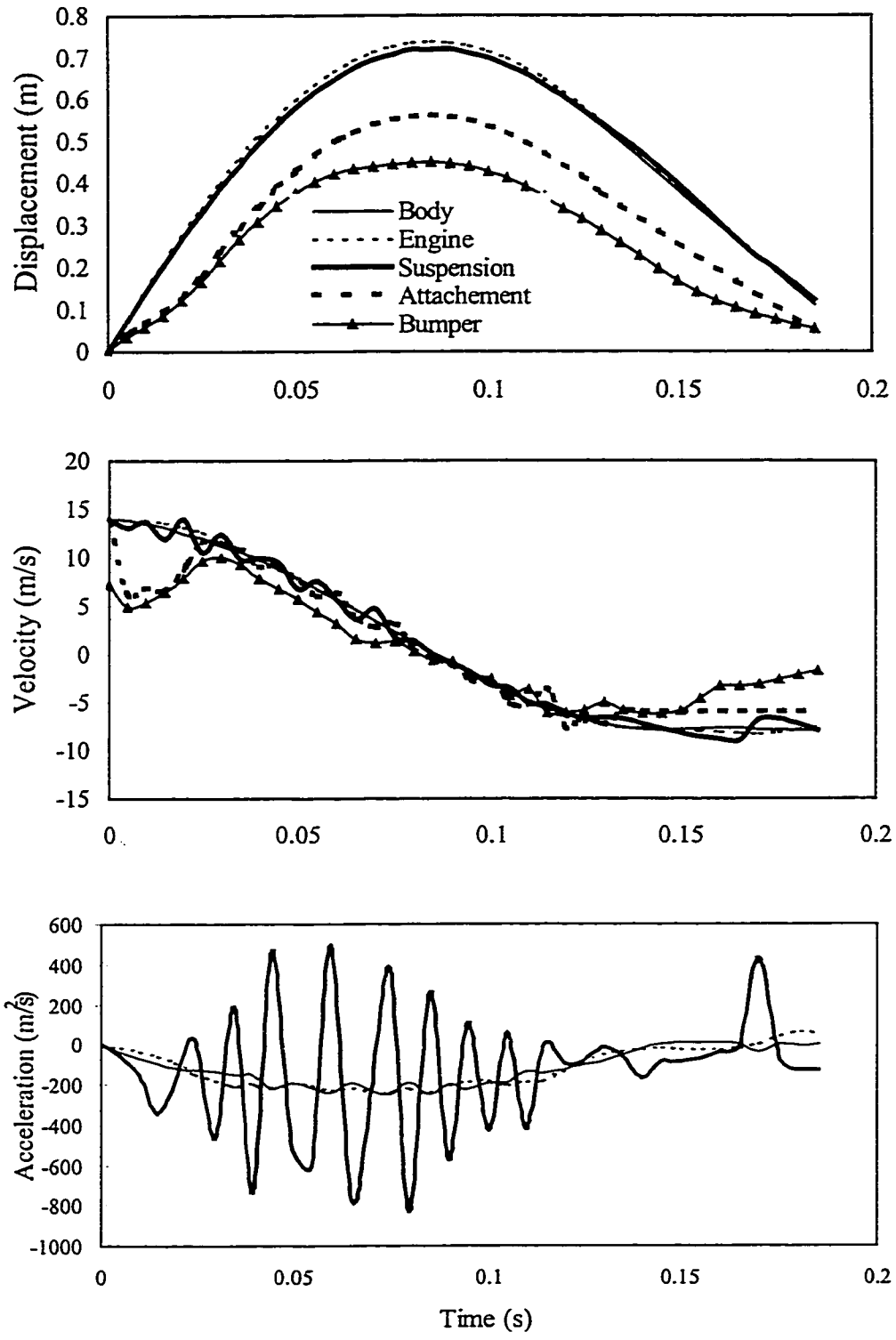

Figure 6.5: Total bumper force of the car (LP model) subject to an impact with a damped guard ($v_0 = 50$ *km/h*).

engine mass experiences a slightly higher value of peak displacement. The peak displacements of all the engine, suspension and body masses are observed to be approximately 0.7 m. While the total impact duration is 0.18 s, the peak displacement occurs at near $t \approx 0.8$ s. The displacement response of these masses further show that the relative displacement between each of them is close to zero. Thus the components connecting these masses, namely, driveline, firewall and the mounts undergo minimal deformations. The peak displacement of the bumper mass is described as the intrusion of the car the guard, which approaches 0.43 m for the limit constraint selected in the study. The peak displacement response of the attachment mass (m_{c5}) is higher than that of the bumper mass, but lower than those of m_{c1}, m_{c2} and m_{c3}. It should be noted that the peak difference in displacements of m_{c4} and m_{c5} could be related to the deformation of the crush elements. The results show that the peak deformation is approximately 0.13 m.

The velocity response characteristics of the body, engine and suspension masses are similar to those observed for impact with a rigid under-ride impact, with the exception of the duration of the impact. The acceleration response characteristics of masses due to the body, engine suspension and the bumper also show trends similar to those observed in the case of rigid under-ride. The magnitude of acceleration of the attachment mass m_{c5} was observed to be extremely high as observed under barrier impact. The acceleration response of the masses reveals that the car body mass experiences a peak acceleration of 248 m/s^2.

The performance measures of the optimal damped guards corresponding to the selected constraint limits are compared with those obtained for rigid barrier impact of the LP model of the car with the crush elements. The comparison of the performance

measures illustrated in Table 6.3, clearly demonstrates the potential performance benefits of the damped guard. The impact with the damped guard yields peak acceleration transmitted to the car body of 248 m/s^2 when the peak intrusion is limited to 0.43 m in the case of damped guard. This acceleration level is considerably lower (27%) than the 340 m/s^2 encountered under an impact with a rigid barrier. The final rebound velocities of the car body mass impacting the optimal damped guard tends to be considerably larger than that obtained under rigid guard impact. The increased rebound velocity with the damped guard is attributed to energy stored and relaxed by the flexible guard.

The results further show that the damped guard dissipates a significant portion (38.4%) of the initial kinetic energy. A relatively larger fraction of the kinetic energy, however, is absorbed through deformations of the structural components of the automobile. It should be noted that the total energy absorbed is attributed to the plastic deformations of the structural members and that of the crush elements. A lower value of relative displacement between the car masses, as discussed earlier, reveals that the energy absorbed by the structural components is minimal. The damped guard tends to dissipate 38% of the total energy, when the peak intrusion is limited to 0.45 m. An impact with a rigid guard/barrier yields absorption of 97.8% of the total energy through plastic deformations of the members. The absorbed energy reduces to only 55.6% with the damped guard with peak intrusion limited to 0.43 m. The energy absorbed by the structural members of the car impacting a damped guard is only 43% lower than absorbed under impact with a rigid guard.

Table 6.3: Performance Comparison of the Optimal Damped and Rigid Guards using LP Model ($v_0 = 50$ *km/h*).

Performance Variable	Damped Guard	Rigid Barrier Guard
Maximum intrusion (*m*)	0.43	-
Final velocity (*m/s*)	-6.5	-3.4
Peak acceleration (m/s^2)	-248	-340
Normalized dissipated energy (%)	38.4	-
Total plastic energy of springs (%)	55.6	97.8
Total Energy (%)	94.2	97.8

6.4 IMPACT ANALYSIS USING FINITE ELEMENT MODEL

The car-truck collision analysis is further carried out using the FE model of the car incorporating the crush elements coupled with both rigid and damped guards. The number of crush elements is limited to 4 in case of impact with a rigid guard, and 3 in case of impact with a damped guard. The results of the analysis, presented in terms of the performance measures discussed in Section 6.3, are discussed to illustrate the relative performance potentials of the damped guard.

6.4.1 Impact with Rigid Under-ride Guard

Finite element analysis of the impact between a modern light weight car and rigid under-ride guard model is performed using DYNA3D for an impact velocity of 50 *km/h*. The car was modeled using beam, shell, and brick elements as discussed earlier, while the under-ride guard primarily consisted of shell elements. The analyses were performed for a duration of 110 *ms*, when it was observed that the car velocity was observed to approach a nearly constant value. Figure 6.6 shows the crushing of the car at four different instants during the impact. While crushing of the front end of the car is evident,

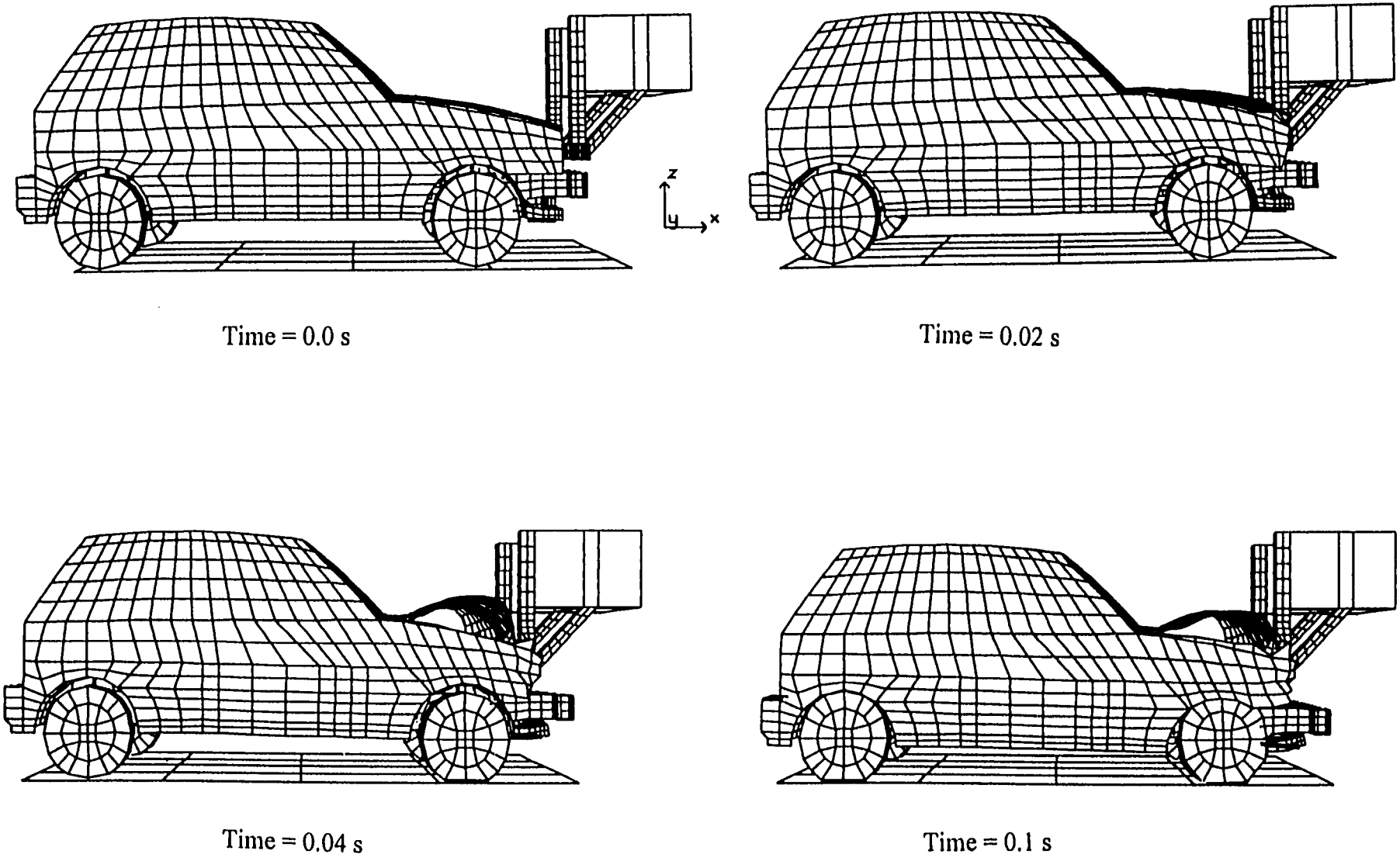

Figure 6.6: Crushing of car structure with crush elements impacting a rigid guard at four different instants.

the degree of crush is observed to be considerably lower than that observed for the car without crush elements (Figure 4.17).

The average displacement, velocity and acceleration response characteristics of different structural components of the car and the rigid under-ride guard under an impact at 50 *km/h* are illustrated in Figure 6.7. The results show the response characteristics of sheet metal, car bumper, engine cradle, engine block, under-ride guard bumper and car c.g block along the X-axis. While different components of the car body experience different magnitudes of displacement, velocity and acceleration, the passenger casualty can be approximately assessed in terms of the kinematics and dynamics of the c.g. block of the car. The displacement response illustrated in Figure 6.7 reveals that the car bumper and the c.g. block undergoes similar deflections. It should be noted that the car bumper does not make contact with under-ride guard due to the difference in ground clearance, and the c.g. block undergoes displacement due to the deformation of various displacements. The displacement response of the car bumper and the c.g. thus an estimate of the amount of intrusion under the truck. The peak displacement of the car c.g. is observed to be approximately 0.44 *m* for the selected geometry and properties of the car. While the displacements of other components of the car are observed to be less than 0.44 *m*, the rigid under-ride guard experiences only 0.05 *m* peak displacement. The displacement, velocity and acceleration response characteristics of various structural components along the Y and Z axes were observed to be considerably small and these are not presented.

The average velocity response characteristics of various members are further illustrated in Figure 6.7. The velocity response reveals that the component velocities

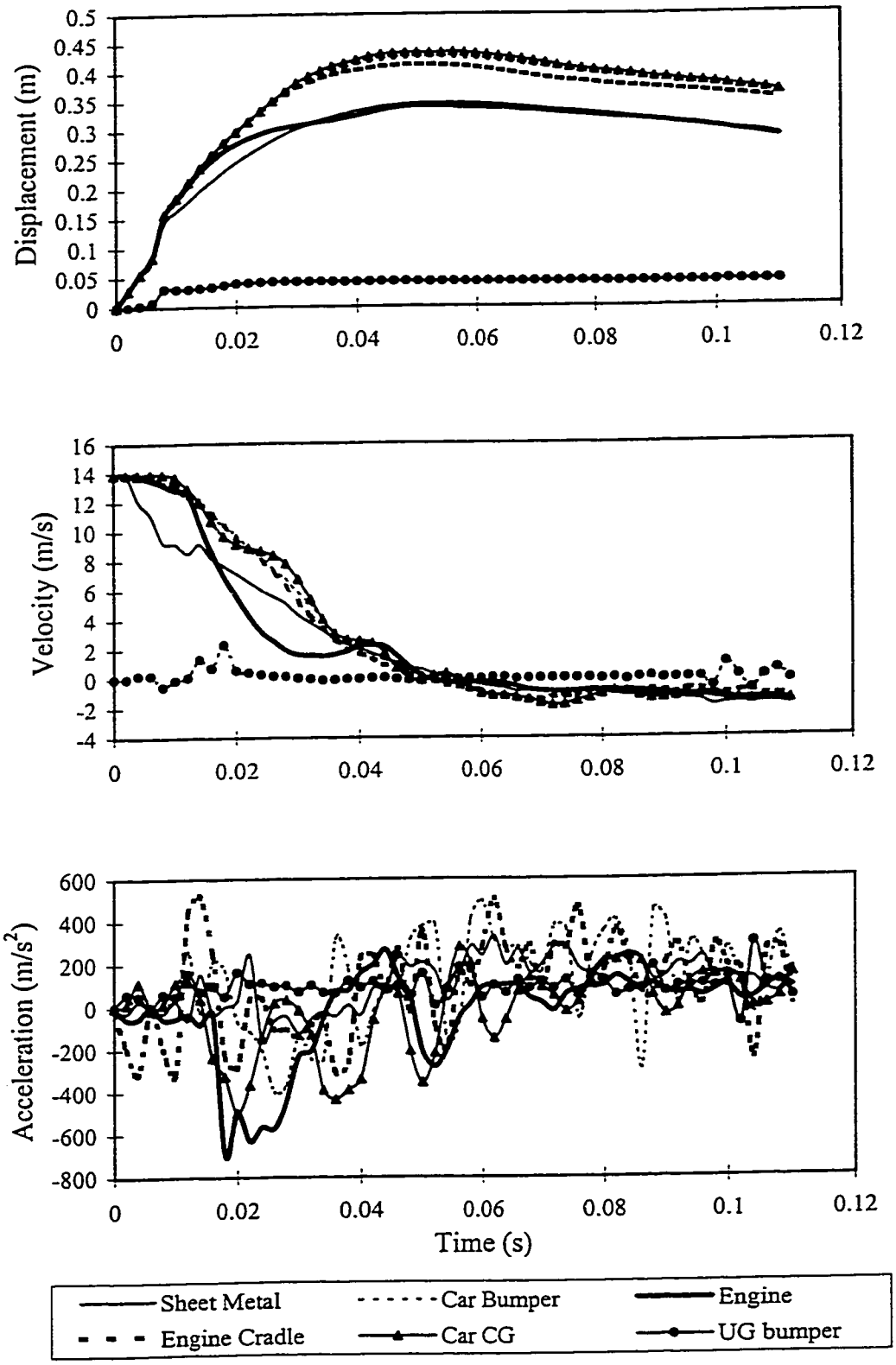

Figure 6.7: Displacement, velocity and acceleration response of the different components of the car subject to impact with rigid UG using FE analysis (v0 = 50 km/h).

approach to zero near $t \approx 0.05$ *s* where the displacements approach maximum. The vehicle then rebounds due to the transfer of energy stored in the under-ride guard. The velocities of the car components remain at approximately –0.8 *m/s* for the later stages of impact. The under-ride guard bumper experiences a peak velocity response of 2 *m/s* near $t \approx 0.02$ s and approaches zero velocity during the later stages of impact. The acceleration response characteristics reveal that the c.g. block experiences a peak acceleration of –440 m/s^2, along the X-axis, while the other members are observed to experience higher values of acceleration. The total amount of energy absorbed by the structural members are evaluated as described in Section 4.4.2, and the results are compared to those absorbed and dissipated by the damped guard in the next section.

A comparison of performance criteria for car with and without the crush elements impacting a rigid under-ride guard is illustrated in Table 6.4. The results clearly show the performance benefits of the crush elements in reducing the acceleration levels transmitted to the car body. While the impact of the car without the crush elements yields a peak acceleration of -710 m/s^2 at the c.g. block the addition of crush elements resulted in peak acceleration level to -440 m/s^2. The addition of crush elements, however, increases the peak intrusion only slightly. The peak intrusion of the car with crush elements is observed to be of the order of 0.04 *m*, which is slightly higher than 0.03 *m* attained without the crush element. In both the cases, almost entire kinetic energy of the car is absorbed by the plastic deformation of different structural members of the car and under-ride guard. The car with crush elements revealed a slight increase in the total amount of plastic work, which may be attributed to the increased level of intrusion. It should be noted that, deformations of the crush elements absorbs part of the kinetic energy and thus

the acceleration level transmitted to the passenger cabin reduces by approximately 39%. The peak acceleration level of the car with crush elements impacting a rigid under-ride guard is still higher than the 32g acceleration level recommended by the HIC.

Table 6.4: Comparison of Performance Measures of car with and without the Crush Elements Impacting a Rigid Under-ride Guard Obtained using FE analysis.

Performance Measure	without crush elements	with crush elements
Peak body displacement (m)	0.4	0.44
Final velocity	-1.8	-0.8
Peak body acceleration (m/s^2)	720	440
Total energy absorbed (%)	96.6	98.9

6.4.2 Impact with Damped Under-ride Guard

Discrete non-linear spring-damper elements are used to model the proposed under-ride guard in DYNA3D, while the crush elements are modeled as non-linear spring elements using measured force-deflection properties. The crush elements are assumed to be made of Kevlar/epoxy and the force-deflection characteristics equivalent to 3 crush elements are included to the DYNA3D input file during the analysis. The analyses are performed using the optimal guard obtained for the LP model (Table 6.2). The response characteristics of the car model comprising crushing elements and impact of damped guard are evaluated. The performance measures are further derived and compared with those obtained under impact with a rigid under-ride guard. The crushing of the front structure appeared to be quite similar to that observed from the FE analysis of model in front crush elements presented in section 4.6.2. Although some differences were observed

they were of minor nature. The qualitative crushing behavior of the automobile with crush elements is thus not shown.

The displacement, velocity and acceleration response characteristics of different structural components of the car impacting the under-ride guard are illustrated in Figures 6.8 and 6.9. The response characteristics of sheet metal, car bumper, engine block, engine cradle, car c.g. block and the under-ride guard bumper along the X-axis are presented in Figure 6.8 for the duration of impact. The displacement response of all the components with the exception of the bumper reveal similar trends with peak displacements ranging from 0.42-0.47 m. The c.g. block is observed to experience a peak displacement of 0.47 m at $t \approx 0.16$ s. However the peak displacement of the bumper along the X-axis is limited to 0.22 m, due to constraints posed by all the structural components approach a final rebound velocity of –0.3 m/s. The velocity response of the components in the X-direction further reveal similar trends. Figure 6.8 reveals that the peak acceleration of the car c.g. block is $\approx$ -198 m/s^2 which occurs at $t \approx 0.07$ s. The under-ride guard, however, reveals a high acceleration level owing to the high stiffness and damping properties of the guard. The high stiffness due to the crush elements, which are directly connected to the car bumper, also yield high acceleration of the car bumper (-400 m/s^2). The acceleration levels encountered by different structural components along the Z-axis are considerably lower than those experienced along the X-direction, as shown in Figure 6.9. The displacement response characteristics of different components in the Y and Z axis are also considerably smaller than those obtained along X-axis. Although the lateral deflection of the guard is nearly zero due to the constraints, various structural components of the car undergo lateral deformations attributed to the local crushing and

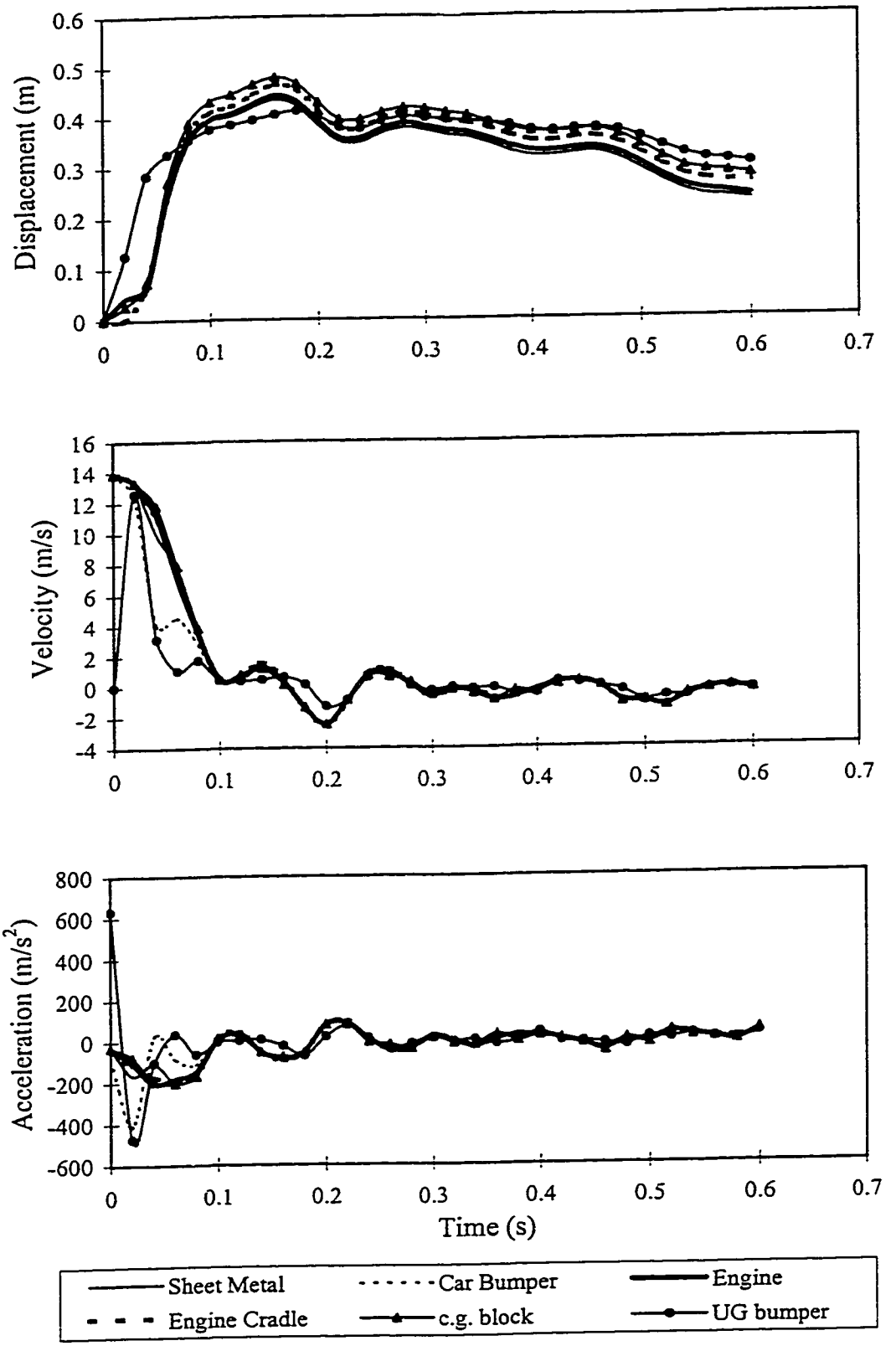

Figure 6.8: Displacement, velocity and acceleration response of the different components of the car along X-direction subject to impact with damped UG using FE analysis (v_0 = 50 km/h).

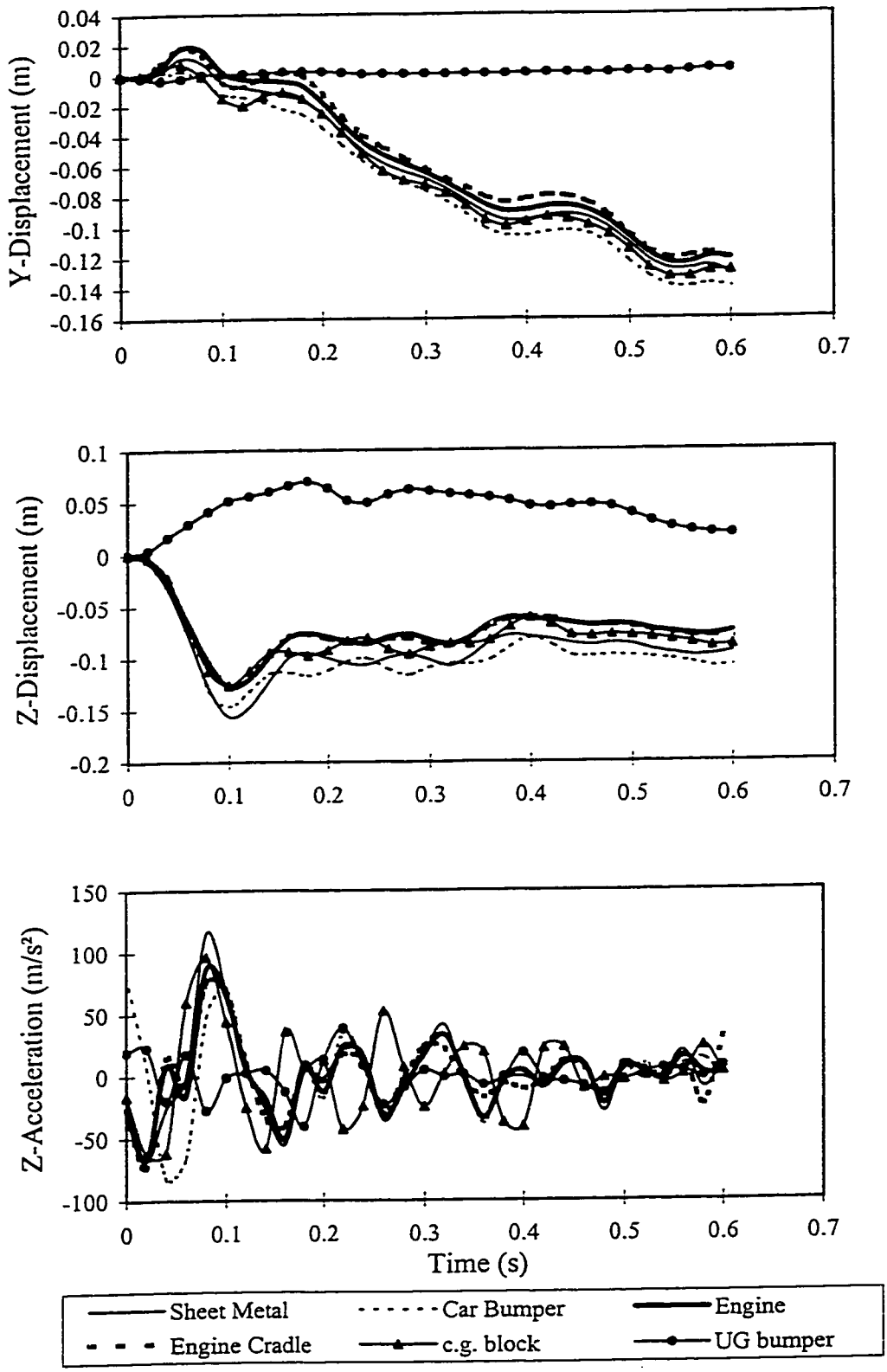

Figure 6.9: Displacement, velocity and acceleration response of the different components of the car along Y and Z-directions subject to impact with damped UG using FE analysis (v_0 = 50 km/h).

slippage. Various structural components exhibit deflections along the Z-axis, which is mostly attributed to the nose-diving of the automobile.

Table 6.5 further summarizes the performance measures for the car with and without the crush elements impacting a damped under-ride guard obtained using the finite element analysis. The performance measures for the car without the crush elements are summarized for three different designs for the optimal guard, as discussed in section 4.6.2. It should be noted that the performance measures of the elements correspond to the 'Opt2' design of the damped guard ($q_1 = 0.15$, $q_2 = 0.85$). The energy dissipated by the under-ride guard damper is evaluated using the relative displacement and velocity of the spring-damper unit with respect to the rigid frame of the truck. The resultant velocity and displacement of the spring-damper unit is obtained by vector addition of the respective quantities along the X and Z directions at each time interval. The total energy absorbed by the structural members is obtained directly from the DYNA3D post-processor which estimates the total internal energy internally by summing the energy absorbed by individual components. Table 6.5 shows that the peak intrusion of the car with the crush elements is slightly higher than that obtained from the analysis of car without the crush elements. While the 'Opt2' design of the guard, impacted by a car without crush elements resulted in peak intrusion of 0.186 m, the corresponding value for a car with the crush elements is observed to be 0.22 m. The final velocity of the car with the crush elements is also observed to be considerably reduced. The damped guard dissipates up to 45.0% of the initial kinetic energy of the car when no crush elements are used, while the amount of energy dissipated by the guard reduces to 41% for a car with crush elements. The remaining energy is absorbed by plastic deformation of different structural members, in

both the cases. The total amount of plastic energy absorbed by the different components also increase in the case of a car with crush elements owing to the additional energy absorbed by the crush elements.

The use of crush elements together with the damped guard considerably reduces the peak acceleration level of the car c.g. block. While an impact of the car without the crush elements resulted in peak acceleration levels in the range of –265 to – 307 m/s^2, for the three sets of optimum guard parameters, the addition of crush elements resulted in a peak acceleration of 198 m/s^2. The energy absorbed and dissipated during impacts with different of optimal guards are further compared in Table 6.5. A comparison of total amount of energy absorbed/dissipated by the structural members and the damper shows an improved performance by the car incorporating crush elements.

Table 6.5: Performance Comparison of the Optimized Damped Guard and Rigid Guard using Finite Element Model ($v_0 = 50$ *km/h*).

	Constraint set			
Performance Variable	Opt1	Opt2	Opt3	Car with crush elements (Opt2)
Maximum intrusion (m)	0.142	0.186	0.234	0.22
Final velocity (m/s)	-2.0	-3.35	-4.0	-0.3
Peak acceleration (m/s^2)	-307.0	-289.1	-264.9	-198.0
Normalized dissipated energy (%)	45.0	43.6	17.2	41.3
Total plastic energy of springs (%)	50.8	44.8	66.2	58.1
Total Energy (%)	95.8	88.4	83.4	99.4

6.5 SUMMARY

The performance benefit potentials of composite materials crush elements are investigated under car-truck collisions involving rigid and damped under-ride guards. The car-to-truck collision analyses are performed using lumped parameter and finite element models in conjunction with crush elements made of Kevlar/epoxy tubes. The performance benefits of the crush elements alone, and in conjunction with the damped guard in reducing the associated safety risks are illustrated in terms of the performance measures. The response characteristics of the guard and car components obtained using FE and LP analysis are discussed, while the results for car with and without the crush elements are compared. A comparison of performance measures obtained using LP and FE analysis is presented to assess the relative benefits of each method in analyzing the car-to-truck collision.

CHAPTER 7

CONCLUSIONS AND FURTHER WORK

7.1 INTRODUCTION

The energy absorption properties of the automobile are severely reduced in a car-to-truck collision due to its intrusion under the heavy vehicle structure and high rigidity of the conventional guard. The severity of such collisions can be considerably reduced by transferring the impact forces to primary energy absorbing element (bumper) of the car, and by dissipating portion of the crash energy. A flexible and damped under-ride guard implemented to the heavy vehicle can easily meet the above requirements. A systematic study is performed in this dissertation to evaluate the performance potentials of a concept of a damped under-ride guard in reducing the crash severity. The performance of the guard is evaluated in terms of performance measures related to peak intrusion, peak acceleration and the percentage of energy dissipated and absorbed by different components of the vehicle. The highlights of the thesis research are briefly outlined in the following section.

7.2 HIGHLIGHTS AND CONTRIBUTIONS OF THE WORK

Upon recognizing the necessity of analytical modeling and analysis of car-to-truck collision, the problem is approached by different methods in this dissertation. A concept of a damped under-ride guard is proposed and analyzed using three different modeling approaches for the car: (i) A single degree-of-freedom lumped parameter model; (ii)

Multi- degrees- of- freedom lumped parameter model; and (iii) an elastic plastic analysis using FE model. The influence of various parameters of the vehicle, guards, and impact speed and angle are investigated through a parametric study. The performance of the damped under-ride guard in reducing the crash severity is assessed in all the three cases in terms of a performance criterion comprising the degree of intrusion, peak acceleration and dissipated absorbed energy. The validation of the single degree of freedom model of the car-truck collision is performed using HIL simulation and test technique. The guard parameters are further optimized for all the three cases of modeling by defining an objective function based on the performance criterion. The development and incorporation of crush elements to reduce the crash severity is further studied in this dissertation.

The major contributions of this thesis dissertation thus can be summarized as follows:

- Development of a concept of a energy dissipating under-ride guard.
- Impact analysis of the proposed guard under direct and oblique impacts.
- Determination of nonlinear and asymmetric damping properties of the proposed guard to maximize the dissipation of crash energy.
- A methodology to assess the performance potentials of the guards based on the degree of intrusion, peak acceleration and dissipated/absorbed energy.
- Study of crush elements made of different composite materials.
- A Hardware-in-the-loop methodology to evaluate the energy dissipated by the damped guard under direct impacts, and to validate the analytical model.
- Lumped parameter and finite element modeling and analysis of the impact between the car and under-ride guard.

7.3 CONCLUSIONS

The systematic analysis of the car-truck collision using various methods provided a better understanding of the problem. The relative performance benefits of the proposed damped guard and the crush elements are clearly demonstrated, irrespective of the method or model employed. The major conclusions derived from the study can be summarized and listed as follows:

- A study of the impact response with two designs of conventional guards using rigid body, lumped parameter and FE analysis showed that these guards either yield excessive acceleration or intrusion of the car mass. While a stiff conventional guard resulted in peak acceleration, as high as 203g, a softer guard revealed unlimited intrusion.

- An under-ride guard with rotational flexibility and adequate damping can dissipate a considerable amount of kinetic energy, while limiting the intrusion and acceleration to acceptable levels.

- A parametric study on the performance of damped guard revealed that a heavily damped guard with stiff spring results in low intrusion, and high car mass acceleration and dissipated energy. The lightly damped and soft guard, on the other hand, yields excessive under-ride with lower car body acceleration

- The peak acceleration and the magnitude of intrusion of the car mass are observed to be related in a nearly linear manner. An increase in the permissible intrusion resulted in lower peak acceleration. The results of the optimization study revealed that a direct impact at 50 *km/h* yields peak accelerations of 312.8 m/s^2, 235.4 m/s^2 and 156 m/s^2 corresponding to permissible intrusion of 0.3 *m*, 0.398 *m* and 0.6 *m*, respectively, when the automobile is considered as a rigid mass.

- The results derived from the HIL and analytical model showed a very good correlation in terms of displacement, velocity, and peak acceleration and damper force, specifically during the contact duration, thus validating the analytical model of the car-truck collision. The differences in the measured and computed values of displacement, acceleration and, damping force, observed after the loss of contact, were primarily attributed to the time lag of the servo-hydraulic control loop.

- The HIL simulation further revealed that at low speeds of impact nearly all the kinetic energy (85% at 0.5 *m/s*) can be dissipated by the damper, while the experimental percentage of kinetic energy dissipated reduces with the impact speed (57% at 2 *m/s*).

- Impact analysis between the car and under-ride guard at different angles of impact revealed that the performance measures of the guard are strongly influenced by the impact angle and the friction properties of the contacting surfaces in a non-linear manner. It is concluded that the proposed damped guard can dissipate up to 80% of the kinetic energy under a direct impact.

- While a direct impact resulted in highest intrusion and acceleration response of the car mass, impact angles up to 17° resulted in gradual reduction of all the performance variables. The impacting car mass revealed a tendency to straighten itself during the impact process.

- The performance measures were observed to decrease gradually when the impact angle was increased beyond 30° due to rapid side-slippage and loss of contact of the two bodies.

- The energy dissipated by the guard subject to an oblique impact tends to be lower than that obtained for a direct impact, due to lower magnitude of intrusion of the car mass.

- The results also revealed that high friction impacting surfaces yield improved performance under low angles of oblique impacts. High values of surface friction, however, yield poor performance under higher angles of impact due to reduced side-slippage of the car mass.

- A comparison of the response characteristics of these guards with those of the proposed guard clearly established the superior performance of the proposed guard in limiting the peak acceleration and intrusion of the car mass. While some designs of conventional guards may yield up to 203g acceleration, a damped guard can reduce the peak acceleration level to 16g.

- Impact analysis between a car and a conventional under-ride guard derived using LP and FE models, respectively, resulted in peak acceleration response of 502 m/s^2 and 710 m/s^2 The damped guard on the other hand, resulted in much lower peak acceleration levels in both cases depending on the optimization constraint selected. A guard design using Opt1 limit constraint, for example, resulted in 312 m/s^2 and 307 m/s^2 respectively, for the two modeling approaches.

- Both LP and FE analysis of the car-truck collision revealed that most of the kinetic energy of the car is absorbed by the structural deformations, when the impact occurs with the conventional guard. The damped guard, on the other hand, reduces the magnitude of plastic deformations and hence the energy absorbed, while dissipating up to 50% of the energy in the damper. The energy absorbed by plastic deformation reduces to 44%.

- The static and dynamic tests and further analysis of the crush elements revealed that both graphite/epoxy and Kevlar/epoxy perform better as energy absorbers, when

compared to the glass/epoxy element. All the three materials revealed higher peak and average crush forces under static loading, when compared to those obtained under dynamic loads. The crush elements thus revealed negative strain rate effect on the crush force.

- The incorporation of crush elements in the LP and FE models resulted in considerable reductions in the peak acceleration levels for cars impacting rigid and damped under-ride guards. The LP model showed a reduction of peak acceleration level for an impact with conventional guard from 502 m/s^2 to 340 m/s^2, while the peak body displacement increased from 0.35 m to 0.41 m. The use of crush elements along with the damped guard further reduced the peak acceleration of the car body to 248 m/s^2. Similar reduction in the peak acceleration levels is revealed by the FE analysis. The damped guard along with crush elements resulted in a peak acceleration of 198 m/s^2.

- While a damped guard enhances the crashworthiness of the automobile involved in a collision with a heavy vehicle, the addition of crush elements further reduces the crash severity.

7.4 SUGGESTIONS FOR FURTHER WORK

The car-truck collision problem is analytically modeled and analyzed in this study. The relative performance benefits of the damped guard are established from the results obtained using different approaches. Although, the study provided comprehensive information on the car-truck collision behavior, considerable further work is necessary to derive methodologies, and design of the damped guards and crush elements. It is thus proposed to continue the efforts to realize implementable designs.

The model validation by HIL simulation method was limited to low speeds due to the limitations in available hardware. The validation can be further extended to higher impact speeds using improved hardware. A prototype of the damped under-ride guard should be developed and full-scale crash tests may be conducted to quantify the performance potentials of guard, and to verify the analytical and HIL simulation methodologies. The HIL simulation tools, comprising a high speed servo-control

mechanism, can be effectively used as a standard tool for the development and design of damped guards, which needs to be coupled with only limited number of full scale tests. The car-truck collision study, using LP and FE models can be extended, to angular impacts of the car under front-and side-under runs. The results of the car-truck rear under-ride guard study can thus be extended to side and front-end collisions. While the side impact speed may be comparable to the rear impacts, the design requirements for a front end guard may be much severe due to high relative speed between the two vehicles.

The composite material crush elements can be implemented in the front end of the automobile to reduce the crash severity with a rigid barrier or damped guard. The study, however, has to be continued to establish the crash energy absorption capacity with the attachments. The attachments on the crush element may deteriorate its performance due to local damages. Several impact tests at higher speeds should be undertaken to understand the strain rate effect on the energy absorption behavior at higher speeds.

REFERENCES

1. Murray, N.W., "Road Vehicles as Deformable Bodies in Crash Situations Especially those Involving Cars and Trucks," Proceedings of the University of Adelaide Special Symposium on the Occasion of George Sveds 80th Birthday, June 1990.

2. Riley, B.S., "Fatal accidents involving heavy goods vehicles," VDI-Berichte Nr. 367, 1980.

3. Kahane, C.J., "The National Highway Traffic Safety Administration's Evaluations of Federal Motor Vehicle Standards," SAE 840902, 1984.

4. SAE Recommended Practice, "Rigid Barrier Collision Test – Fixed Barrier (SAE J850), Moving Barrier (SAE J972)," SAE Handbook, Vol. 3, Sections 34.292, 34.289, 1996.

5. Curtis, F.V., "Dynamic Modeling of Automobile Structures from Test Data," General Motors Research Corporation, Report No. GM-197, 1979.

6. Wilson, R.A., "A Review of the Vehicle Impact Testing: How it Began and What is Being Done," SAE Transactions, Vol. 79, Paper No. 700043, 1970.

7. Macmilan, R.H., "Vehicle Impact Testing," International SAE Automobile Safety Conference Compendium, Paper No. 700404, 1970.

8. Herridge, J.T., and Mitcchell, R.K., "Development of a Computer Simulation Program for Collinear Car/Car and Car/Barrier Collisions," ASME Intersociety Conference on Transportation, Paper No. 73-ICT-34, 1973.

9. Ishisaka, T., "Analysis of Crashworthiness of Automobile Body in Collision," Mitsubishi Heavy Industries Technology Review," Vol. 132, No. 2, 1976.

10. Wierzbicki, T. and Abramowicz, W., "CRASH-CAD – A Computer Program for Design of Columns for Optimum Crash," SAE Transactions, Vol. 99, Paper No. 900462, 1990.

11. Tong, P., and Rosettos, J.N., "Modular Approach to Structural Simulation for Vehicle Crashworthiness Prediction," Report No. DOT-TSC-NHTSA-74-7, DOT, Cambridge, 1975.

12. Chang, D.C., "A Design-Analysis Method for the Frontal Crush Strength of Body Structures," SAE Transactions, Vol. 86, Paper No. 770593, 1977.

13. "Energy Absorption of High Strength Steel Tubes under Impact Crash Conditions," SAE Transactions, Vol. 86, Paper No. 770213, 1977.

14. Melosh, R.J. and Kelly, D.M., "The Potential for Predicting Flexible Car Crash Response," SAE Automotive Safety Dynamic Model Symposium, Anaheim, California, 1967.

15. Sato, T.B., "Dynamical Considerations on Automobile Collision," Journal of Society of Automotive Engineers of Japan, Vol. 20, No. 5, 1966 and Vol. 21, No. 9, 1967.

16. Tani, M. and Emori, R.I., "A Study in Automobile Crashworthiness," Automotive Engineering Congress, Detroit, Michigan, January 12-16, 1970, SAE Pap No. 700175.

17. Hamon, J., "Influence of the Behavior of the Vehicle Structure on Occupants During Collision," Ingenieurs de l'Auto, Vol. 41, No. 11, 1968.

18. Emori, R.I., "Analytical Approaches to Automobile Collisions," Automotive Engineering Congress, SAE Paper No. 680016, 1968.

19. Mayor, R.P., Theiss, C.M and Schring, D.J., "Basic Research in Automobile Crashworthiness-Analytical Studies," Cornell Aeronautical Laboratory, CAL Report No. YB-2684-4-5, 1969.

20. Egli, A., "Stopping the Occupants of a Crashing Vehicle – A Fundamental Study," Automotive Engineering Congress, SAE Paper No. 670038, 1967.

21. Kamal, M.M., "Analysis and Simulation of Vehicle to Barrier Impact," International Automobile Safety Conference, Detroit, Michigan, May 13-17, 1970, SAE Paper No. 700414, 1970.

22. Lin, Kuang-Huei, "A Rear-End Barrier Impact Simulation Model for Uni-body Passenger Cars," Research Publication of General Motors Corporation, GMR 1169, SAE Paper No. 730156, 1973.

23. Wingenbach, W.J. and Schwarz, R., "Experimental safety Vehicle Crashworthiness Design," Automotive Engineering Congress, SAE Paper No. 720070, 1972.

24. Tomassoni, J.E., "Simulation of a Two-car Oblique Side Impact Using a Simple Crash Analysis Model," SAE Paper No. 840858, 1984.

25. Winter, R., Mantus, M. and Pifko, A.B., "Finite Element Crash Analysis of a Rear-Engine Automobile," SAE Paper No. 811306, 1981.

26. Winter, R., Crouzet-Pascal J., and Pifko, A.B., "Front Crash Analysis of a Steel Frame Auto using a Finite Element Computer Code," SAE Fifth International Conference on Vehicular Structural Mechanics, April 1984.

27. Thompson, J.E., "Vehicle Crush Prediction Using Finite Element Techniques," SAE Paper No. 730157, 1973.

28. Hallquist, J.O., Benson, D.J., Igarshi, M., Shkolnikov, M.B. and Mizuno, M., "The Application of DYNA3D Large Scale Crashworthiness Calculations," 1991.

29. Vander, D.A., Chen, R.J. and Deshpande, A.S., "Passenger Car Frontal Barrier Simulation Using Finite Element Methods," SAE Paper No. 871958, 1987.

30. Johnson, J.P. and Skynar, M.J., "Automotive Crash Analysis using Explicit Finite Element Method," ASME Winter Annual Meeting, San Francisco, California, 1989.

31. Hallquist, J.O., "Theoretical Manual for DYNA3D," University of California, Lawrence Livermore National Laboratory, Report UCID-19401, 1982.

32. "DYCAST Nonlinear Structural Dynamics Finite Element Computer Code, User's Manual," Grumman Aerospace Corporation, 1981.

33. Nakamura, K. and Wasaka, Y., "Analytical Technique for Predicting Crash Response of Car Body Structural Components and Its Application," SAE Transactions, Vol. 93, Paper No. 840450, 1984.

34. Ni, C.M. and Lin, K.H., "A Mixed Method of Crash Analysis for Vehicle Structures," AIAA Paper No. 77-310, 1977.

35. Clark, J.N., Barnhart, D.F. and Hayes, W.F., "Stress Analysis of Industrial Components with Plastic and Finite Element Models," SAE Transactions, Vol. 83, Paper No. 740706, 1974.

36. Gravel, D.G., "Fatigue Analysis using Finite Element Technique," Thesis, General Motors Institute, 1974.

37. Johnson, T.M., "A Computerized Model of Material Characteristics," Noise and Vibration Laboratory, General Motors Proving Ground, 1971.

38. Kecman, D. and Miles, J., "Application of the Finite Element Method to the Door Intrusion and the Roof Crush Analysis of a Passenger Car," SAE Transactions, Vol. 88, Paper No. 790990, 1979.

39. Hallquist, J.O. and Benson, D.J., "DYNA3D-An Explicit Finite element Program for Impact Calculations," ASME Winter Annual Meeting, San Francisco, California, 1989.

40. Shkolnikov, M.B., Bhalsod D. M. and Tzeng, B., "Barrier Impact Test Simulation Using DYNA3D," ASME Winter Annual Meeting, San Francisco, California, 1989.

41. Khalil, T.B. and Vander, D.A., "Identification of Vehicle Front Structure Crashworthiness by Experiments and Finite Element Analysis," ASME Winter Annual Meeting, San Francisco, California, 1989.

42. Nalepa, E., "Crashworthiness Simulation of the Opel Vectra using the Explicit Finite Element Method," International Journal of Vehicle Design, Vol. 11, No. 2, 1990.

43. Mclvor, T.K., "Modeling and Simulation as Applied to Vehicle Structures and Exteriors," Vehicle Safety Research Integration Symposium, US Department of Transportation, 1973.

44. Hagiwara, I. and Sasakura, Y., "Vehicle Crash Simulation using Hybrid Model," SAE Transactions, Vol. 90, Paper No. 810476, 1981.

45. Hagiwara, I., Satoh, Y. and Tsuda M., "Study of an Analytical Technique and System for Conducting Vehicle Crash Simulations," International Journal of Vehicle Design, Vol. 11, No. 6, 1990.

46. Wierzbicki, T. and Abramowicz, W., "On the Crushing Mechanics of Thin Walled Structures," Journal of Applied Mechanics, Vol. 50, 1983.

47. Abramowicz, W., "Plastic Bending of Closed and Open Section Thin Walled Beams," Institute of Fundamental Technological Research, Polish Academy of Science, 1979.

48. Mahmood, H.M. and Paluszny, "Design of Thin Walled Columns for Crush Energy Management - Their Strength and Mode of Collapse," SAE 4th International Conference on Vehicle Structural Mechanics, 1981.

49. Mahmood, H.M. and Paluszny, "Stability of Plate type Columns under crush loading," ASME Computational Methods in Ground Transportation Vehicles, AMD-Vol. 50, November 1982.

50. Mahmood, H.M. and Paluszny, "Axial Collapse of Thin Walled Cylindrical Column," SAE 5th International Conference on Vehicle Structural Mechanics, 1984.

51. Mahmood, H.M. and Paluszny, "Analytical Technique for Simulating Crash Response of Vehicle Structures Composed of Beam Elements," SAE Paper No. 860820, 1986.

52. "Automotive Engineering," SAE International, June 1995.

53. Grossman, N. and Davis, S., "The United States Technical Presentation on ESV Development by Fairchild Industries," Report on the Second International Conference on Experimental Safety Vehicles, Sindenfingen, Germany, 1971.

54. Roth, A.H., "The United States Technical Presentation on ESV Development by AMF Inc.," Report on the Second International Conference on Experimental Safety Vehicles, Sindenfingen, Germany, 1971.

55. Ohkubo, Y., Akamatsu, T. and Shirasawa, T., "Mean Crushing Strength of Closed-hat Section Members, SAE Transactions," Vol. 83, Paper No. 740040, 1974

56. Gloyns, T., "The General Motors Hydraulic-Pneumatic Energy Absorber Applied to 1974 Bumper Systems," SAE Paper No. 740061, 1974.

57. Desjardins, S.P., "Aircraft Crash Survival Design Guide," Vol. 4, Aircraft Seats, Restraints, Litters and Padding, Report No. USARTL-TR-22D, 1980.

58. Kerth, S. and Maier, M., "Numerical Simulation of the Crashing of Composite Tubes," Composite Material Technology, Vol. 4, 1994.

59. Lin, K.H. and Mase, G.T., "An Assessment of Add-on Energy Absorbing Devices for Vehicle Crashworthinesss," ASME Winter Annual Meeting, San Francisco, California, 1989.

60. Thornton, P.H., "Energy Absorption in Composite Structures," Journal of Composite Materials, Vol. 13, May 1979.

61. Thornton, P.H. and Edwards, P.J., "Energy Absorption of Composite Tubes," Journal of Composite Materials, Vol. 13, November 1982.

62. Thornton, P.H., "The Crush Behavior of Glass Fiber Reinforced Plastic Sections," Composite Science and Technology, Vol. 27, 1986.

63. Farley, G.L., "Energy Absorption of Composite Materials," Journal of Composite Materials, Vol. 17, May 1983.

64. Farley, G.L., "The Effects of Crushing Speed on the Energy-Absorption Capability of Composite Tubes," Journal of Composite Materials, Vol. 25, October 1991.

65. Farley, G.L., "Crushing Characteristics of Continuous Fiber-Reinforced Composite Tubes," Journal of Composite Materials, Vol. 26, No. 1, 1992.

66. Farley, G.L., "Prediction of Energy Absorption capacity of Composite Tubes," Journal of Composite Materials, Vol. 26, No. 3, 1992.

67. Farley, G.L., "Effects of Stacking Sequence on the Impact Resistance of Carbon Fiber Reinforces Thermoplastic Toughened Epoxy Laminates," Journal of Composite Materials, Vol. 26, No. 12, 1992.

68. Berry, J. and Hull, D., "Effect of Speed on Progressive Crushing of Epoxy-Glass Cloth Tubes," Proceedings of 3rd Conference on Mech. Prop. High Rates of Strain, Oxford, 1984

69. Price, J.N. and Hull, D., "Axial Crushing of Glass-Fiber Polyester Composite Cones," Composite Science and Technology, Vol. 28, 1987.

70. Mamalis, A.G., Yuan, Y.B. and Viegelahn, G.L., "Collapse of Thin-Wall Composite Sections Subjected to High-Speed Axial Loading," Int. J. of Vehicle Design, Vol. 13, No. 5/6, 1992.

71. Mallick, P.K., "Fiber-reinforced Composites Materials, Manufacturing and Design," Second Edition, Mercel Dekker Inc., New York, 1993.

72. "Engineering Materials Handbook," Vol-1, Composites, ASM International.

73. Lo, K.H. and Gottenberg, W.G., "Design of Composite Automotive Parts: A General Discussion," CoGSME AUTOMCOM '87 Conference, June 1987.

74. Yoshiaki Ohkami (Isuzu Motor Ltd.), Kenji Takada (Honda), Kazuyoshi Motomura (Toyota), Munemasa Shimamura (Nissan) Hitohiro Tomizawa (Kanto Auto Works) and Matsuo Usuda (Nippon Steel Corp.), "Collapse of Thin-Walled Curved Beam with Closed-Hat Section - Part 1: Study on Collapse Characteristics," SAE Paper No. 900460, 1990.

75. Meadows, D.J. and Seeds, A.D., McGregor, I.J. and Kenyon, M., "Aluminum Crash Members in Axial and Bending Collapse," SAE Paper No. 922113, 1992.

76. Kirsch, P.A. and Jahnie, H.A., "Energy Absorption of Glass Polyester Structures," SAE Paper No. 810233, 1981.

77. Schmueser, D.W. and Wickliff, L.E., "Impact Energy Absorption of Continuous Fiber Composite Tubes," Journal of Engineering Material Transactions, ASME, Vol. 72, 1987.

78. Kecman, D. and Sadeghi, M., "The Compound Beam Element With Non-Linear Moment-Rotation Curves for the Side Impact and Roof Crush Analysis using DYNA3D Program," SAE Paper No. 921072, 1992.

79. Tammy, S., "The Linear Elastic-Plastic Vehicle Collision," SAE Paper No. 921073, 1992.

80. Kaiser, A., "Some Examples of Numerical Simulation in Vehicle Safety Development," SAE Paper No. 921074, 1992.

81. SAE Information Report, "Human Tolerance to Impact Conditions as Related to Motor Vehicle Design – SAE J885 JUL86," SAE Handbook, Vol. 3, Section 34.287, 1995.

82. Sheh, M.Y., Reid, J.D., Lesh, S.M. and Cheva, W., "Vehicle Crashworthiness Analysis Using Numerical Methods and Experiments," SAE Paper No. 921075, 1992.

83. Walker, B.D., Miles, J.C. and Keer, T.J., "Vehicle Crashworthiness from Lumped Parameter to Continuum Models," Crashworthiness and Occupant Protection in Transportation Systems, ASME 1993.

84. Kecman, D. Sadeghi, M.M., and Hardy, R.N., "Early Design Stages in the Development of Crashworthy Structures," Crashworthiness and Occupant Protection in Transportation Systems, ASME 1993.

85. Dandekar, B. and Van, V., "Transient Dynamic Analysis of an Automotive Bumper System," SAE Paper No. 921076, 1992.

86. Reid, J.D. and Sheh, M.Y., "Load Path Analysis in Vehicle Crashworthiness," Crashworthiness and Occupant protection in Transportation Systems, ASME 1993.

87. Toyama, A, "Numerical Analysis of Vehicle Frontal Crash Phenomena," Nissan Motor Company, SAE SP-906, Analytical Modeling and Occupant Protection Technologies, 1992.

88. Kurimoto, K., "Simulation and Crashworthiness and its Applications," Mazda Motor Company, 12th ESV Conference Proceedings, 1989.

89. Belingardi, G and Vadori, R, "On the Role of Geometrical Imperfections in the Impact Collapse of Thin-Walled Spot-Welded Beam: Numerical and Experimental Results," Crashworthiness and Occupant protection in Transportation Systems, ASME 1993.

90. Logan, R.W., Burger M.J., McMicheal, L.D. and Parkinson, R.D., "Crahworthiness Analysis Using Advanced Material Models in DYNA3D," Crashworthiness and Occupant protection in Transportation Systems, ASME 1993.

91. "Highway Accident Situations," Accident Reconstruction Magazine, June 1993.

92. Burger, H., "Bedeutung und rangfoolge von sicherheitsma Bnahmen am lastkraftwagen," VDI-Berichte Nr. 367, 1980.

93. Gloyns, P.F., "Cars in Conflict with Larger Vehicles - The Problem of Under-run," SAE Paper No. 890746, 1989.

94. Otte, D., "Collision Situation and Consequences of Injuries in Traffic Accidents of Heavy Trucks," 1993

95. Clarke, R., "Heavy Vehicle Rollover," SAE TOPTEC, Heavy Vehicle Rollovers: A Safety Issue, Atlanta, April 1993.

96. "Federal register Rear Impact Guards – fr24ja96-15," Federal Register, Volume 61, No. 16, January 1996.

97. Seiff, H., "Large Truck Accidents Exposure in the US," Proceedings of the OECD Symposium on the Role of Heavy Freight Vehicle in Traffic Accidents, Montreal, 1987.

98. Fructus, J., "Highlights of Heavy Vehicle Accidents," Proceedings of the OECD Symposium on the Role of Heavy Freight Vehicle in Traffic Accidents, Montreal, 1987.

99. Persicke, G. and Child, J.R., "A Development in Truck Rear End Safety Devices," VDI-Berichte Nr. 367, 1980.

100. Beermann, H.J., "Behavior of Passenger Cars on Impact with Under-ride Guards," International Journal of Vehicle Design, Vol. 5, No. 1&2, 1984.

101. SAE Recommended Practice, "Rear Under-ride Guard Test Procedures," SAE J260, SAE Handbook, Vol. 3, Section 34.298, 1995

102. Whirley, R.G., "DYNA3D User's Manual," Lawrence Livermore National Laboratory. 1992.

103. Jones, N., "Structural Impact," Cambridge University Press, Cambridge, 1989.

104. Material Properties of Steel., ASME Handbook, 1995

105. Thomson, W.T., "Theory of Vibrations with Applications," 4th Edition, Prentice Hall Inc. New Jersy, 1993.

106. User's Manual, "IMSL/MATH LIBRARY – Subroutines for Mathematical Applications," Problem Solving Software Systems, Version 1.1, 1989.

107. Rao, S.S., "Optimization – Theory and Applications," 2nd Edition, Wiley Eastern Limited, Bangalore, 1989.

108. Warner, B., "An Analytical And Experimental Investigation of High Performance Suspension Dampers," Ph.D. Thesis, Concordia University, 1996.

109. Besinger, F.H., Cebon, D., and Cole, D.J., "Damper Models for Heavy Vehicle Ride Dynamics," Vehicle System Dynamics, March 1993.

110. Cole, J.S., "Hardware-in the-Loop Simulation at the US Army Missile Command," SPIE Proceedings, Vol. 2741, 1996.

111. Skalka, M.S., "Twenty Years of Hardware-in the-Loop Simulation at the Eglin Air Force Base," SPIE Proceedings, Vol. 2741, 1996.

112. Murrer, R.L., "Technologies for Synthetic Environment: Hardware-in the-Loop Testing," SPIE Proceedings, Vol. 2741, 1996.

113. Kempf, D., Bonderson, L.S. and Slafer, L.I., "Real time simulation for applications to ABS Development," SAE Paper No. 870336, 1987.

114. Krohm, H., "Hardware-in-the-Loop Simulation for an Electronic Clutch Management System," SAE Paper No. 95, 1995.

115. Hanselmann, H., "Hardware-in-the-Loop Simulation as a Standard Approach for Development, Customization, and Production Test," SAE Paper No. 930207, 1993.

116. Hanselmann, H., "DSP-Based Automotive Sensor Signal Generation for Hardware-in-the-Loop Simulation," SAE Paper No.940185, 1994.

117. Ochner, U. and Hennecke, D., "Hardware in the Loop put into Practice and Applied to the Development of Suspensions," VDI Bericcte Nr. 974, 1992.

118. Blau, P.J., "Static and Kinetic Friction Coefficients of Selected Materials," ASM Handbook, Vol. 8, Page 70-75, 1995.

119. Lin, K, Augustitus, J.A. and Kamal, M., "Computer Simulation of Vehicle-to-Barrier Impact - A User Guide," General Motors Research Publications, GMR-1943, 1975.

120. Ray, M. "Automobile Crash Analysis with Rigid Post Model," AEPCO/FHWA, June 1994.